Repair, Evaluation, Maintenance, and Rehabilitation Research Program

Technical Report REMR-CS-54
July 1997

Evaluating the Stability of Existing Massive Concrete Gravity Structures Founded on Rock

by Robert M. Ebeling, Michael E. Pace

U.S. Army Corps of Engineers
Waterways Experiment Station
3909 Halls Ferry Road
Vicksburg, MS 39180-6199

Ernest E. Morrison, Jr.

N.A.S. Fallon
4755 Pasture Road
Fallon, NV 89496

Final report

Approved for public release; distribution is unlimited

Prepared for U.S. Army Corps of Engineers
Washington, DC 20314-1000

Under Work Unit 32640

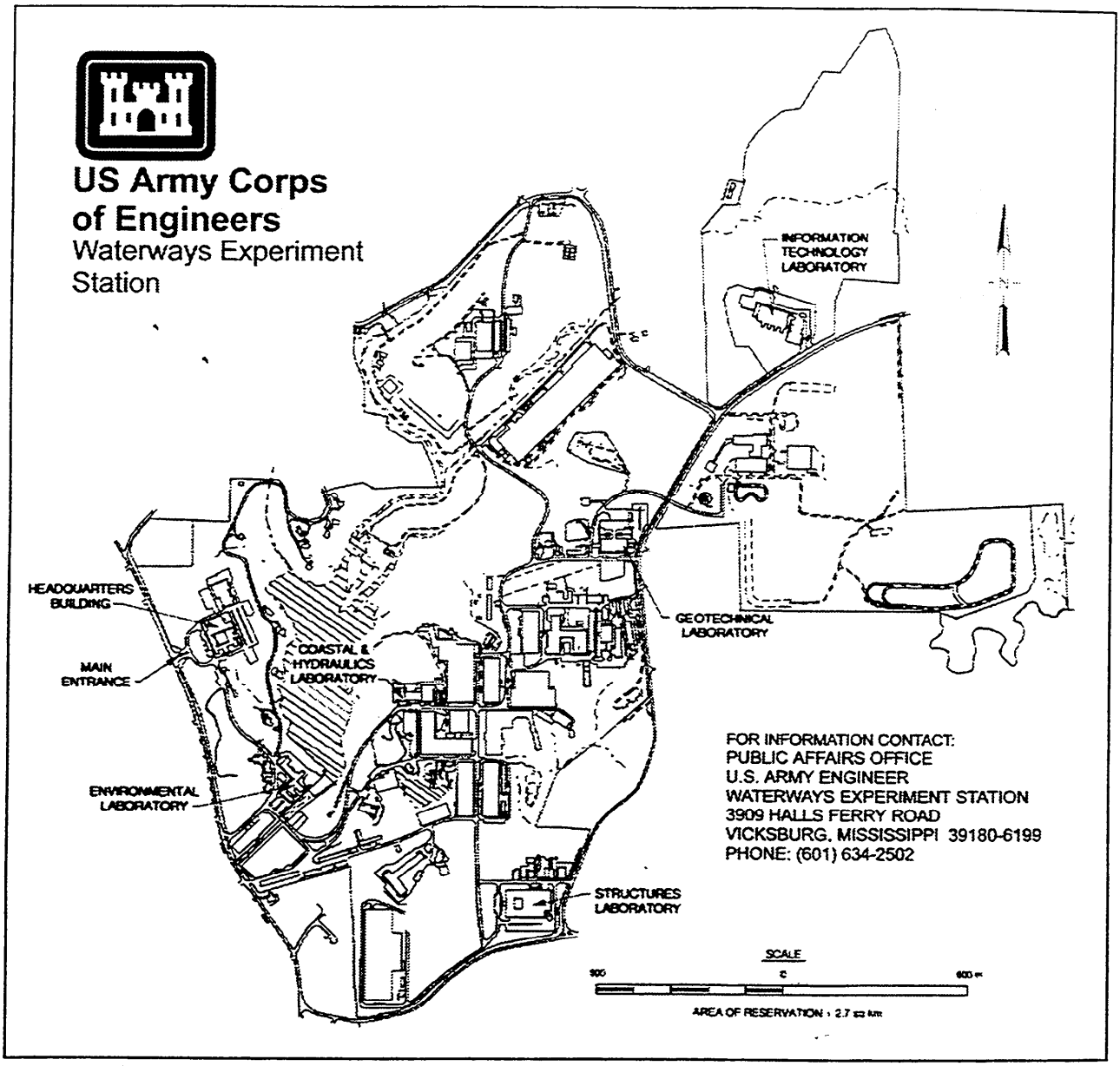

Waterways Experiment Station Cataloging-in-Publication Data

Ebeling, Robert M., 1954-

Evaluating the stability of existing massive concrete gravity structures founded on rock / by Robert M. Ebeling, Michael E. Pace, Ernest E. Morrison, Jr. ; prepared for U.S. Army Corps of Engineers.

265 p. : ill. ; 28 cm. — (Technical report ; REMR-CS-54)

Includes bibliographic references.

1. Gravity dams — Maintenance and repair — Evaluation. 2. Gravity dams — Stability —Evaluation. 3. Concrete dams — Stability — Evaluation. 4. Retaining walls — Stability —Evaluation. I. Pace, Michael E. II. Morrison, Ernest E. III. United States. Army. Corps of Engineers. IV. U.S. Army Engineer Waterways Experiment Station. V. Repair, Evaluation, Maintenance, and Rehabilitation Research Program. VI. Title. VII. Series: Technical report (U.S. Army Engineer Waterways Experiment Station) ; REMR-CS-54.

TA7 W34 no.REMR-CS-54

Contents

Preface

The work described herein was sponsored by Headquarters, U.S. Army Corps of Engineers (HQUSACE), as part of the Concrete and Steel Structures Problem Area of the Repair, Evaluation, Maintenance, and Rehabilitation (REMR) Research Program. The work was performed under Civil Works Work Unit 32640, "Stability and Remedial Measures for Existing Concrete Structures," for which Mr. James E. McDonald, Structures Laboratory (SL), U.S. Army Engineer Waterways Experiment Station (WES), was the Problem Area Leader and Dr. Robert M. Ebeling, Computer Aided Engineering Division (CAED), Information Technology Laboratory (ITL), WES, was the Principal Investigator. The HQUSACE Technical Monitor was Mr. Jerry Foster.

Dr. Tony C. Liu (CERD-C) was the REMR Coordinator at the Directorate of Research and Development, HQUSACE. Mr. Harold C. Tohlen (CECW-O) and Dr. Liu served as the REMR Overview Committee. Mr. William F. McCleese, SL, was the Program Manager.

The work was performed at ITL by Dr. Ebeling and Mr. Michael E. Pace, ITL, and Mr. Ernest E. Morrison, Jr., N.A.S. Fallon. A conventional equilibrium-based analysis of the Locks 27 gravity retaining wall was conducted by engineers of the St. Louis District and is cited in this report. The MERLIN analysis of the Locks 27 gravity retaining wall was conducted at the University of Colorado, Boulder, CO, by Drs. Victor Souma and Ron Reich. The equilibrium calculations of the SOILSTRUCT-ALPHA finite element results of Locks 27 gravity retaining wall were done by Mr. Jose Arroyo, summer student from the University of Puerto Rico at Mayaguez. The CG-DAMS analysis of Locks 27 gravity retaining wall was begun by Mr. Victor F. Diaz, summer student from the University of Puerto Rico at Mayaguez and completed by Mr. Kevin Abraham, ITL. Dr. Reed Mosher, SL, and Dr. Ebeling were the authors of the scope of work for this work unit. The report was prepared by Dr. Ebeling and Mr. Pace under the direct supervision of Mr. H. Wayne Jones, Chief, CAED, ITL, and Dr. N. Radhakrishnan, Director, ITL.

At the time of publication of this report, Director of WES was Dr. Robert W. Whalin. Commander was COL Bruce K. Howard, EN.

1 Introduction

The U.S. Army Corps of Engineers is responsible for designing and maintaining a large number of navigation and flood-control structures. Many of the older massive concrete gravity hydraulic structures are being examined to determine if rehabilitation is required to meet stability criteria. The procedures currently used for evaluating the safety of existing massive hydraulic structures are the conventional equilibrium methods. These methods are the same general methods used in the design of these structures. These engineering procedures have been used for decades by civil engineers to design new hydraulic structures and analyze existing structures. Because the conditions of equilibrium are insufficient for a complete analysis of all aspects of structure-foundation interaction involved in the stability and performance of these structures (soil-structure-foundation interaction in the case of earth-retaining structures), these conventional equilibrium methods necessarily involve assumptions regarding aspects of the loading forces and the resisting forces that act on the hydraulic structures.

Although the conditions and assumptions employed in the conventional equilibrium-based design methods are generally accepted as providing reasonable engineering procedures, and although there have been few reported failures of hydraulic structures designed using these procedures, there is some uncertainty concerning their accuracy. Differences between actual field performance and calculations from conventional analysis have been noted for some existing hydraulic structures. Conventional design methods were developed based largely on classical limit equilibrium analysis without regard to deformation-related concepts. Today, analytical tools such as the finite element method (FEM) are available that consider the manner in which the loads and resistance are developed as a function of the stiffnesses of the foundation rock, the structure-foundation interface, and rock joints within the foundation. These analytical tools provide a means to evaluate the conventional equilibrium-based design methods used to evaluate the safety of existing hydraulic structures. Specifically, these advanced analytical tools are used to identify and investigate key assumptions used in safety calculations from the conventional analysis.

The research investigation described in this report was undertaken to study the behavior of gravity hydraulic structures using the FEM of analysis and to compare the results of the finite element (FE) analysis with the results of conventional analysis. Specifically, the FEM of analysis of rock-founded, massive concrete hydraulic structures and gravity retaining structures was used to study:

a. The magnitude and distribution of stresses developed along the base of the monolith.

b. The progressive development of excessive tensile stresses which result in a gap being formed at the interface between the base of the monolith and the rock foundation.

c. The magnitude of the stabilizing shear force developed on the back of a gravity earth retaining monolith with back geometry comprising a vertical lower section and a sloped upper section.

d. The magnitude and distribution of uplift pressures developed along the base of the monolith.

e. Progressive joint closure and opening within the rock foundation of a massive concrete dam and its impact on uplift pressures with the raising and lowering of the reservoir.

The evaluation of the stability of rock-founded, massive concrete hydraulic structures and gravity retaining structures using the FE of analysis is well established in the case of concrete monoliths and rock foundations which are modeled as continuous media and are in full contact along the base-to-foundation interface. However, the FE procedure of analysis has only recently been applied to massive concrete hydraulic structures that are loaded so heavily that excessive tensile stresses develop and result in a gap being formed along the monolith to foundation interface and/or within the foundation. During the first Repair, Evaluation, Maintenance, and Rehabilitation (REMR) Research Program, a finite-element-based analytical procedure was developed to model the separation of the base of a monolith from its rock foundation during loading. This procedure was applied to a limited number of rock-founded gravity earth retaining structures. The resulting procedure is referred to as the ALPHA method (Ebeling et al. 1992) and was implemented in the FE computer code SOILSTRUCT, referred to as SOILSTRUCT-ALPHA (Ebeling, Duncan, and Clough 1990).

Two additional analytical procedures for analyzing hydraulic structures which may exhibit cracking during loading have been made available since the conclusion of the first REMR Research Program. One procedure is based on smeared crack theory and has been implemented in the computer program CG-DAMS (ANATECH 1993). The second procedure uses the discrete crack theory and has been implemented in the computer program MERLIN (Reich, Cervenka, and Souma 1993).

CG-DAMS, MERLIN, and SOILSTRUCT-ALPHA were used during this research program to investigate the response of a massive concrete hydraulic structure to loadings which would induce cracking along the monolith-to-foundation interface according to calculations using the conventional equilibrium-based method of analysis of the structure. The hydraulic structure used in this comparative study is a gravity retaining wall at Locks 27 on the Mississippi River at St. Louis, MO. These results are discussed in Chapter 2.

Calculation of the downdrag or shear forces on the backs of rock-founded concrete gravity retaining walls is discussed in Chapter 3. The calculation of this stabilizing shear force by use of a simplified procedure or by a complete soil-structure interaction analysis is discussed. These procedures are restricted to walls with engineered backfills that do not creep.

The procedures that are commonly used to calculate uplift pressures along the concrete monolith to rock foundation interface are reviewed in Chapter 4 using a series of example problems which illustrate key aspects of the procedures used to calculate uplift pressures. These procedures include (a) assignment of empirical uplift pressure distributions, (b) uplift pressure distributions resulting from confined, one-dimensional (1-D) steady-state flow, (c) uplift pressure distributions resulting from confined, 1-D steady-state flow within a tapered rock joint, and (d) uplift pressure distributions resulting from two-dimensional (2-D) flow net analysis of steady-state seepage within "homogeneous" rock foundations.

Chapter 5 discusses the results of an example of a complete gravity dam-rock foundation-rock joint interaction and the uplift pressures resulting from changes in rock joint aperture with the loading and unloading of the joint due to changes in reservoir elevation.

Chapter 6 summarizes the results of this research study and the factors affecting the stability calculations of existing massive concrete gravity structures.

Appendix A presents results of equilibrium calculations of the SOILSTRUCT-ALPHA FE following load results of Locks 27 gravity retaining wall analyses.

Appendix B describes the results of settlement calculations for a 1-D column of partially submerged backfill due to self-weight using SOILSTRUCT-ALPHA and Janbu's modulus method. These calculations were used to finalize the values assigned to stiffness parameters of the hyperbolic stress-strain soil model of the soil comprising the backfill in the SOILSTRUCT-ALPHA analysis of Locks 27 gravity retaining wall.

Appendix C shows a derivation of the nominal Poisson's ratio used in SOILSTRUCT-ALPHA for soils. The interrelationship between the value for the nominal Poisson's ratio and the variables, at-rest earth pressure coefficient, effective angle of internal friction, and the failure ratio R_F (from the hyperbolic stress-strain soil model) is derived. This appendix also shows the interrelationship between the parameters used in the bulk modulus formulation with the nominal Poisson's ratio and the modulus number K (from the hyperbolic stress-strain soil model).

Appendix D gives the theoretical development of a relationship for vertical strain in a 1-D soil column using Janbu's tangent modulus method. This relationship is used in Appendixes E and F.

Appendixes E and F provide the relationships used in Appendix B to calculate the settlement of a partially submerged soil column due to self-weight using

Janbu's tangent modulus method. Appendix E gives the theoretical development of the settlement analysis of the submerged portion of a 1-D soil column using Janbu's tangent modulus method. A concurrent rise of a hydrostatic water table with placement of backfill is assumed.

Appendix F gives the theoretical development of the settlement analysis of the "moist" portion of a 1-D soil column using Janbu's tangent modulus method. A concurrent rise of a hydrostatic water table with placement of backfill is assumed.

Appendix G gives the theoretical development of the settlement analysis of a moist 1-D soil column using Janbu's tangent modulus method. The soil column comprises two soil regions, each with a constant total unit weight. No water table (i.e., pore water pressures equal to zero) was assumed to be present in the backfill.

Appendix H gives the theoretical development of the rebound analysis of a 1-D soil column due to a postconstruction rise in the water table using Janbu's tangent modulus method. The soil column comprises two soil regions, each with a constant total unit weight. The relationships given in Appendix G are used to calculate the settlement of a moist soil column due to self-weight, while the rebound due to a postconstruction rise in the water table is calculated using the relationships derived in this appendix. Hydrostatic pore water pressures are assumed in this derivation.

2 Calculation of Progressive Development of a Gap Between Monolith Base and Rock Foundation of Gravity Retaining Walls

Corps guidance for the stability analysis of existing massive concrete gravity hydraulic structures is centered around the use of the conventional equilibrium method of analysis, which is based largely on classical limit equilibrium analysis without regard to deformation. Because the conditions of equilibrium are insufficient for a complete analysis of all aspects of structure-foundation interaction involved in the stability and performance of these structures (soil-structure-foundation interaction in the case of earth retaining structures), these conventional equilibrium methods necessarily involve assumptions regarding aspects of the loading forces and the resisting forces that act on the hydraulic structures. Examples of typical assumptions made regarding the loading forces acting on the free body of the concrete monolith through which imaginary section(s) are made are the magnitude and distribution of uplift pressures acting normal to the base of the monolith and the magnitudes and distribution of normal pressures and shear stresses along the backs of gravity earth retaining structures. An example of typical assumptions made regarding the resisting forces acting on the free body of the concrete monolith is the magnitude and distribution of the effective compressive stress (and effective tensile stress in some instances) acting normal to the base of the monolith through which imaginary section(s) are made. The effective compressive stresses can, in turn, impact the ultimate shearing resistance computed for the interface when an effective stress-based shear strength criterion such as Mohr-Coulomb is used.

Today, analytical tools such as the FEM are available that can consider the manner in which loads and resistance are developed as a function of the stiffness of the foundation rock (or soil), stiffness of the structure, and the structure-to-foundation interface. Recent research efforts have been directed toward developing analytical procedures using the FEM to analyze problems regarding loss of contact between the retaining wall base and its foundation. This situation arises

when structures are loaded so heavily that excessive tensile stresses develop and result in a gap being formed along the monolith-to-foundation interface and/or within the foundation. Three approaches have been used to analyze this type of problem, one involving the modeling of a predetermined plane along which separation is presumed to develop using interface elements, the second involving the use of concepts of fracture mechanics and discrete crack analysis, and the third involving the use of concepts of smeared crack theory.

Three procedures formulated using the FEM are employed to evaluate the conventional equilibrium method on the existing earth retaining structure. The gravity wall, Monolith 7E, forms part of one side of Locks No. 27, an existing navigation structure and its auxiliary lock, on the Mississippi River.

Monolith 7E was selected for study based on the results of a conventional equilibrium-based method of analysis. These results are summarized in this chapter, along with those of the three FEM analyses of Monolith 7E using SOILSTRUCT-ALPHA, MERLIN, and CG-DAMS.

Locks 27 Gravity Retaining Wall

Locks 27, located at mile 185.1 (297.89 km) of the Mississippi River Navigation Channel, is a gravity monolith on the east land wall of the main navigation lock approximately 200 ft (60.96 m) downstream from the upstream lock gate. Figure 1 shows a typical cross section of the 34.5-ft- (10.52-m-) wide Monolith 7E, which was constructed in a 3-ft- (0.91-m-) deep key into rock. For the analyses described herein, the effect of the key is ignored, and it is assumed that the foundation-to-rock interface is at elevation 340.[1] Throughout this report, every elevation is in feet referenced to mean sea level. The idealized monolith (Figure 2) is 45 ft (13.72 m) wide at the base and 92 ft (28.04 m) tall and retains 82.7 ft (25.1 m) of backfill.

The water table was assigned to el 396 based on piezometric recordings within the backfill. Hydrostatic water pressures were assigned within the backfill for all analyses described herein, and a dewatered lock was assumed with the pool at el 340.

Following Loads Applied to Locks 27 Gravity Retaining Wall

In all analyses described in this chapter, it was assumed that the monolith was loaded by a predefined lateral pressure of given magnitude and distribution. The soil backfill was not represented in the analysis. Lateral pressures were established using conventional concepts for earth and water loadings on retaining wall

[1] All elevations (el) cited herein are in feet referenced to the National Geodetic Vertical Datum.

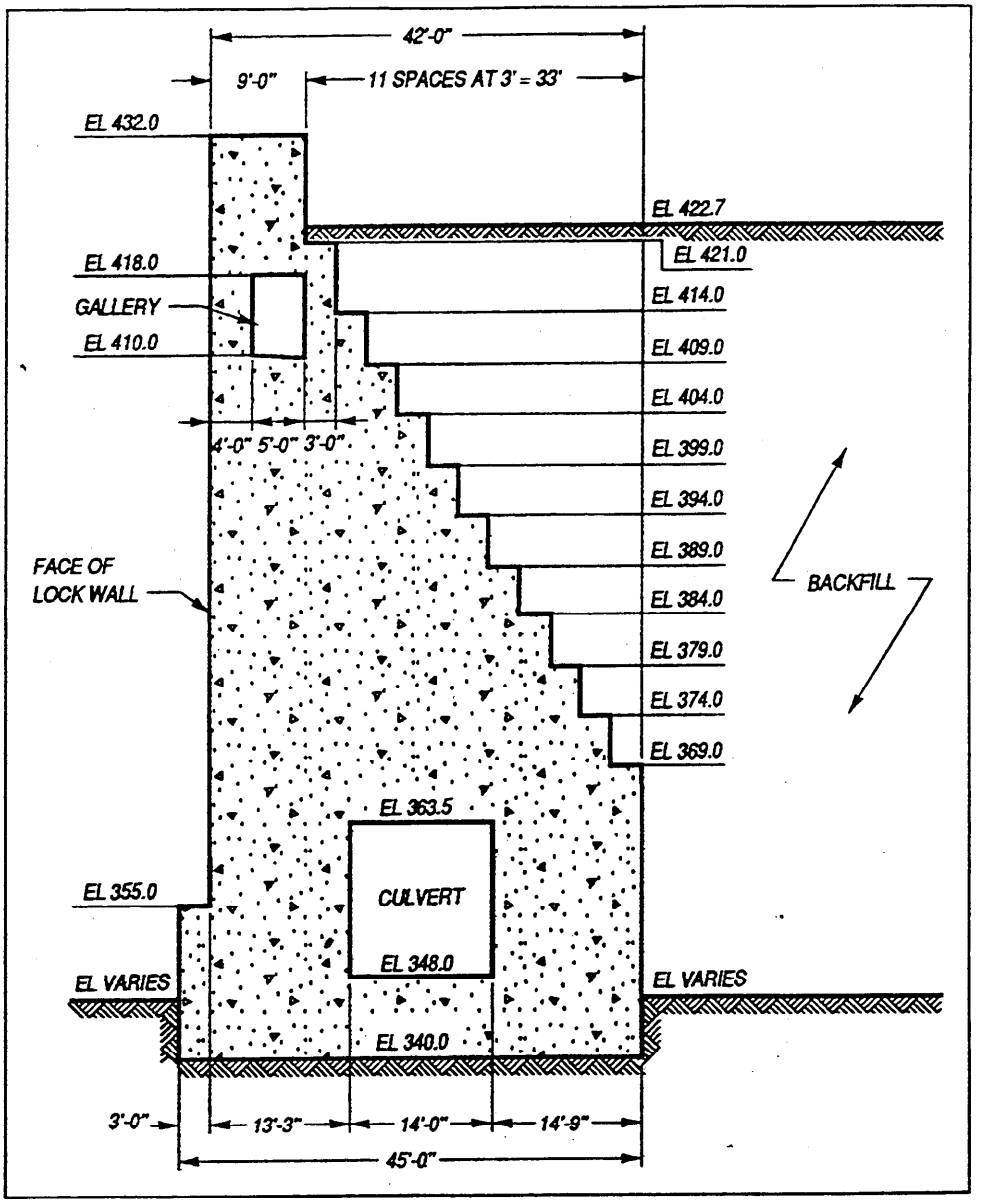

Figure 1. Locks 27 Monolith 7E cross section (1 ft = 0.305 m)

systems and were applied to the wall in a series of steps to determine the response of the structure to gradually increasing loads. Therefore, the magnitudes and distributions of the loadings were uncoupled from the action of the wall-foundation system. Regardless of how much the wall moved or of the form of the structure movement, the loading was not changed. This form of loading is termed "following load analysis."

The loading scheme used in the following load analyses and shown in Figure 3 has four basic components. First are the vertical loads induced by the weight of the monolith, the weight of the wedge of soil backfill contained in the region bounded by the monolith-backfill interface, and the vertical plane

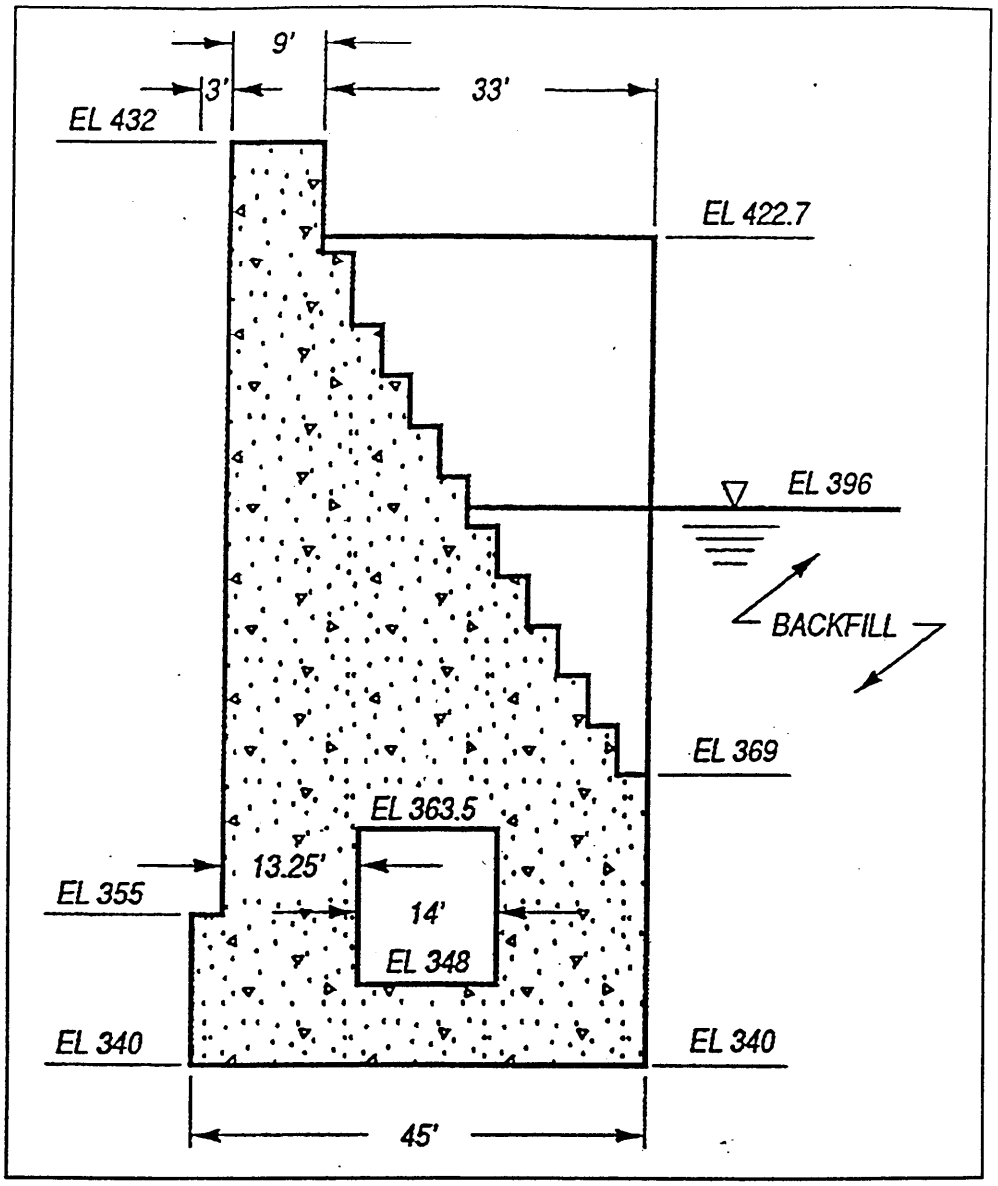

Figure 2. Idealized Locks 27 Monolith 7E cross section (1 ft = 0.305 m)

originating at the heel of the monolith. Second is the lateral effective stress assumed to be generated by the soil backfill and water in the backfill. Third is the vertical shear force directed downward along the plane extending vertically from the heel of the wall through the backfill (sometimes referred to as a down-drag force). Fourth is the water pressure acting along the base of the monolith and the pressure resulting from water flow along the interface between the monolith and the rock foundation.

At-rest earth pressures were assigned normal to the plane extending vertically from the heel of the wall through the backfill (Figure 3). Lateral earth pressures corresponded to an at-rest earth pressure coefficient K_o of 0.45. A vertical shear force (also referred to as a downdrag force) was assigned to this plane. A shear

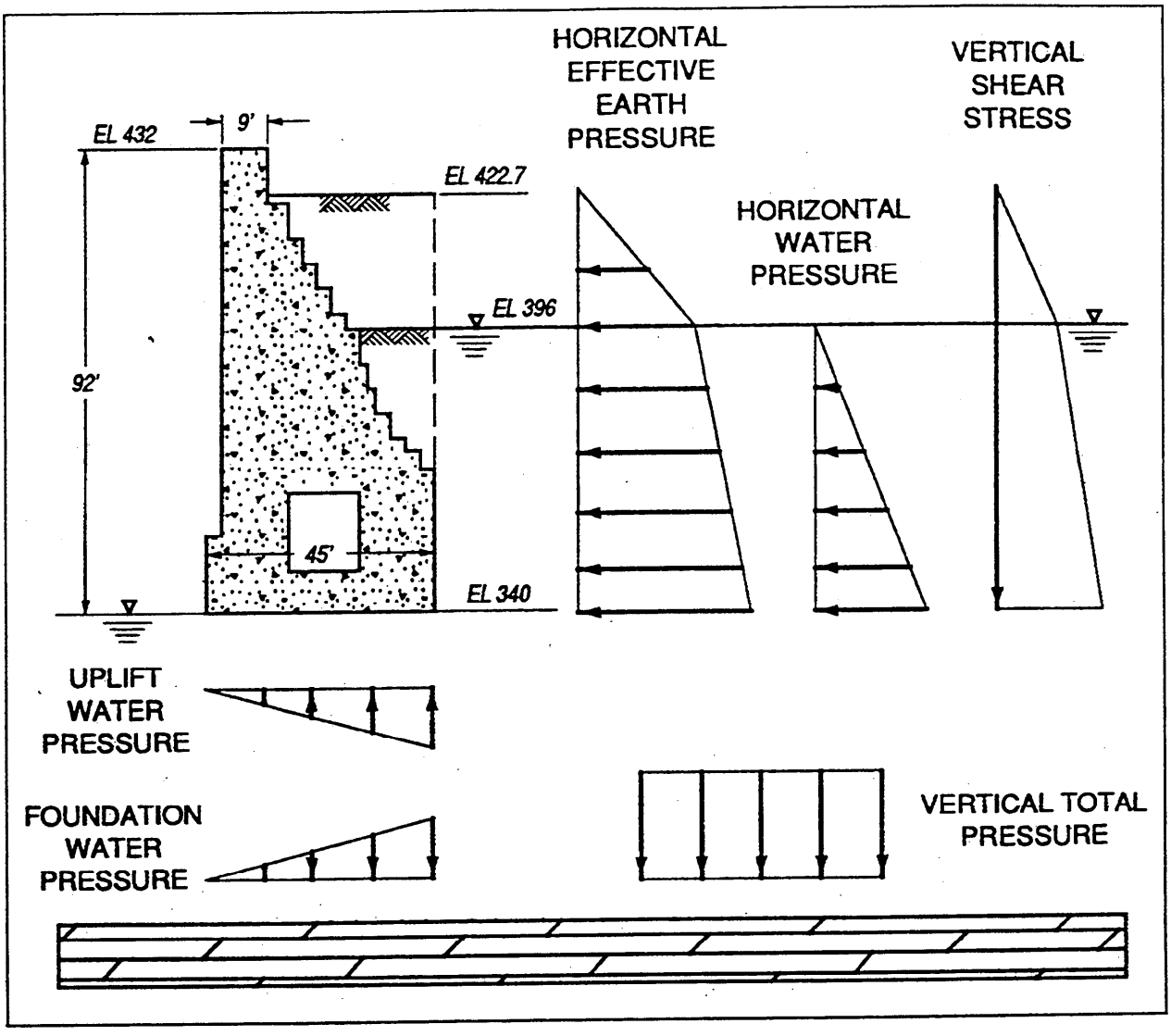

Figure 3. Applied pressures - full contact along the base (1 ft = 0.305 m)

force corresponding to a vertical earth pressure cefficient K_v of 0.09 was assigned in all analyses.

The monolith and foundation were assumed to be impervious. Water flow from the backfill to the pool in front of the monolith was confined to the interface between the base of the monolith and the foundation. A linear head loss was assigned to this interface region where the monolith retained contact with the foundation. For the interface region where the monolith had separated from its foundation, hydrostatic water pressures corresponding to the hydrostatic head within the backfill were assigned. Water pressures were assigned along the interface as shown in Figures 3 and 4 in all analyses.

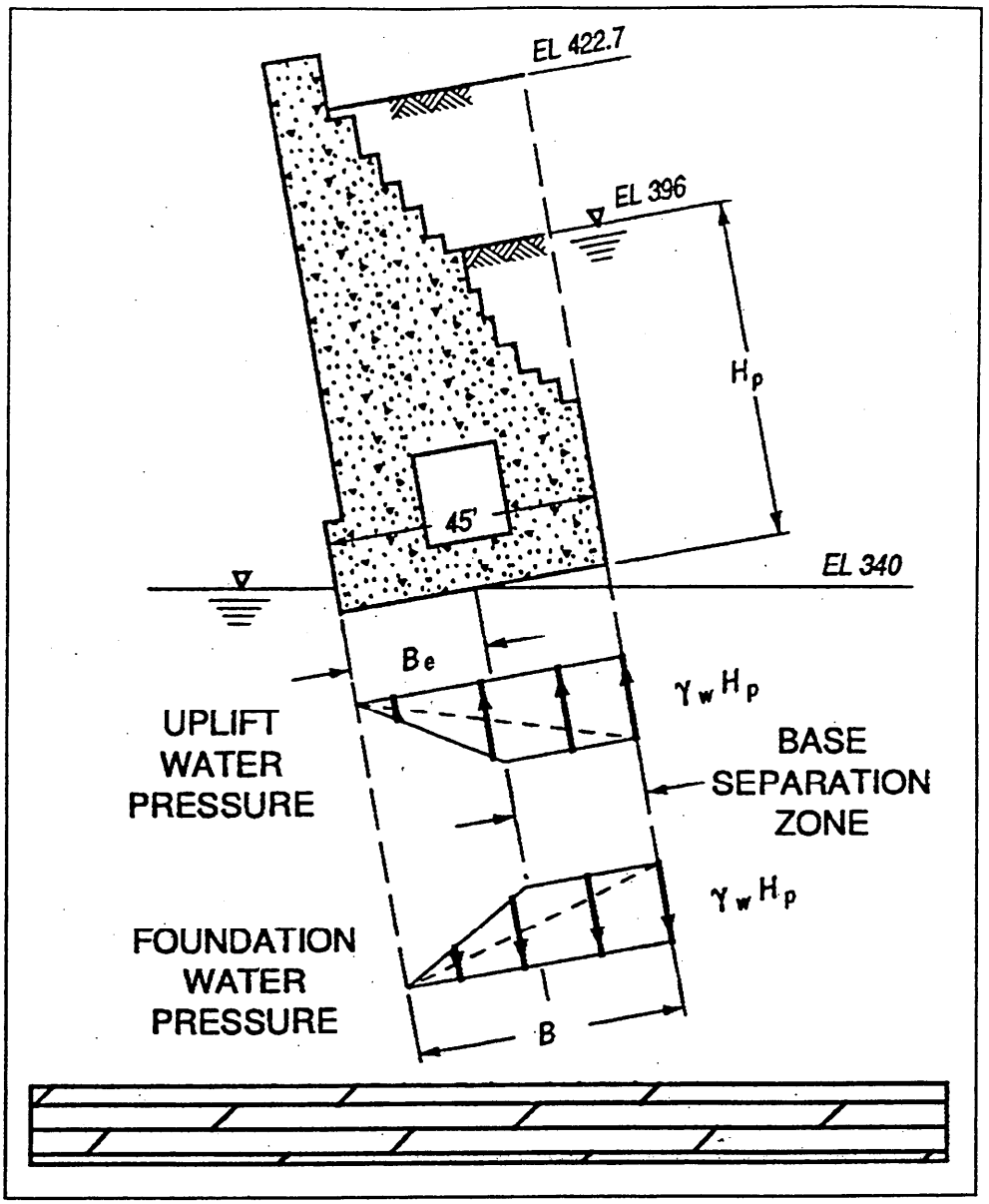

Figure 4. Uplift pressures - applied during base separation (1 ft = 0.305 m)

Conventional Equilibrium-Based Analysis of Locks 27 Gravity Retaining Wall

The conventional equilibrium method of analysis of the Locks 27 gravity retaining wall is based on classical limit equilibrium analysis without regard to deformation. The forces acting on the free body of the concrete monolith are shown in Figure 5(a). The force W equals the sum of the weight of the monolith plus the weight of soil backfill contained in the region bounded by the monolith-backfill interface and the vertical plane originating at the heel of the monolith. A unit weight of concrete equal to 150 pcf (2,402.76 kg/m^3) was used to compute

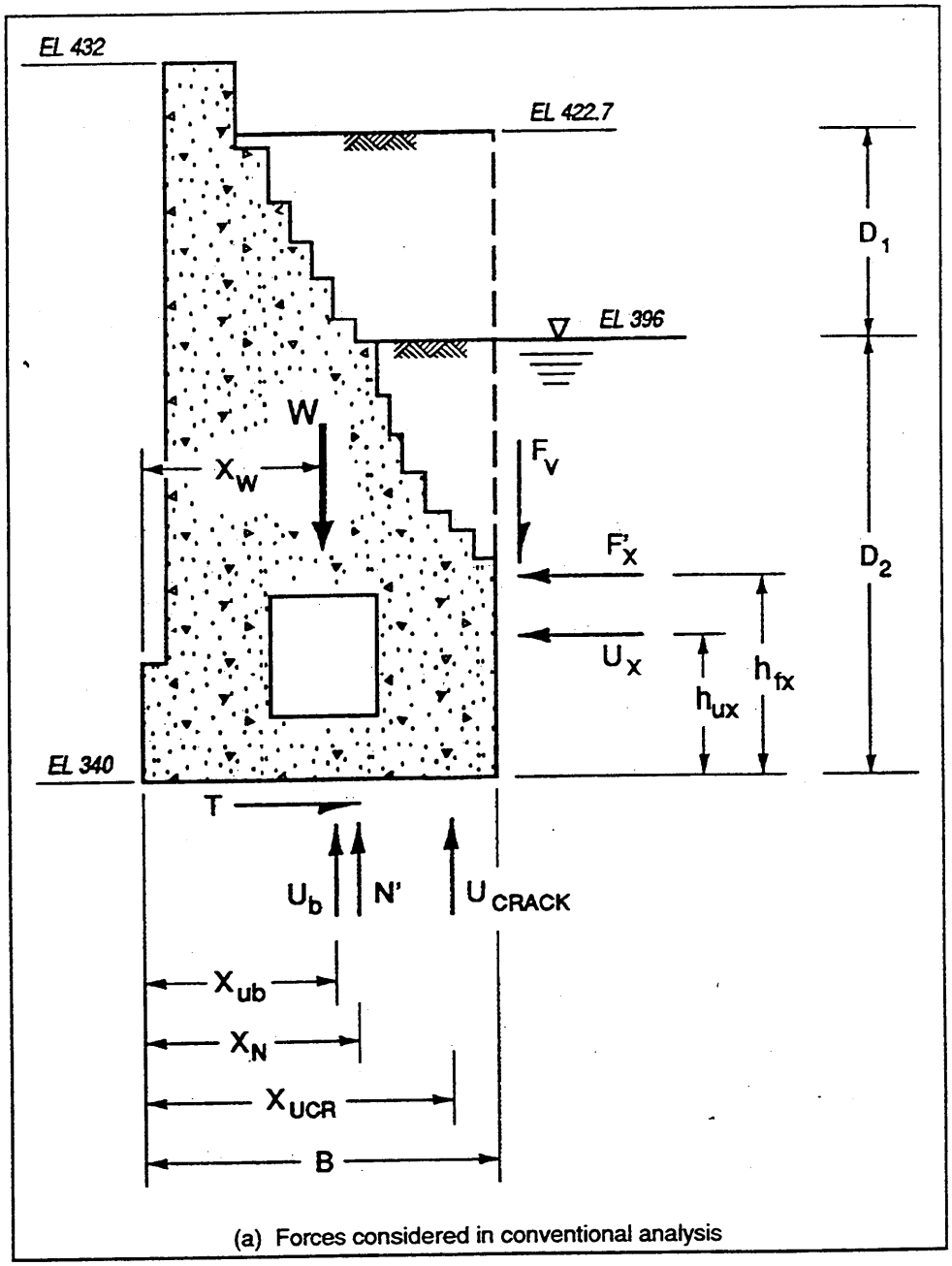

(a) Forces considered in conventional analysis

Figure 5. Forces acting on monolith (Continued)

the weight of the monolith. F'_x in Figure 5(a) equals the resultant of the horizontal effective earth pressure distribution shown in Figure 3 and was computed using K_o equal to 0.45 with hydrostatic water pressures within the backfill.

$$F_x' = K_o \cdot \left[\frac{1}{2} \gamma_{moist} (D_1)^2 + \gamma_{moist} (D_1 D_2) + \frac{1}{2} \gamma_b (D_2)^2 \right] \quad (1)$$

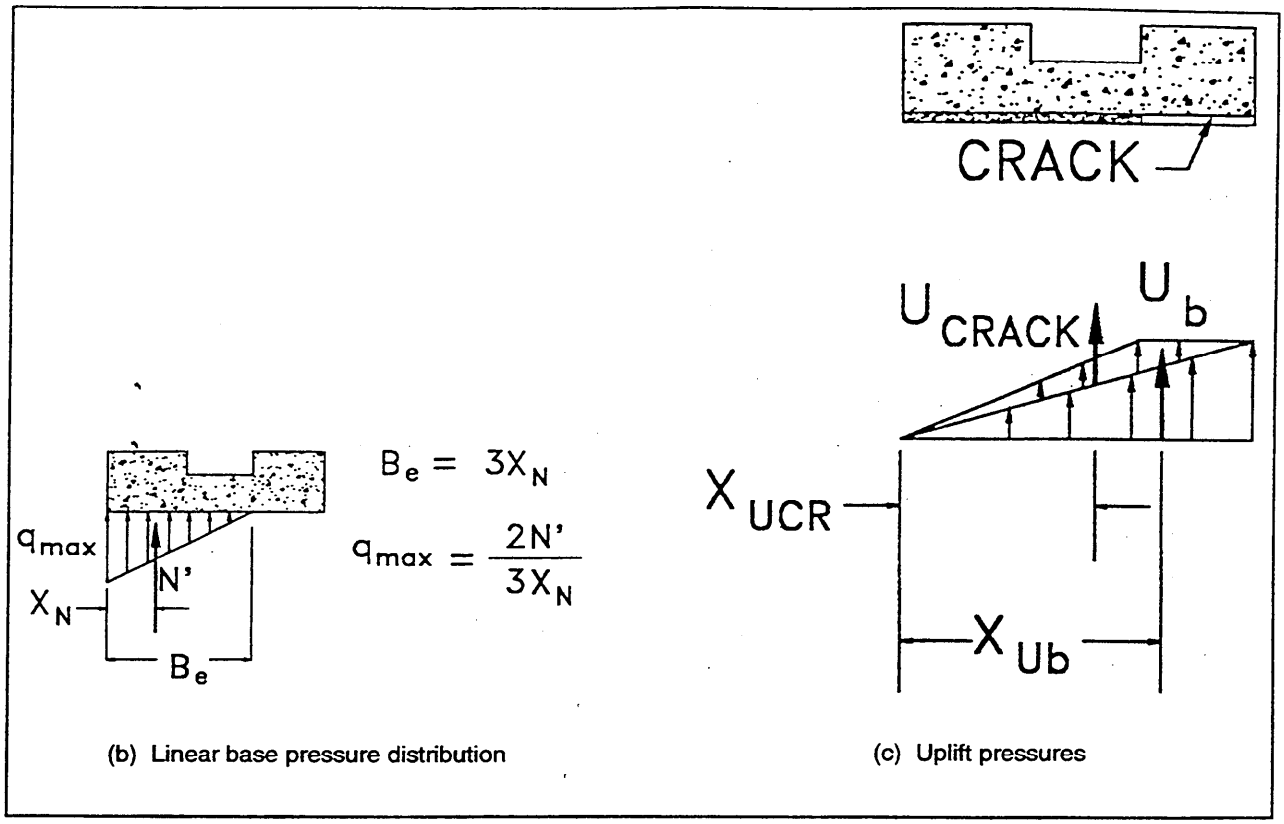

Figure 5. (Concluded)

where

γ_{moist} = moist unit weight of backfill (above the water table)
= 125 pcf (2,002.3 kg/m^3)

D_1 = thickness of moist backfill above the hydrostatic water table

D_2 = thickness of submerged backfill above the base of the wall

γ_b = buoyant unit weight of submerged backfill, $\gamma_{sat} - \gamma_w$
= 67.6 pcf (1,082.85 kg/m^3)

γ_{sat} = saturated unit weight of submerged backfill
= 130 pcf (2,082.39 kg/m^3)

γ_w = unit weight of water
= 62.4 pcf (999.55 kg/m^3)

As indicated in Figure 5(a), the total height of the backfill against the wall is the sum of thicknesses D_1 and D_2:

$$H = D_1 + D_2 \tag{2}$$

F_v in Figure 5(a) equals the resultant of the vertical shear stress distribution shown in Figure 3 and was computed using K_v equal to 0.09.

$$F_v = K_v \cdot \left[\frac{1}{2}\gamma_{moist} (D_1)^2 + \gamma_{moist} (D_1 D_2) + \frac{1}{2} \gamma_b (D_2)^2 \right] \tag{3}$$

U_x in Figure 5(a) equals the resultant of the horizontal water pressure distribution shown in Figure 3.

$$U_x = \frac{1}{2} \gamma_w (D_2)^2 \tag{4}$$

The assumed linear effective base pressure distribution is shown in Figure 5(b) for the case of a crack extending from the heel to the point along the base in which the effective normal pressure is in compression. Zero tensile strength is assumed for the material comprising the monolith-to-rock foundation interface in this problem. The term B_e is the width of the effective base contact. Hydrostatic water pressures are assumed along the cracked portion of the base in this figure. The total uplift force normal to the imaginary section through the base of the monolith in Figure 5(c) is equal to the sum of the uplift forces U_b and U_{CRACK}. U_b is the resultant force for a linear uplift pressure distribution along the interface. U_{CRACK} is the resultant force of uplift pressures in excess of the linear uplift pressure diagram extending from the heel to the toe of the wall. When no crack is present, U_{CRACK} equals zero, and the total uplift equals U_b.

Figures 6, 7, and 8 summarize the three equations of equilibrium used in solving for the values of three unknowns; the resultant shear force T along the base, the effective force N' normal to the base, and the distance $x_{N'}$ from the toe to N'.

A wall is safe against sliding along the bottom of the wall and the rock foundation when the magnitude of the ultimate shear force that resists sliding along this interface (T_{ult}) is greater than the magnitude of the driving shear force (T in Figure 6). The safety of the wall against sliding can be determined by evaluating the mobilized angle of interface friction along the base. In this report, the base interface friction angle is called δ_{base}, and the value of δ_{base} required for horizontal equilibrium of the wall is called $\delta_{mobilized}$. The subscript mobilized signifies the mobilized value of δ_{base}. The value of $\delta_{mobilized}$ can be expressed as follows:

$$\delta_{mobilized} = \tan^{-1} \left(\frac{T}{N'} \right) \tag{5}$$

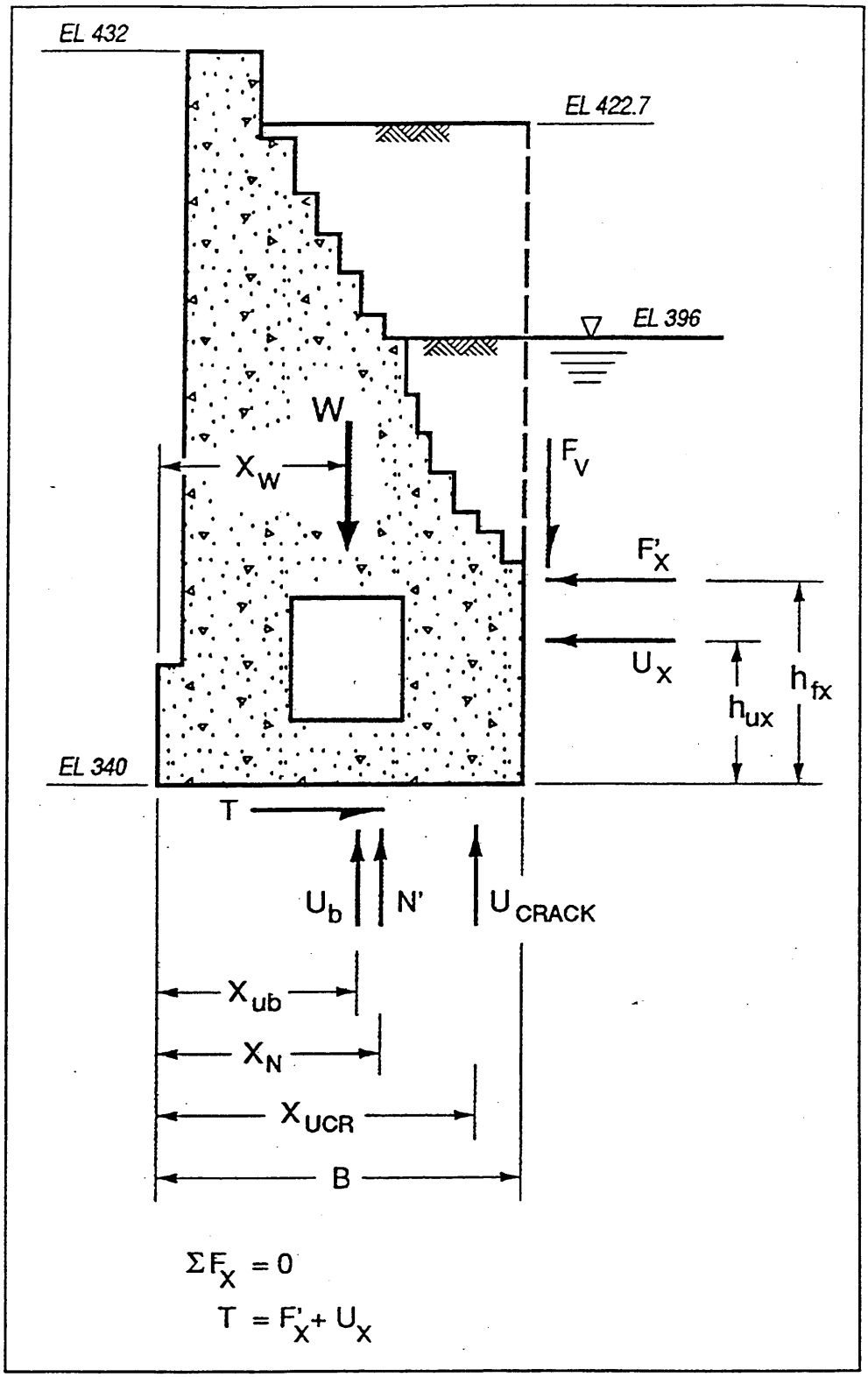

Figure 6. Equilibrium of horizontal forces

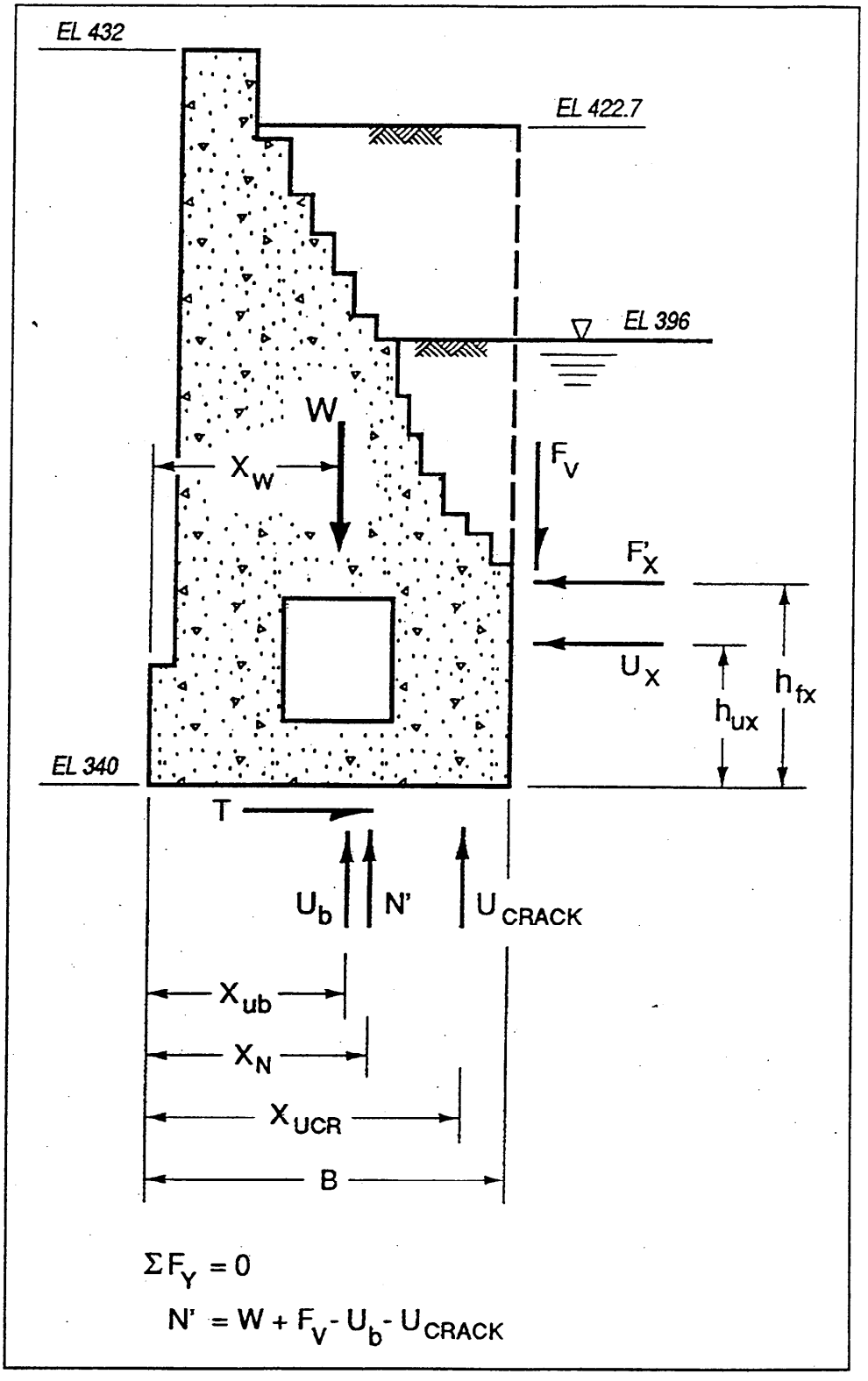

Figure 7. Equilibrium of vertical forces

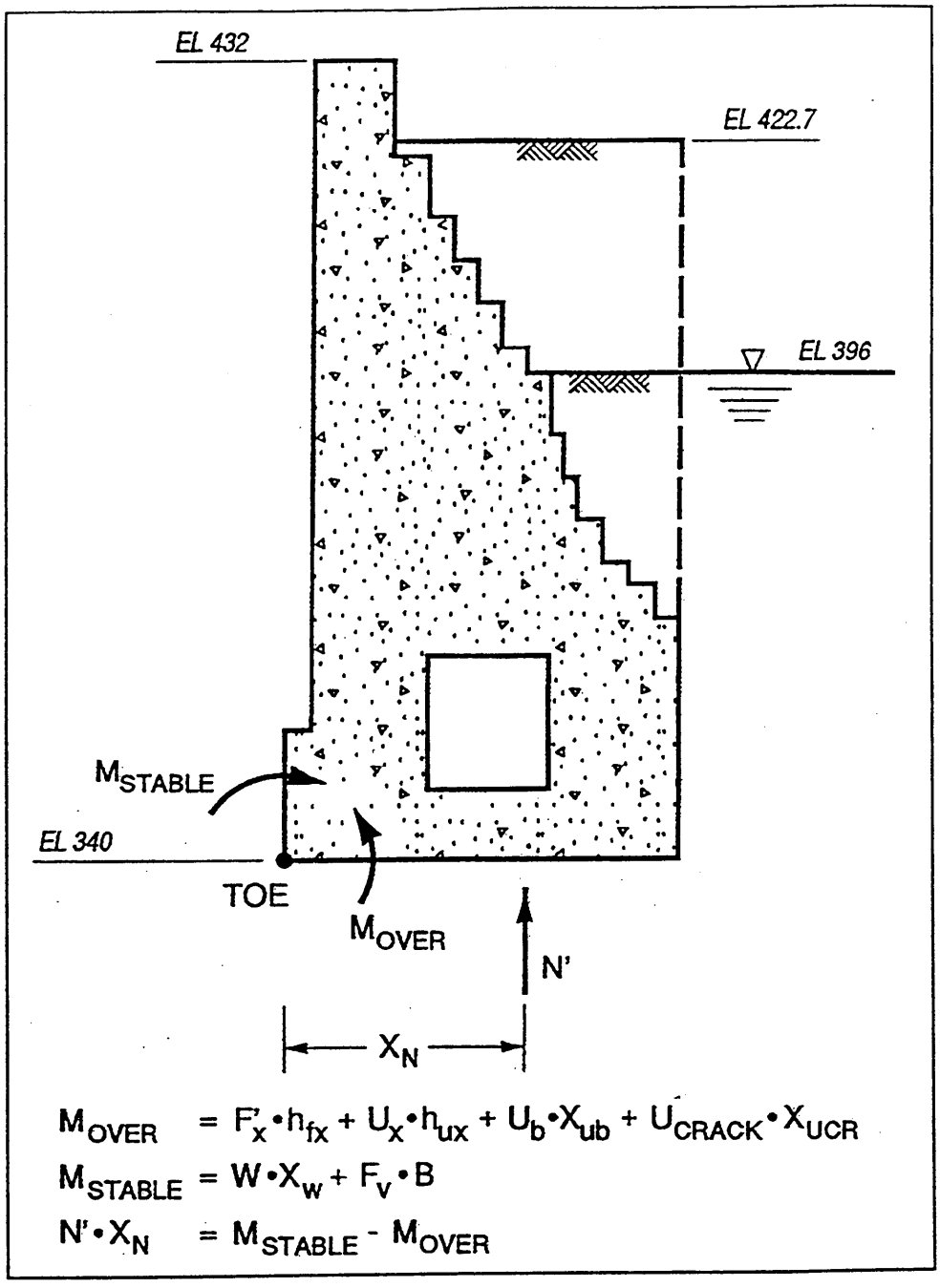

Figure 8. Moment equilibrium

The solution for the value of shear force T is straight forward for a given set of backfill loads (Figure 6). The solution for the value of effective normal force N' is described later. The factor of safety against sliding of the wall is equal to the ratio of the friction angle of the interface to the mobilized angle of interface friction:

$$F_s = \frac{\tan \delta_{base-max}}{\tan \delta_{mobilized}} \quad (6)$$

where $\delta_{base-max}$ is the maximum possible value of the base interface friction angle, a value that would cause sliding of the wall. For a wall to be safe with regard to sliding, the value of F_s should be greater than 1.0. A frequently used criterion of safety for earth retaining structures is that the factor of safety against sliding should be at least 1.5 for usual loadings representing normal operations (e.g., Engineer Manual (EM) 1110-2-2502 (Headquarters, Department of the Army 1989)). For new navigation locks, the minimum factor of safety against sliding is 2.0 for usual loadings (EM 1110-2-2602). Stability criteria for existing navigation locks are discussed in Engineering Technical Letter (ETL) 1110-2-310 (Headquarters, Department of the Army 1987).

The factor of safety against sliding may also be expressed in terms of shear forces.

$$F_s = \frac{T_{ult}}{T} \quad (7)$$

Where the maximum possible shear force to resist sliding along the base, T_{ult} is expressed as follows:

$$T_{ult} = N' \tan \delta_{base-max} \quad (8)$$

Equation 7 is equivalent to Equation 6.

The safety of the retaining wall against overturning can be expressed in terms of the width of the effective base contact B_e. B_e is also referred to as the effective base area in compression when zero tensile strength is assigned to the interface as shown in Figure 5(b). The overturning criteria for new navigation locks require that the minimum base area in compression for a rock-founded retaining lock wall should be greater than 100 percent of the base width B for usual loadings (representing normal operations) and greater than 75 percent of B for unusual loadings (EM 1110-2-2602). Note that new navigation locks have more stringent requirements than other rock-founded earth retaining structures (75 percent of B for usual loadings and 50 percent of B for unusual loadings (EM 1110-2-2502)). The distribution of effective bearing pressure between the base of the monolith and the underlying rock is assumed linear. When x_N, the distance from the toe to the resultant N', is computed to be within the middle third of the base (within the kern), the entire base is in compression. Otherwise, tensile stresses are computed (e.g., using the flexure formula) within the interface region below the toe.

Assuming that the bearing pressure between the base of the monolith and the underlying rock varies linearly from a maximum at the toe to zero at the inner

edge of the area of effective base area in compression, as shown in Figure 5(b), the value of B_e will be three times the value of x_n. The effective base contact equals B_e/B.

To compute the safety of the wall against overturning, an iterative procedure is used. A value of B_e is assumed, and the values for N' and x_N are computed. The value of x_N is then used to compute a new value for base area in compression ($= 3*x_N$), which is then compared to the assumed value of B_e. The set of calculations is repeated until the value for base area in compression (computed from the value of x_N) equals the assumed value for B_e.

The first series of calculations typically assume that B_e equals B, corresponding to the case of full contact along the base. The value for the uplift pressure force U_{CRACK} is set equal to zero for this case (Figure 5(c)). The two pairs of equilibrium equations given in Figures 7 and 8 are then solved for the values of N' and x_N. The computed value for x_N is then multiplied by three, and the product is compared with the value of B_e that was initially assumed in this pair of calculations. The case of $3*x_N$ less than the assumed B_e (= B) value implies that the following loads cause a gap to develop at the heel of the wall for the case of zero tensile strength along the interface. A second iteration of calculations is then made with a new value for B_e set equal to the value of $3*x_N$ computed in the first iteration. A gap, identified as a "crack" in Figure 5(c), is assumed to extend along the interface from the heel to a distance equal to $(B - B_e)$. Uplift pressures equal to the hydrostatic water pressure within the backfill are now applied within the gap. The two pairs of equilibrium calculations are then repeated with a non-zero value assigned to U_{CRACK}. The iterative calculations continue until the value computed for $3*x_N$ for the current calculation iteration converges to the value for B_e. The maximum compressive effective stress, q_{max}, is then computed at the toe for the assumed linear effective base pressure distribution using the relationship

$$q_{max} = \frac{2\ N'}{3\ x_N} \tag{9}$$

The dewatered navigation Locks 27 Monolith 7E was analyzed using the conventional equilibrium-based analysis outlined in this section for the following loads computed using Equation 1 with K_o set equal to 0.45 and Equation 3 with K_v equal to 0.09. The results of these calculations indicate that a gap extends 23.12 ft (7.05 m) along the interface, as measured from the heel. The base area in compression B_e was computed to be 21.88 ft (6.67 m) and corresponds to 48.6 percent of the base. The maximum effective compressive stress computed below the toe of the monolith equals 35,534 psf (1,701.37 kP_a). The computed value for B_e does not meet the design requirement of 75 percent of B for new structures of this type subjected to an unusual loading (i.e., a dewatered lock).

In summary, four key assumptions were made in the conventional equilibrium-based analysis of navigation Locks 27 Monolith 7E. These assumptions are as follows:

a. The effective base pressure distribution was assumed linear (Figure 5(b)).

b. The tensile strength along the interface was assumed equal to zero.

c. The following earth loads (both horizontal and vertical shear) were assumed constant (i.e., independent of wall movement).

d. Hydrostatic uplift pressures were assumed within the gap along the interface while a linear variation in uplift pressures was assumed from crack tip to the toe of the monolith (Figure 5(c)).

The first assumption will be further examined in subsequent sections of this chapter using the results of three different types of FE analyses. The other assumptions will be examined in subsequent chapters of this report.

ALPHA Method of Analysis of Locks 27 Gravity Retaining Wall Using SOILSTRUCT

Recent research efforts have been directed toward developing analytical procedures using the FEM analysis for problems concerned with loss of contact between the base of a gravity wall and its foundation. This situation arises when structures are loaded so heavily that a gap develops in the interface region. This section describes an approach used to analyze base separation by modeling a predetermined plane along which separation is presumed to develop using interface elements.

The FEM program SOILSTRUCT was expanded during the first REMR Research Program to model the loss of contact between the base of a gravity wall and its foundation using a procedure called the Alpha method (Ebeling, Duncan, and Clough 1990 and Ebeling et al. 1992). SOILSTRUCT is a general-purpose FEM program for 2-D plane strain analysis of soil-structure interaction problems. It calculates displacements and stresses due to incremental construction and/or load application and can model nonlinear stress-strain material behavior. Two types of finite elements are used to represent the behavior of different materials comprising the monolith, its rock foundation, and the interface between them: (a) a 2-D continuum element and (b) an interface element.

During each incremental following load analysis, each interface element along the base of the wall is checked to detect tensile stress at its center. If none is found, the following load analysis proceeds as usual. When tensile stresses are observed in the interface elements, the incremental analysis is repeated using the Alpha method. Briefly, the principle of the procedure is to (a) factor the applied incremental load vector so that zero normal stress will result at the center of each of the interface elements which previously developed tensile stress at its center, (b) make the interface stiffness equal to zero, (c) convert the shear stress regime into an equivalent set of nodal point forces, (d) transfer this equivalent force into adjacent elements by applying it as an external force at the nodes, and

(e) maintain equilibrium by subtracting the equivalent internal stress from within the interface element(s) used to formulate this force. The procedure is repeated until the total initial load increment has been applied. Further details regarding the Alpha method are given in Ebeling et al. (1992), pp 64- 67.

Figure 9 shows the FE mesh of Locks 27 Monolith 7E and its rock foundation used in the following loads analysis with SOILSTRUCT-ALPHA. The FE mesh comprises 14122-D elements, 26 interface elements, and 1,519 nodal points. Tables 1 and 2 summarize the material properties assigned to the 2-D elements and interface elements used to model the various regions of the FE mesh, respectively. In order to make a direct comparison between conventional limit equilibrium method and the finite element analysis (FEA), it was assumed that the wall was loaded by the same predefined lateral pressure of given magnitude and distribution as was used in the conventional equilibrium-based analysis (Figure 3). Recall that the magnitudes and distributions of the loadings were uncoupled from the action (i.e., the displacements) of the wall-foundation system.

The self-weight of the monolith and the weight of the soil wedge above the heel were introduced into the FE model of the monolith, the rock foundation, and the interface using a gravity turn-on analysis. All subsequent loadings of the FE model of Monolith 7E are summarized using the Figure 3 idealization for each type of loading, a total of five in all. The respective lateral following earth (both horizontal and vertical shear) and water loadings were then applied to the back of the monolith. Water pressures were applied normal to and along each face of the interface elements, acting upward on the impervious monolith and downward on the impervious rock foundation. The (total) overburden pressure of the backfill was applied to the rock foundation, concurrent with the other four types of loadings.

Lateral pressures and vertical shear loads were established using the conventional concepts for earth and water loadings on retaining wall systems described in the previous section and were applied to the wall in a series of 14 steps to determine the response of the structure to gradually increasing loads. Lateral earth pressures corresponded to an at-rest earth pressure coefficient K_o of 0.45. A vertical shear force corresponding to a vertical earth pressure coefficient K_v of 0.09 was also assigned in all analyses. Figure 10 shows how the backfill placement was simulated in 14 lifts. The average thickness of the 14 lifts was 5.9 ft (1.80 m) and ranged from a maximum 8.5-ft (2.59-m) thickness for lift 2 to a minimum 1.7-ft (0.52-m) thickness for lift 14.

Figure 11 shows the incremental application of the distribution of horizontal earth pressures that were applied incrementally as following loads in 14 steps as placement of the 14 lifts were simulated in the analysis. The cumulative sum of lateral earth pressures applied at any given lift and for all preceding lifts corresponds to an at-rest earth pressure coefficient K_o of 0.45. This same approach was used to incrementally apply the vertical shear stress loads along this vertical section. The horizontal water pressures were applied using this same incremental approach and for the same lift elevations as shown in Figure 10 but were concluded at lift 8 when the water table reached el 396. Uplift pressures were

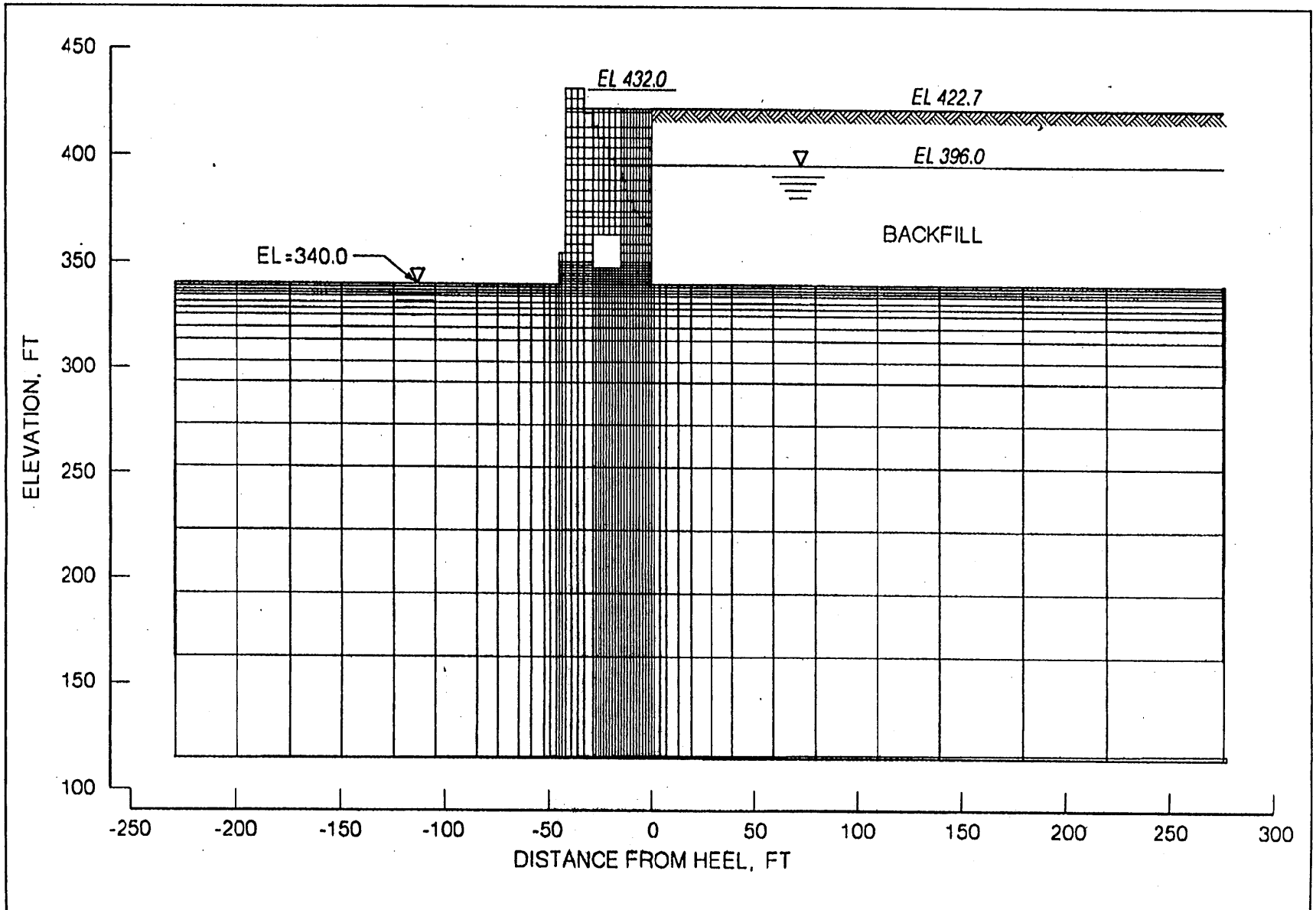

Figure 9. Finite element mesh of Locks 27 Monolith 7E - SOILSTRUCT-ALPHA following loads analyses (1 ft = 0.305 m) (Continued)

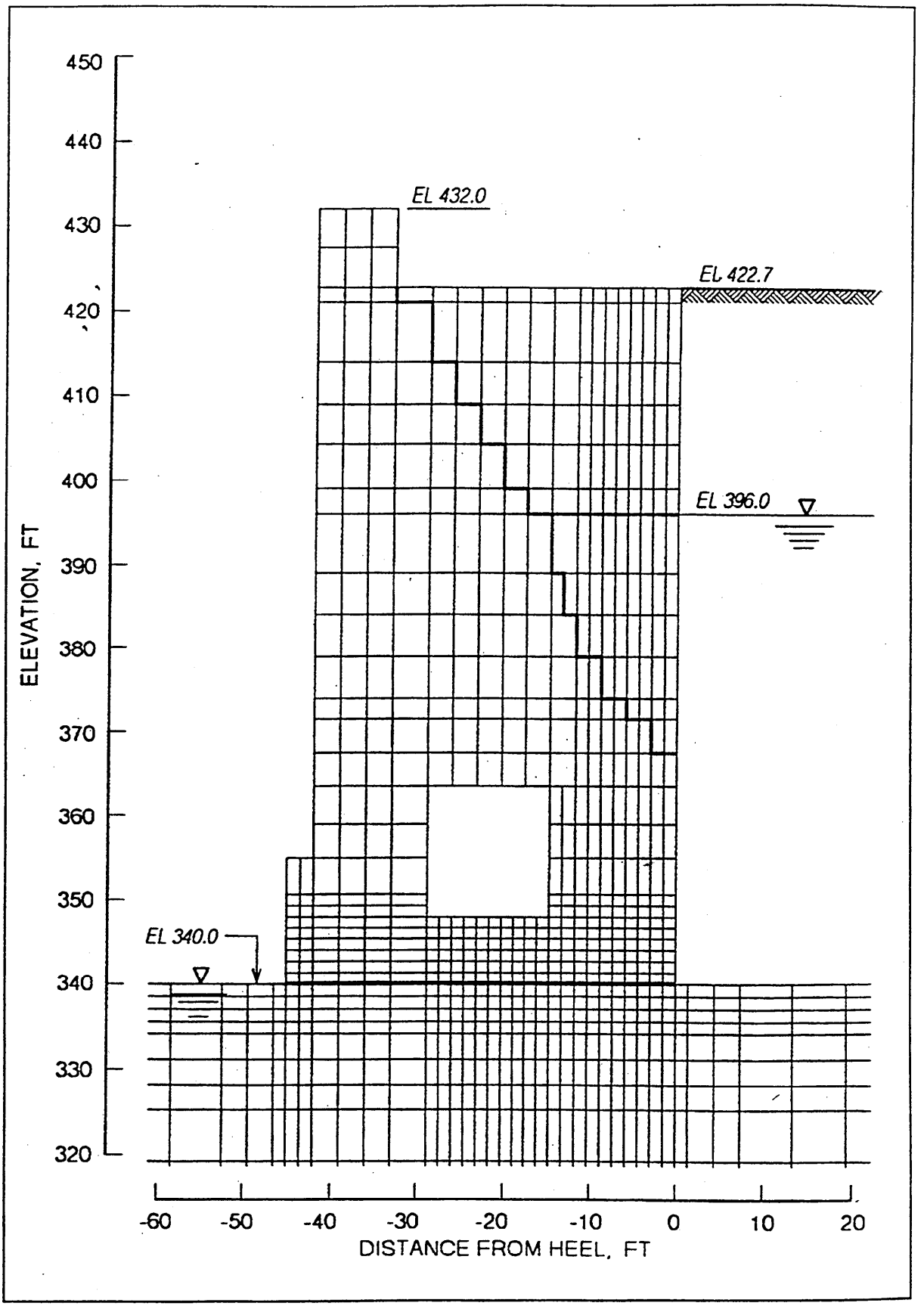

Figure 9. (Concluded)

Table 1
Elastic Material Properties for 2-D Elements Comprising the SOILSTRUCT-ALPHA Finite Element Model of Locks 27 Monolith 7E for the Following Load Analysis

Material Type	Unit Weight pcf (kg/m^3)	E psi (MPa)	υ
Concrete	150 (2,403)	3,500,000 (24,131.8)	0.2
Moist Soil	125 (2,002)	3,500 (24.13)	0.35
Submerged Soil	130 (2,082)	3,500 (24.13)	0.35
Rock	-	3,500,000 (24,131.8)	0.2

Table 2
Material Properties for Interface Elements Comprising the SOILSTRUCT-ALPHA Finite Element Model of Locks 27 Monolith 7E for the Following Load Analysis[1]

Material Region	k_n pst/ft (MPa/m)	k_s psi/in. (MPa/m)
Concrete-to-Rock Interface	1.0 x 10^8 (15,708.7)	10,000 (2,717.4)

[1] Equations for Interface Model: The normal stress at the center of the interface element is given by

$$\sigma_n = k_n \Delta_n$$

where Δ_n is the average relative displacement normal to the interface element. The shear stress at the center of the interface element is given by

$$\tau_s = k_s \Delta_s$$

where Δ_s is the average relative shear displacement along the interface element.

incrementally applied along both the monolith face and rock foundation face of the interface elements (Figure 3) during the first eight stages of loading.

The value for B_e computed using SOILSTRUCT-ALPHA with interface elements was 32.65 ft (9.95 m), or 72.5 percent of the base area in compression after completion of the incremental following load analysis. This value for B_e/B is 1.5 times the 48.6 percent value computed using the conventional

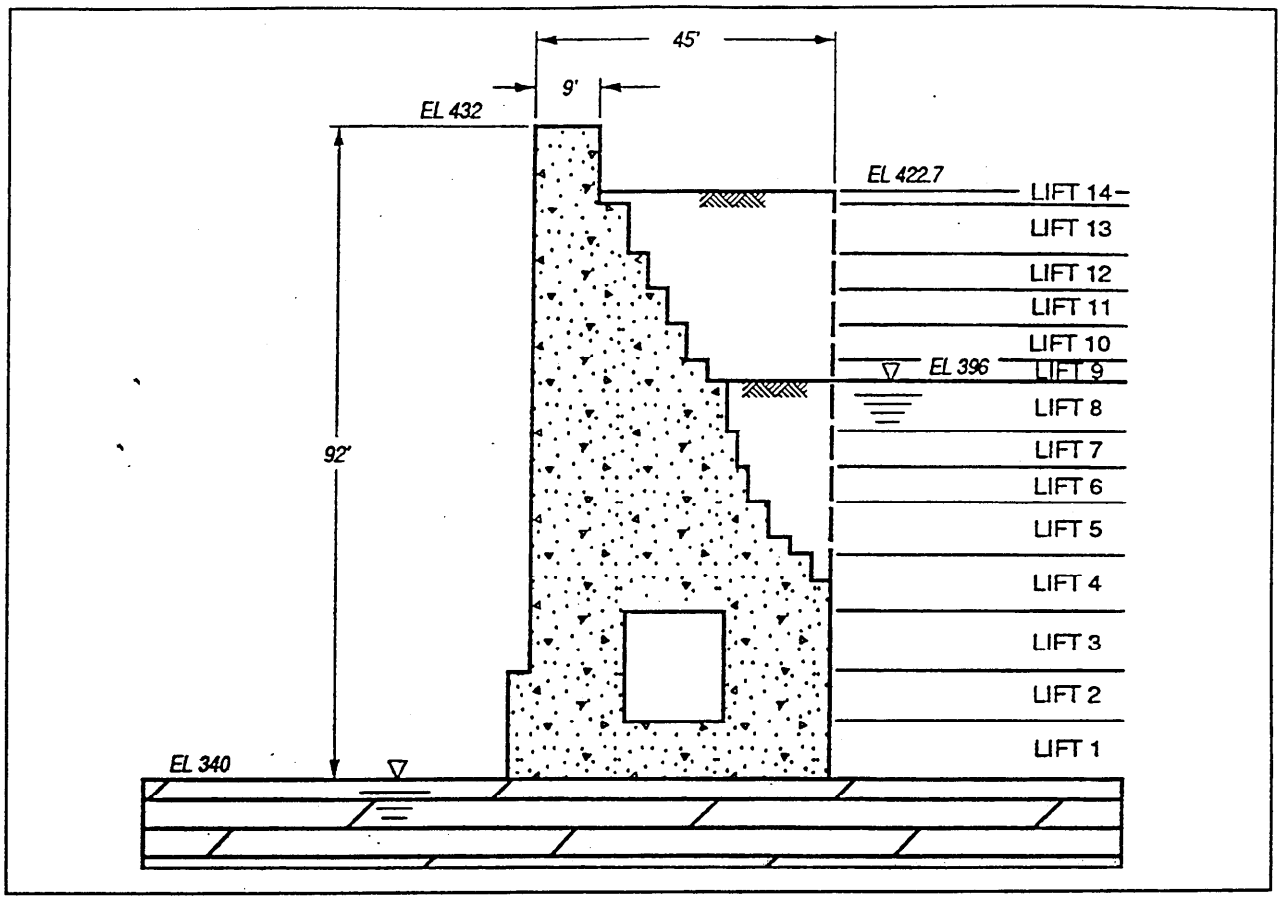

Figure 10. Backfill placement simulated using following loads (1 ft = 0.305 m)

equilibrium-based method of analysis. Figure 12 shows the normal effective stress distribution along the interface computed using both SOILSTRUCT-ALPHA with interface elements and using the conventional equilibrium-based method of analysis. The resulting normal effective stress distribution from the SOILSTRUCT-ALPHA analysis is distinctly nonlinear. The maximum normal effective pressure computed at the toe was 70,698 psf (3,385.02 kPa) by the FEA method and 35,534 psf (1,701.37 kPa) by the conventional equilibrium-based method.

Additional results from each stage of the 14 incremental FEA are summarized in Appendix A. Comparisons are made to the results from the conventional equilibrium-based method of analyses for each stage of loading in Appendix A.

Discrete Crack Analysis of Locks 27 Gravity Retaining Wall Using MERLIN

A second FEM-based procedure for modeling crack propagation at the base of an earth retaining structure in a following load analysis uses fracture mechanics

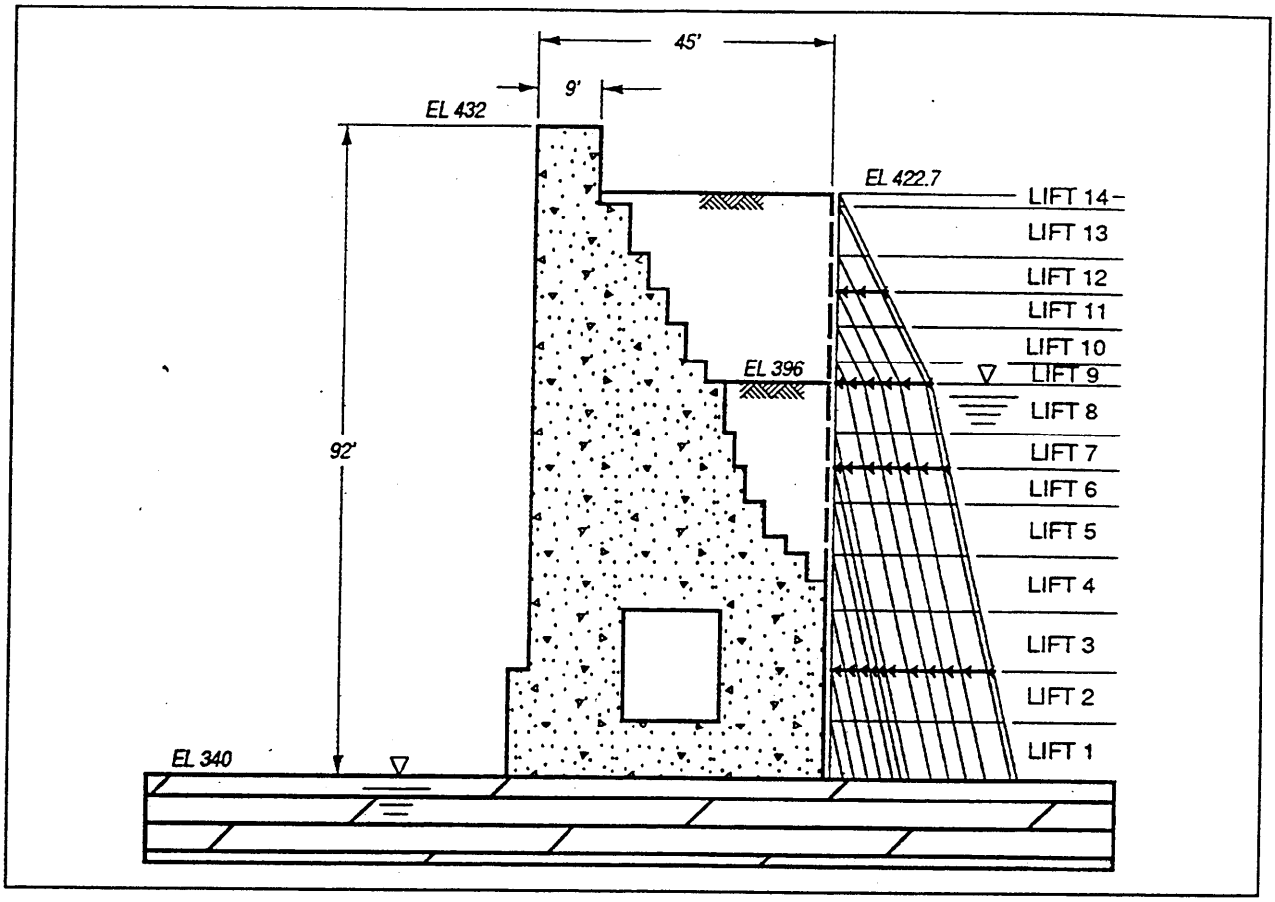

Figure 11. Effective horizontal earth pressures applied during the following loads (1 ft = 0.305 m)

concepts to model the propagation of a discrete crack. Generally, linear elastic fracture mechanics (LEFM) relate the stress magnitude and distribution at the crack tip to the nominal stress applied to the structure; to the size, shape, and orientation of the crack or discontinuity; and to the material properties. The "demand" due to the loading(s) applied to the retaining structure, and specifically, to the region of cracking, is represented by stress intensity factors, K_I, K_{II}, and K_{III} for three cracking modes. Cracking Mode I is an opening mode, Mode II is a shearing mode, and Mode III is a tearing mode. Conceptually, the stress intensity factors indicate the rate at which the stress approaches infinity ahead of the crack tip for each of the three displacement modes. The stress intensity factors characterize the magnitude of the crack tip stress field for the potential cracking modes. The "capacity" of the material is characterized by the fracture toughness, K_c. Crack advance is monitored in an LEFM analysis by comparing the demand to capacity (e.g., K_I to K_{Ic}). The special-purpose FEM code MERLIN (Reich, Cervenka, and Souma 1993) was used to perform the LEFM analysis for this study. The LEFM analysis of Locks 27 Monolith 7E is described in detail in Engineer Technical Letter (ETL) 1110-2-344 (Headquarters, Department of the Army 1993). Results pertaining to this study are summarized in this section.

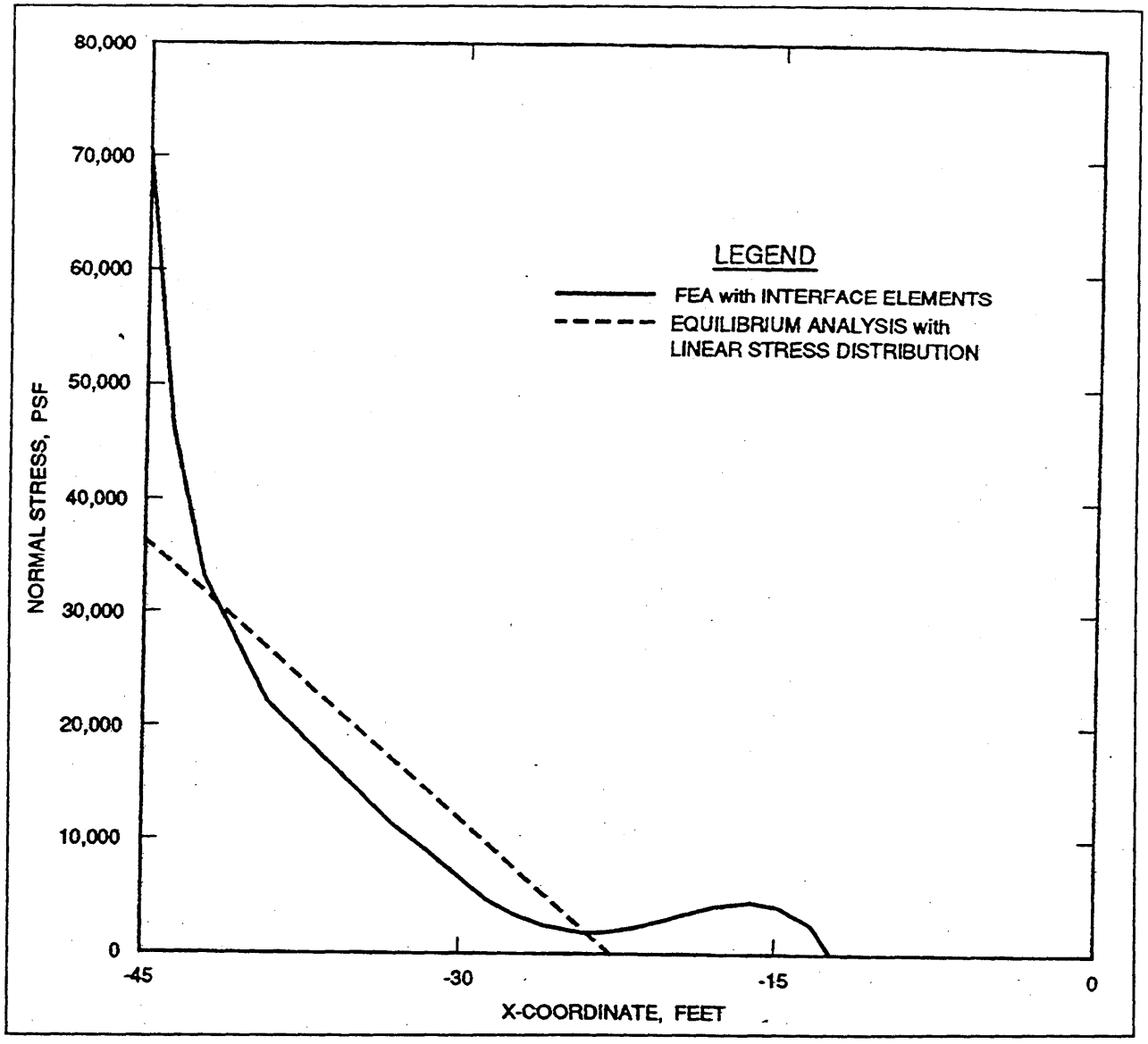

Figure 12. Normal stress distributions along the base of Monolith 7E (1 ft = 0.305 m, 1 MPa = 20,885.5 psf)

LEFM discrete crack analysis is used to assess if a crack will propagate or arrest for each increment in loading. No formal criteria in the context of LEFM have been accepted universally within the engineering community (to date) regarding crack initiation. In this problem, a small crack was inserted into the FE mesh along the monolith-to-rock interface at the heel of the monolith. The potential for propagation of this small crack was checked by comparing the computed values for K_I with the value for K_{Ic} at each stage of incremental loading. Recall that according to LEFM, the crack advances when the value for K_I is greater than K_{Ic}. When the value computed for K_I exceeds K_{Ic}, the mesh is then modified to reflect the longer crack and analyzed for the same set of following loads. The elongation of the crack continues with no increase in loading, along with the

modification of the FE mesh, until the recomputed value for K_I is less than K_{Ic}. The value for K_{Ic} was set equal to zero along the monolith-to-rock interface, with values greater than zero assigned to K_{Ic} for the concrete monolith and the rock foundation in these analyses. Thus, crack propagation was restricted to the interface, as was the case for the SOILSTRUCT-ALPHA analyses of the monolith. Additionally, a zero value for K_{Ic} is the smallest value that can be assigned in LEFM, which is consistent with the material characterization of the interface in the SOILSTRUCT-ALPHA analyses.

The FE mesh used in the LEFM analysis of Monolith 7E is shown in ETL 1110-2-344 and is similar to the mesh shown in Figure 9. The LEFM analysis of Monolith 7E was conducted using MERLIN for the same following earth and water loadings used in both the conventional equilibrium analysis and in the FEM analysis using SOILSTRUCT-ALPHA (Figure 3). The self-weight of the monolith and the weight of the soil wedge above the heel were introduced into the FE model of the monolith and the rock foundation, using a gravity turn-on analysis. Uplift pressures were applied along the base as described previously. Six analyses, each with a different specified crack length, were performed using MERLIN to obtain an estimate of the crack length. The specified crack lengths for these analyses ranged from 6.0 to 13.5 ft (1.83 to 4.11 m) in 1.5-ft (0.46-m) increments. A crack length of 12.99 ft (3.96 m) was estimated by interpolation of results of K_I for the analysis with a crack length of 12 ft (3.66 m) and the analysis with a crack length of 13.5 ft (4.11 m). An additional analysis was performed with refined meshes to determine a precise value for the final crack length. This procedure was repeated until the value of K_I was less than 0.001 ksi[in]^{½} (0.0011 MN/m$^{3/2}$). The final crack length computed using this approach was 13.02 ft (3.97 m), corresponding to B_e of 31.98 ft (9.75 m) (B_e/B = 71.1 percent).

Figure 13 shows the normal effective stress distribution along the interface computed using both the FEA with interface elements and LEFM. Both analyses resulted in nonlinear normal effective stress distributions that were similar in shape. The maximum normal effective pressure was 70,698 psf (3,385.02 kPa) by the finite element analysis (FEA) with interface elements and 105,603 psf (5,056.27 kPa) by the LEFM.

Figure 14 shows the shear stress distribution along the interface computed using both the FEA with interface elements and using LEFM. Both analyses resulted in nonlinear shear stress distributions of similar shape. No shear stress distribution was *assumed* for the resulting shear force along the interface computed by the conventional equilibrium analysis.

Smeared Crack Analysis of Locks 27 Gravity Retaining Wall Using CG-DAMS

A third FEM procedure based on the concepts of smeared crack theory was used for modeling crack initiation and propagation at the base of Locks 27 Monolith 7E retaining structure in a following load analysis. The special-purpose

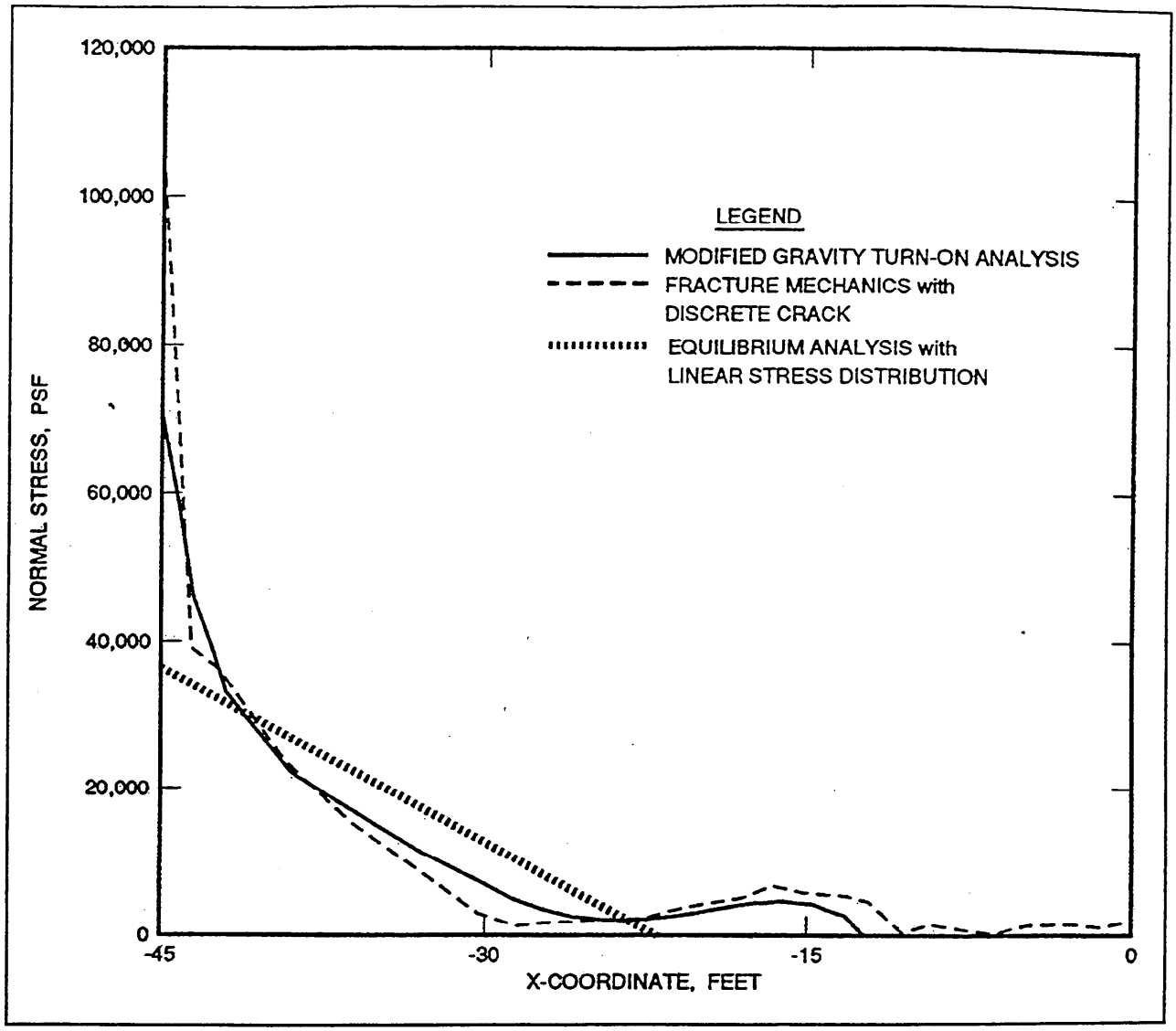

Figure 13. Normal stress distributions along the base of wall (1 ft = 0.305 m, 1 MPa = 20,885.5 psf)

FEM code CG-DAMS (ANATECH 1993) was used to perform a smeared crack analysis for this study. The smeared crack theory uses a strength-of-materials approach to evaluate crack initiation potential and/or crack propagation in a material. According to the theory, cracks may develop on planes on which tensile strain and tensile stress act. The largest tensile strain(s) and stress(es) will develop on the principal planes. In CG-DAMS, the potential for cracking is evaluated on the three principal planes at each integration point within every element comprising the mesh and for each stage of loading. CG-DAMS uses the strains acting on an infinitesimal cube at an integration point to determine the orientation of the three principal planes. If the material is isotropic and there is no pre-existing crack, then the three principal planes of strain and stress are coincident and can be determined from the stresses acting on the faces of an infinitesimal cube at the integration point as shown in Figure 15. The principal values for

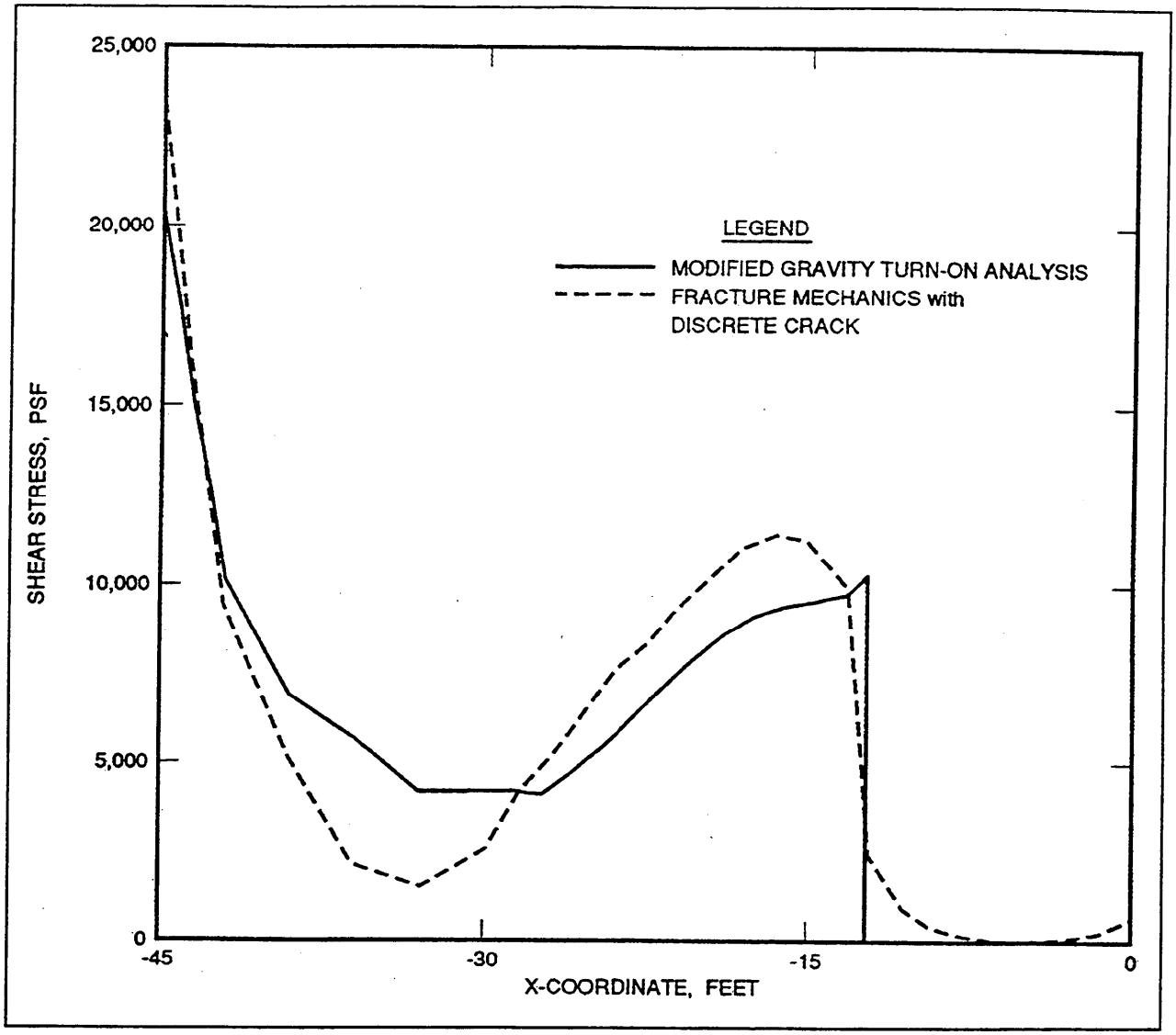

Figure 14. Shear stress distributions along the base of wall (1 ft = 0.305 m, 1 MPa = 20,885.5 psf)

tensile strain and tensile stress on each of the three principal planes are then compared to the smeared crack criterion specified for that material. Figure 16 shows an example of the criterion used in CG-DAMS. The diagonal line distinguishes crack initiation potential in Figure 16 and is defined by the two concrete material properties, the tensile fracture strain ϵ_{φ} and Youngs Modulus E(t). If any of these three pairs of principal strains and stresses are tensile (i.e., tensile fracture strains and tensile fracture stresses) and exceed the diagonal solid line in Figure 16, a crack develops on that plane. Otherwise, no cracking occurs on that plane. Unlike LEFM, crack *initiation* is an explicit aspect of smeared crack theory.

Figure 17 shows the FE mesh of Locks 27 Monolith 7E and its rock foundation used in the following loads analysis with CG-DAMS. The FE mesh

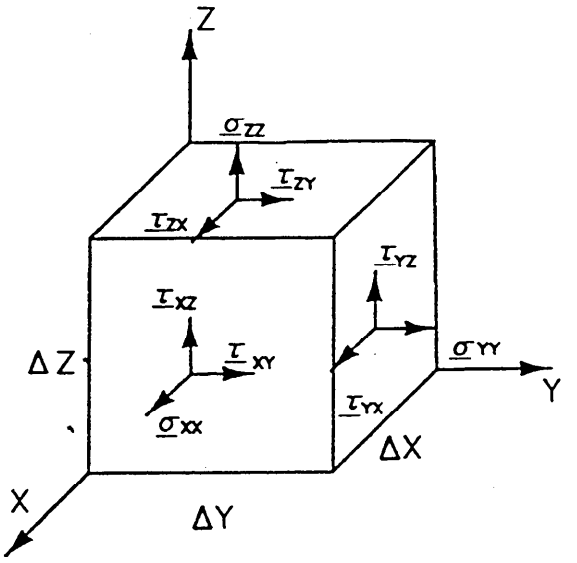

(a) General stress rate

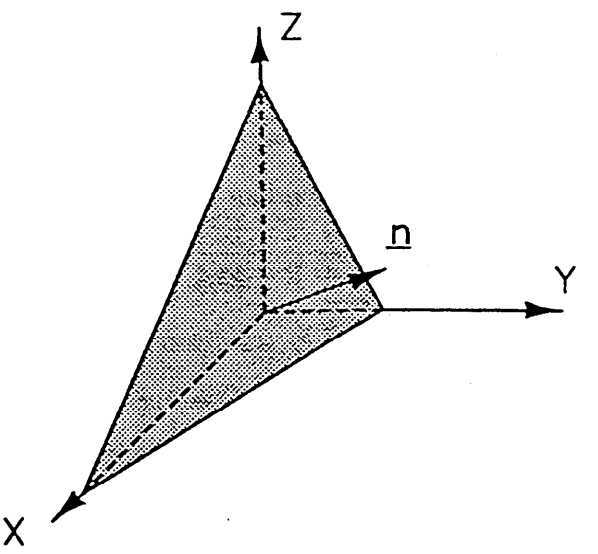

(b) Maximum principal plane

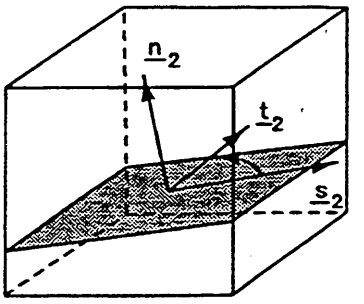

SECOND CRACK

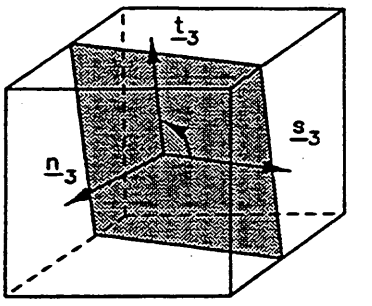

THIRD CRACK

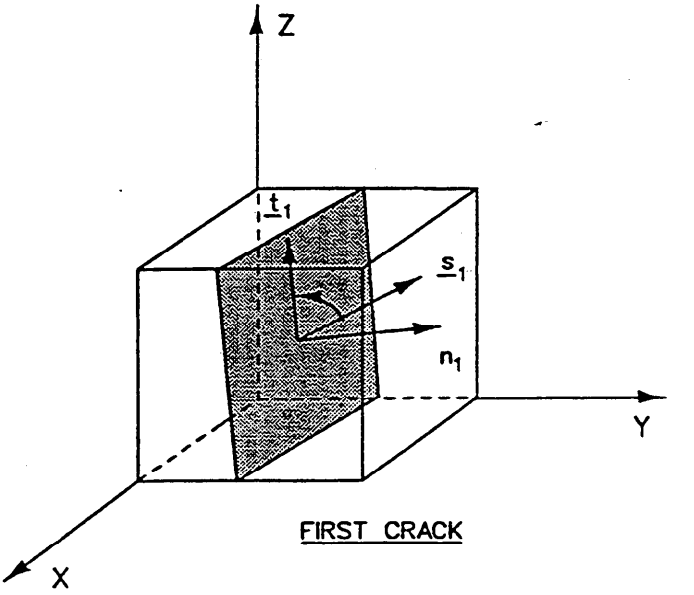

FIRST CRACK

(c) Possible crack orientation

Figure 15. Smeared crack model used in CG-DAMS

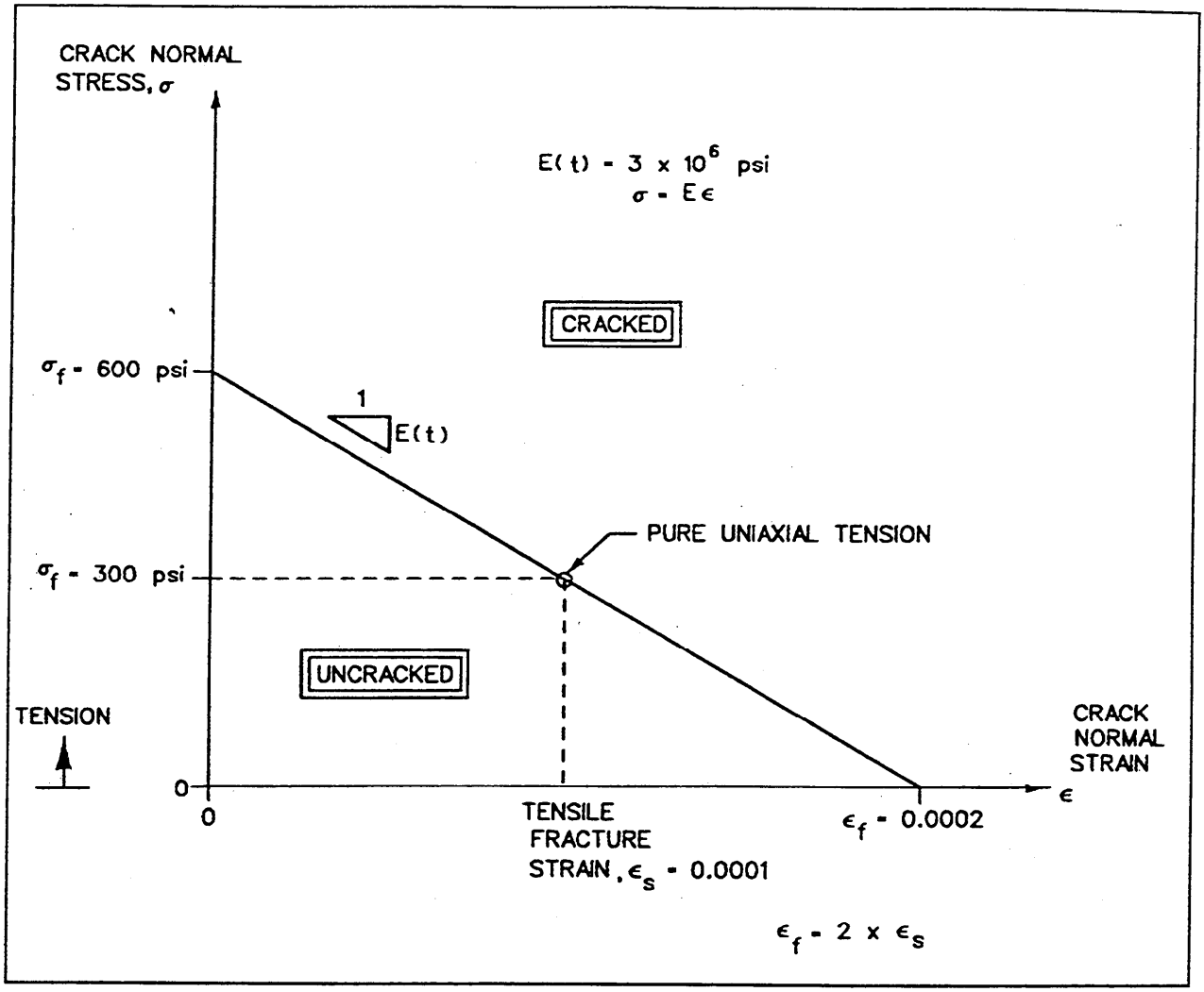

Figure 16. Example of smeared crack criterion used in CG-DAMS (1 MPa ≒ 145.04 psi)

comprises 527 2-D elements and 1,717 nodal points. The smeared crack analysis of Monolith 7E was conducted for the same following earth and water loadings used in all previously described analyses (Figure 3). The material properties assigned to the 2-D elements used to model the various regions of the FE mesh are given in Table 1. The monolith-to-rock interface is modeled using 2-D elements. The self-weight of the monolith and the weight of the soil wedge above the heel were introduced into the FE model of the monolith, the rock foundation, and the interface using a gravity turn-on analysis. All subsequent following loads that were applied to the FE model are idealized in Figure 3. These are the same loadings that were used in the conventional equilibrium, SOILSTRUCT-ALPHA, and MERLIN analyses of Locks 27 Monolith 7E. Water pressures were applied upward along the top face of the elements used to model the interface and downward along the bottom face of these elements, as shown in Figure 4, using one of the three uplift profiles incorporated in CG-DAMS.

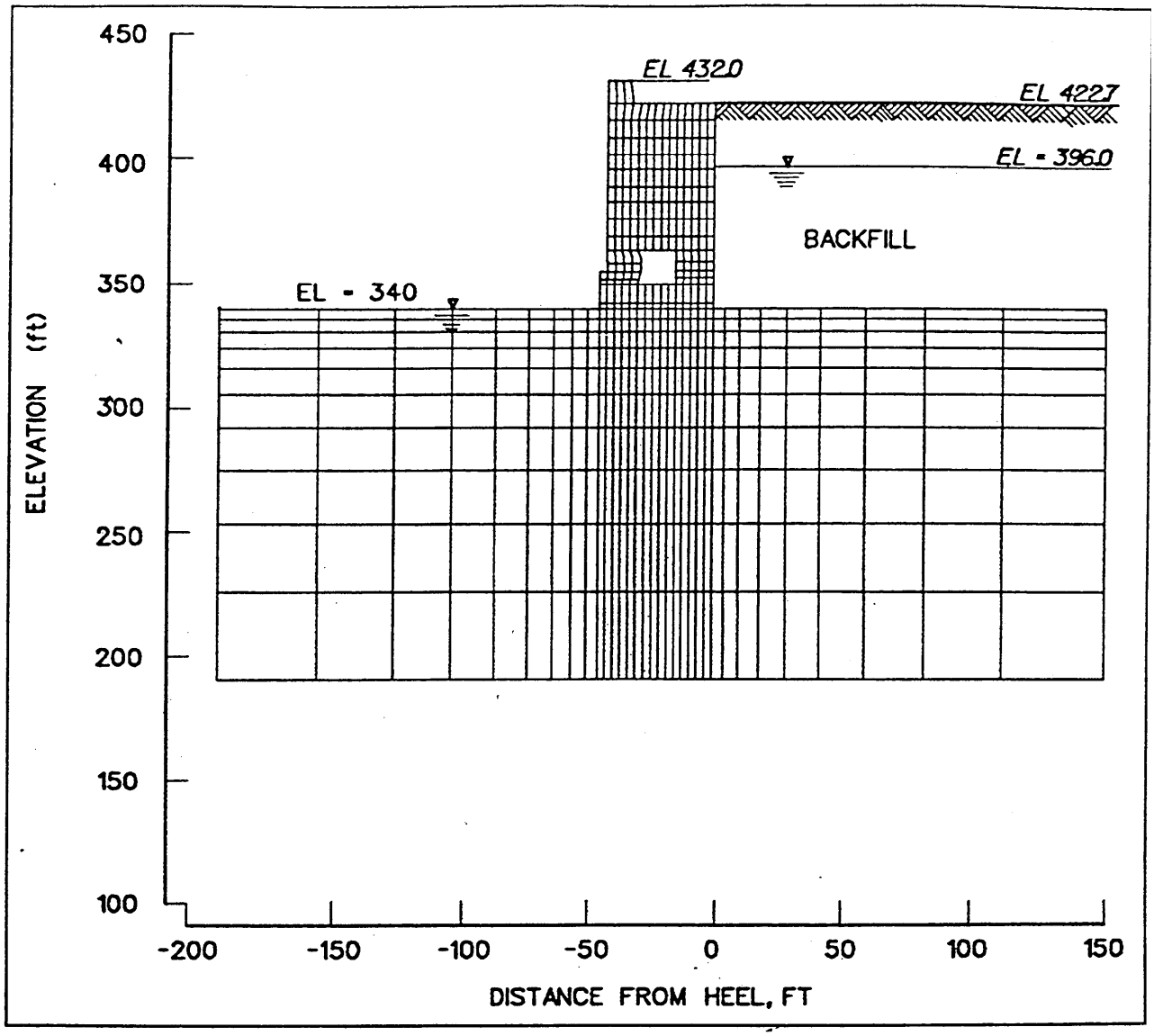

Figure 17. CG-DAMS finite element mesh of Locks 27 (1 ft = 0.305 m)

Four following load analyses of Locks 27 Monolith 7E were performed using CG-DAMS to obtain an estimate of the crack length. Each analysis was conducted using a different smeared crack criterion for the interface region. The first analysis used interface material parameters corresponding to a no-tensile strength criterion, which is consistent with the conventional equilibrium, SOILSTRUCT-ALPHA, and MERLIN analyses that had been described earlier. The three parametric analyses of the smeared crack criterion interface considered variations in the orientation of the planes for which there was the potential for cracking, as well as a variation in the tensile strength capacity of the interface.

The first CG-DAMS analysis had a tensile fracture strain ϵ_s of 0, and the potential for cracking was restricted to planes parallel to and perpendicular to the interface. This type of analysis is referred to as a directed crack analysis.

Figure 18 shows the crack pattern computed at the integration points within the interface elements and a final crack length of 12 ft (3.66 m), corresponding to B_c of 33 ft (10.06 m) (B_c/B = 73.3 percent). Figure 19 shows the normal total and effective stresses, the shear stress, and uplift pressure distributions computed along the interface. The maximum normal effective pressure was 69,850 psf (3,344 kPa) at the toe of the monolith.

CG-DAMS following load analysis of Locks 27 Monolith 7E was repeated with a homogeneous crack criterion and a tensile fracture strain ϵ_s maintained equal to 0. This allowed for the evaluation of the potential of cracking on planes at any orientation. Figure 20 shows the crack pattern computed at the integration points within the interface elements and a final crack length of 37.5 ft (11.43 m), corresponding to B_c of 7.5 ft (2.29 m). The value for base area in compression B_c/B reduced from 73.3 percent to 16.7 percent with the change from directed crack criteria along the interface to homogeneous crack criteria (Table 3). Figure 21 shows the corresponding normal total and effective stresses, the shear stress, and uplift pressure distributions that were computed along the interface. The maximum normal effective pressure was 79,350 psf (3,799.28 kPa) at the toe of the monolith, nearly 10,000 psf (478.8 kPa) greater than for the case shown in Figure 19 (directed crack and $\epsilon_s = 0$).

The last two parametric analyses were conducted with a directed crack criterion along the interface and a homogeneous crack criterion. The tensile fracture strain ϵ_s was set equal to 0.0001 (100μ) for both analyses. Both CG-DAMS analyses resulted in no potential for cracking along the interface. Figure 22 shows the resulting normal total and effective stresses, the shear stress, and uplift pressure distributions computed along the interface for the directed crack analysis. Figure 23 shows the resulting stress and pressure distributions for the homogenous crack analysis.

Parametric Study of Initial Stress Distributions Within the Lock-Wall-to-Rock-Foundation Interface

This section discusses the results of a parametric study of initial stress distributions within the lock-wall-to-rock-foundation interface of Locks 27 Monolith 7E. The additional analyses were conducted using SOILSTRUCT-ALPHA for the FE model shown in Figure 9. Recall that the self-weight of the monolith and the weight of the soil wedge above the heel were introduced using the gravity turn-on analysis in all three types of FEA discussed in previous sections of this chapter. Figure 24 shows two alternative methods used for computing the initial stress distribution along the interface due to the self-weight of the monolith and soil wedge. The two alternative methods are referred to as a monolith build-up analysis and an analysis with prescribed stresses equal to the overburden pressure.

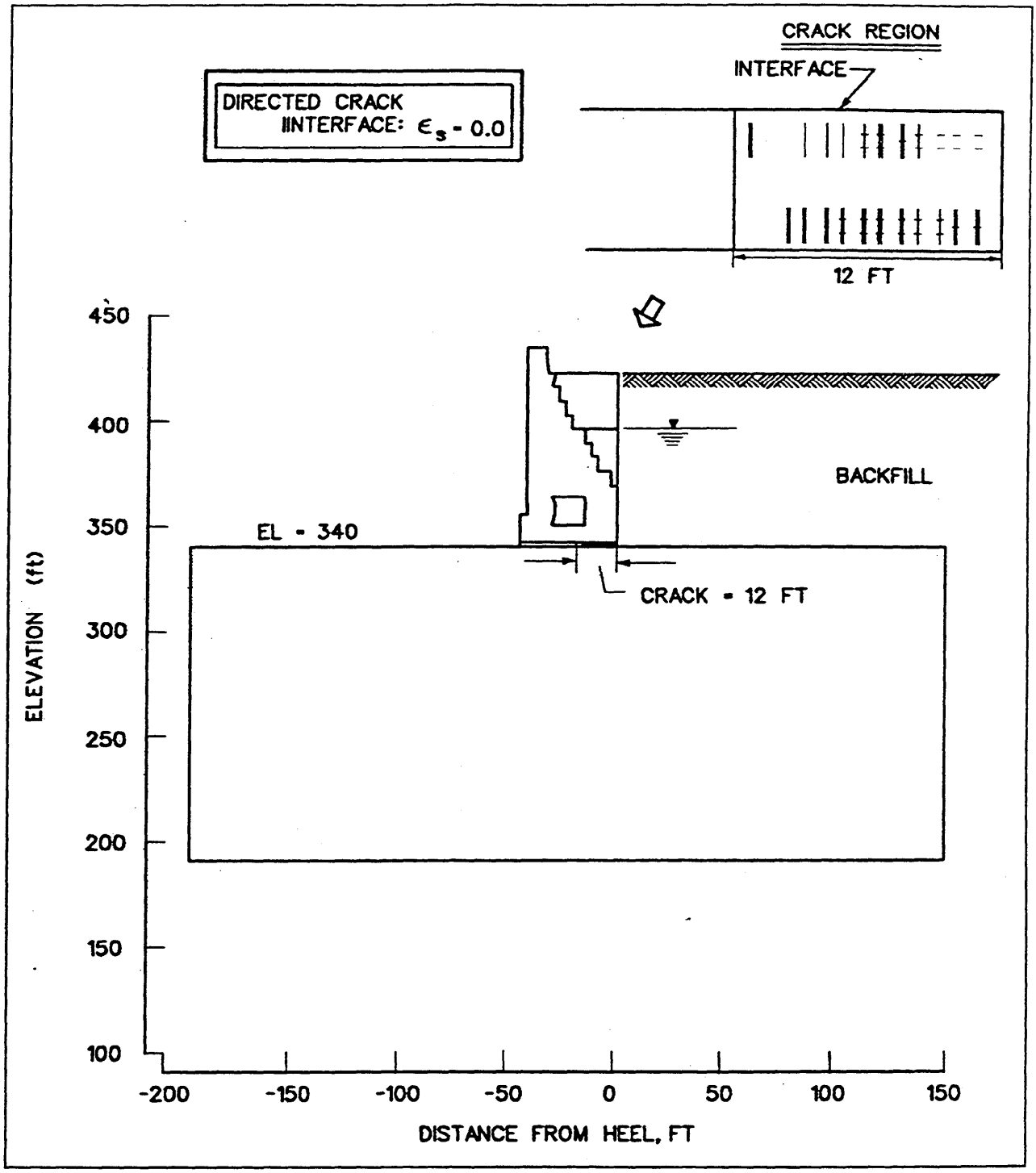

Figure 18. CG-DAMS results along interface of Locks 27 directed crack fracture criteria (1 ft = 0.305 m)

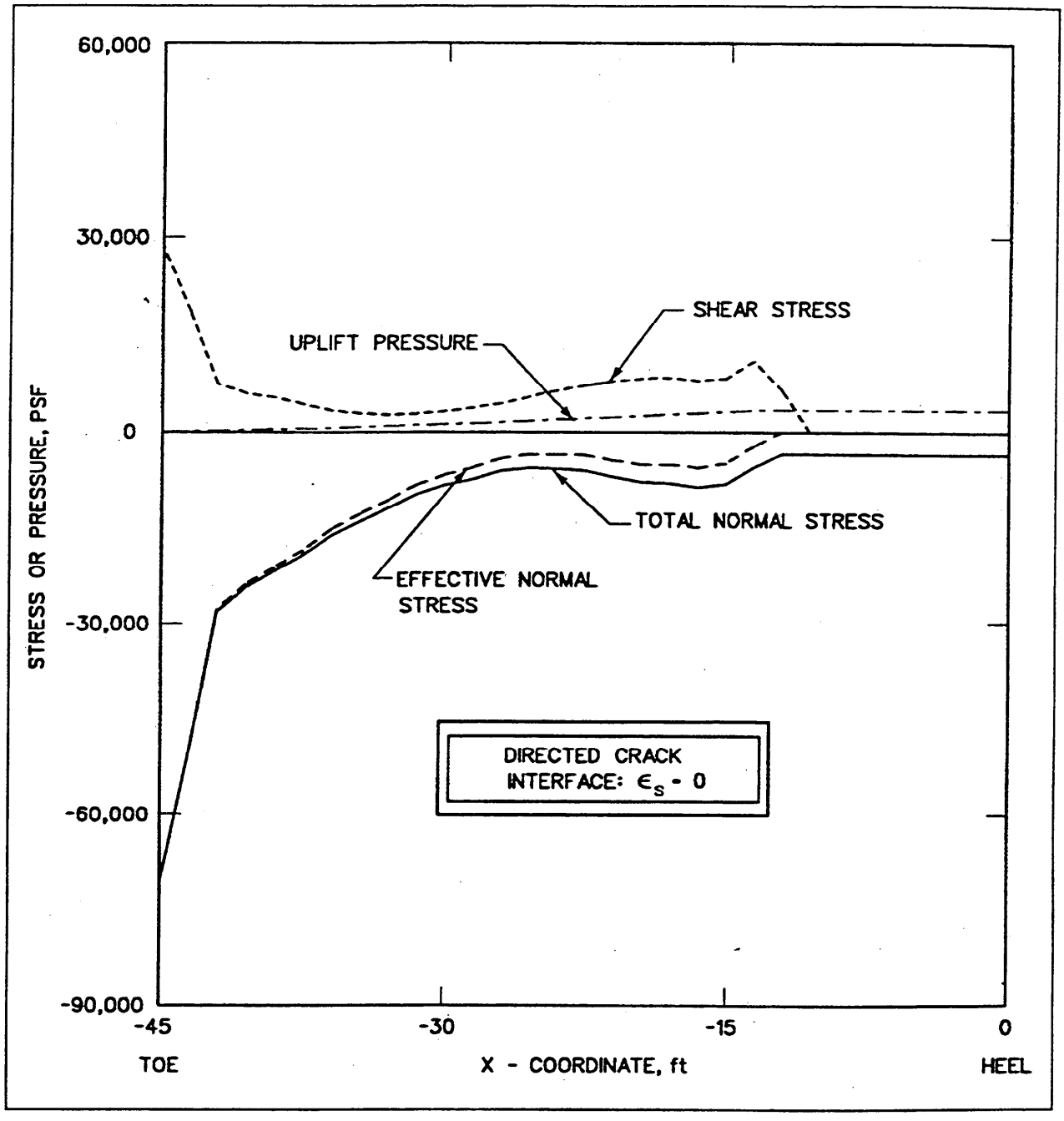

Figure 19. Stress profiles along interface of Locks 27 - directed crack fracture criteria (1 ft = 0.305 m, 1 MPa = 20,885.5 psf)

In the monolith build-up analysis, the incremental construction of the FE model of the monolith shown in Figure 9 is simulated using SOILSTRUCT. A total of 25 lifts were used in this analysis. The lifts ranged from a minimum thickness of 1.33 ft (0.41 m) near the base of the monolith to a maximum thickness of 9.3 ft (2.83 m) near the top, as shown in Figure 24. Note that if

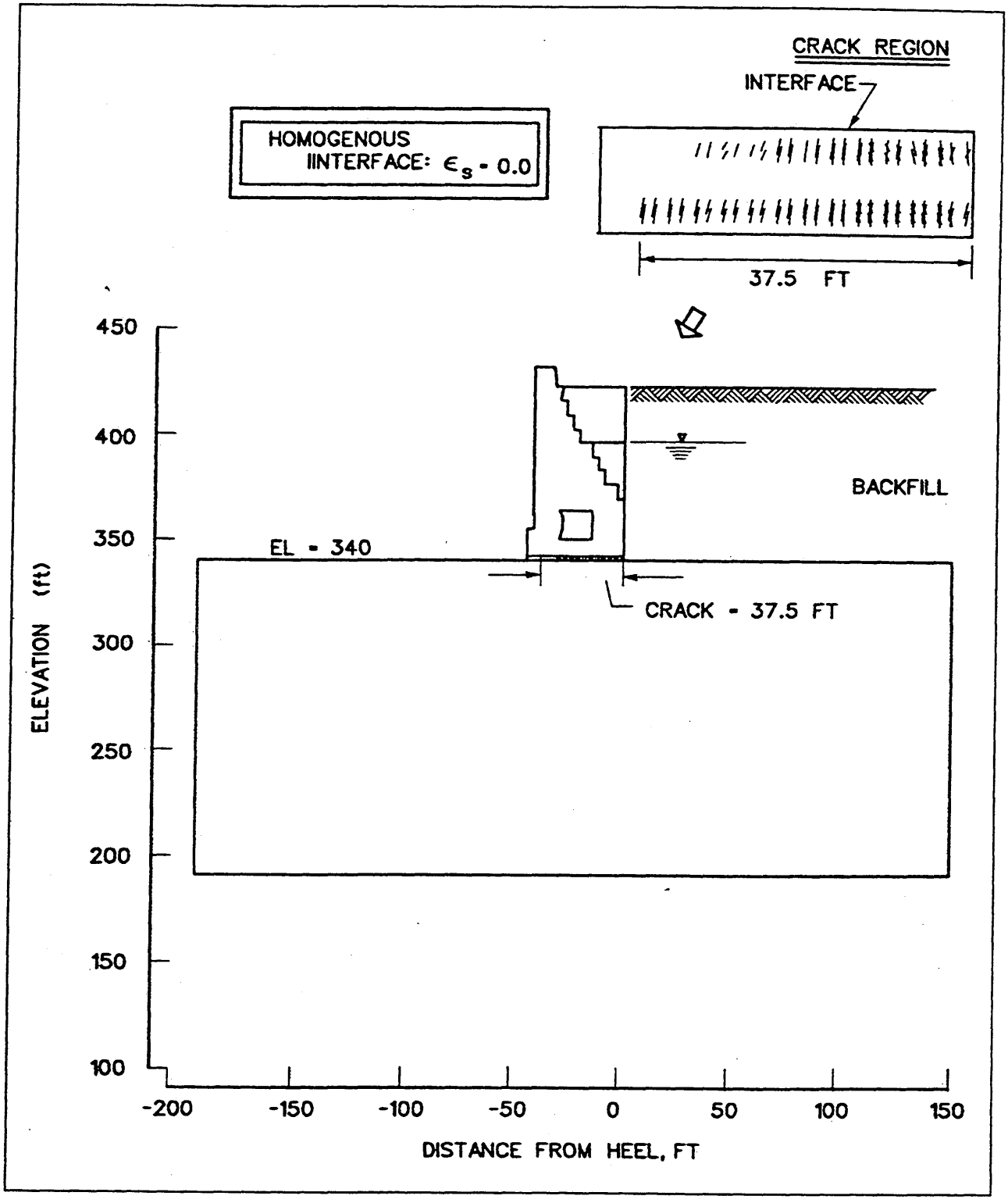

Figure 20. CG-DAMS results along interface of Locks 27 - homogeneous fracture criteria (1 ft = 0.305 m)

Table 3
CG-DAMS Results Along Interface of Locks Monolith 7E

ϵ_s	Smeared Crack Criteria Along Interface	Crack Length, ft (m)	B_c/B, %
0	Directed Crack	12.0 (3.66)	73.3
0	Homogeneous	37.5 (11.43)	16.7
0.0001	Directed Crack	0 (0)	100.0
0.0001	Homogeneous	0 (0)	100.0

construction records had been available, the recorded lift thickness would have dictated the lift thicknesses used in the model.

Figure 25 shows the resulting normal and shear stress distributions along the interface after monolith build-up. The results of the gravity turn-on analysis are also shown in Figure 25 for comparison. Other than at the ends of the monolith-to-rock interface, the stress distributions are coincident. Higher stresses are to be anticipated at "corners" of elastic structures due to edge effects associated with abrupt changes in geometry. For example, at the toe of the lock wall interface (x = -45 ft (-13.71 m)), the value of normal stress computed in the gravity turn-on analysis is twice the value computed from the monolith build-up analysis, 51,200 psf (2,451.46 kPa) and 25,500 psf (1,220.94 kPa), respectively. The differences between the magnitudes of stresses computed at each end of the interface in the two analyses are attributed to differences in the means by which the two finite-element analyses are conducted.

In the gravity turn-on analysis, the stiffness of the entire monolith is represented in the global stiffness matrix, and the self-weight of the entire monolith is applied in one calculation step. This is in contrast to the incremental monolith build-up analysis. In the first incremental analysis, the global FE stiffness matrix for the rock foundation and interface is loaded under the self-weight of the first lift of wet ("fluid") concrete elements of virtually no stiffness. The second incremental analysis begins with the first layer of monolith concrete elements having cured and their stiffnesses being added to the global FE stiffness matrix for the rock foundation and interface, which, in turn, is loaded under the self-weight of the second newly placed lift of wet ("fluid") concrete elements of virtually no stiffness. This incremental construction analysis is repeated for a total of 25 analyses and concludes with the construction of the entire monolith in the FE model. Thus, both details in the global stiffnesses as well as differences in the stages and magnitudes of the loadings contribute to the differences in the stress distributions in Figure 25. Incremental build-up analyses have been shown in case studies of instrumented retaining structures to provide more accurate results

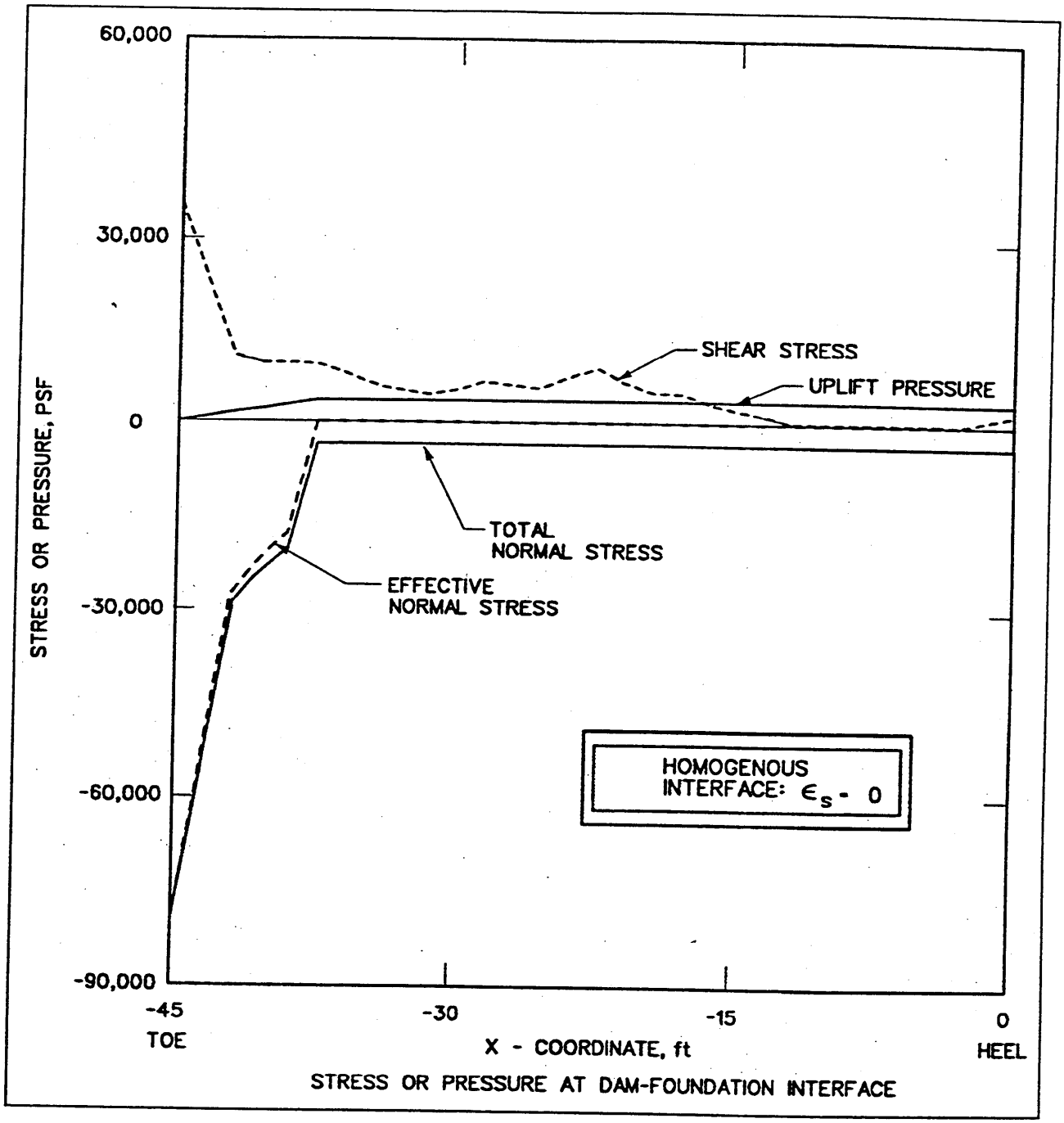

Figure 21. Stress profiles along interface of Locks 27 - homogeneous fracture criteria (1 ft = 0.305 m, 1 MPa = 20,885.5 psf)

than those obtained through use of a gravity turn-on analysis (Clough and Duncan 1969).

A third procedure for determining the distribution of interface stresses due to the self-weight of the monolith and soil wedge is to prescribe stresses equal to the overburden pressure along the interface. The results of this procedure, along with

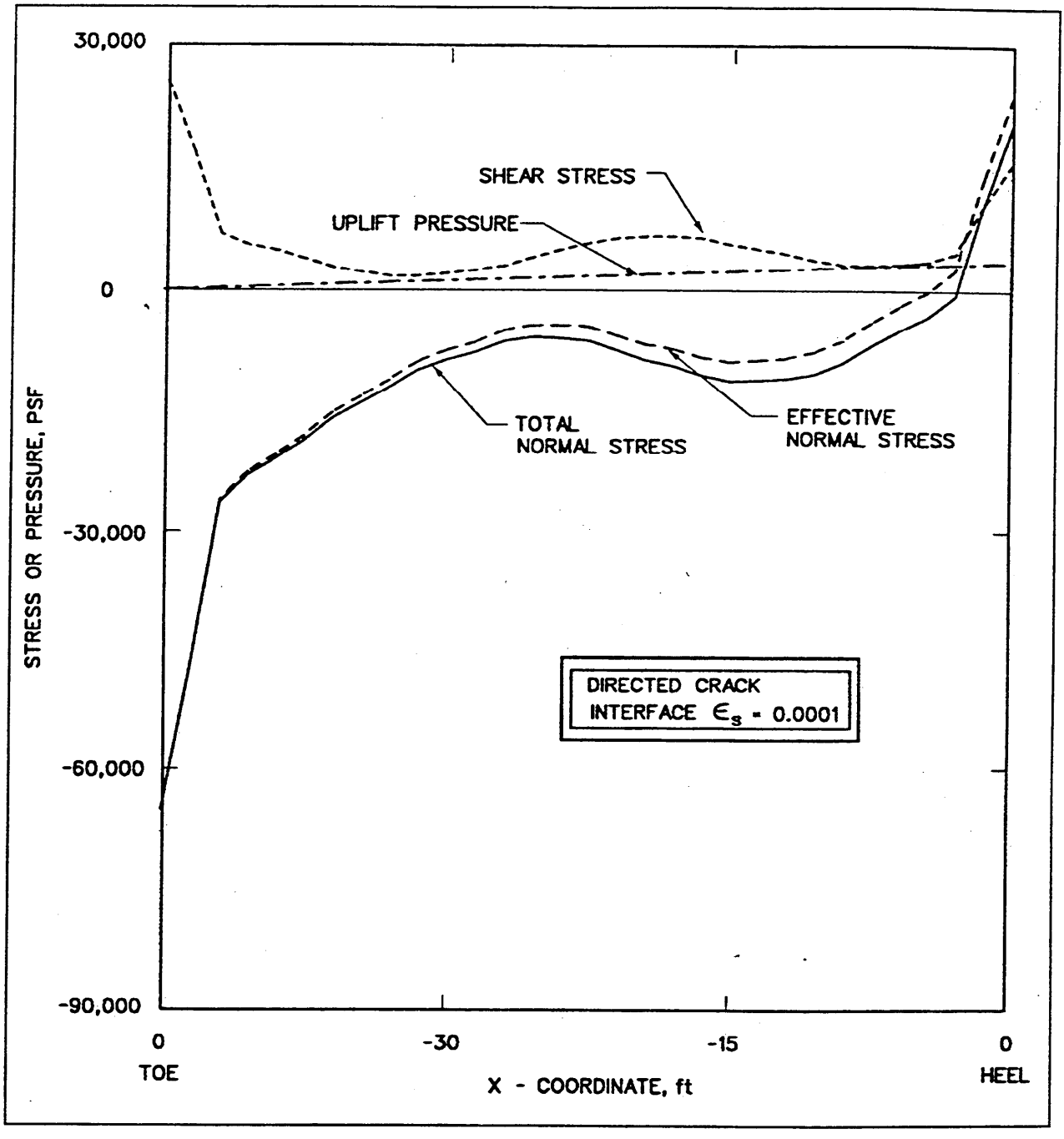

Figure 22. Stress profiles along interface of Locks 27 - directed crack fracture criteria (1 ft = 0.305 m, 1 MPa = 20,885.5 psf)

those of the monolith build-up and gravity turn-on analyses, are shown in Figure 26. The differences in distributions between the overburden calculation and the other two analyses are pronounced.

The results of the gravity turn-on analysis shown Figure 26 have been modified to reduce the high stresses at the corners and be more consistent with the

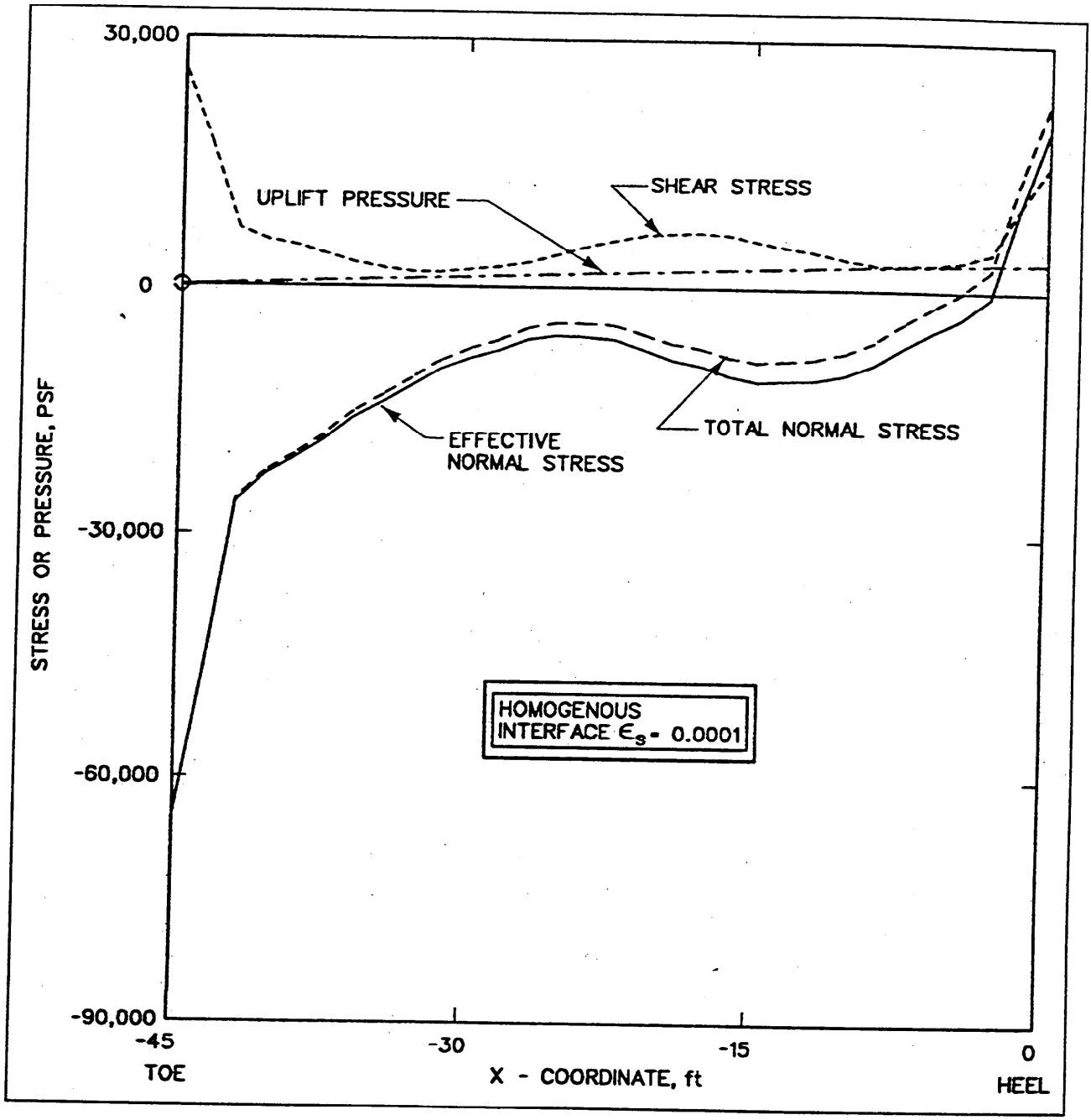

Figure 23. Stress profiles interface of Locks 27 - homogeneous fracture criteria (1 ft = 0.305 m, 1 MPa = 20,885.5 psf)

results of the build-up analysis. The modified gravity turn-on analysis normal and shear stress distributions have the same resultant normal and shear forces and the same points of force applications along the interface as the unmodified gravity turn-on analysis.

The variation of stress distributions along the interface for three different initial stress distributions after application of following loads is shown in

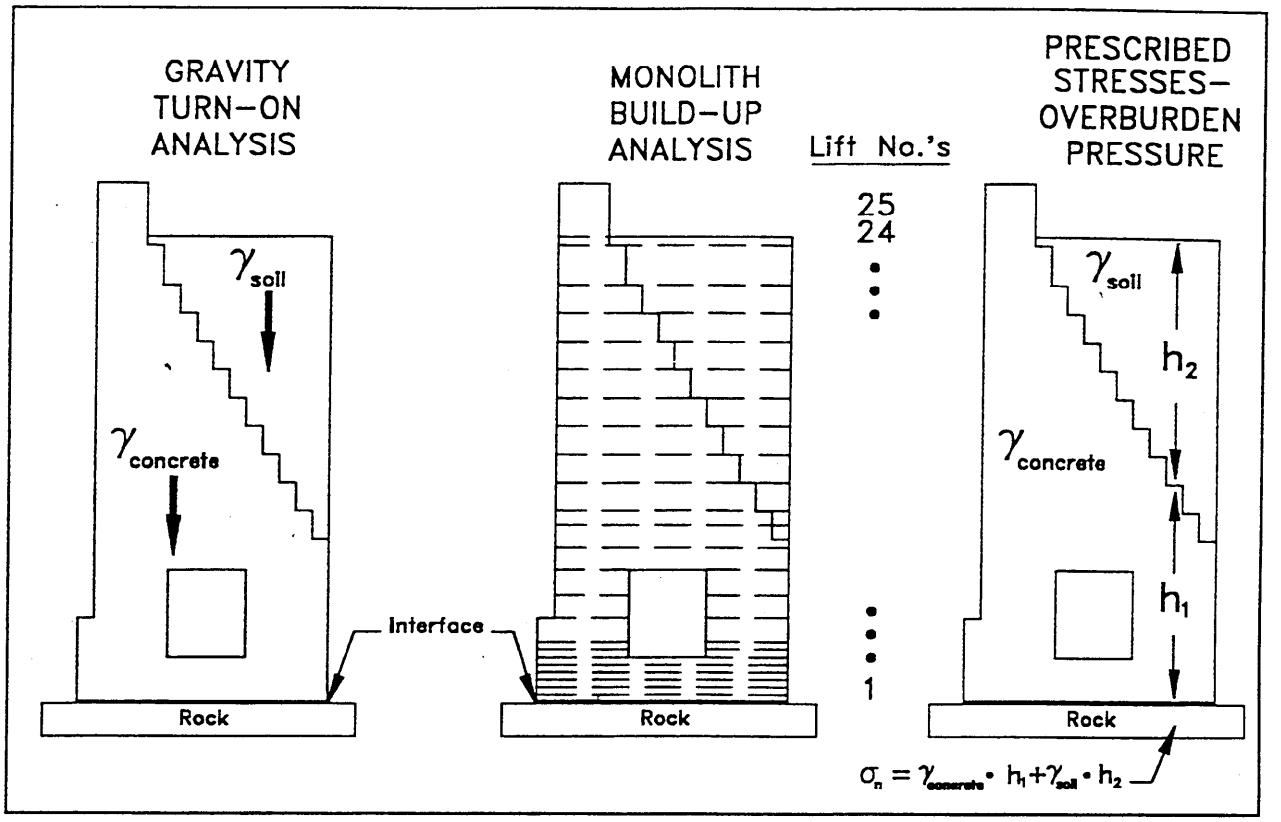

Figure 24. Three methods for computing initial stress distributors along the interface

Figure 27. All stress distributions are distinctly nonlinear. The resulting effective normal stress distributions for the monolith build-up and modified gravity turn-on analysis are nearly identical, as are the values for the effective base areas in compression (Table 4). Starting with an initial stress distribution computed along the interface using overburden pressures results in a value of effective base area in compression equal to 61 percent, which is approximately 10 percent less than those values computed using the other two analyses.

Parametric Study of Composite Rock Foundation Stiffness

The results of a parametric study of composite rock foundation stiffnesses are discussed in this section. The additional analyses of Locks 27 Monolith 7E were conducted using SOILSTRUCT-ALPHA for the FE model shown in Figure 9. The material properties assigned to the rock foundation were based on data contained in a report by Benson (1986) and sponsored by U.S. Army Engineer Waterways Experiment Station (WES). The composite rock foundation stiffness value, the rock mass modulus E_m, used in each FEA reflects the influences of joints and discontinuities within the foundation rock mass. The approach taken by Benson was to correlate the condition of the rock to modulus using data from Bieniawski

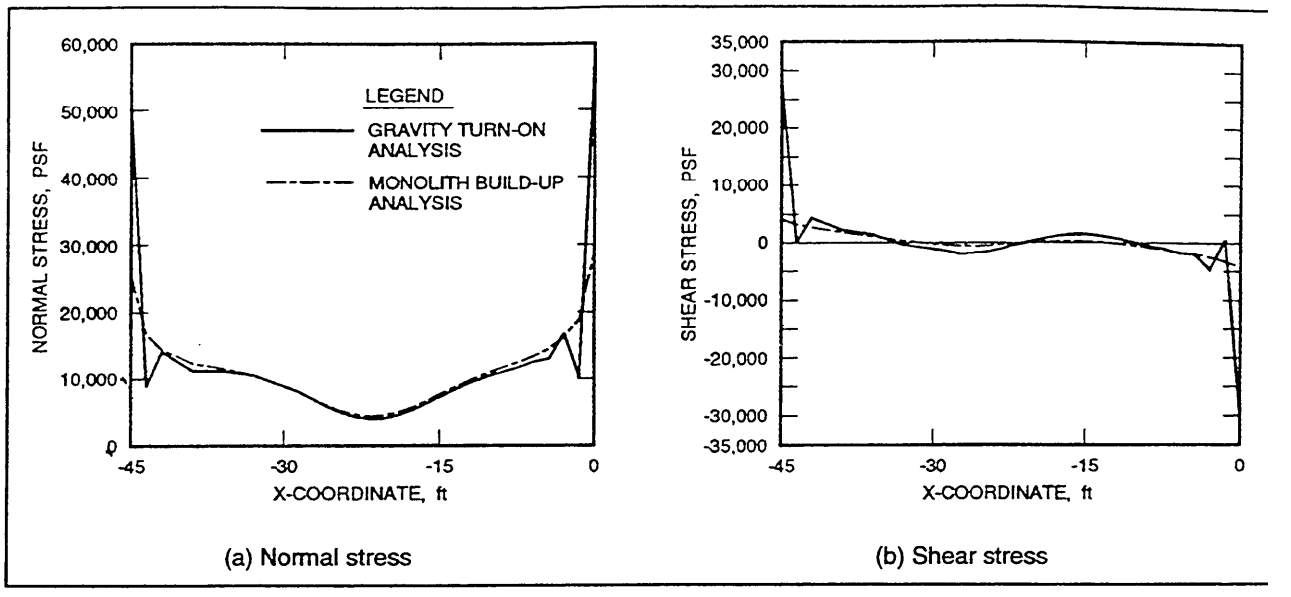

Figure 25. Initial stress distributions along the base (1 ft = 0.305 m, 1 MPa = 20,885.5 psf)

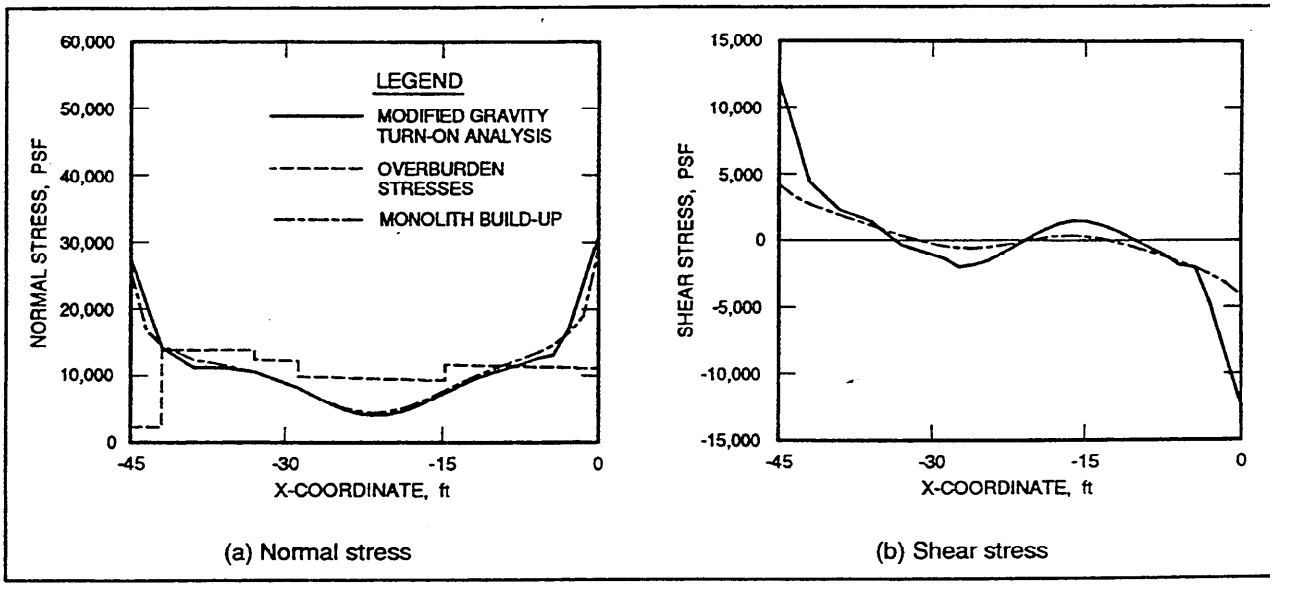

Figure 26. Initial stress distributions along the base following load analyses (1 ft = 0.305 m, 1 MPa = 20,885.5 psf)

(1978) as well as to consider several other factors including geomechanical model calculations using data from Duncan and Goodman (1968) and Kulhawy (1978). The resulting empirical relationship is shown in Figure 28. This figure correlates the deformation modulus of the rock mass (in the field) to the rock mass rating (RMR), a geomechanics classification system.

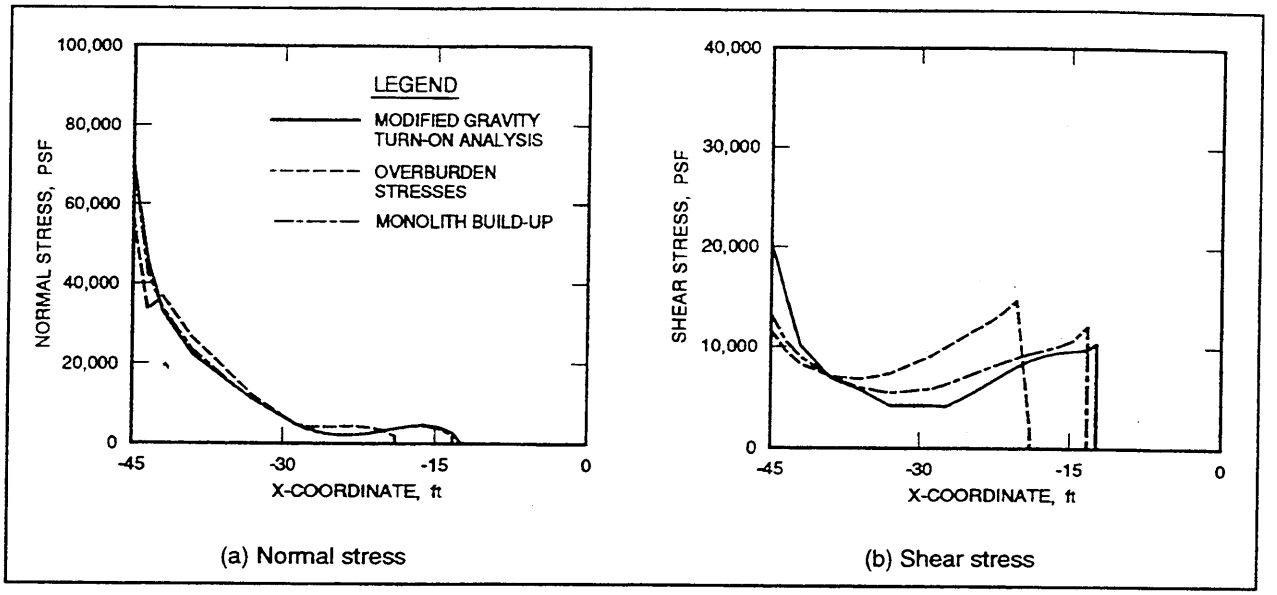

Figure 27. Variation of stress distributions along the base for different initial stress distributions after application of following loads (1 ft = 0.305 m, 1 MPa = 20,885.5 psf)

Table 4
Summary of Base Area In Compression and Crack Lengths for Three Different Initial Stress Distributions After Application of Following Loads

Methods of Initial StressCalculation	B_c ft (m)	Crack Length ft (m)	B_c/B %
Monolith Build-Up Analysis	31.71 (9.66)	13.29 (4.05)	70.5
Modified Gravity Turn-On Analysis	32.65 (9.95)	12.35 (3.76)	72.5
Overburden Stresses	27.45 (8.37)	17.55 (5.34)	61.0

The geomechanics classification is based on summing numerical values relating to the quality or condition of six rock mass parameters. These parameters are (a) point load or uniaxial compressive strength, (b) drill core quality (Rock Quality Designation (RQD)), (c) discontinuity spacing, (d) condition of discontinuities, (e) presence of groundwater, and (f) attitude of joints with respect to loading. A classification is obtained from the summation of the numeric designations for each of the six categories. Figure 28 also includes Bieniawski's (1974) five categories ranging from "very poor" to "very good" which result from the RMR rating.

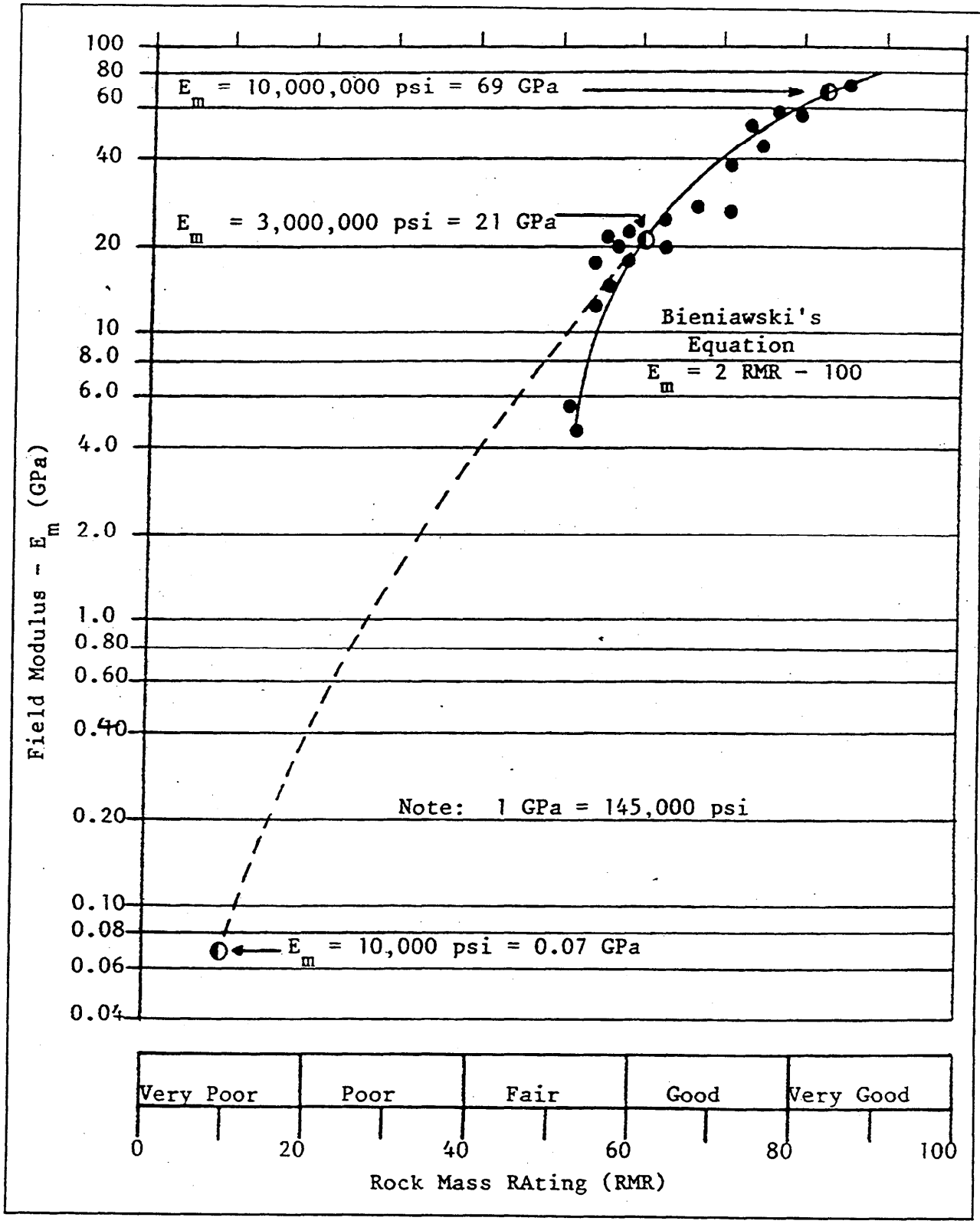

Figure 28. Relationship between rock modulus and rock mass rating (from Benson (1986), after Bieniawski (1978)) (1 MPa = 145.04 psi)

Benson's review (1986) of rock mass modulus values showed that the values ranging from a lower bound of 10,000 psi (68.95 MPa) to an upper bound of 10,000,000 psi (68,948 MPa) could be reasonably anticipated in the field. The lower bound represents a relatively soft rock with closely spaced fractures. The upper bound represents unfractured granite. The upper bound modulus, as described by the Bieniawski (1978) RMR method, would apply to a "good" or "very good" rock mass. In addition, Benson recommended a value of 3,000,000 psi (20,684.4 MPa) to represent the average case, a value rated as "fair" rock by the RMR classification procedure (Figure 28). The composite rock foundation stiffness values for E_{ROCK} assigned to each of the three FE analyses equal 10,000,000, 3,500,000, and 500,000 psi (68,948, 24,131.8, and 3,447.4 MPa). (Note that E_{ROCK} is equivalent to E_m.)

The variation of initial stress distributions along the interface for the three different composite rock foundation stiffnesses are shown in Figure 29. All three calculations were made using the gravity turn-on analysis described previously. The distributions of both normal and shear stresses are nonlinear for the three analyses. The normal stress distributions computed using E_{ROCK} equal to 10,000,00 psi (68,948 MPa) have "edge" stresses smaller by a factor of 2.5 than those computed using E_{ROCK} equal to either 3,500,000 or 500,000 psi (24,131.8 or 3,447.4 MPa).

The results of the gravity turn-on analysis for E_{ROCK} equal to 500,000 psi (3,477.4 MPa) were modified to reduce the high stresses at the corners and, thus, be more consistent with the results of the build-up analysis, as was discussed previously for the results shown in Figure 26. The original and modified gravity turn-on analysis stress distributions are compared in Figure 30 for E_{ROCK} equal to

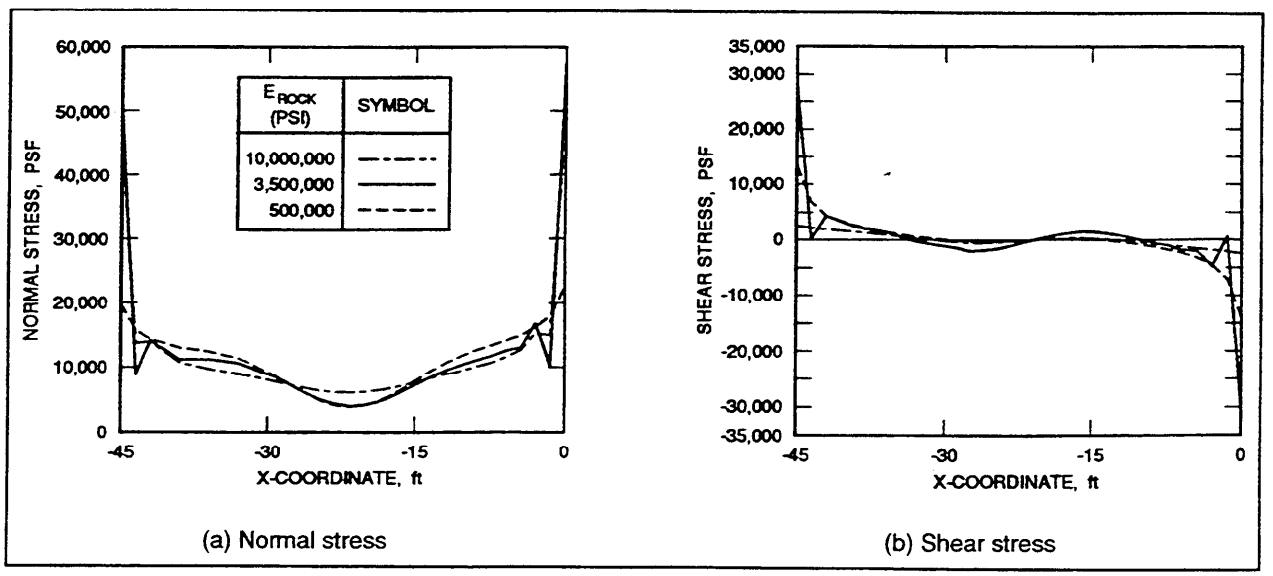

Figure 29. Variation of initial stress distributions along the base for different E_{ROCK} (1 ft = 0.305 m, 1 MPa = 20,885.5 psf)

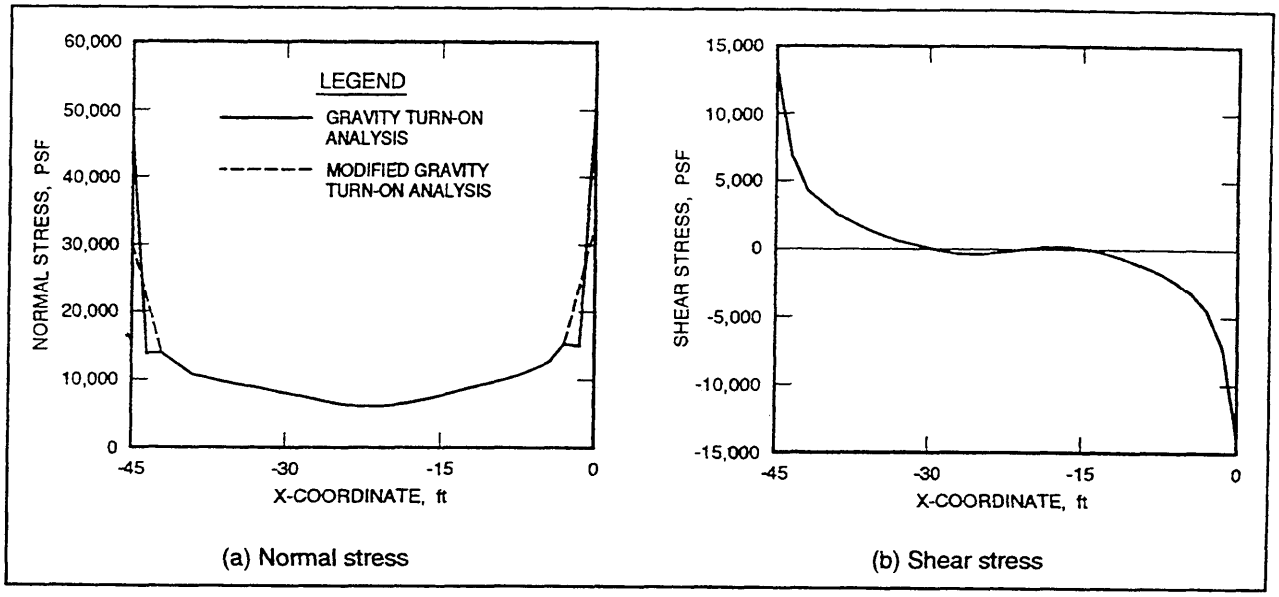

Figure 30. Initial stress distributions along the base - E_{ROCK}= 500,000 psi (1 ft = 0.305 m, 1 MPa = 20,885.5 psf)

500,000 psi (3,447.4 MPa). The modified gravity turn-on analysis normal and shear stress distributions have the same resultant normal and shear forces and the same points of force applications along the interface as the unmodified gravity turn-on analysis. Figure 31 compares the resulting initial normal and shear stress distributions for the two modified gravity turn-on analyses (E_{ROCK} equal to 3,500,000 and 500,000 psi (24,131.8 and 3,447.4 MPa)) with the stress distributions from the unmodified gravity turn-on analysis with E_{ROCK} equal to 10,000,000 psi (68,948 MPa).

The variation of stress distributions along the interface for three different initial stress distributions (Figure 31) after application of following loads is shown in Figure 32. All stress distributions are distinctly nonlinear. The resulting values for the effective base areas in compression for the three different composite rock foundation stiffnesses are nearly identical (Table 5). The three effective normal stress distributions shown in Figure 32 are similar but show a trend of increasing values of effective normal stress below the toe of the monolith (x = -45 ft (-13.7 m)) with decreasing composite rock foundation stiffness. This trend is reversed when the shear stresses computed below the toe of the monolith are compared for the three composite rock modulus values; the magnitude of shear below the toe of the monolith decreases with decreasing rock modulus.

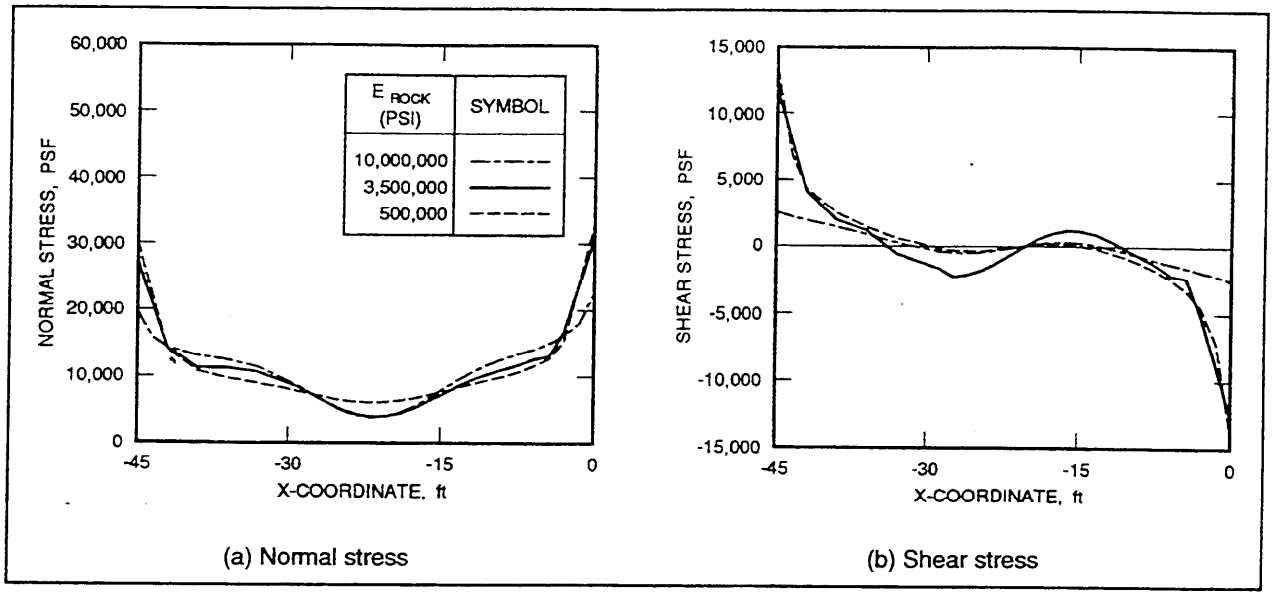

Figure 31. Variation of initial stress distributions along the base for different E_{ROCK} (1 ft = 0.305 m, 1 MPa = 20,885.5 psf)

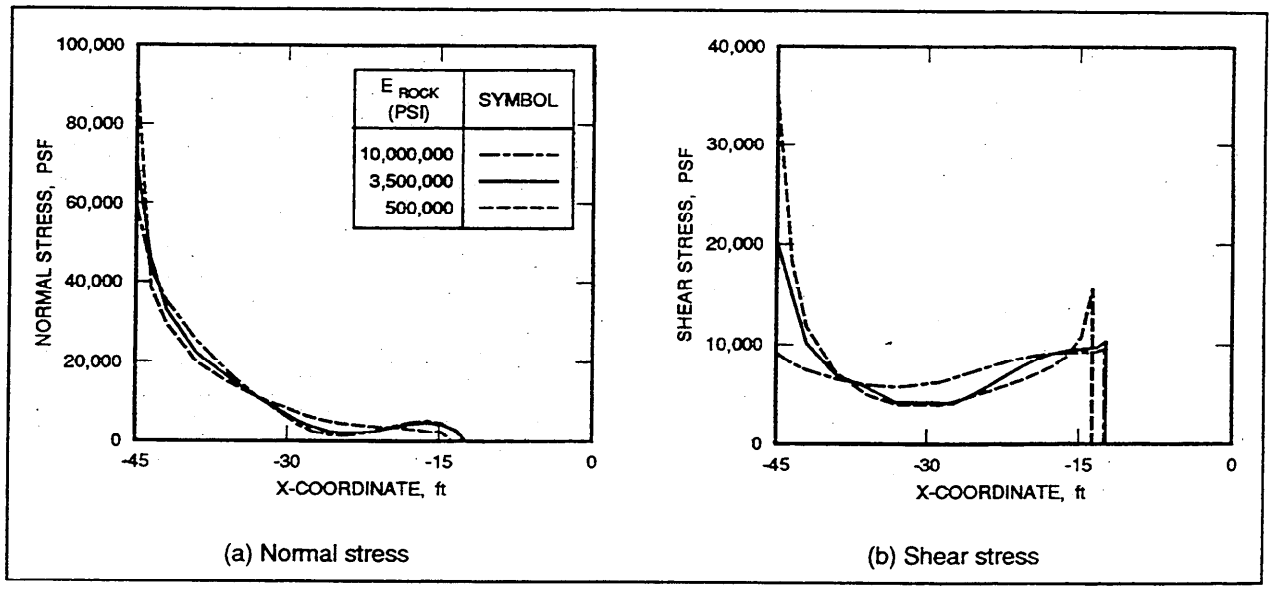

Figure 32. Variation of stress distributions along the base with rock modulus-following loads (1 ft = 0.305 m, 1 MPa = 20,885.5 psf)

Table 5
Summary of Base Area In Compression and Crack Lengths for Three Different Composite Rock Foundation Moduli After Application of Following Loads

Composite Rock Foundation Modulus E_{ROCK}, psi (MPa)	$\frac{E_{ROCK}}{E_{Concrete}}$	B_e ft (m)	Crack Length ft (m)	B_e/B %
10,000,000 (68,948)	2.86	32.50 (9.91)	12.5 (3.81)	72.2
3,500,000 (24,131.8)	1.0	32.65 (9.95)	12.35 (3.76)	72.5
500,000 (3,447.4)	0.14	31.30 (9.54)	13.70 (4.18)	69.6

Summary of Following Load Analyses of Locks 27 Gravity Retaining Wall

This chapter summarizes the results of a series of base case and parametric following load analyses of Locks 27 Monolith 7E gravity retaining wall. The principal results of the four base case following load analyses of Locks 27 Monolith 7E gravity retaining wall are as follows:

a. The four values of B_e/B computed using the conventional equilibrium analysis, SOILSTRUCT-ALPHA with interface elements, the discrete crack analysis using MERLIN, and smeared crack analysis using CG-DAMS are given in Table 6. The values of B_e/B computed using the three FE analyses were within 2 percent of each other and averaged 72 percent.

Table 6
Summary of Base Area in Compression and Crack Lengths Computed by Use of Four Analytical Methods

Method of Analysis	B_e ft (m)	Crack Length ft (m)	B_e/B %
Conventional Equilibrium Analysis	21.88 (6.67)	23.12 (7.05)	48.6
FEA with Interface Elements	32.65 (9.95)	12.35 (3.76)	72.5
Fracture Mechanics with Discrete Crack	31.98 (9.75)	13.02 (3.97)	71.1
Smeared Crack - Directed	33.0 (10.06)	12.0 (3.66)	73.3

b. The values of B_f/B computed using SOILSTRUCT-ALPHA, MERLIN and CG-DAMS were significantly greater than the 48.6 percent computed using the conventional equilibrium analysis.

c. All three FE analyses resulted in nonlinear normal effective stress distributions, contrasting with the assumed linear stress distributions assumed in the conventional equilibrium analysis.

The principal results of the parametric study of initial stress distributions within the lock wall on the results of the following load analyses of Locks 27 Monolith 7E gravity retaining wall are as follows:

a. The magnitude and distribution of initial stresses computed along the lock-wall-to-rock-foundation interface are dependent on the method used for computing the effects of self-weight of the monolith and soil wedge above the heel of the wall.

b. Differences were observed among the distributions of interface stresses computed after application of the following loads. The extent to which the stress distributions were different was found to be dependent upon the method used to establish the distributions of initial normal and shear stresses along the interface.

c. The values of B_f/B computed after application of the following loads in the three analyses differed by as much as 10 percent.

d. Among the three methods (gravity turn-on analysis, monolith build-up analysis, and an analysis with prescribed stresses equal to the overburden pressure), the incremental build-up analysis is the preferred method of analysis since it has been shown in case studies of instrumented retaining structures to provide more accurate results than those obtained through use of a gravity turn-on analysis (Clough and Duncan 1969).

The principal results of the parametric studies of composite rock foundation stiffness on the results of the following load analyses of Locks 27 Monolith 7E gravity retaining wall are as follows:

a. Variations in the value of composite rock foundation stiffness from a low value of 500,000 psi (3,447.4 MPa) to a high value of 10,000,000 psi (68,948 MPa) results in differences among the computed initial stress distributions along the lock-wall-to-rock-foundation interface and differences among the stress distributions after application of the following loads. Differences between initial stress distributions for the different composite rock foundation stiffnesses are most pronounced at the two "edges" of the monolith-to-rock interface.

b. The values of B_f/B computed after application of the following loads in the three analyses were nearly the same, with less than a 3-percent difference.

3 Downdrag on Backs of Rock-Founded Concrete Gravity Retaining Walls

The evaluation of the stability of rock-founded gravity retaining structures using a complete soil-structure interaction analysis was investigated during the first REMR Research Program, as reported by Ebeling, Clough, Duncan, and Brandon (1992) and Ebeling, Duncan, and Clough (1990). This study found that the conventional equilibrium analysis, according to Corps guidance in use prior to publishing the results from the REMR study, did not include all forces acting on these massive retaining structures. Specifically, a shear force acting along the wall-to-backfill interface was not included in the conventional equilibrium analysis. The Ebeling et al. (1990, 1992) REMR study found that this shear force acts downward along the back of the wall and results from the differential settlement within the backfill region adjacent to the wall. The moment (about the toe of the wall) due to this shear force acts to counter the overturning moment due to the earth pressure force acting normal to the wall-to-backfill interface. Thus, the shear force along the back of the wall is a stabilizing force. This shear force is also referred to as "downdrag."

Two methods are used to calculate the magnitude of the downdrag force acting along the backs of rock-founded gravity retaining walls. The first, referred to as the simplified procedure, makes use of design charts. These design charts are limited to a "standard" set of wall proportions which are typical of several of the Corps' rock-founded lock walls. Calculations involve vertical earth pressure coefficients and correction factors for wall geometry, surcharge loadings, and sloped backfills. The simplified procedure is summarized in the first section to follow this introduction.

The second method for calculating downdrag along the backs of gravity walls is the Clough and Duncan (1969) backfill placement method of analysis. It is a finite-element-based method of analysis, and unlike the simplified method, is applicable to all wall proportions and geometries. A complete backfill placement analysis of Locks 27 Monolith 7E was conducted using SOILSTRUCT-ALPHA (Ebeling, Duncan, and Clough (1990) and Ebeling et al. 1992), and results are reported later in this chapter. The Locks 27 Monolith 7E geometry is outside the realm of the wall proportions used to develop the empirical methods described in this chapter. The lower third of the Monolith 7E-to-backfill interface is vertical,

whereas the upper two-thirds is step-tapered, as shown in Figure 1 (Chapter 2). This geometry is common to several Corps lock walls.

Both calculation procedures to be described in this chapter are restricted to walls with engineered backfills that do not creep. Thus, the procedures are applicable to walls backfilled with soils classified as SW, SP, GW, and GP according to the Unified Soil Classification System (American Society for Testing and Materials (ASTM) 1990). They are also applicable to select SM backfills with nonplastic fines that do not creep.

Simplified Procedure for Calculating the Downdrag Force

A simplified design procedure was developed to calculate the downdrag (or shear) force along a vertical plane extending through the backfill from the heel of rock-founded gravity monoliths of select wall proportions. This empirical procedure was first reported in ETL 1110-2-352 (Headquarters, Department of the Army 1994). The simplified calculations described in this section reflect improvements made since publication (1994) of the ETL using the results from additional soil-structure interaction studies of rock-founded gravity retaining walls, reported in Ebeling and Filz (1997) and Filz, Duncan, and Ebeling (1997). It can be applied to walls retaining "dry" backfills (no water table) or to walls in which the groundwater level rises as the backfill is being placed.

The simplified design procedure for calculation of the vertical shear force evolved from data reported in Ebeling, Duncan, and Clough (1990), Ebeling et al. (1992) and Ebeling and Filz (1997). The gravity retaining walls used to generate these data were modeled after the proportions typical of rock-founded gravity lock walls found at several (but not all) Corps lock and dam sites. Vertical shear forces have been measured on walls retaining "nonyielding" backfills in numerous model tests and field situations (Terzaghi 1934a, 1934b; Gould 1970; Kany 1972; Matsuo, Kenmochi, and Yagi 1978; Fukuoka 1980; Sherif, Ishibashi, and Lee 1982; Vogt et al. 1986; Hilmer 1986; and Filz and Duncan 1992). The collective results of these case histories are summarized in Filz, Duncan, and Ebeling (1997).

The simplified procedure described in this section is restricted to walls retaining nonyielding backfills. A nonyielding backfill is one in which wall movements are not sufficient to fully mobilize the shear resistance within the backfill. U-frame lock walls and rock-founded gravity retaining walls, including gravity lock walls, are examples of walls with nonyielding backfills. Examples of a wall retaining a "yielding" backfill are the cases in which wall movements away from the backfill are sufficient to result in active earth pressures. Wall movements of sufficient magnitude into the backfill result in the other limit state of passive earth pressures. Limiting earth pressure states such as active or passive earth pressures are examples of yielding backfills, in which the soil shear strength is fully mobilized. Guidance regarding the magnitude of the wall movements to

achieve active and passive earth pressures is described in numerous references on retaining structures, including Clough and Duncan (1991).

The relationship given in ETL 1110-2-352 (Headquarters, Department of the Army 1994) for the vertical shear force, F_v, on the vertical plane extending through the level backfill from the heel of the Figure 33 wall is

$$F_v = K_v \cdot \left[\frac{1}{2}\gamma_{moist} (D_1)^2 + \gamma_{moist} (D_1 D_2) + \frac{1}{2} \gamma_b (D_2)^2 \right] \qquad (3 \text{ bis})$$

where

K_v = vertical earth pressure coefficient

γ_{moist} = moist unit weight of backfill (above the water table)

D_1 = thickness of backfill above the hydrostatic water table

D_2 = thickness of submerged backfill above base of wall

γ_b = buoyant unit weight of submerged backfill, $\gamma_{sat} - \gamma_w$

γ_{sat} = saturated unit weight of submerged backfill

γ_w = unit weight of water = 62.4 pcf (9.81 kN/m^3)

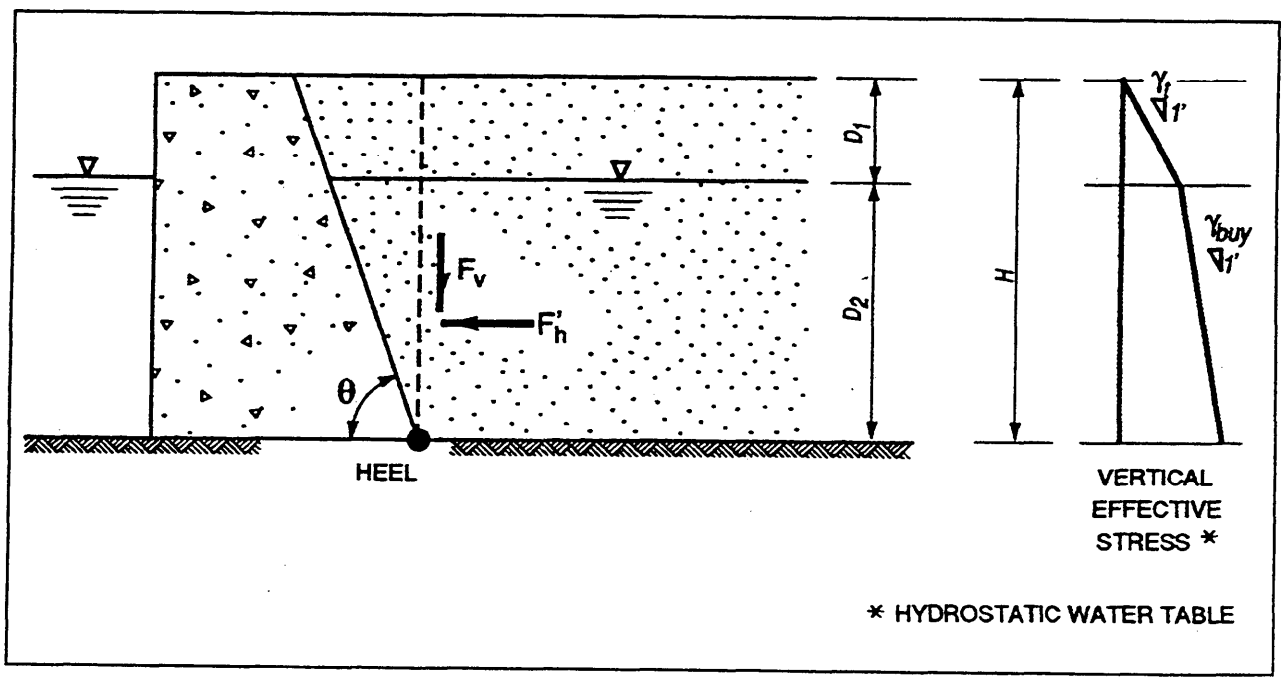

Figure 33. Vertical and effective horizontal earth pressure forces on vertical plane extending through the backfill from the heel of the monolith

A procedure using design charts and correction factors is given in this ETL for computing the appropriate value for K_v. Further, this equation assumes that water pressures are hydrostatic within the backfill and the rise in water table concurrent with the placement of the soil lifts. As indicated in Figure 33, the sum of the thickness D_1 and D_2 equals the total height of the level backfill. This procedure is based on the results of the complete soil-structure interaction analyses of rock-founded gravity walls of "select" proportions, made using the backfill placement method of analysis as incorporated in SOILSTRUCT-ALPHA (Ebeling, Duncan, and Clough 1990).

Equation 3 was first discussed in Chapter 2 regarding the vertical shear force applied to the following load analyses of Locks 27 Monolith 7E. The ETL procedure for assigning the value to K_v was not used in the following load analyses of Locks 27 Monolith 7E.

The Ebeling and Filz (1997) study expanded Equation (3) to include the effects of surcharge and sloping backfill. In the case of rock-founded gravity walls with the inclined backfill surface shown in Figure 34, F_v is calculated using

$$F_v = F_{v,soil} + F_{v,q} \tag{10}$$

where

$$F_{v,soil} = K_{v,soil} \cdot \left[\frac{1}{2}\gamma_{moist} (D_1)^2 + \gamma_{moist} (D_1 D_2) + \frac{1}{2} \gamma_b (D_2)^2 \right] \tag{11}$$

$K_{v,soil}$ = vertical shear force coefficient for self-weight of backfill (equivalent to K_v in Equation 3)

and

$$F_{v,q} = K_{v,q} \, q \, H \tag{12}$$

where

$K_{v,q}$ = vertical shear force coefficient for sloping backfill and surcharge

$$q = \textit{applied surcharge pressure} = \Delta H \gamma_{moist} \tag{13}$$

The height H is measured along the vertical plane extending through the backfill and ΔH is equal to $[H_b - H]$, as shown in Figure 34.

The vertical shear force coefficient for self-weight of the backfill $K_{v,soil}$ is computed using

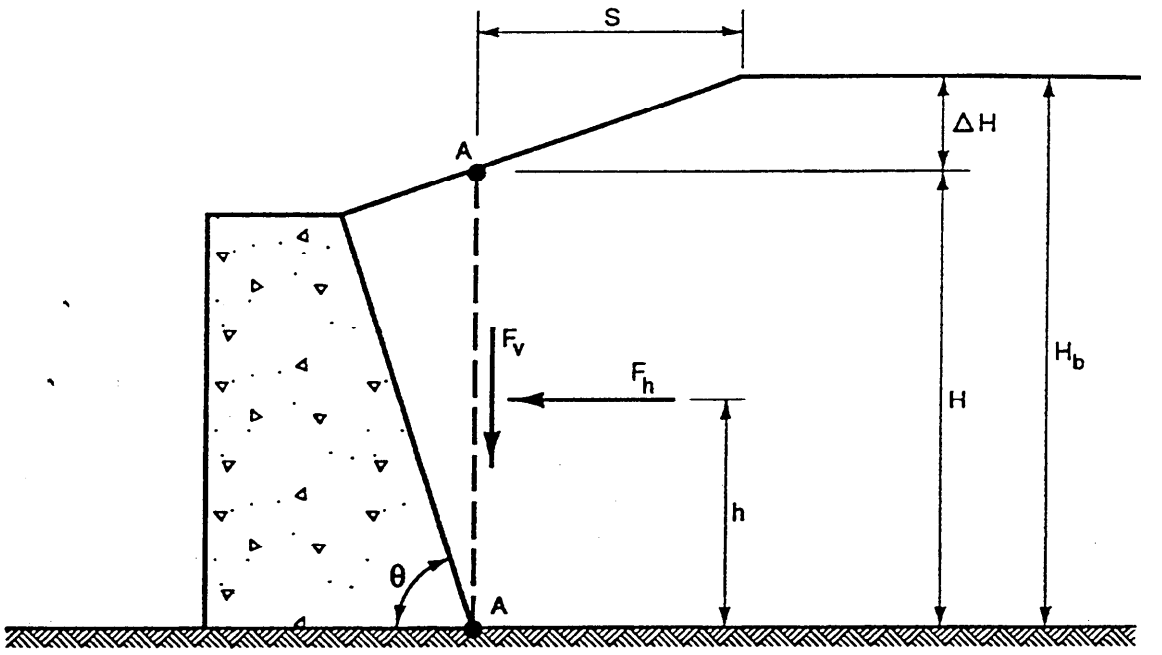

(a) Mass concrete wall with a planar, sloping backside and an inclined backfill surface

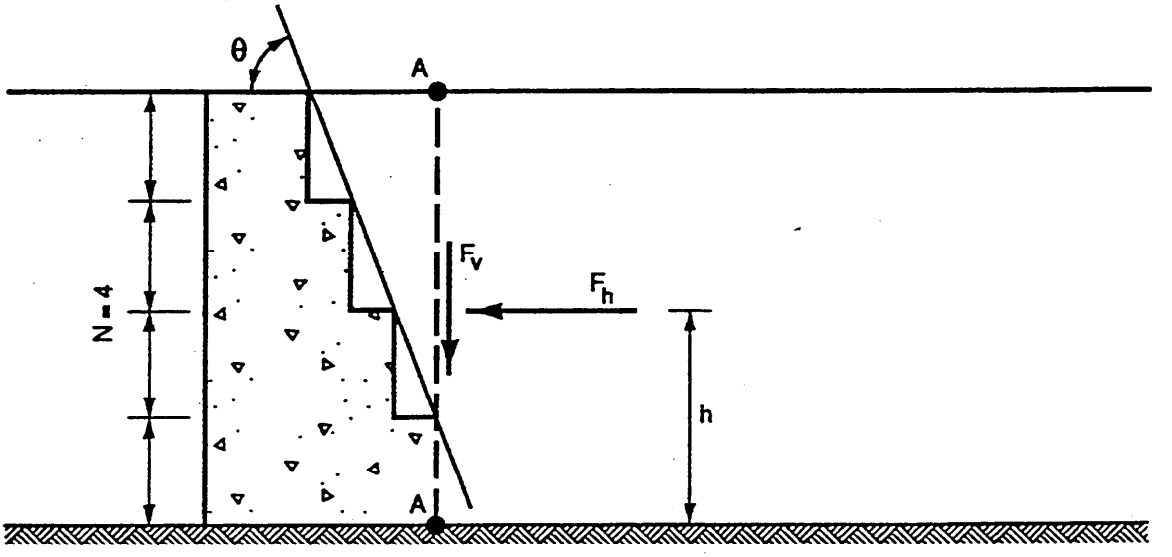

(b) Mass concrete wall with a stepped backside

Figure 34. Rock-founded gravity retaining wall definition sketches

$$K_{v,soil} = (1 - C_\theta \, C_N) \, K_{v,soil,ref} \quad (14)$$

where

$K_{v,soil,ref}$ = reference value of $K_{v,soil}$ obtained for a value of $\theta = 90$ degrees

C_θ = correction factor for inclination of the back side of a rock-founded gravity wall

C_N = correction factor for the number of steps in the back side of a rock-founded gravity wall. Calculation of the value for N is shown in Figure 34.

Given the density of the backfill and the Figure 34 definition of height H, values for $K_{v,soil,ref}$ are obtained from Figure 35 using the curves designated as "design" curves. The data designated as "FEM" are based on the results of complete soil-structure interaction analyses using SOILSTRUCT-ALPHA (Ebeling and Filz 1997 or Filz, Duncan, and Ebeling 1997) and are for reference only. The correction factors C_θ and C_N are given in Figure 36. The vertical shear force coefficient for sloping backfill and surcharge $K_{v,q}$ is given by

$$K_{v,q} = C_S \, K_{v,q,ref} \quad (15)$$

where

$K_{v,q,ref}$ = reference value of $K_{v,q}$ obtained for a value of $S = 0$

S = horizontal distance from the plane above the wall heel to the top of the backfill slope, as shown in Figure 34

C_S = correction factor for a rock-founded gravity retaining wall with an inclined backfill surface.

Given the density of the backfill and the Figure 34 definition of height H, values for $K_{v,q,ref}$ are obtained from Figure 37 using the curves designated as "design" curves. The data points designated as "FEM" are the results of the finite element method as applied in the backfill placement method of soil-structure interaction analysis (Ebeling and Filz 1997 or Filz, Duncan, and Ebeling 1997) and are for reference only. The correction factor C_S is given in Figure 36.

Filz, Duncan, and Ebeling (1997) present a complete example calculation using this simplified procedure for F_v for a 30-ft (9.14-m) -high, step-tapered, rock-founded, gravity wall retaining dense sand with surcharge (no groundwater table). This example shows the impact of including F_v in equilibrium calculations used to (size) design a rock-founded gravity wall, as compared with the case in which F_v is ignored. Specifically, a 14-percent reduction in base width is realized by including F_v without compromising the design safety requirements.

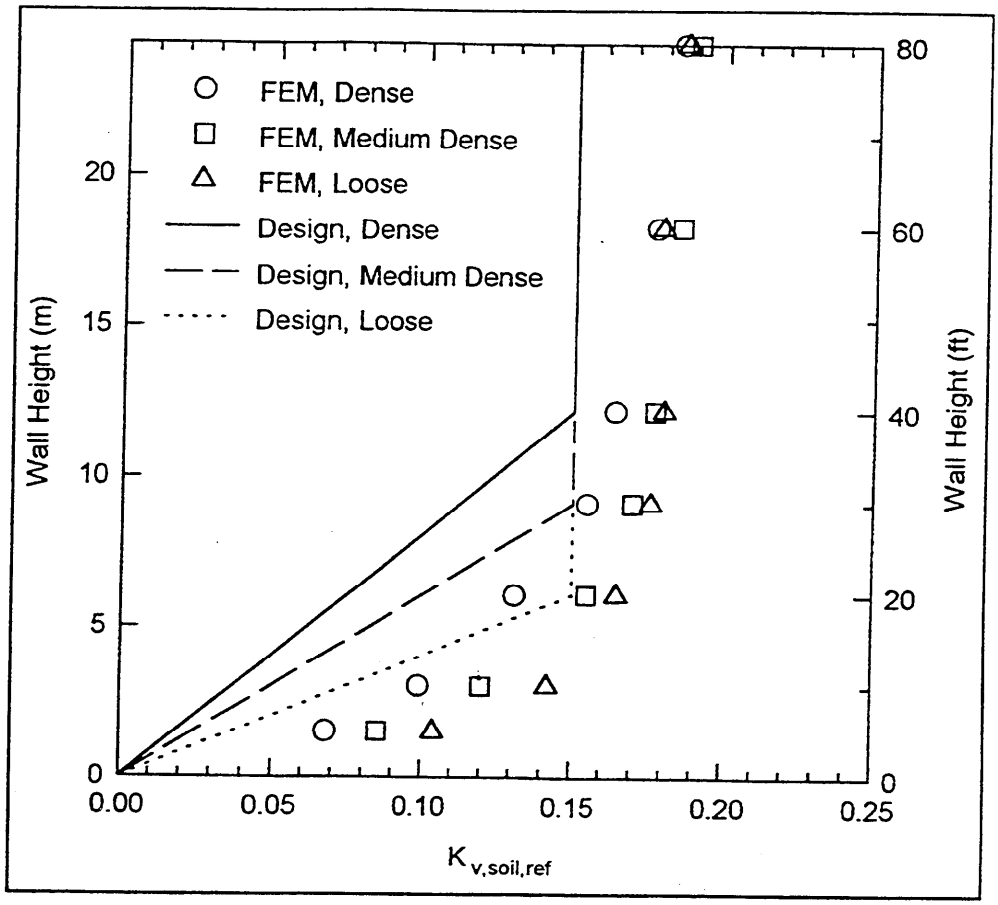

Figure 35. Values of $K_{v,\,soil,\,ref}$ recommended for design (1 ft = 0.305 m)

Soil-Structure Interaction Analysis of Gravity Retaining Wall at Locks 27

This section describes the results of a complete soil-structure interaction analysis of Locks 27 Monolith 7E using the backfill placement method of analysis incorporated in SOILSTRUCT-ALPHA. This type of analysis is applicable to all types of retaining structures. Locks 27 Monolith 7E is described in Chapter 2 and shown in Figure 1. Its wall geometry differs from the lock walls shown in Figure 34 (for the simplified procedure) in that there are two distinct "slopes" along the back of the wall, a vertical back for the lower third of wall height, and a step-tapered back along the upper two-thirds of wall height. This geometry is similar to those found at other Corps lock sites.

The simplified procedure was not applied to Locks 27 Monolith 7E due to the back-of-wall configuration. Recall that one restriction to the simplified procedure has to do with the wall configurations used in the soil structure interaction studies (Ebeling, Duncan, and Clough 1990, Ebeling et al. 1992, and Ebeling and Filz 1997) upon which the simplified procedure is based. Figure 34 shows that the

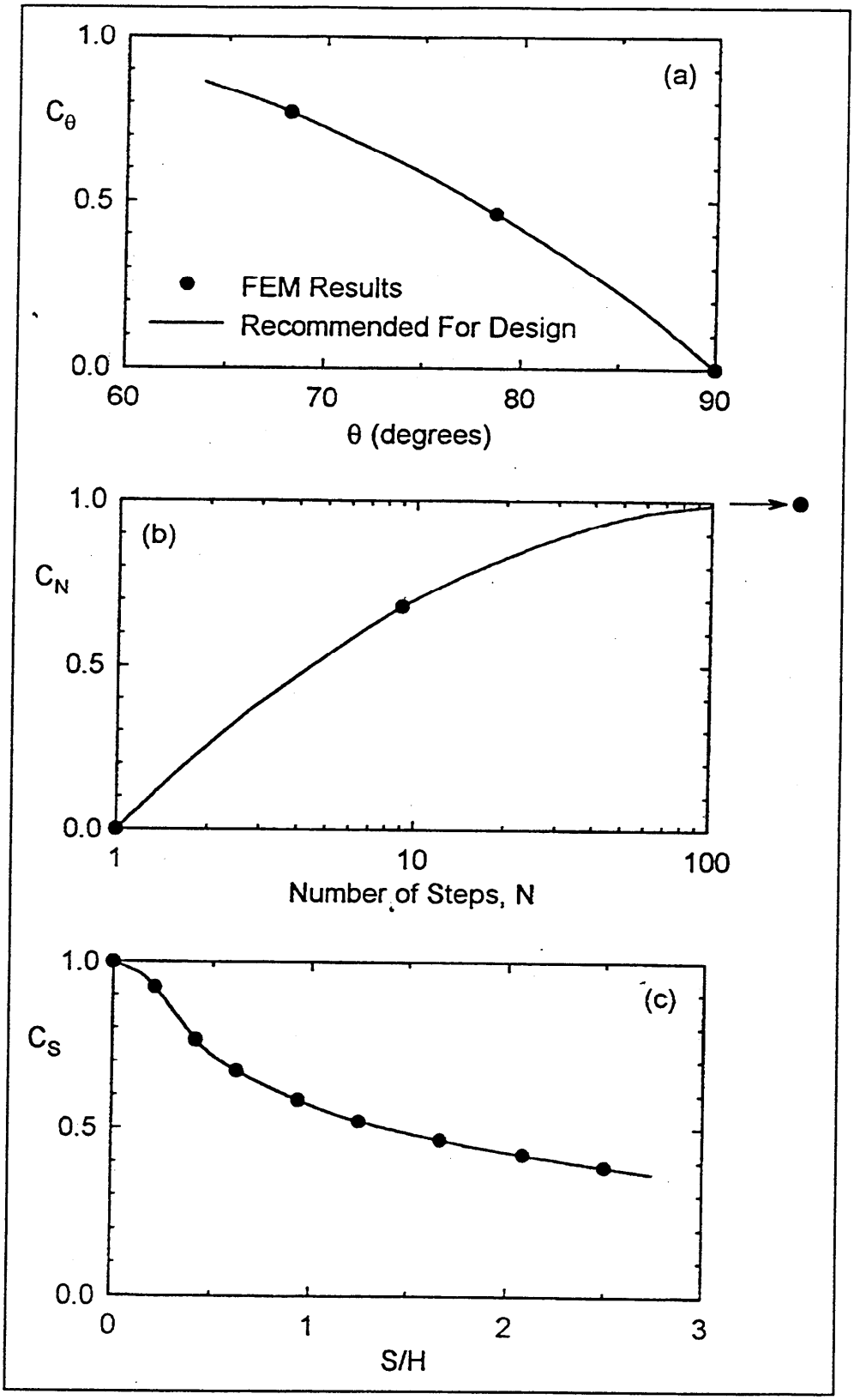

Figure 36. Correction factors C_σ, C_m and C_s

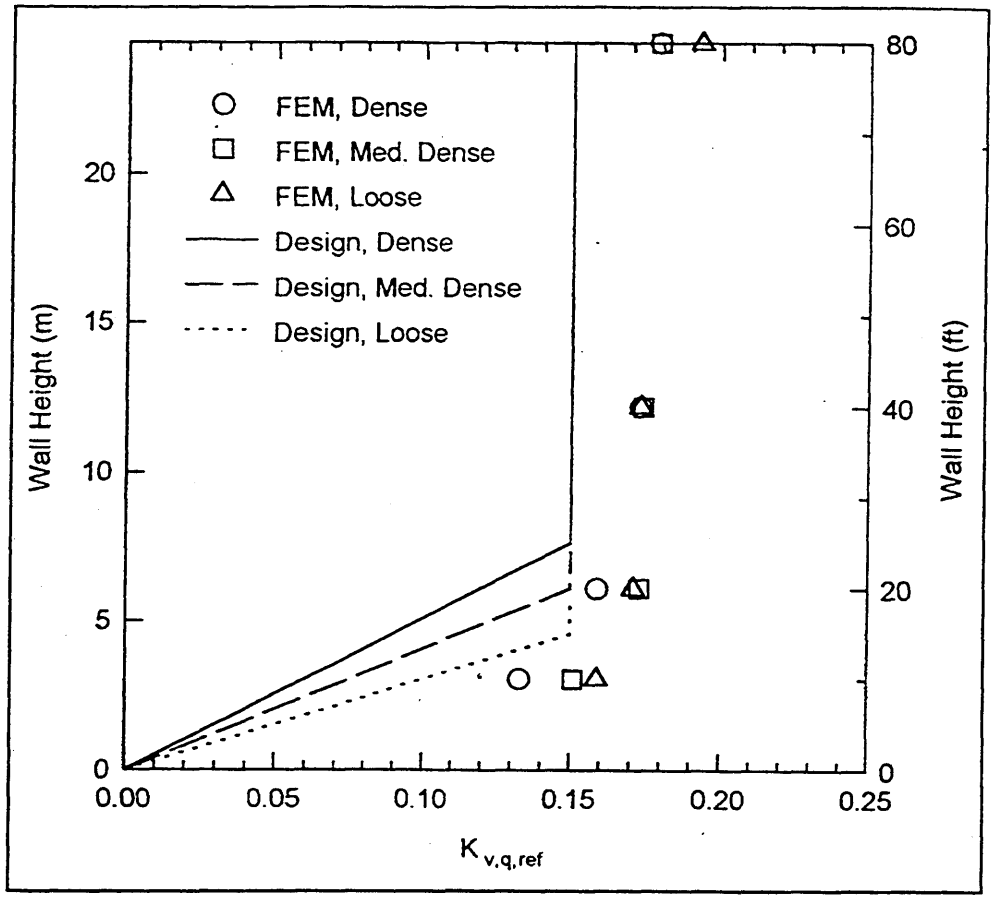

Figure 37. Values of $K_{v,q,ref}$ (1 ft = 0.305 m)

slope (or step taper) along the backs of the walls in this figure is constant. Thus, the simplified procedure is applicable to many, but not all, rock-founded gravity retaining walls and lock walls.

One of the earliest successful applications of soil-structure interaction analysis was performed by Clough and Duncan (1969) in their analysis of the two reinforced concrete U-frame locks at Port Allen and Old River. These two locks had been extensively instrumented. Prior to Clough and Duncan's analysis, the instrumentation data had been thought to be unreliable and contrary to the perceived understanding of the behavior of locks to loadings encountered during lock operation. Clough and Duncan's study showed that the best agreement between results computed using the finite element method and those obtained through instrumentation measurements is obtained when the actual construction process is simulated as closely as possible in the analysis. During their study, Clough and Duncan developed what is referred to as a *backfill placement analysis* in which the loads exerted by the backfill on the lock wall are generated automatically during simulated placement of backfill behind the wall (i.e., predetermined earth pressure force distributions between the soil and the lock are *not* specified). This requires that the soil backfill and foundation soil strata be included in the finite element mesh. This procedure involved the use of incremental finite element

analysis with nonlinear, stress-dependent, stress-strain behavior for the soil. Linear elastic behavior was assumed for the concrete lock wall. An additional requirement is that interface elements be incorporated within the finite element mesh to allow for relative movement between the soil and structure. Since the Clough and Duncan study, soil-structure interaction analysis using the backfill placement procedure has been successfully applied to a variety of earth retaining structures and was also applied in this study. Since the development of SOIL-STRUCT, much progress has been made in the development and numerical implementation of constitutive models for soils. However, for static soil-structure interaction problems, the simplicity of SOILSTRUCT and its hyperbolic stress-strain model still make it an effective engineering tool.

SOILSTRUCT (Ebeling, Peters, and Clough 1992) is a special-purpose, finite element program for 2-D plane-strain analysis of soil-structure interaction and soil-inclusion interaction problems. SOILSTRUCT calculates displacements and stresses resulting from incremental construction, excavation, dewatering, and/or load application. Nonlinear, stress-path-dependent, stress-strain behavior of the backfill was approximated in the finite element analysis using the tangent modulus method. In the tangent modulus method, new values of tangent moduli are assigned to each soil element at each increment of loading (i.e., dewatering, lock construction, and backfilling) or unloading (i.e., excavation).

SOILSTRUCT was expanded during the first REMR Research Program to model the loss of contact between the base of a wall (a lock in this case) and its rock foundation using a procedure called the Alpha method (Ebeling, Duncan, and Clough 1990; Ebeling et al. 1992). SOILSTRUCT-ALPHA was used in the analysis of Locks 27 Monolith 7E because of this capability.

Figure 38 shows the finite element mesh used to model Locks 27 Monolith 7E. The mesh comprises 2,473 nodal points and 2,348 continua and interface elements. Of the 2,249 continua elements, 504 model the concrete monolith, 1,020 model the rock foundation, and 725 model the backfill. Of the 99 interface elements, 30 model the monolith-to-rock foundation interface, 25 model the rock-to-backfill interface, and 29 model the monolith-to-backfill interface. The remaining 15 interface elements are in the rock foundation along a vertical plane extending through the rock foundation from the heel of the wall. These 15 interface elements are "locked" together with the assignment of high normal and shear stiffnesses.

The step-tapered portion of the back of Locks 27 Monolith 7E (Figure 1) was modeled as a constant slope and with interface elements between the wall and the backfill. To compensate for the "roughness" that the steps impart on the backfill (with respect to sliding along the back of the wall), a high value of effective angle for interface friction $\delta'_{interface}$ was assigned ($\delta'_{interface} = \phi'_{sand}$). This simplification in the finite element model results in the calculation of a slightly lower value of F_v compared to what the results would be for a more complex finite element model of this region, and, thus, is conservative.

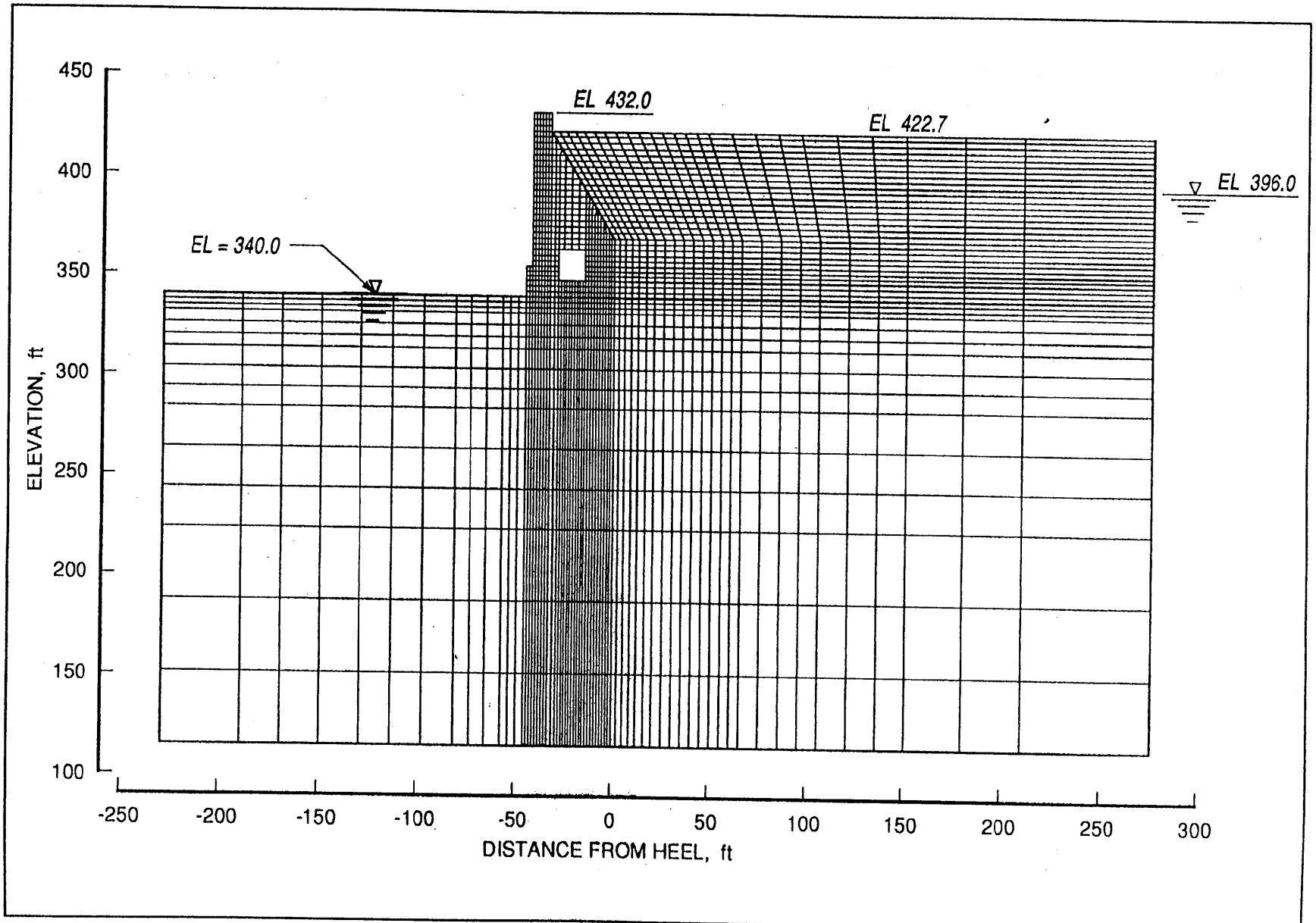

Figure 38. Finite element mesh of Locks 27 Monolith 7E, SOILSTRUCT-ALPHA backfill placement analysis (1 ft = 0.305 m)

The values assigned to the elastic parameters of the concrete were the same as those used in the following load analyses of Locks 27 Monolith 7E (Chapter 2, Table 1); Young's modulus of concrete equal to 3,500,000 psi (24,131.8 MPa) and Poisson's ratio equal to 0.2.

Similarly, the values assigned to the elastic parameters of the rock foundation were the same as those used in the following load analyses of Locks 27 Monolith 7E (Chapter 2, Table 1): Young's modulus of concrete equal to 3,500,000 psi (24,131.8 MPa) and Poisson's ratio equal to 0.2. This value of composite rock-foundation stiffness is consistent with a "fair" rock by the RMR classification procedure (Chapter 2, Figure 28).

The soil that comprises the Locks 27 backfill is a medium dense to dense sand. Site-specific triaxial test data were unavailable for the backfill. Material parameters were assigned in the finite element analysis based on empirical correlations to the results for similar types of soils (and with the same density) for which hyperbolic stress-strain curve material parameters are available (e.g., Duncan, Byrne, Wong, and Mabry 1978). An additional requirement for the soil model was that the assigned soil properties correspond to an at-rest earth pressure coefficient equal to 0.45. Appendix B (with supporting calculations made in Appendixes C, D, E, and F) describes the calculations that were made which resulted in the assignment of values for the hyperbolic stress-strain soil model of the backfill given in Table 7. These calculations include two settlement analyses of a partially submerged 1-D soil column due to self-weight of the soil. Settlement calculations were made using both SOILSTRUCT-ALPHA and Janbu's tangent modulus method.

Similarly, no specific tests were performed to define the hyperbolic shear stress-relative displacement relationship for the interface element used in SOILSTRUCT-ALPHA. The assignment of material parameters to the interface elements was based on empirical correlations to the results for similar types of soils (and with the same density) for which hyperbolic stress-strain curve material parameters are available (e.g., Clough and Duncan 1969 and Peterson, Kulhawy, Nucci, and Wasil 1976). Table 8 summarizes the interface model and strength parameters assigned to the concrete-to-sand and rock-to-sand interface regions. Zero tensile strength is assumed for the material comprising the monolith-to-rock foundation interface in this analysis. Table 2 (Chapter 2) summarizes the material properties assigned to the interface between the monolith and the rock foundation.

The initial stresses due to the self-weight of the monolith and along the monolith-to-rock foundation interface were computed in a monolith buildup analysis. Construction of the monolith was modeled in 25 lifts with $\gamma_{concrete}$ equal to 150 pcf (2,402.76 kg/m^3). The concrete lifts ranged from a minimum thickness of 2.33 ft (0.71 m) within the lower portion of the monolith to a maximum thickness of 9.3 ft (2.83 m) near the top.

Table 7
Hyperbolic Stress-Strain and Strength Parameters[1]

Backfill	Unit Weight pcf (kg/m³)	Strength Parameters		Hyperbolic Parameters						
		c′ psf (kPa)	ϕ′ deg	K	n	K_{UR}	K_B	m	υ_{nom}	R_F
Moist Sand	125.0 (2,002)	0 (0)	35	500	0.5	600	200	0.5	0.088	0.7
Submerged Sand	130.0 (2,082)	0 (0)	35	500	0.5	600	200	0.5	0.088	0.7

[1]Note:

$$\textit{Tangent Modulus, } E_t = E_i \left(1 - R_F\, SL \right)^2$$

$$\textit{Initial Modulus, } E_i = K\, P_a \left(\frac{\sigma_3'}{P_a} \right)^n$$

$$\textit{Stress Level, } SL = \left(\sigma_1 - \sigma_3 \right) / \left(\sigma_1 - \sigma_3 \right)_{Failure}$$

$$\left(\sigma_1 - \sigma_3 \right)_{Failure} = \frac{2\, c' \cos \phi + 2\, \sigma_3' \sin \phi}{1 - \sin \phi}$$

$$\textit{Unload-Reload Modulus, } E_{UR} = K_{UR}\, P_a \left(\frac{\sigma_3'}{P_a} \right)^n$$

$$\textit{Bulk Modulus, } B = \frac{E_i}{\left(3 - 6\, \upsilon_{nom} \right)}$$

$$\textit{Bulk Modulus, } B = K_B\, P_a \left(\frac{\sigma_3'}{P_a} \right)^m$$

υ_{nom} = *Nominal value of Poisson's ratio*

$$\textit{Poisson's ratio, } \upsilon = \frac{1}{2} \left[1 - \left[\left(1 - 2\, \upsilon_{nom} \right) \left(1 - R_F\, SL \right)^2 \right] \right]$$

P_A = atmospheric pressure

Table 8
Material Properties for Interface Elements Comprising SOILSTRUCT-ALPHA Finite Element Model of Locks 27 Monolith 7E for Backfill Placement Analysis[1]

Interface Region	Hyperbolic Parameters				Normal Stiffness
	ϕ'_i deg	K_j	n_i	R_{fi}	k_m psf/ft (MPa/m)
Concrete-to-Sand	35	1.0×10^4	0.8	0.9	1.0×10^8 (15,708.7)
Rock-to-Sand	35	1.0×10^4	0.8	0.9	1.0×10^8 (15,708.7)

[1]Notes:

Equations for the Interface Model

The normal stress at the center of the interface element is given by

$$\sigma_n = k_n \Delta_n$$

where Δ_n is the average relative displacement normal to the interface element. For each load increment, the change in shear stress at the center of the interface element is given by

$$\Delta\tau_s = k_{st} \Delta_s$$

where Δ_s is the average change relative shear displacement along the interface element.

$$k_{st} = k_{si} (1 - R_{fi} SL_i)^2$$

$$k_{si} = K_j \gamma_w \left(\frac{\sigma'_n}{P_a} \right)^{nj}$$

$$SL_i = \tau / \tau_{Failure} = \tau / (\sigma'_n \tan \phi_i)$$

γ_w = unit weight of water

P_A = atmospheric pressure

Figure 39 shows the resulting normal and shear stress distributions along the monolith-to-rock interface after monolith buildup. Both shear and normal stress distributions are nonlinear. As anticipated, greatest values of stress were computed below the toe of the monolith (x = -45 ft (-13.71 m)) because the greatest concrete mass is concentrated above this region.

Placement of the backfill proceeded once the monolith was constructed in the finite element model. The backfill placement analysis was modeled in 29 lifts. The thickness of the soil lifts varied within a narrow range, from a minimum

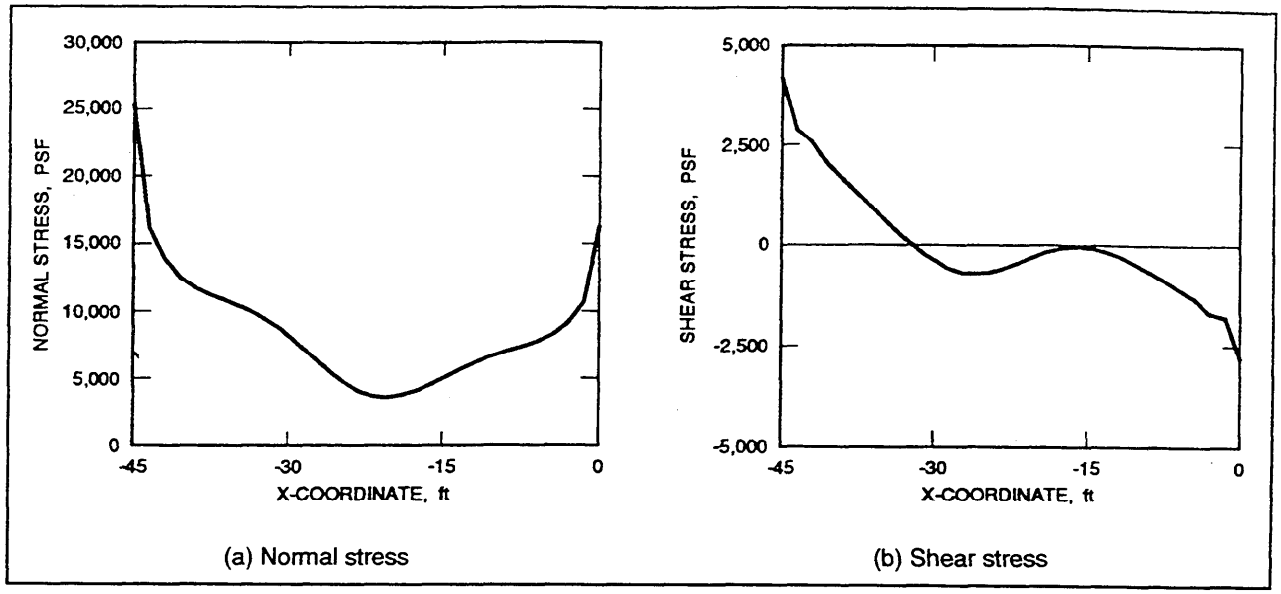

Figure 39. Initial stress distributions along the base, backfill placement analysis (1 ft = 0.305 m, 1 MPa = 20,885.5 psf)

thickness of 2.33 ft (0.71 m) to a maximum thickness of 3.0 ft (0.91 m). A con current rise in groundwater level with fill placement was assumed. With water pressures assumed hydrostatic within the backfill, the buoyant soil unit weight (67.6 pcf (1,082.8 kg/m^3)) was assigned to the submerged soil during the backfill placement analysis.

Boundary water pressures were assigned (incrementally) for each lift placement along the back of the monolith and along the top of rock foundation below the backfill. One-dimensional confined flow was assumed along the monolith-to-rock interface with a linear variation in uplift pressures from the heel to the toe along this interface (for full monolith-to-rock contact). Within this interface, uplift pressures were applied upward along the base of the monolith and downward along the top of the rock foundation. The incremental application of these water pressures continued with application of each new lift in the backfill until el 396 was attained. Locks 27 field instrumentation show a hydrostatic water table at el 396 in the backfill. When base separation occurred along the heel of the monolith-to-rock interface during backfill placement using SOILSTRUCT-ALPHA, uplift pressures within the "crack" were increased to values equal to the hydrostatic water pressures within the backfill (Chapter 2, Figure 5c). The assignment of hydrostatic water pressures within the cracked portion of a monolith's interface is consistent with Corps stability criteria.

Figure 40 shows the resulting normal effective and shear stress distributions along the monolith-to-rock interface after placement of the 29 lifts of backfill. The resultant base area in compression B_e equals 37.29 ft (11.37 m), 82.9 percent of the base. Both shear and effective normal stress distributions are nonlinear. The greatest stress values are computed below the toe of the monolith, as anticipated.

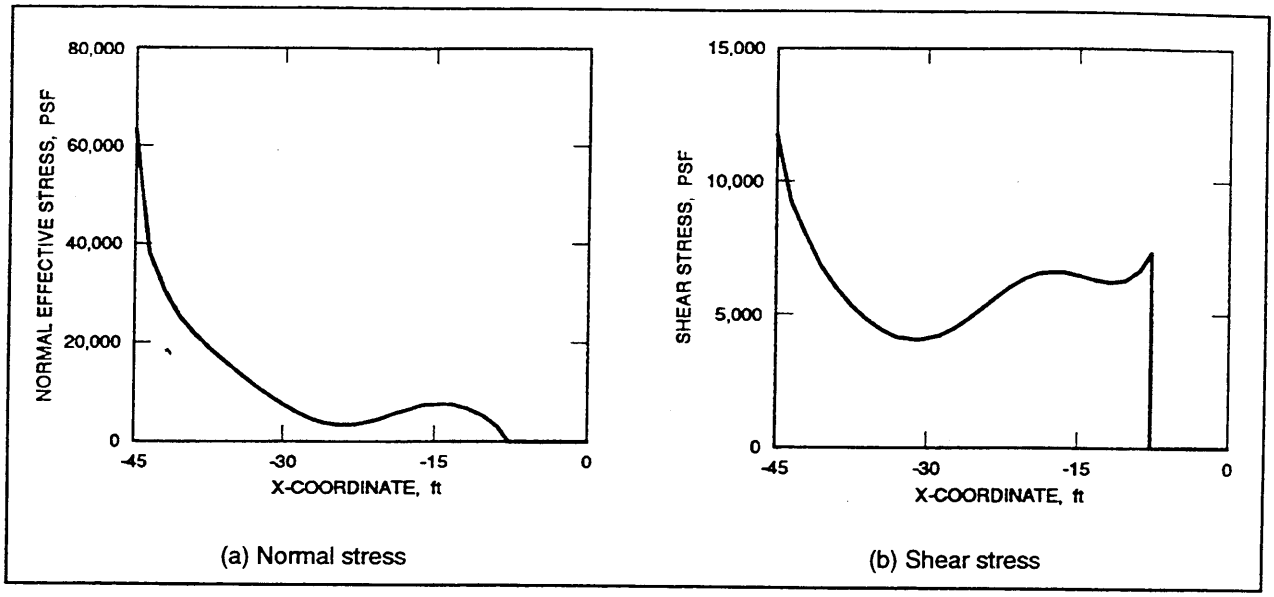

Figure 40. Variation of stress distributions along the base after backfill placement analysis (1 ft = 0.305 m, 1 MPa = 20,885.5 psf)

Figure 41 shows the variation of horizontal effective stress with elevation in the backfill and variation in horizontal earth pressure coefficient K_h, along select vertical sections within the backfill. K_h varies from a low value of 0.371 adjacent to the wall to a high value of 0.448 at free field in Figure 41 (x = 243 ft (74.06 m), $x/H_{backfill} = 2.94$). Note that K_h equal to 0.448 in the free field is consistent with 1-D soil column settlement analyses reported in Appendix B and with the requirement that K_o equal 0.45 for the backfill. Recall that the conditions corresponding to K_o stress state within the soil exist in the region designated as free field in the backfill.

Figure 42 shows the variation of shear stress with elevation in the backfill and variation in vertical earth pressure coefficient K_v (by Equation 3 or, equivalently, $K_{v,soil}$ in Equation 11) along select vertical sections within the backfill. K_v varies from a high of 0.143 adjacent to the wall to 0.0 approximately 25 ft (7.61 m) from the heel of the wall in Figure 42 (x = 25 ft (7.61 m), $x/H_{backfill} = 0.3$).

The value of K_v along the entire vertical section extending through the backfill from the heel of the wall equals 0.143. Recall that there is a change in back slope of the wall at el 369. The vertical earth pressure coefficient was recomputed along this section for the lower section below el 369 (designated Region A) and the upper section (designated Region B) using the relationships

$$Region\ A : K_v = \frac{F_v\ for\ Region\ A}{\int_{El\ 369}^{El\ 422.7} \sigma'_{overburden}\ dy} \tag{16}$$

and

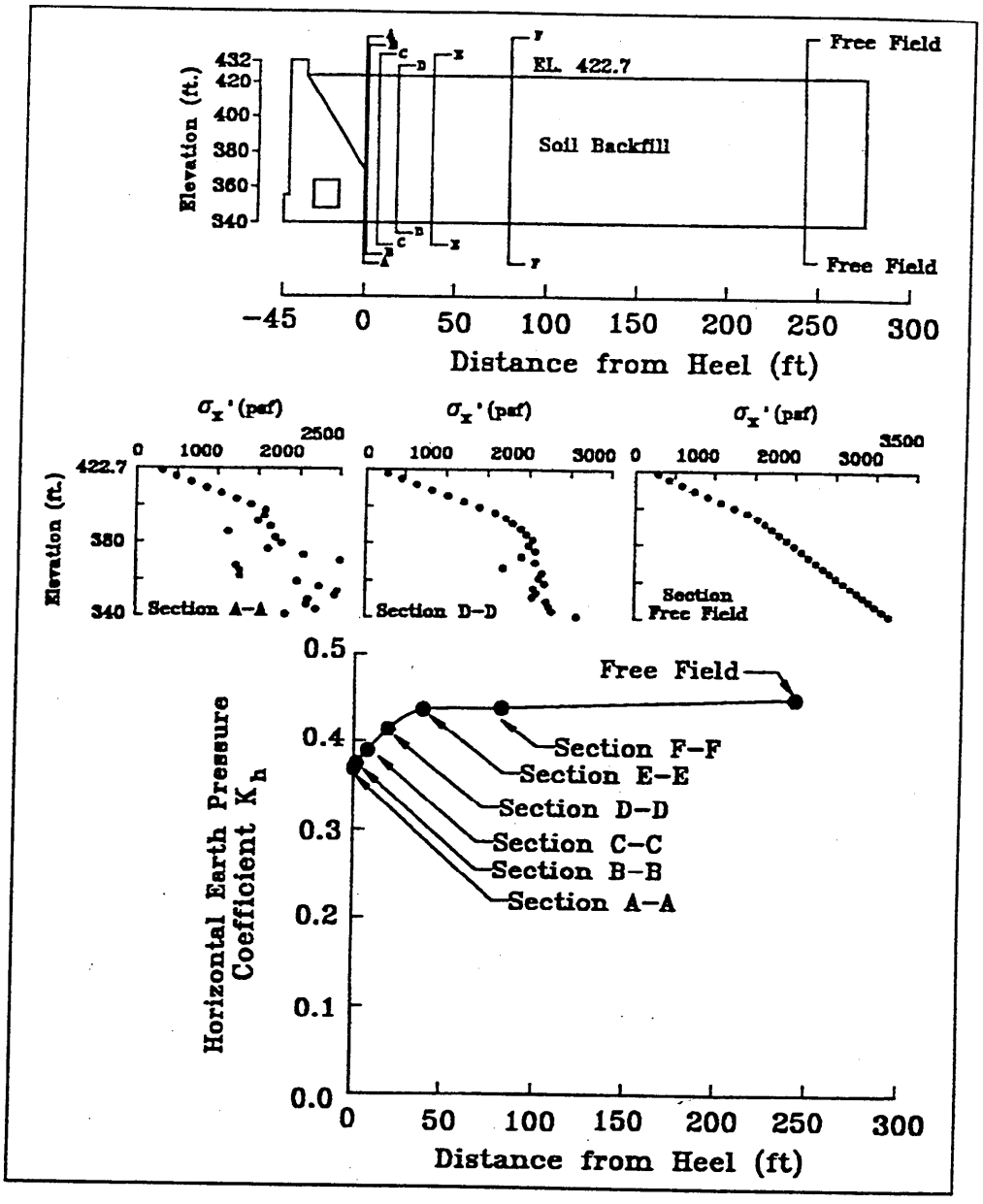

Figure 41. Variation of horizontal effective stress and horizontal earth pressure coefficient with distance from heel of Locks 27 Monolith 7E (1 ft = 0.305 m, 1 MPa = 20,885.5 psf)

$$Region\ B : K_v = \frac{F_v\ for\ Region\ B}{\int_{El\ 340}^{El\ 369} \sigma'_{overburden}\ dy} \tag{17}$$

The resulting values of K_v for Regions A and B equal 0.1257 and 0.1583, respectively. Figure 43 shows the variation of shear stress τ_{xy} divided by the effective overburden pressure $\sigma'_{overburden}$ with elevation in the backfill (29 values

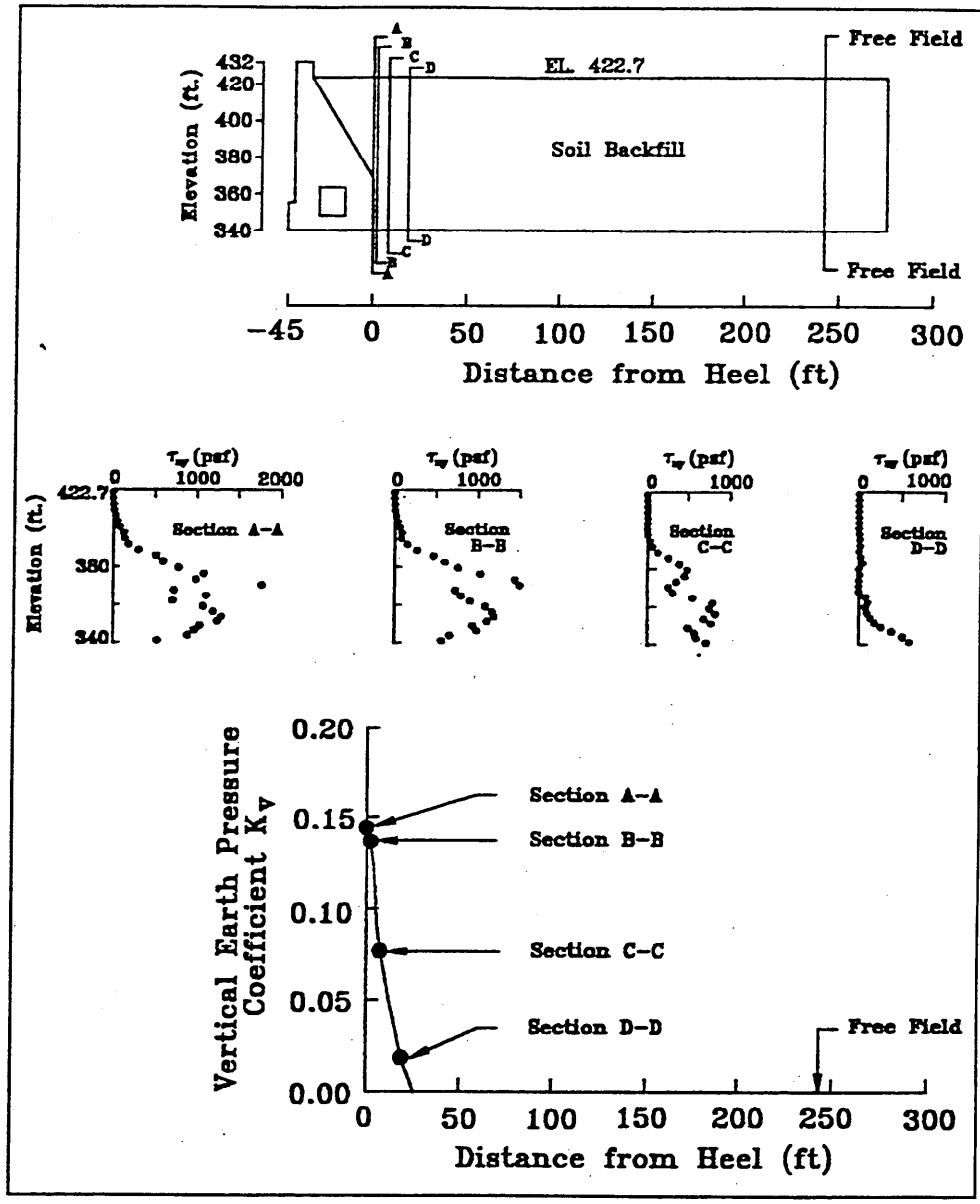

Figure 42. Variation of shear stress and vertical earth pressure coefficient with distance from the heel of Locks 27 Monolith 7E (1 ft = 0.305 m, 1 Mpa = 20,885.5 psf)

corresponding to the 29 soil lifts that comprise the backfill) compared to the values of K_v for Regions A and B. Using the data shown in this figure, the average value of $[\tau_{xy}/\sigma'_{overburden}]$ is computed to be 0.0846 for Region A (18 soil lifts) and 0.1606 for Region B (11 soil lifts). Note that the average values of $[\tau_{xy}/\sigma'_{overburden}]$ for the two regions are not equivalent to the K_v values. Thus, F_v should be computed using K_v value(s) and not by using average $[\tau_{xy}/\sigma'_{overburden}]$ value(s).

The percent of base in compression computed in this complete soil-structure interaction analysis, B_c/B equal to 82.9 percent, is greater by 10.4 percent than

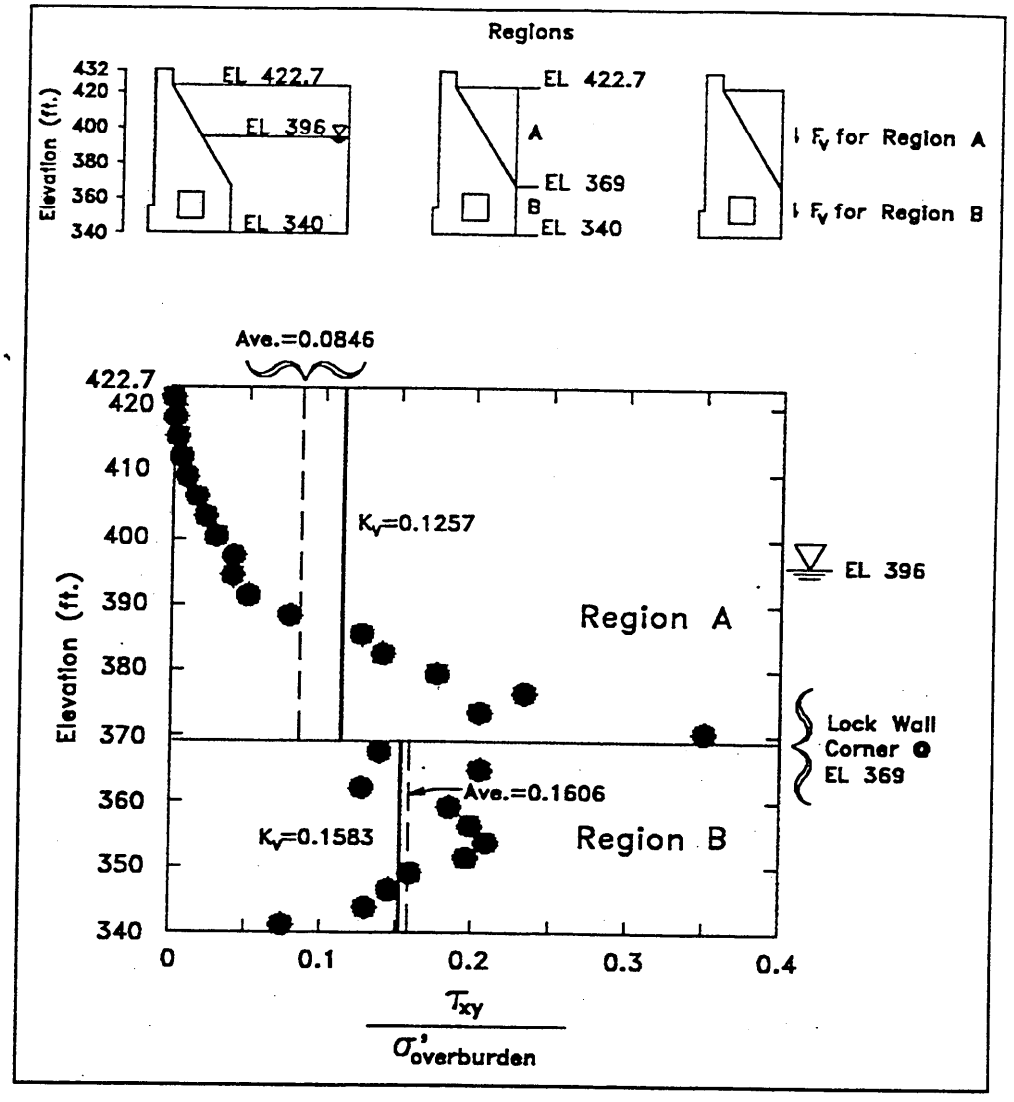

Figure 43. Variations in [τ_{xy}/ $\sigma'_{overburden}$] with elevation and K_v for two soil regions (1 ft = 0.305 m)

the value computed in the Chapter 2 base case following load analysis (B /B = 72.5 percent). Two factors contributing to this difference are the lower value for K_h (along the vertical plane extending through the backfill) resulting from the complete soil-structure interation (SSI) (analysis compared to that specified in the following load analysis (0.37 versus 0.45); and the higher value for K_v resulting from the complete SSI analysis compared to that specified in the following load analysis (0.143 versus 0.09).

Summary

This chapter reviews the simplified procedure for calculating the vertical shear force (or downdrag) F_v, and summarizes the calculation of F_v for Locks 27

Monolith 7E by a complete soil-structure interaction analysis using SOILSTRUCT-ALPHA. The principal results are as follows:

a. A simplified procedure which makes use of design charts for calculating F_v acting along the backs of rock-founded gravity retaining walls is described. The simplified procedure is restricted to "standard" walls (of select geometry) retaining "dry," nonyielding backfills. A standard wall denotes a gravity wall with a constant back slope. The simplified procedure is applicable for walls retaining nonyielding backfills for which the rise in water table is concurrent with the placement of the soil lifts. It also assumes that the water pressures within the backfill are hydrostatic.

b. The complete soil-structure interaction analysis of Locks 27 Monolith 7E resulted in nonlinear normal effective stress distributions.

c. The value of B_e/B computed for Locks 27 Monolith 7E in the complete soil-structure interaction analysis was 10 percent greater than the value computed in the base case following load analysis. The difference is attributed to assumptions made in the following load analysis regarding values for the horizontal earth pressure coefficient K_h and the vertical earth pressure coefficient K_v. Both calculations were made using SOILSTRUCT-ALPHA. Results of the complete soil-structure interaction analysis are judged to be more accurate since the backfill placement procedure considers the complete interaction between the wall and the backfill.

d. Among the results computed in a backfill placement analysis is the distribution of shear stress throughout the backfill. The value assigned to the vertical shear force F_v is computed from the distribution of shear stress τ_{xy} along a vertical plane extending through the backfill from the heel of the wall. The value for F_v should not be computed using average $[\tau_{xy}/\sigma'_{overburden}]$ values.

The two procedures described in this chapter are restricted to walls with engineered backfills that do not creep. Thus, the procedures are applicable to walls backfilled with soils classified according to the ASTM Unified Soil Classification System as SW, SP, GW, GP, and to select SM backfills with nonplastic fines that do not creep.

For walls in which there is a postconstruction rise in the groundwater level in the backfill, a rebound of the soil can occur. This results in a reduction in effective stress and can result in a reduction in the shear force F_v. This occurred at Red River Lock No. 1 (Ebeling et al. 1993 or Ebeling and Mosher 1996). A complete soil-structure interaction analysis modeling the rise in water table and the corresponding "unloading" of the backfill using SOILSTRUCT-ALPHA can be used to compute F_v (Ebeling et al. 1993, Ebeling and Mosher 1996). The complete soil-structure-foundation interaction analysis of the new roller-compacted concrete lock (rock founded) at McAlpine Locks by Ebeling and Wahl (1997) is an example of this type of analysis.

4 Calculation of Uplift Pressures Along Base of Monolith

A key stage in a stability evaluation of lock monoliths is the calculation (or assignment) of uplift pressures along the base of the hydraulic structure and/or along a critical rock joint or joints within the foundation. Using accurate piezometric instrumentation data at a site along with knowledge of the site geology is the preferred method for establishing uplift pressures. However, when instrumentation data are not available or when the reservoir levels to be analyzed exceed those for which the piezometric measurements were made, other procedures must be used to establish the distribution of flow and the corresponding uplift pressures. Four procedures are widely used by engineers to establish the uplift pressures along an imaginary section or sections through the structure-foundation interface and/or along a section or sections within the rock foundation. These four procedures are (a) a prescribed uplift distribution as given, for example, in an engineering manual specific to the particular hydraulic structure; (b) uplift pressures computed from confined, 1-D steady-state flow within a rock joint; (c) uplift pressures resulting from confined, 1-D steady-state flow within a tapered rock joint; or (d) flow-net-computed uplift pressures. Each of these procedures is discussed in the following sections. An alternative procedure for modeling flow (and computing uplift pressures) that uses statistical methods is briefly mentioned, and references are cited.

Assignment of Empirical Uplift Pressure Distributions

An empirical procedure for assigning uplift pressure distributions along the base of gravity monoliths like those at Locks 27 (Figure 1, Chapter 2) uses the relationships given in the EM 1110-2-2200 for Gravity Dam Design (Figures 3-1 through 3-5). The uplift pressure distributions without foundation drainage are shown in Figure 44 for the cases of full contact between the base of the monolith and its rock foundation and with a crack along a portion of this interface. These uplift pressure distributions are consistent with the guidelines provided in EM 1111-2-2200.

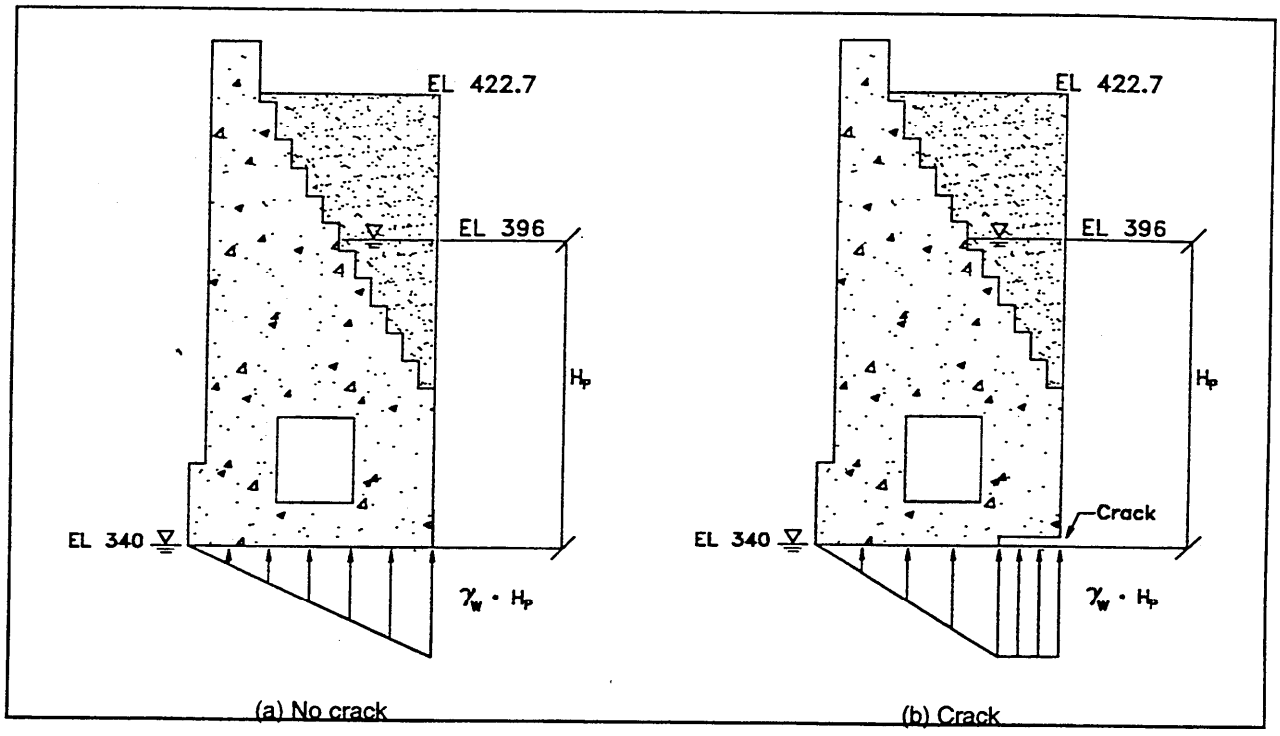

Figure 44. Emperical uplift water pressure distributions (from EM 1110-2-2200)

Figure 44(a) shows a linear uplift pressure distribution extending from below the heel to below the toe of the monolith. Hydrostatic pore pressures within the backfill and within the lock chamber are specified as boundary conditions at each end of the interface. Figure 44(b) shows a bilinear uplift pressure distribution. Hydrostatic pore water pressures are specified within the "cracked" portion of the interface region.

Empirical uplift pressure distributions such as those given in EM 1110-2-2200 and shown in Figure 44 often do not include a description of the flow regime on which empirical uplift pressure distribution(s) are based. An understanding of the type of flow regime(s) which can result in uplift water pressures corresponding to the empirical relationship(s) being used may be important in some situations.

The uplift distribution is linear from the heel to the toe of the monolith in Figure 44(a) and linear from the crack tip to the toe of the monolith in Figure 44(b). A1-D confined steady-state flow along a single rock (or monolith-to-rock interface) joint of constant aperture results in a linear uplift pressure distribution, as shown in these figures. This is a special case of confined 1-D flow within a tapered joint, to be shown using the relationships given in the following section. The assignment of full (hydrostatic) uplift pressures within the "cracked" base is based on Corps design guidance (EM 1110-2-2200) and not the result of hydraulic modeling.

Confined 1-D Flow Within a Tapered Joint

In 1992, investigators at the engineering consulting firm of Stone & Webster completed a study of 17 existing concrete gravity dams for the Electric Power Research Institute (EPRI). The objective of this study was to identify key factors influencing uplift pressures. All dams were on instrumented rock foundations, and all had different foundation geology. An analysis of the uplift pressure measurements from each of these dams showed that foundation geology strongly influences the uplift pressure distribution and that the geology controls the response of uplift pressure to changes in dam loading. The investigators discovered that an understanding of the flow within rock joints and the factors which affect the flow lead to a better understanding of the uplift measurements at the damsites, especially those rock formations possessing "tight" rock joints. Lee and Farmer (1993), using data from Barton (1973), classified a tight rock joint as a joint with a *mechanical* aperture less than 8.2×10^{-4} ft (250 μm or 0.25 mm).

This section presents the results of a study involving 1-D steady-state laminar flow through a single permeable joint within a rock foundation. Its purpose is twofold: to introduce the fundamentals of flow within rock joints and to show how the dimensions of the joint (referred to as joint aperture) influence the computed uplift pressures. Specifically, the results show the impact of *a tapered aperture (i.e., constant change in taper with distance along a single rock joint)* on the distributions of permeability and computed uplift pressures. The example considered is that of a *horizontal rock joint* located below the base of a concrete dam monolith for the cases of low, medium, and high reservoir elevations.

Modeling joint flow: the cubic law

Laminar flow within a rock joint can be characterized in a simplistic form as flow between a pair of smooth parallel plates separated by a constant distance. This distance is the joint opening or aperture, e (units of length). The flow rate per unit width is given by

$$Q = \frac{\gamma\, e^2}{12\,\mu} \cdot \left[- \frac{\partial h}{\partial l} \right] \cdot e \qquad (18)$$

where γ is the unit weight of water (units of force per length cubed), e is the *conducting aperture*, and μ is the dynamic viscosity in lb-sec/ft^2 or slug/ft-sec in English units. The quantity of flow varies with the cube of the aperture e; hence, the name "the cubic law." By analogy with Darcy's law, the equation for a single joint may be rewritten as

$$Q = K_{joint} \cdot [\, i \,] \cdot AREA_{flow} \qquad (19)$$

where K_{joint} is the permeability, i is the hydraulic gradient, and $AREA_{flow}$ is the area of flow at any point along the single joint. The above equation can be used to compute the steady-state quantity of flow and distribution of uplift pressures given known values for γ and μ, the heads at each end of the joint, and the variation in aperture e with distance along the joint. Conventional 1-D steady-state seepage computer program packages that are commercially available can be used to perform the seepage analysis for any distribution of e.

The conducting aperture of a rock joint is distinguished from its mechanical aperture. The differences in their magnitudes are shown using the example problems in Chapter 5.

In the special case of a tapered joint, it is possible to develop closed-form solutions for the quantity of flow within the joint and the distribution of uplift pressures along the length of the joint. These solutions are described in the following section.

Tapered joint

A tapered joint such as that shown in Figure 45 is one that has linear variation in aperture with distance x along the joint (where x ranges in value from 0 to L). The equation for conducting aperture e is given as

$$e(x) = \left[\frac{e_{out} - e_{in}}{L} \right] * x + e_{in} \tag{20}$$

By Equation 18, the permeability at any point x varies in proportion to the square of the value of e

$$K_{joint}(x) = \frac{\gamma}{12\ \mu} [\ e(x)\ ]^2 \tag{21}$$

The area of flow (per unit width) at any point along the joint is given as

$$Area_{flow} = e(x) \tag{22}$$

By introducing Equations 20, 21, and 22 into Equation 18 with $Q_{in} = Q(x) = Q_{out}$ and for the known head boundary conditions on either side of the joint as shown in Figure 45, the following relationships are obtained after some mathematical manipulations are performed:

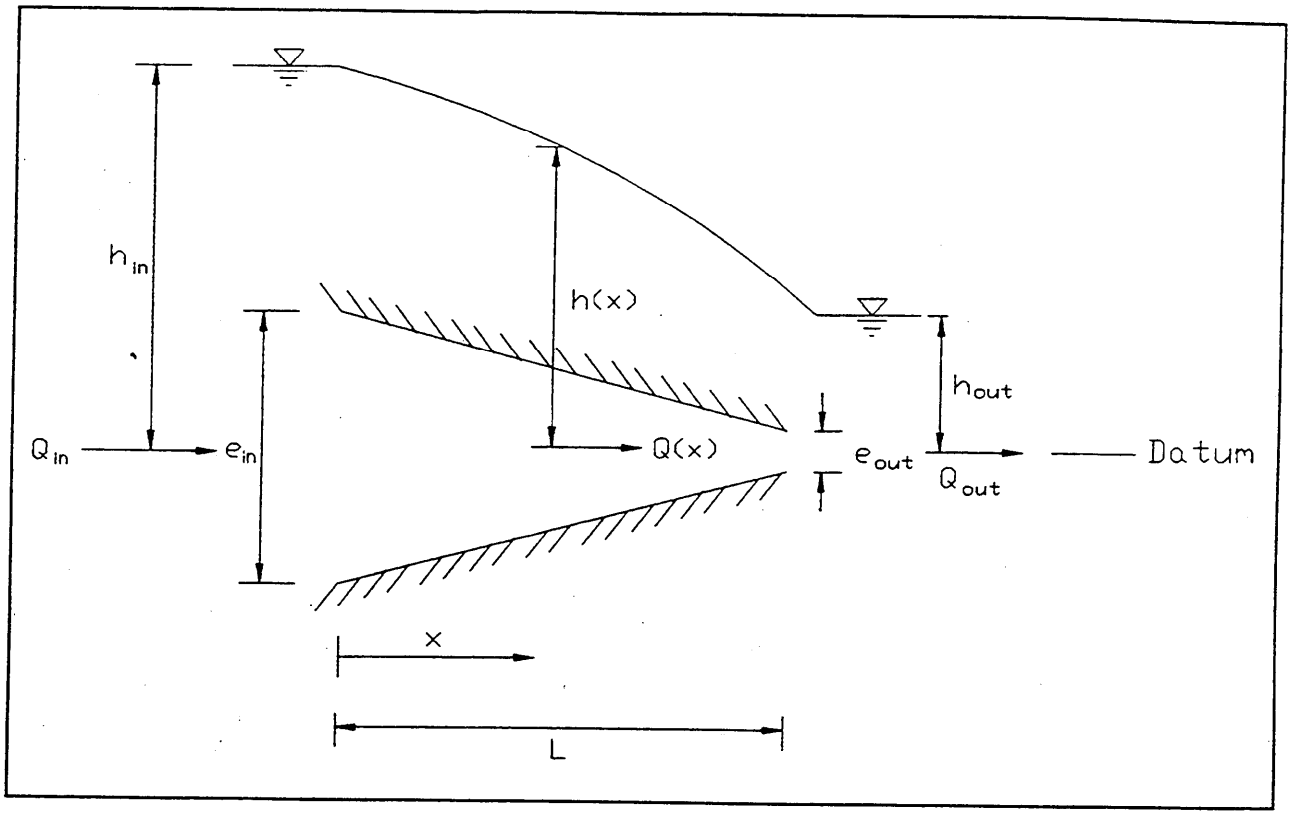

Figure 45. Variation of head along tapered joint as a function of position

$$Q = 2\left[\frac{\gamma}{12\,\mu}\right] e_{in}^{2}\,(h_{in} - h_{out})\,\frac{1}{L}\left[\frac{e_{out}^{2}}{e_{out} + e_{in}}\right] \tag{23}$$

and

$$h(x) = h_{in} - \left[\left[(h_{in} - h_{out})\,\frac{1}{L}\left[\frac{e_{out}^{2}}{e_{out} + e_{in}}\right]\right]\left[\frac{mx^{2} + 2xe_{in}}{(mx + e_{in})^{2}}\right]\right] \tag{24}$$

where

$$m = \frac{e_{out} - e_{in}}{L} \tag{25}$$

Equation 24 shows that the variation in head within a *tapered joint* is defined by five variables: the length of joint, the conducting apertures at the two ends of the joint, the reservoir head, and the tailwater head. Note that Equation 24 does not explicitly include the term K_{joint}

Example problem: raising pool behind gravity dam founded on single rock joint

The case of a single horizontal rock joint located below the base of a concrete monolith for the cases of low, medium, and high reservoir elevations is used to show the impact of joint aperture on uplift pressures. Figure 46 shows the hypothetical dam to be 300 ft (91.46 m) high and 235 ft (71.6 m) wide. It was assumed that jointing within the rock foundation was simplistic, i.e., a single rock joint parallel to and immediately below the dam-to-foundation interface. Changes in joint aperture during loading and/or unloading of the joint as a result of the construction of the dam and subsequent filling of the reservoir are not included in these calculations.

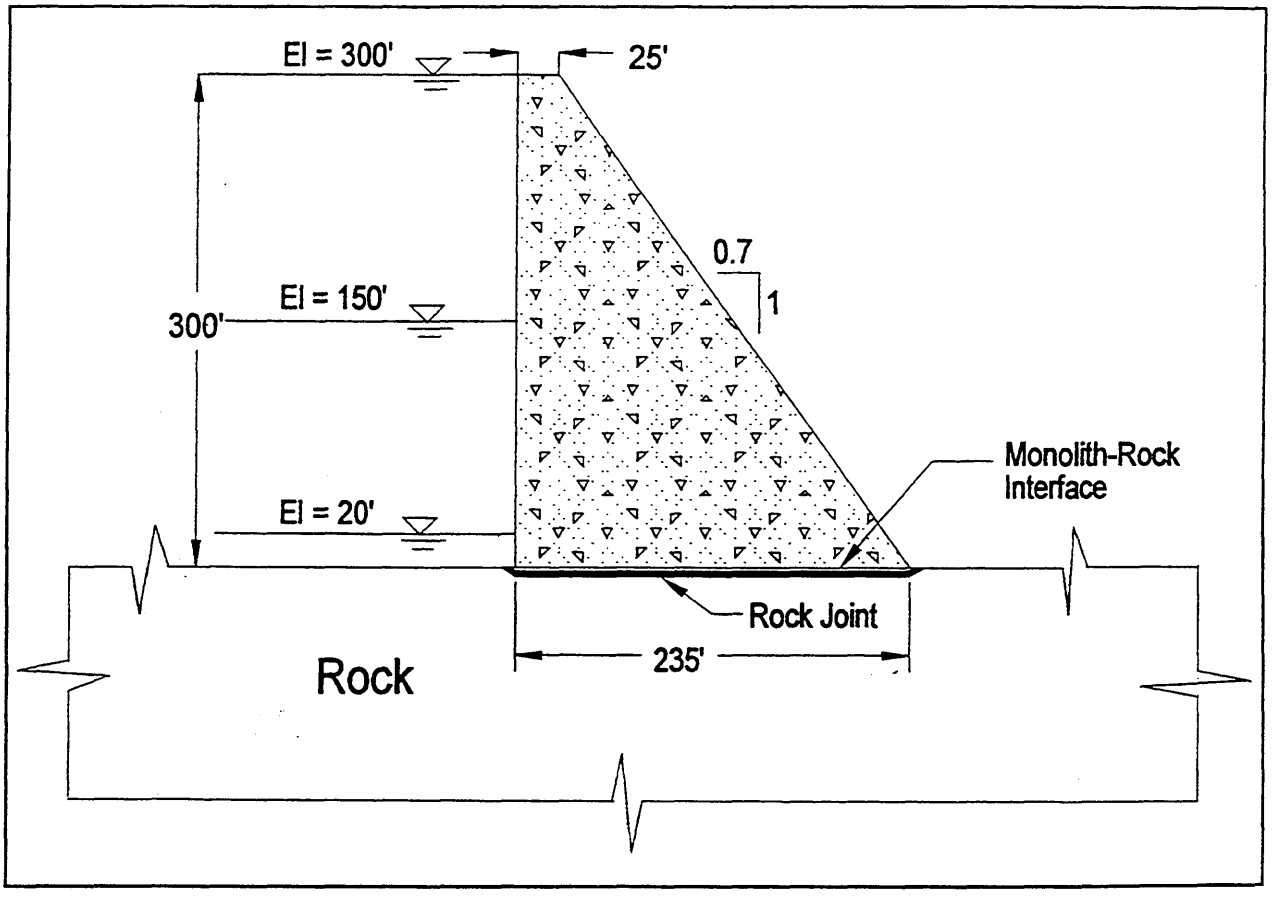

Figure 46. Geometry of dam used in study (1 ft = 0.305 m)

Three different tapers for the rock joint in Figure 46 were investigated using Equation 24: no taper, uniform aperture ($e_{in} = e_{out}$); taper downstream ($e_{in} > e_{out}$); and taper upstream ($e_{in} < e_{out}$). By assigning the datum to be the center line of the horizontal rock joint (Figure 46), the uplift pressure at any point is equal to the head at the point times the unit weight of water (with elevation head equal to zero and the velocity head being negligible).

The variation in head (and thus, uplift pressure) along the 235-ft- (71.6-m-) long rock joint is shown in Figure 47 for the pool elevations equal to 20, 150, and 300 ft (6.1, 45.7, and 91.46 m) for $e_{in} = e_{out} = 4.92 \times 10^{-4}$ ft (= 150 μm or 0.15 mm). This figure shows that the uplift pressures vary linearly along the joint for constant aperture.

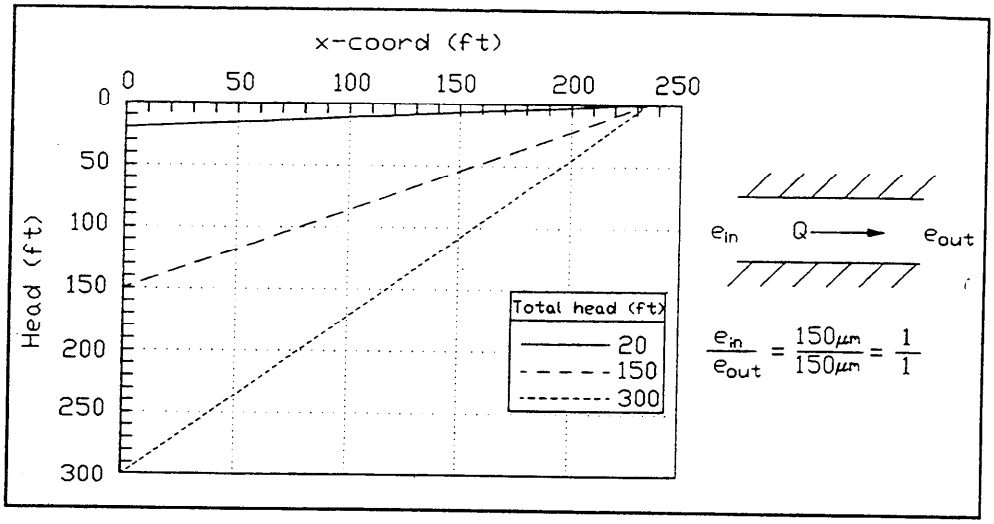

Figure 47. Variation in head along rock joint, $e_{in}/e_{out} = 1$ (1 ft = 0.305 m)

Figure 48 shows the resulting variation in head with the joint tapered in the direction of flow (downstream) for the three pool elevations. In this example, e_{in} is set equal to $2e_{out}$, which results in the value of permeability at the toe (out) being one-fourth the magnitude of permeability at the heel (in). Comparison of the distribution of head or, equivalently, uplift pressure in Figure 48 with that shown in Figure 47 indicates that for a given pool elevation, a taper downstream results in larger uplift pressures compared to the case of uniform aperture.

Figure 49 shows the resulting variation in head with the joint tapered in the direction opposite to flow (upstream) for the three pool elevations. In this example, e_{in} is set equal to $e_{out}/2$, which results in the value of permeability at the toe being four times the magnitude of permeability at the heel. Comparison of the distribution of head or, equivalently, uplift pressure in Figure 49 with those shown in Figure 47 indicates that for a given pool elevation, a taper upstream results in smaller uplift pressures compared to the case of uniform aperture.

When the taper of the joint downstream is increased from a factor of 2 (Figure 48) to a factor of 10 (Figure 50), larger uplift pressures result. Conversely, when the taper of the joint upstream is decreased from a factor of 1/2 (Figure 49) to a factor of 1/10 (Figure 51), smaller uplift pressures result. Lastly, the results in Figure 52 show that in the case of a tapered joint, the *ratio* of e_{in} to e_{out} dictates the distribution of uplift pressures. The *magnitudes* of e_{in} and e_{out} impact the quantity of flow (see Equation 23).

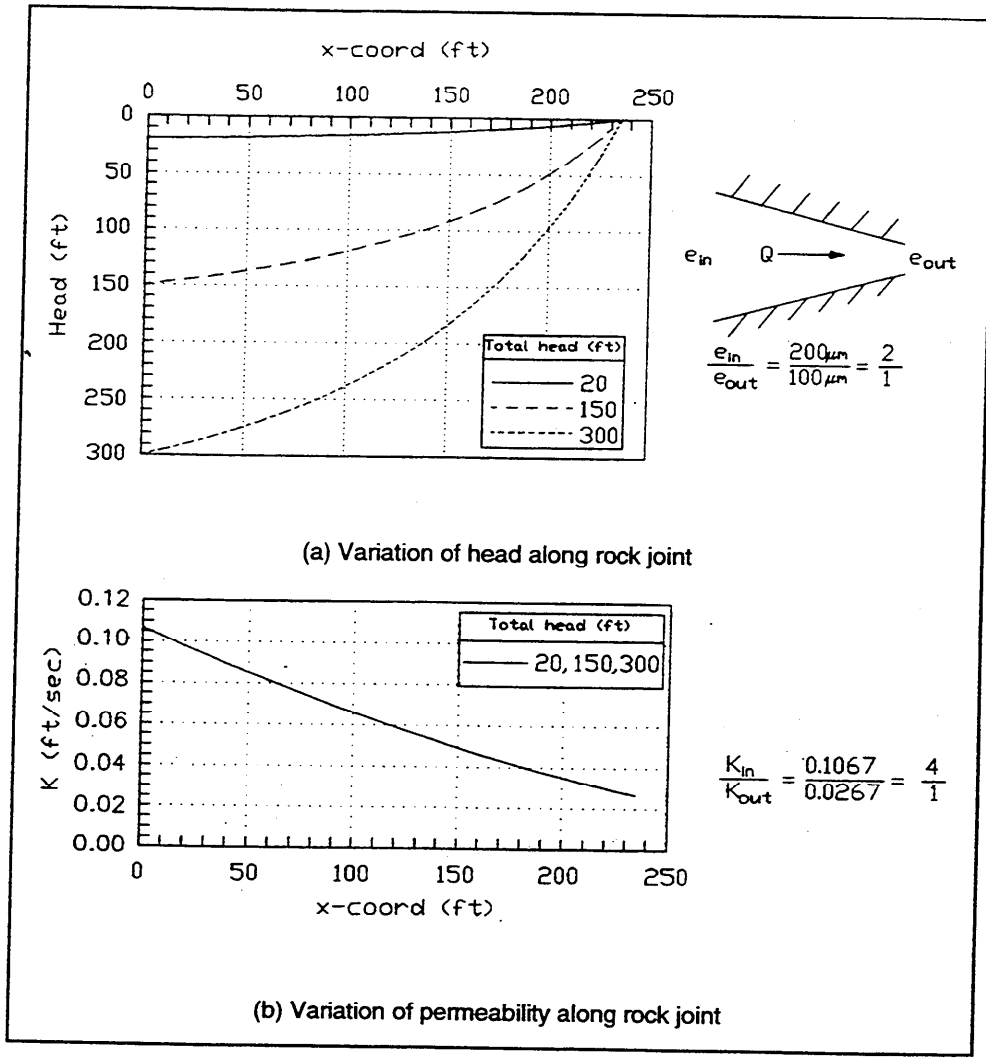

Figure 48. Head and permeability variation along rock joint, e_{in}/e_{out}= 2/1 (1 ft = 0.305 m, 1 ft/s = 0.305 m/s)

Chapter 5 expands upon this problem to include the effects of changes in stress on the mechanical aperture of joints for the problem of steady-state flow along a single rock joint below a dam. Included in this chapter are two examples of a complete hydraulic structure-rock foundation-rock joint interaction. The construction of two dams, followed by the raising and lowering of their reservoirs was modeled in the analyses. A single rock joint immediately below and parallel to the dam-to-rock foundation interface was included. Uplift pressures resulting from changes in rock joint aperture with the loading and unloading of the joint due to changes in reservoir elevation were tracked throughout the analyses.

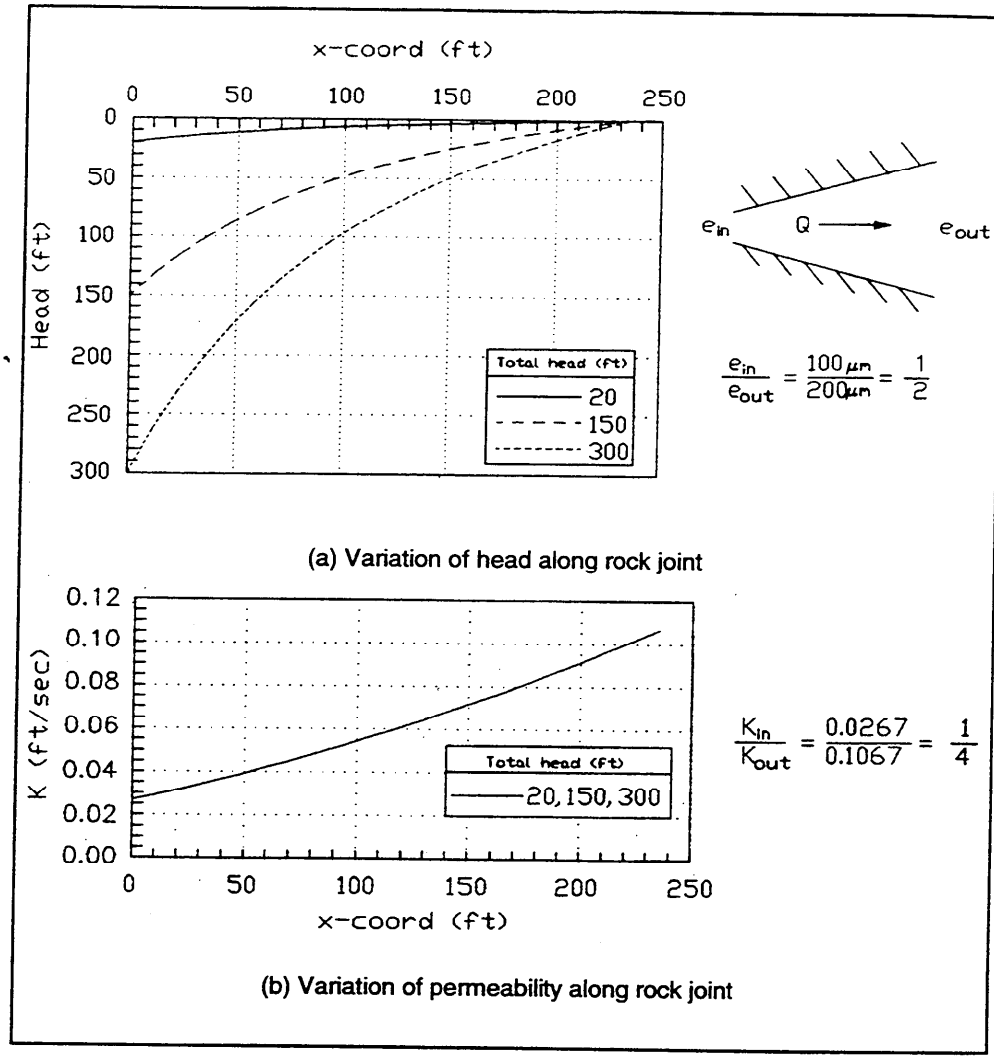

Figure 49. Head and permeability variation along rock joint, e_{in}/e_{out}= 1/2 (1 ft = 0.305 m, 1 ft/s = 0.305 m/s)

Two-Dimensional Flow Net Analysis of Steady-State Seepage

This section presents the results of a study involving 2-D steady-state flow through a "permeable" rock foundation. A permeable rock foundation connotes a highly fractured rock foundation in which the steady-state flow model, with regional assignments of permeabilities (isotropic or anisotropic), provides a reasonably accurate numerical model of the actual fluid flow within the numerous fractures and joints in the rock foundation. The results show the impact of homogeneous, anisotropic permeabilities (i.e., $K_x \neq K_y$) and the impact of base separation on the uplift pressures along the base of a rock-founded retaining monolith.

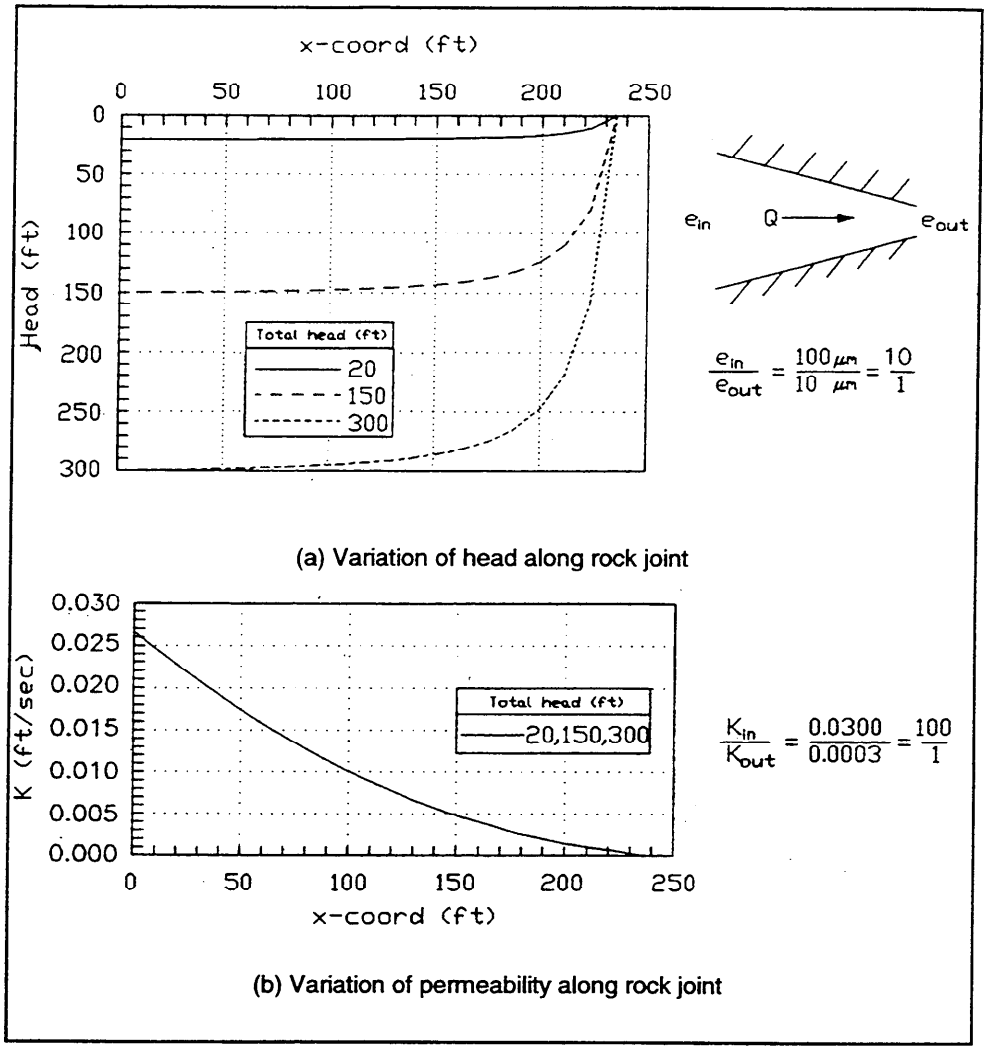

Figure 50. Head and permeability variation along rock joint, e_{in}/e_{out}= 10/1 (1 ft = 0.305 m, 1 ft/s = 0.305 m/s)

Steady-state seepage analysis

Today, analytical tools such as the FEM are available to compute the distribution of heads and flow within permeable foundations. Most problems involve the analysis of steady-state seepage given problem-specific geometry and boundary conditions. An FEM model of two- (2-D) or three-dimensional (3-D) steady-state seepage can consider homogeneous or heterogeneous regions comprising the flow regime as well as isotropic or anisotropic permeability within each of these regions. The Windows version of the Corps FE seepage program (X8202 in the CORPS Library) (Tracy 1983) called FASTSEEP (Engineering Computer Graphics Laboratory 1993) was used in this analytical study of 2-D steady-state seepage.

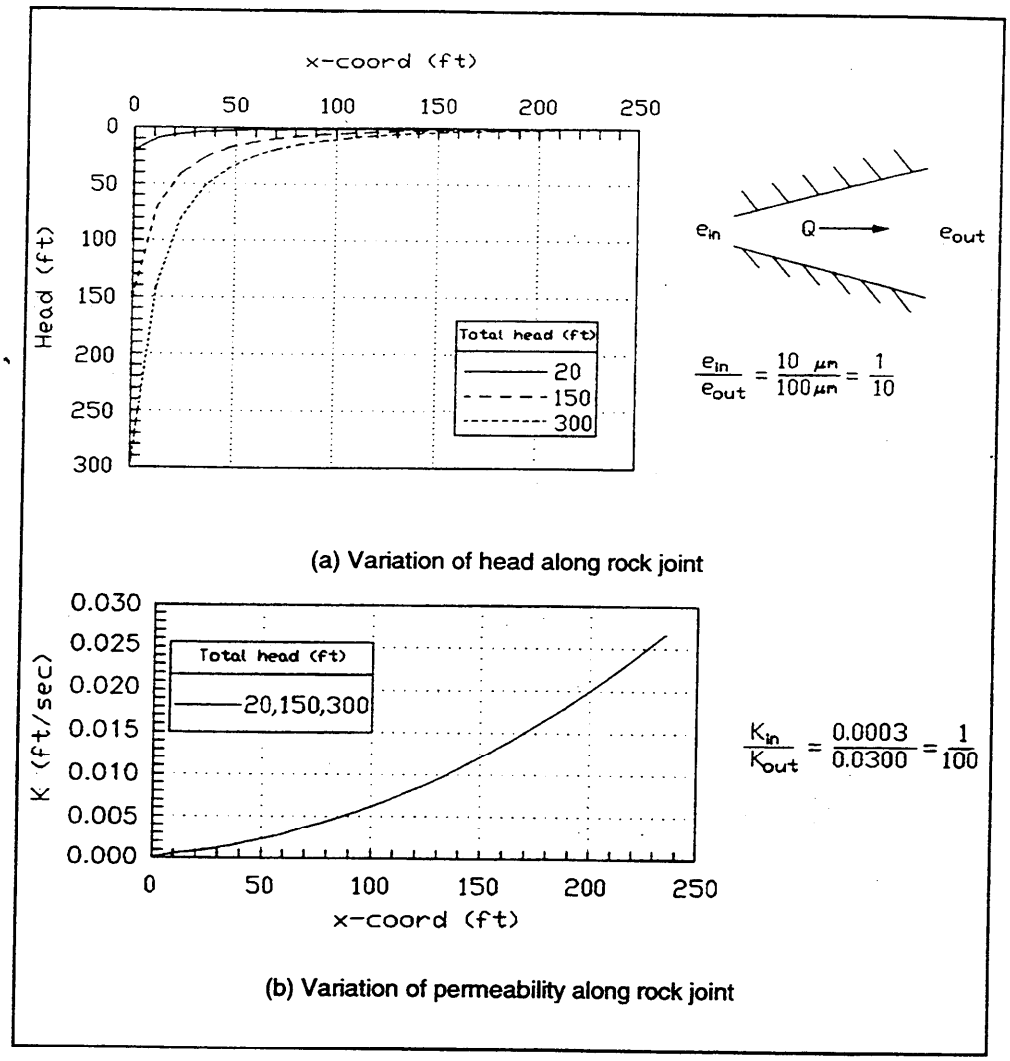

Figure 51. Head and permeability variation along rock joint, e_{in}/e_{out}= 1/10 (1 ft = 0.305 m, 1 ft/s = 0.305 m/s)

Seepage problem analyzed

The case of a concrete gravity lock retaining wall founded on permeable rock was used in this study. The wall geometry was modeled after Locks 27 Monolith 7E (Figure 1, Chapter 2). Figure 53 shows the concrete monolith to be 82.7 ft (25.2 m) high and 45 ft (13.71 m) wide. This monolith has a base-to-height ratio of 0.54, which is within the range (0.33 to 0.7) that is typical for gravity earth retaining monoliths (Ebeling et al. 1992). This particular monolith was chosen for further study because its geometry (e.g., base-to-height ratio) is typical of gravity retaining monoliths and because this monolith has been extensively analyzed in this REMR Research Program for separation along the base of the monolith under extreme loading. The monolith was analyzed by use of the conventional equilibrium method of analysis as well as the FEM using three different crack/crack propagation models; by use of a base separation analysis using

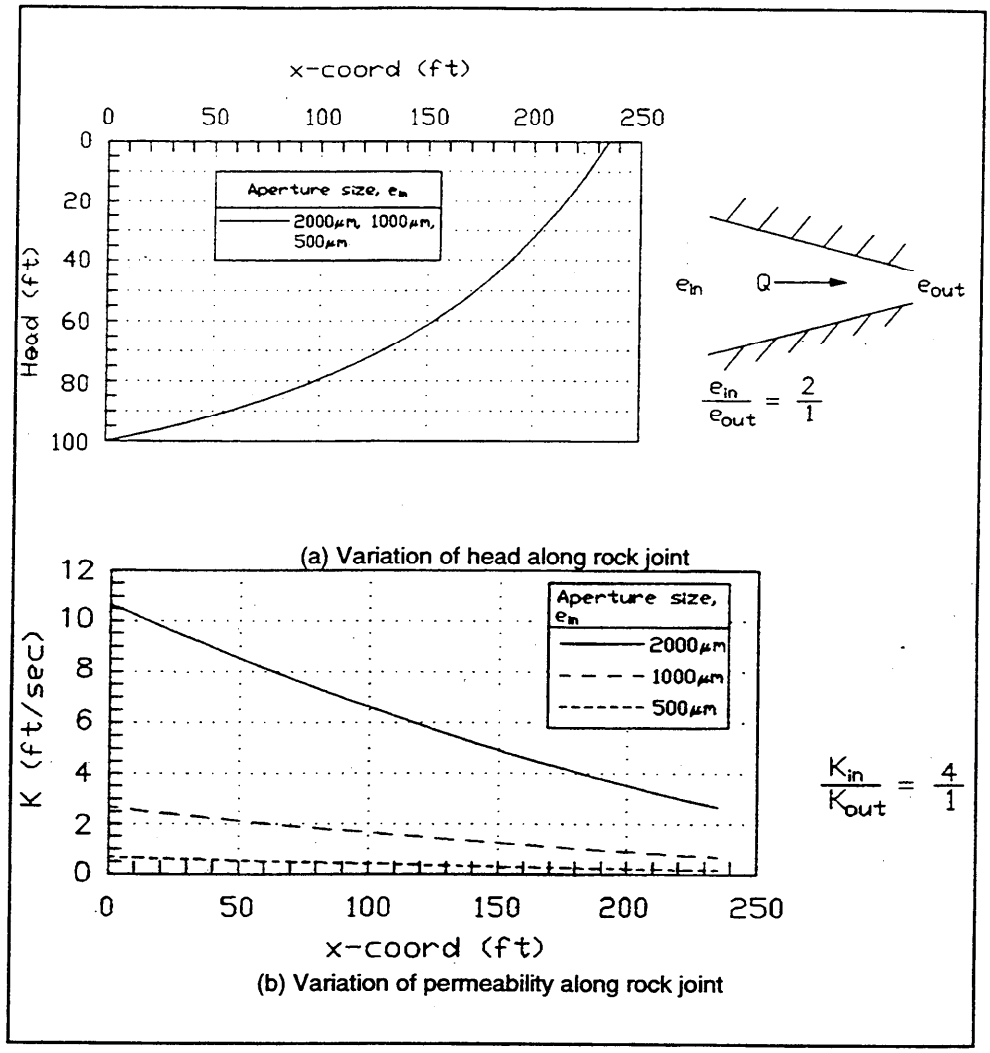

Figure 52. Head and permeability variation along rock joint, e_{in}/e_{out}= 2/1, with varying e_{in} (1 ft = 0.305 m, 1 ft/s = 0.305 m/s)

interface elements; by use of a base separation analysis using the smeared crack approach; and by use of a linear elastic fracture mechanics discrete crack analysis. In the case of the extreme loading (e.g., no lock pool) and a conservative assignment of material properties, all four analytical procedures showed that as much as 50 percent of the base of the monolith may separate from its rock foundation along the interface.

All nine seepage analyses assumed that the monolith was impermeable and that the permeable foundation was homogeneous. No drainage was included within the foundation in these problems. A typical set of dimensions is shown in Figure 53, along with a summary of the parameters that were varied in the nine seepage analyses. Three cases of monolith-to-foundation contacts were considered: (a) full contact along the interface (B_c/B = 100 percent), (b) an intermediate case of three-quarters contact along the interface (B_c/B = 75 percent), and (c) the extreme case of only half of the monolith in contact with the foundation

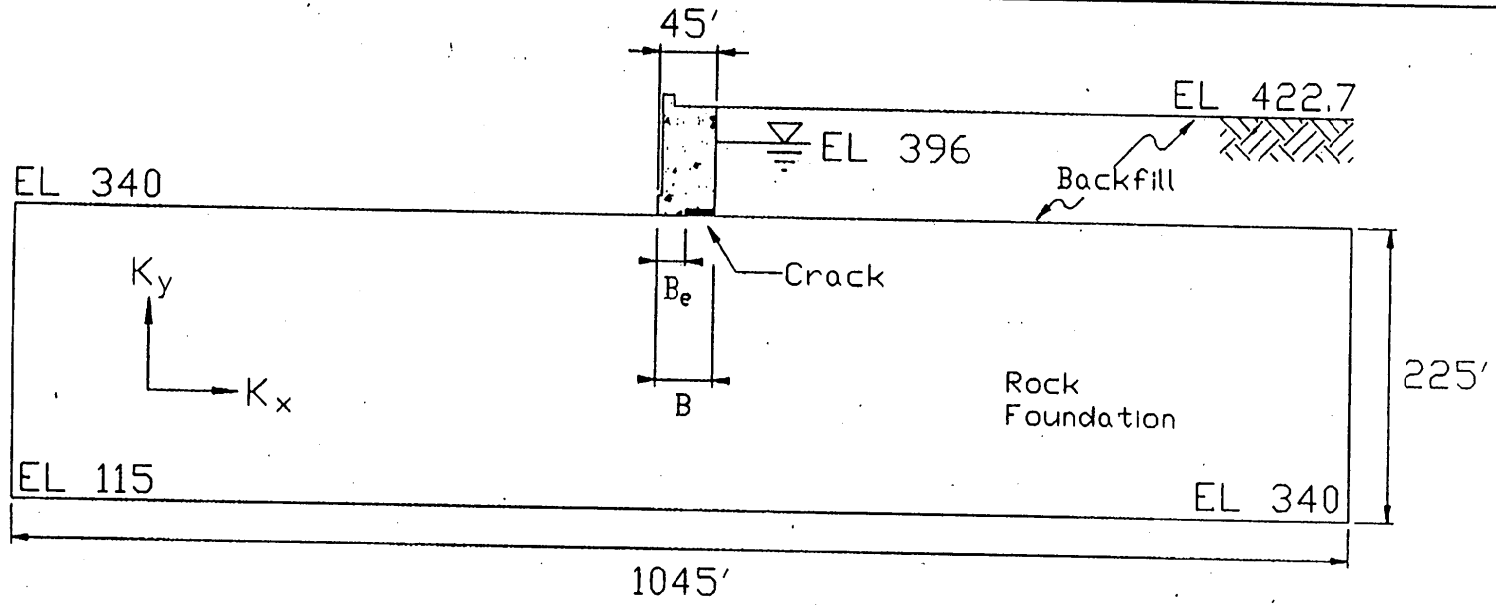

$\frac{B_e}{B}$ = 100%	$\frac{B_e}{B}$ = 75%	$\frac{B_e}{B}$ = 50%
$K_x = K_y$	$K_x = K_y$	$K_x = K_y$
$= 10K_y$	$= 10K_y$	$= 10K_y$
$= \frac{1}{10} K_y$	$= \frac{1}{10} K_y$	$= \frac{1}{10} K_y$

Figure 53. Problem geometry and cases considered (1 ft = 0.305 m)

(B_c/B = 50 percent). For each case, three sets of foundation permeabilities, $K_x = K_y$, $K_x = 10K_y$, and $K_x = K_y/10$, were considered.

Flow nets for anisotropic permeabilities with full contact along interface

Figures 54 through 56 show the steady-state flow nets for the permeable foundation with $K_x = K_y$, $K_x = 10K_y$, and $K_x = K_y/10$, respectively, for a monolith in full contact with the rock foundation (B_c/B = 100 percent). The water table in the backfill is assumed to be at el 396 ft (120.7 m), and the head in front of the monolith is assumed to be at el 340 ft (103.6 m).

A comparison of the flow net in Figure 55 for $K_x = 10K_y$ with that shown in Figure 54 for $K_x = K_y$ shows that along any given flow line below the monolith, there is less of a change in elevation between flow channels than that for the isotropic case (Figure 54). That is to say, the more permeable horizontal direction orients the flow channels in a more horizontal direction. The converse is true when the flow net in Figure 56 for $K_x = K_y/10$ is compared with that shown in Figure 54. In this case, the more permeable vertical direction orients the flow channels in a more vertical direction.

Flow nets for isotropic permeabilities with partial contact along interface

Figures 54, 57, and 58 show the steady-state flow nets for the case of isotropic permeability ($K_x = K_y$) and 100, 75, and 50 percent, respectively, of monolith-to-rock base contact. In all analyses of monoliths with partial contact (i.e., a crack extending from the heel), full hydrostatic water pressures within the backfill (corresponding to a water table at el 396 ft (120.7 m)) were assigned along the cracked portion of the interface. Comparison of the three figures shows that the symmetry of the flow channels is preserved about a vertical line located midway between the toe and the crack tip (which is the heel in Figure 54).

Uplift pressures along interface

The distributions of uplift pressures along the monolith-to-rock interface are shown in Figures 59, 60, and 61 for B_c/B = 100 percent (i.e., full contact), 75 percent, and 50 percent, respectively. Each figure shows the resulting uplift distribution for the cases of $K_x = K_y$, $K_x = 10K_y$, and $K_x = K_y/10$. The linear uplift distributions corresponding to flow confined along the interface (i.e., 1-D flow) are also included in these figures. The three figures show four important results. First, 2-D seepage within the isotropic foundation alters the resulting distribution of uplift pressures when compared to uplift pressures resulting from 1-D flow. Second, the distributions of uplift pressures for the three ratios of permeabilities

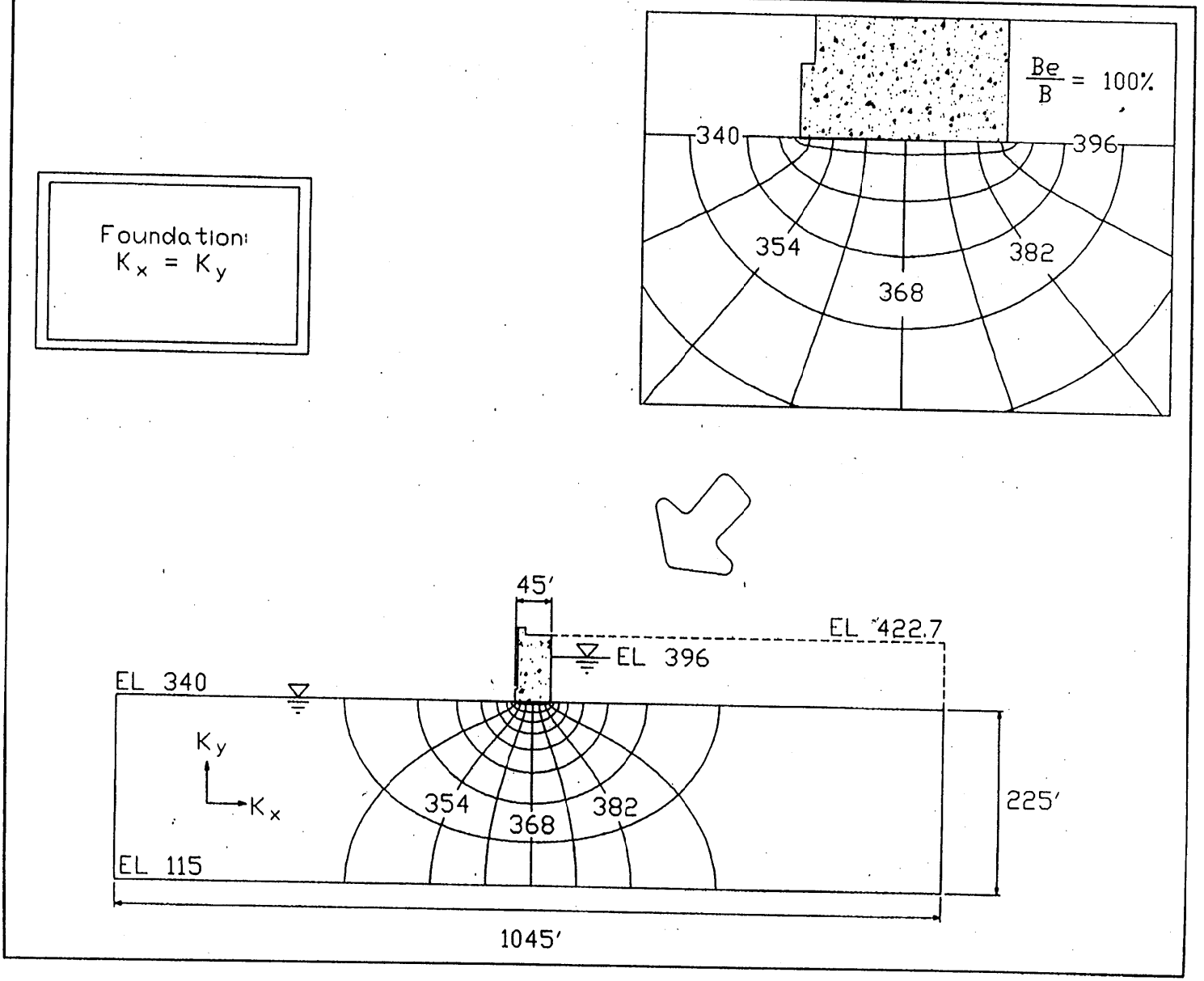

Figure 54. Results for B_e/B = 100 percent, $K_x = K_y$ (1 ft = 0.305 m)

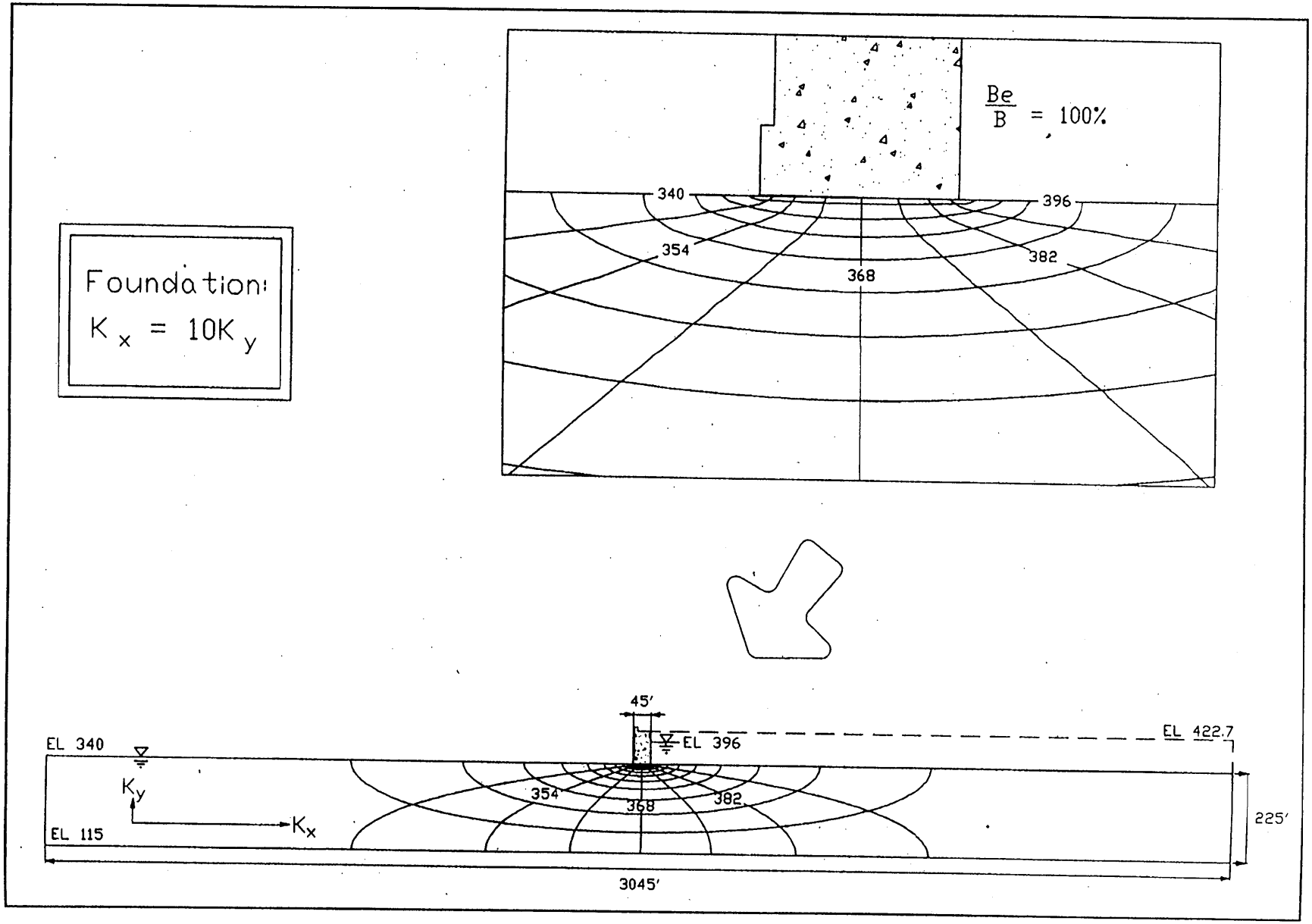

Figure 55. Results for B_e/B = 100 percent, $K_x = 10K_y$ (1 ft = 0.305 m)

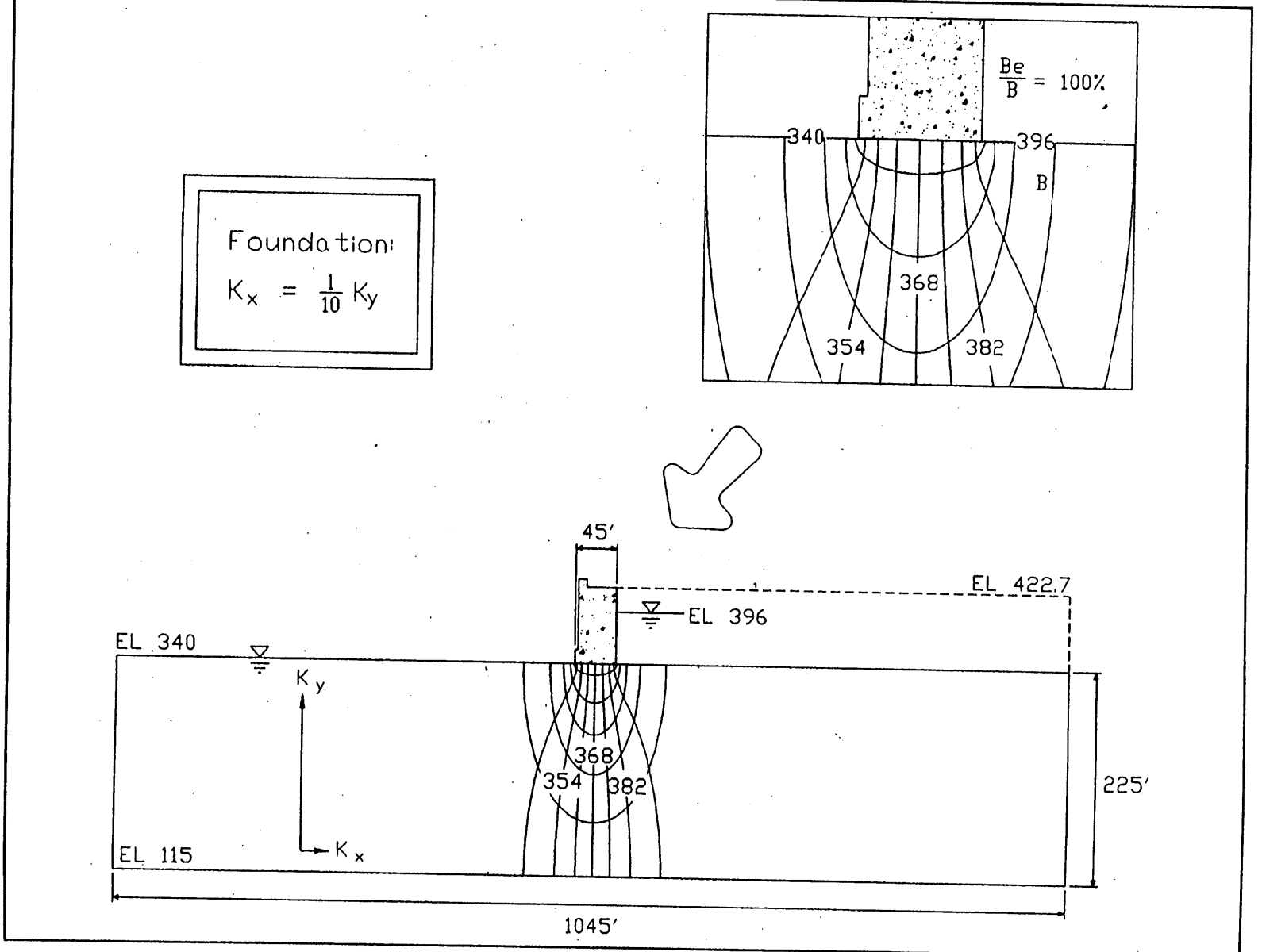

Figure 56. Results for B_e/B = 100 percent, K_x= 1/10 K_y (1 ft = 0.305 m)

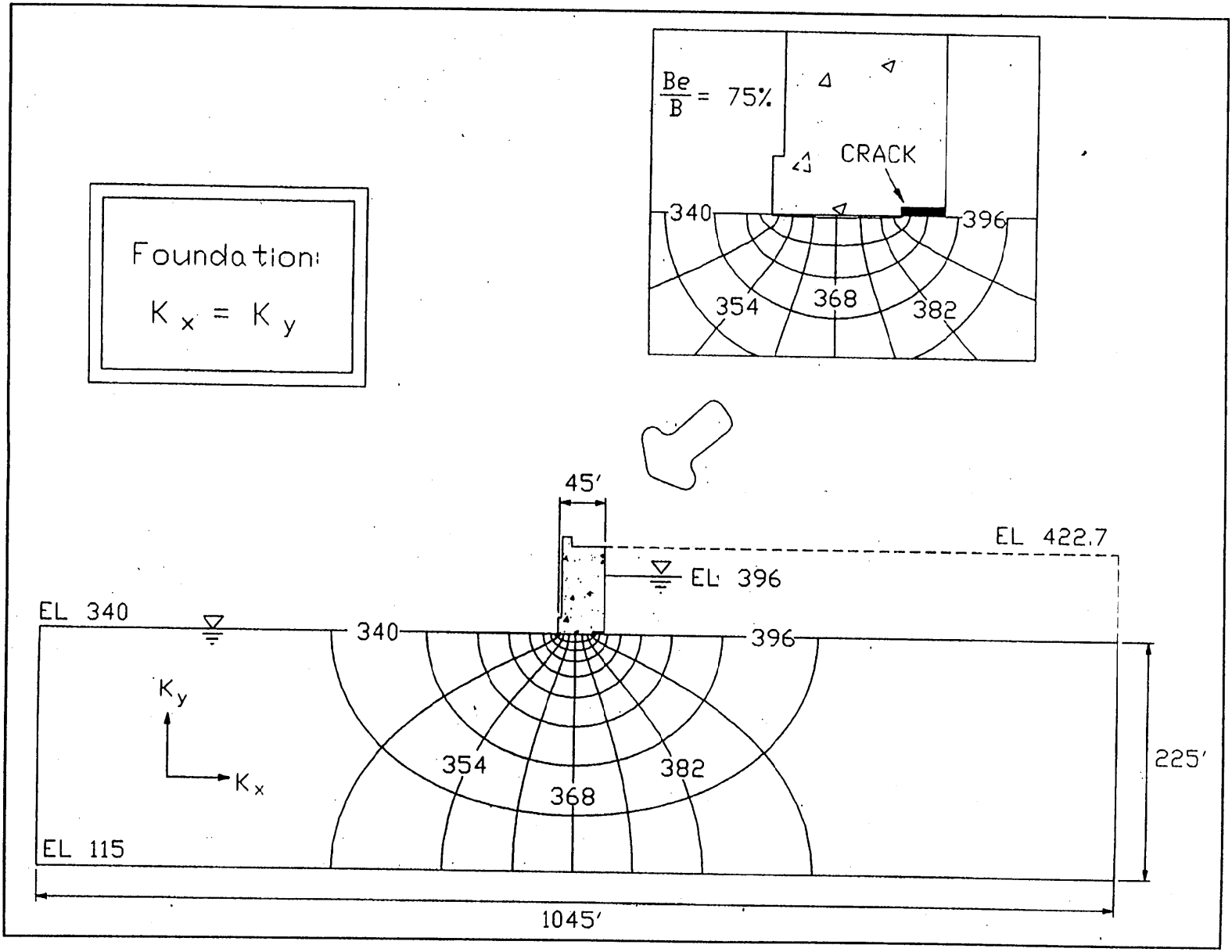

Figure 57. Results for B_e/B = 75 percent, $K_x = K_y$ (1 ft = 0.305 m)

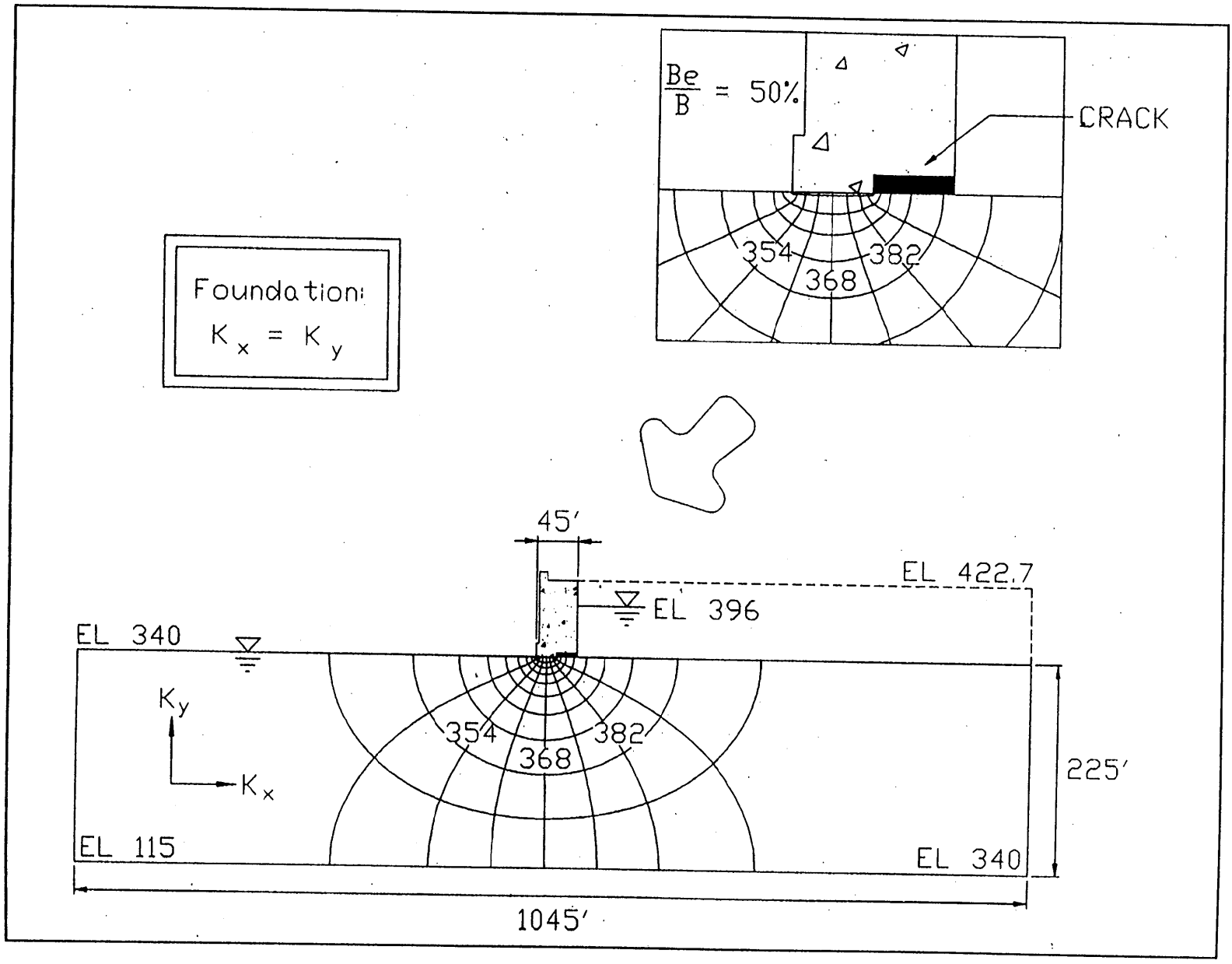

Figure 58. Results for B_e/B = 50 percent, $K_x = K_y$ (1 ft = 0.305 m)

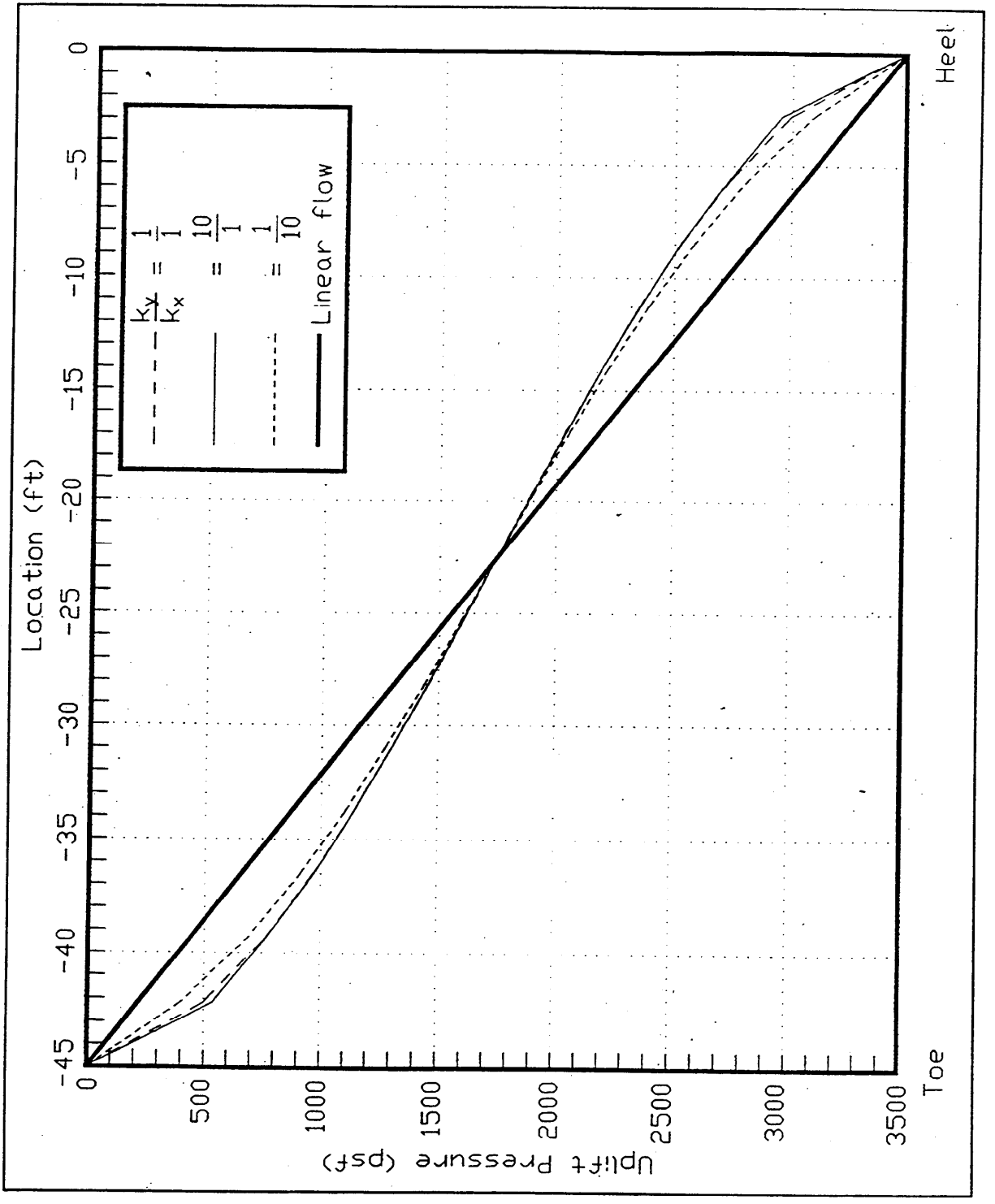

Figure 59. Uplift values for B_e/B = 100 percent (1 ft = 0.305 m, 1 MPa = 20,885.5 psf)

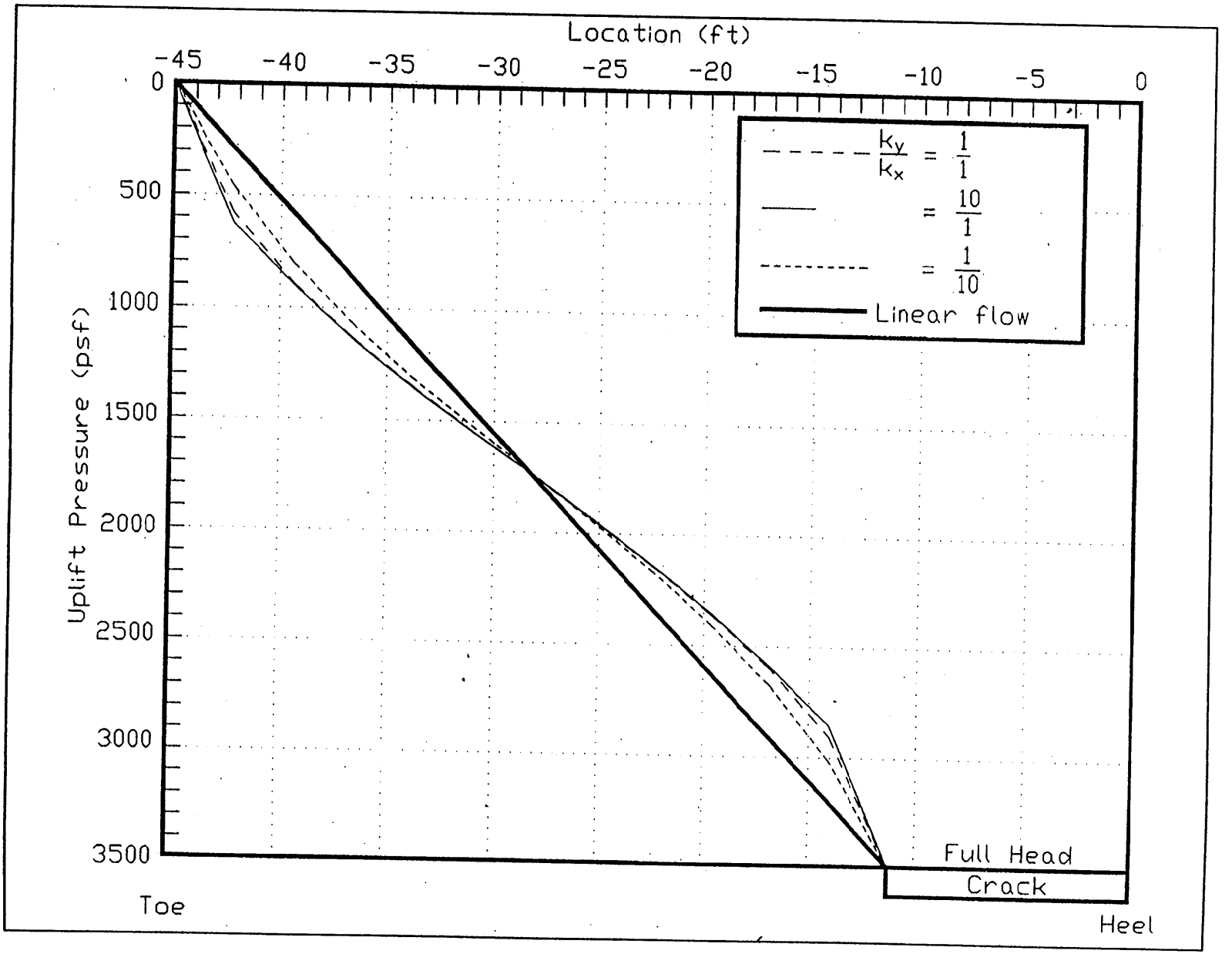

Figure 60. Uplift values for B_e/B = 75 percent (1 ft = 0.305 m, 1 MPa = 20,885.5 psf)

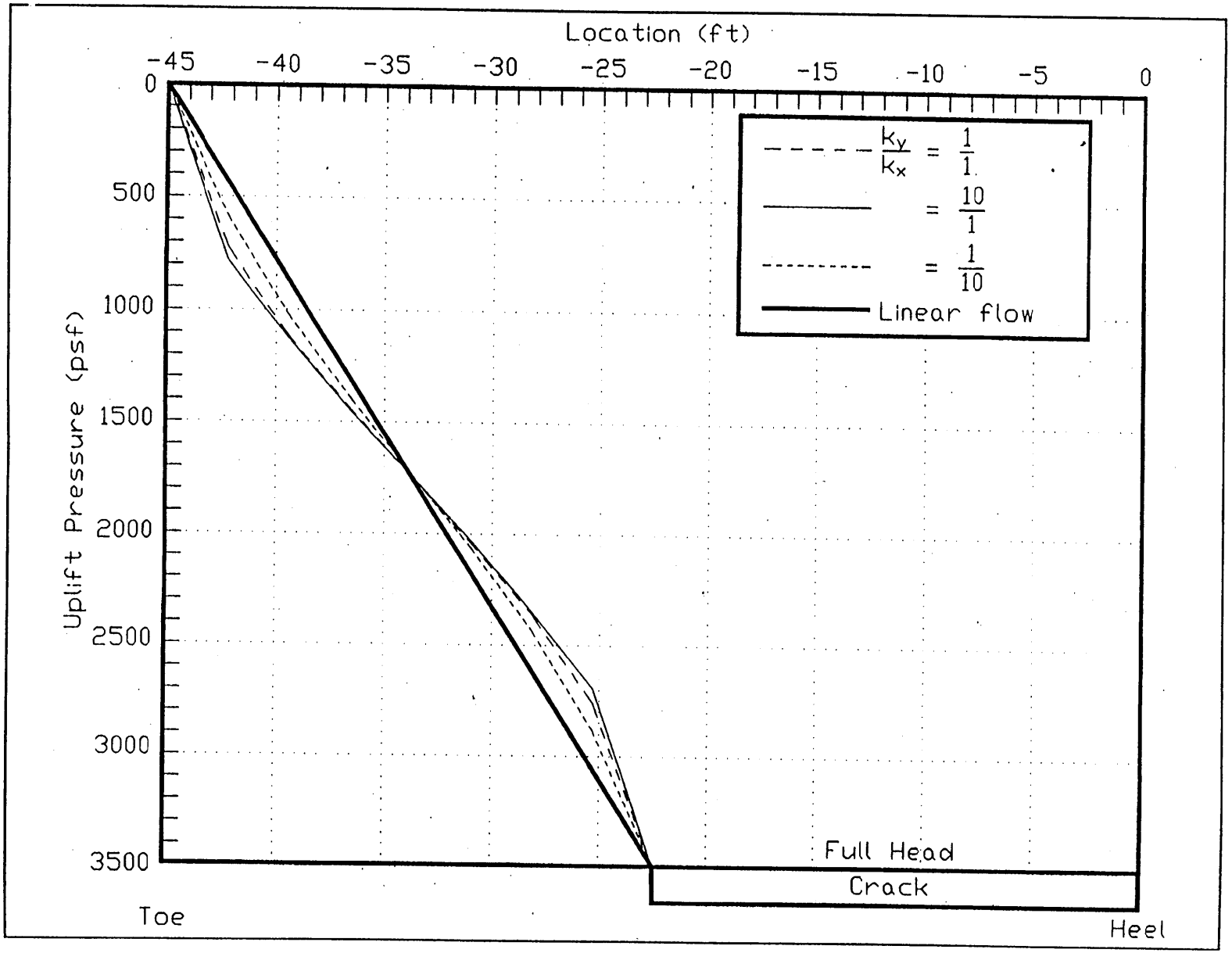

Figure 61. Uplift values for B_e/B = 50 percent (1 ft = 0.305 m, 1 MPa = 20,885.5 psf)

are nearly the same. Third, the distributions of uplift pressures from the 2-D analyses are anti-symmetric to the distribution of uplift pressures for 1-D flow about a point midway between the tip of the crack and the toe of the wall. Finally, the point of antisymmetry is maintained midway between the crack tip and the toe for all crack lengths.

The resultant uplift force, equal to the area under each of the uplift pressure distributions, is the same value for each of the four analyses shown in Figure 59. This is also the case for the results shown in Figures 60 and 61.

The resulting force for the linear uplift pressure distribution in Figure 59 (1-D flow) acts at a point along the interface that is two-thirds the distance from the toe to the heel, acting at a point 30 ft (9.14 m) from the toe ($B_e = B = 45$ ft (13.7 m)). Table 9 presents values of the point of action of the resultant uplift force computed using the results from all nine steady-state seepage analyses. The resultant uplift forces computed from the results of the other three 2-D analyses shown in Figure 59 ($B_e/B = 100$ percent) act at points that are between four and five percent closer to the toe of the wall than the points for the linear uplift distribution. This difference is even less for the results shown in Figures 60 and 61 (where B_e/B equals 75 percent and 50 percent, respectively).

Table 9
Comparison of 1-D Versus 2-D flow

		Uplift on Base, kips/ft (kN/m)		x_n (from Toe), ft (m)		
B_e/B	K_x/K_y	1-D Flow	2-D Flow	1-D Flow	2-D Flow	% Difference
100 %	1	78.62 (7.95)	78.63 (7.95)	30.00 (9.14)	28.48 (8.68)	5.06
	10	78.62 (7.95)	78.64 (7.95)	30.00 (9.14)	28.42 (8.66)	5.26
	1/10	78.62 (7.95)	78.63 (7.95)	30.00 (9.14)	28.83 (8.79)	3.90
75 %	1	98.28 (9.94)	98.20 (9.93)	29.25 (8.92)	28.62 (8.72)	2.16
	10	98.28 (9.94)	98.17 (9.92)	29.25 (8.92)	28.57 (8.71)	2.31
	1/10	98.28 (9.94)	97.99 (9.91)	29.25 (8.92)	28.83 (8.79)	1.45
50 %	1	117.94 (11.93)	117.87 (11.92)	27.50 (8.38)	27.30 (8.32)	0.71
	10	117.94 (11.93)	117.81 (11.91)	27.50 (8.38)	27.28 (8.31)	0.78
	1/10	117.94 (11.93)	117.68 (11.90)	27.50 (8.38)	27.41 (8.36)	0.33

Alternative Procedure

An alternative procedure for development of uplift pressure distributions is based on the development of random discrete fracture network (flow) models. Random discrete fracture network models assume that the exact location of each fracture is unknown. The geometry of the fracture network is constructed from the statistics of the fracture orientation, deviation angle of fracture sets, fracture

lengths, and fracture density. Examples of this approach are given in Zhang et al. 1996; Zhang 1989; Rouleau and Gale 1987; Robinson 1982; and Long et al. 1982.

Summary

Using accurate piezometric instrumentation data at a site along with knowledge of the site geology is the preferred method for establishing uplift pressures. This chapter reviews four procedures that are widely used by engineers to establish the uplift pressures along an imaginary section or sections through the structure-foundation interface and/or along a section or sections within the rock foundation when instrumentation data are not available.

An analysis of uplift pressure measurements at seventeen instrumented concrete gravity dams by Stone & Webster (1992) showed that foundation geology has a strong influence on uplift pressure distribution and that the geology controls the response of uplift pressure to changes in dam loading. The investigators discovered that an understanding of the flow within rock joints and the factors which affect the flow lead to a better understanding of the uplift measurements at the damsites, especially those rock formations possessing tight rock joints. A parametric study of laminar flow along a single, horizontal, tapered rock joint was undertaken. The principal results of this study are as follows:

a. A uniform conducting aperture results in a linear variation in uplift pressures along the joint.

b. A taper *downstream* results in *larger* uplift pressures compared to the case of uniform aperture.

c. A taper *upstream* results in *smaller* uplift pressures compared to the case of uniform aperture.

d. The larger, or smaller, that the ratio of e_{in} to e_{out} is from a value of 1.0, then the greater the departure of the uplift distribution is from a linear relationship along the joint.

e. The *magnitudes* of e_{in} and e_{out} impact the quantity of flow.

The principal results of the study involving 2-D steady-state flow through a permeable rock foundation are as follows:

a. Anisotropic permeabilities (i.e., $K_x \neq K_y$) orient the flow channel in the direction of larger permeabilites. This effect is observed in the resulting 2-D steady-state seepage flow net.

b. Given a prescribed crack length, the *magnitude* of the resulting uplift force is equivalent for the 1-D analysis to the uplift forces computed from the three 2-D analyses ($K_x = K_y$, $K_x = 10K_y$, and $K_x = K_y/10$).

c. The *distributions* of uplift pressure along the monolith-to-rock interface calculated using 2-D FE seepage analyses are similar but not exactly equivalent to the distribution from 1-D seepage analyses. Even though the resultant uplift forces are equal in magnitude (item b), differences in the distributions of uplift pressures between the two analyses result in the uplift forces acting at different points along the interface.

The authors caution against making generalities based on the results of this study to more complicated seepage problems. Many of the similarities in the previously stated 1-D and 2-D study results (items a through b) can be attributed to the following features of the nine idealized problems: the distance from the toe of the monolith to the left extent of the finite element mesh (i.e., a location of a flow or head boundary condition) was large and equal to the distance from the heel to the right extent of the mesh (another flow or head boundary condition); the base of the monolith was parallel to the primary flow channels in all four seepage analyses; the permeable foundation was modeled as homogeneous; the primary flow channel immediately below the monolith was nearly horizontal as was the rock-to-monolith interface; and no drainage features were included in the foundation. Any one of these factors will impact conclusions (a) through (b) and will contribute to larger differences in the results between the different types of seepage analyses when compared to the results of this study.

5 Interaction of Gravity Dam, Rock Foundation, and Rock Joint with Uplift Pressures

The U.S. Army Corps of Engineers' guidance for the design of gravity dams follows conventional equilibrium methods of analysis, which are based largely on classical limit equilibrium analysis without regard to deformations (EM 1110-2-2200 (Headquarters, Department of the Army)). Because the conditions of equilibrium are insufficient for a complete analysis of all aspects of the hydraulic structure and foundation interactions involved in the stability and performance of a hydraulic structure, conventional equilibrium methods involve assumptions regarding the loading and resisting forces that act on the dam. With respect to the loading forces, assumptions are made concerning the magnitude and distribution of uplift pressures acting normal to the base of the dam. For resisting forces, assumptions are made concerning the magnitude and distribution of the effective compressive stresses acting normal to the base of the dam. The objective of this chapter is to investigate these assumptions using advanced numerical methods of analysis that account for the deformable nature inherent in the geologic and man-made materials comprising the foundation and the dam. The stability of a typical rock-founded gravity dam (see Figure 62) designed according to guidance contained in EM 1110-2-2200 will be compared to results from finite element analyses which account for the interaction between the development of loads and resistances as a function of the stiffnesses of both the gravity dam and rock foundation.

The example dam shown in Figure 62 does not include the effects of foundation drains. A single deformable rock joint is assumed to exist near the dam-to-rock foundation interface. The rock joint is continuous from immediately upstream of the heel of the dam to downstream of the toe of the dam, with unrestricted access to the reservoir. This problem allows the investigation of the performance of the single rock joint during loading and unloading of the dam and the interaction of the rock joint with the rock foundation. Comparisons are made between the results of the conventional equilibrium analysis of the gravity dam section and the results of the finite element analyses, primarily in terms of base pressures and uplift water pressures.

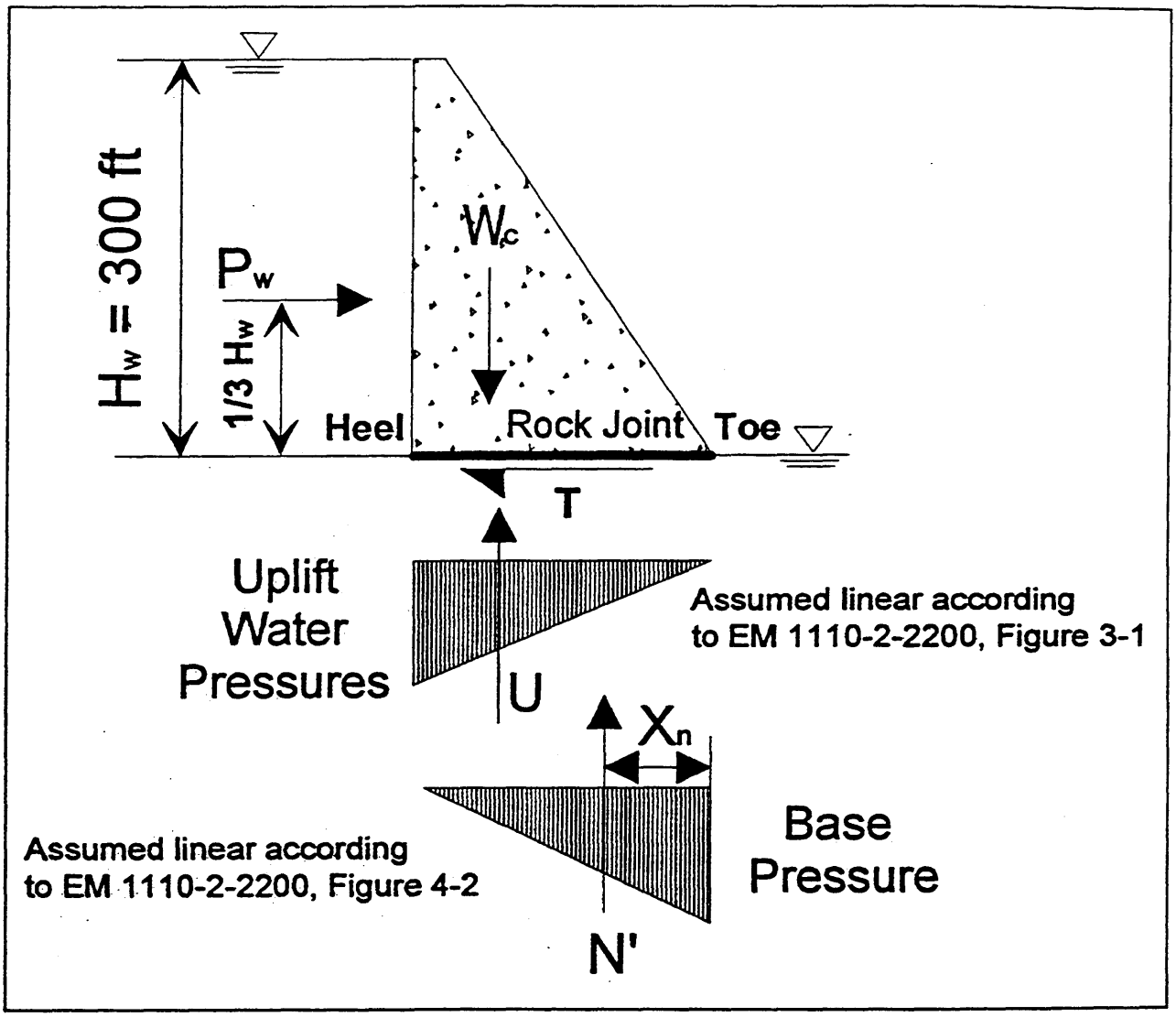

Figure 62. Convertional stability analysis of a rock founded gravity dam according to Corps design guidance (EM 1110-2-2200) (1 ft = 0.305 m)

All loading conditions are assumed to be long-term loadings. Specifically, the pools analyzed are assumed to be maintained for sufficient time such that steady-state seepage conditions are applicable. Modeling of the flow through the rock joint and the modeling of the joint closure and opening in the finite element analyses are discussed in detail. An improved numerical model for rock joints is developed.

Influence of Foundation Geometry on Uplift Pressures

Terzaghi noted as early as 1929 that minor geologic details (such as a single rock joint) that cannot be detected by careful geologic investigations or test borings can have a significant impact on the uplift pressures exerted on structures founded on rock. In 1992, Stone and Webster conducted a comprehensive study for the EPRI of 14 gravity dams founded on rock to ascertain the effect of geology on uplift pressures. Their study concluded that foundation geology significantly influences the uplift pressure distribution and controls the response of the uplift pressure distribution due to changes in dam loading (Stone and Webster 1992).

The EPRI study showed that the uplift pressure distribution is affected by the aperture sizes of the rock joints contained in the foundation. The uplift pressure distribution is coupled with the stresses imposed on the foundation by the dam. Changes in loadings imposed on the rock joints change the joint aperture sizes, which affect the permeability of the joints and ultimately the uplift pressures developed in the joints. The uplift pressures in turn affect the stresses imposed by the structure on the foundation; hence the uplift pressures developed in the rock joints are coupled to the loadings applied to the foundation by the structure. The uplift pressures can be nonlinear and usually are since the rock joint aperture varies across the width of a structure. As an example, a tapered joint will result in a nonlinear uplift pressure distribution. The direction of the taper will influence the distribution of the uplift pressures. That is, a taper with a smaller aperture at the heel than at the toe will result in an uplift pressure distribution that is less than the conventional linear assumption. A taper with a larger aperture at the heel than at the toe will result in an uplift pressure distribution that is greater than the conventional linear distribution (Ebeling and Pace 1996a).

This chapter focuses on the interaction of a gravity dam having a dolerite rock foundation (including a rock joint) with uplift pressures and the corresponding effects on dam stability for a range of pool elevations. The example problem analyzed is shown in Figure 62. The problem involves coupled effective normal stress and flow predictions which must be solved in an iterative manner. A dam on a rock foundation would cause varying stresses in the rock foundation based on the pool elevations. A high pool would tend to lift the heel of the dam off the foundation and compress the toe of the dam. In effect, this would open the rock joint at the heel and close the rock joint at the toe. A low pool would cause a reverse effect. That is, the rock joint would close at the heel and open at the toe. The opening and closing of the rock joint along the entire length of the joint occur relative to the initial rock joint aperture.

Various types of discontinuities exist in rock such as faults, joints, and fissures. Each of these discontinuities has its own physical attributes. In this chapter, the terms "rock joint," "fracture," or "discontinuity" are used interchangeably to represent any rock discontinuity.

Introduction to Example Problem

The example dam shown in Figure 62 was designed using Corps guidance contained in EM-1110-2-2200, Engineering Manual for Design of Gravity Dams, which uses conventional stability calculations. The design guidance in EM 1110-2-2200 requires that the resultant of all forces on the base of the dam lie within the middle third (kern) of the base of the dam for the usual (normal operation) loading condition. Unusual or extreme loading conditions require that the resultant lie within the middle half and anywhere within the base, respectively. If the resultant lies within the middle third of the base, 100 percent of the base of the dam will be in compression. A (nonsite-specific) linear uplift water pressure distribution, as shown in Figure 62, is specified by EM 1110-2-2200 for gravity dam sections without drains. The dam was proportioned using the conventional force equilibrium method to produce compressive stresses across the entire width of the dam. The dam was proportioned such that the resultant of the base pressures was located at the edge of the kern, that is the effective base pressure resultant (N') lies at a point two-thirds of the base length from the heel of the dam. Therefore, the entire base is in compression with an assumed linear base pressure distribution (with zero base pressure below the heel) and an assumed triangular uplift pressure distribution as shown in Figure 62. The overturning stability of the dam was the primary interest in this study, but a complete stability analysis should also include sliding and bearing capacity evaluations.

The dam is a typical cross section situated on a dolerite rock foundation. The effects of foundation drains are not included in this problem. The foundation possesses a single deformable rock joint located at the dam-to-rock foundation interface. The rock joint is assumed to be continuous from immediately upstream of the heel of the dam to downstream of the toe of the dam, with unrestricted access to the reservoir. The example dam is 300 ft (91.43 m) high with a crest width of 25 ft (7.62 m) and a base width of 235 ft (71.6 m). For the given pool elevations and dam geometry shown in Figure 62, a base width of 235 ft (71.6 m) results in a zero base pressure at the heel.

Considerations in Determining Flow Through Rock Joints

In order to model the interaction between the gravity dam, rock joint, and rock foundation during raising and lowering of the reservoir in the finite element analyses, careful consideration must be given to the effects of changes in normal stress on joint closure and opening and the subsequent effects on uplift water pressures. Fluid flow through rock joints has been shown to be coupled with the normal stresses imposed on the joint by many investigators (Noorishad, Witherspoon, and Brekke 1971; Brekke et al. 1972; Iwai 1976; Bandis 1980; Witherspoon et al. 1980; Tsang and Witherspoon 1981; Barton, Bandis, and Bakhtar 1985; Stone and Webster 1992). The permeability of a rock joint varies with its aperture as determined by the cubic law discussed in Chapter 4 and discussed in Ebeling and Pace (1996a). The variation of the aperture of a rock joint is

determined by the physical properties of the rock and the rock joint and the applied loadings. An example of this variation in aperture with changes in normal stresses is given in Ebeling and Pace (1996b). Iwai (1976) determined that the permeability of a natural fracture should be influenced to some extent by its geometrical factors such as roughness and contact area. Bandis, Lumsden, and Barton (1983) listed several factors affecting the normal stiffness of rock joints which ultimately affects the aperture of the rock joint under loading. The factors are:

a. Initial contact area, relative amplitude and vertical distribution of the aperture between the walls.

b. Joint wall roughness.

c. Strength and deformability of asperities.

d. Thickness, type, and physical properties of infilling material.

Factors affecting the flow of fluid in rock joints include tortuosity, contact area, and temperature. This discussion limits itself to roughness, contact area, and wall strength. Iwai (1976) found from his experiments that small-scale roughness could be ignored if the aperture was greater than 4.92×10^{-4} ft (150 μm). The effect of contact area becomes significant if the aperture is less than 4.92×10^{-4} ft (150 μm). Contact area is influenced by strength of rock asperities, number of loading cycles, and whether the sample is being loaded or unloaded. A small change in the seating condition can cause a large change in the flow behavior for small fracture apertures.

The study described in this chapter limits itself to the examination of the effects of normal stresses on uplift pressures developed in a rock joint. Shearing stresses can also produce changes in uplift pressures due to dilatancy effects which alter the aperture of a rock joint. The effects of shear-induced joint dilatancy on a rock joint are discussed in Bandis (1980), Bandis, Barton, and Christianson (1985); and Barton, Bandis, and Bakhtar (1985). Barton, Bandis, and Bakhtar (1985) state that the effects of shear-induced dilation are greater for rock joints having high joint compressive strength, high joint roughness, and low confining stresses. The dilation will be less for joints with low joint compressive strength, low joint roughness, and high confining stresses.

Types of Numerical Analyses Used To Predict Joint Deformation and Fluid Flow

Various flow models exist but can be categorized as either a continuum model or a discrete network model. Continuum models assume the rock is sufficiently fractured such that the rock can be idealized as a homogeneous porous media. Parameters of this media, such as permeability and porosity, are defined statistically. Examples of this type of approach are found in Long et al. (1982), Shapiro

and Andersson (1983), and Long (1985). The discrete network model involves the modeling of individual discontinuities in the foundation. Known discontinuities can be modeled, or a statistical representation of the rock mass based on average joint orientation, deviation angle, lengths, and density may be used. Examples of discrete modeling can be found in Noorishad, Witherspoon, and Brekke (1971); Brekke et al. (1972); Grenoble (1989) and Grenoble et al. (1992).

In this report, two methods are used to model the rock foundation. In Chapter 2, the flexibility of the rock foundation was accounted for by assigning a composite stiffness to the jointed rock foundation using empirical relationships that account for both the type of rock and the jointing and fissures within the rock mass comprising the foundation. The approach discussed in the chapter includes all aspects of the first approach, along with discrete modeling of key joints within the immediate region of the dam-foundation interface.

Hyperbolic Joint Closure/Opening Versus Effective Normal Stress Model

The concept of using a hyperbola to represent the stress-strain behavior of rock or soil is not a new concept (Goodman 1974, Duncan and Chang 1970). The hyperbolic models proposed by these investigators account for the stress-dependent, nonlinear, and inelastic behavior of the geologic materials. There are several mathematical forms of the hyperbolic model that have been used by various researchers. For example, Bandis (1980) used a form of the Duncan and Chang model to represent the relationship between normal stress and joint closure. Both the Duncan and Chang and Bandis hyperbolic models are shown in Figure 63. Figure 63a shows the hyperbolic model applied to soils to represent the stress-strain behavior and Figure 63b shows the hyperbolic model used to represent the normal stress versus joint closure relationship of rock.

The Duncan and Chang model uses the following form of the hyperbolic model for soils

$$\sigma_1 - \sigma_3 = \frac{\varepsilon}{a + b\varepsilon} \tag{26}$$

while Bandis uses the following form for rocks

$$\sigma_n = \frac{\Delta V_j}{a - b\Delta V_j} \tag{27}$$

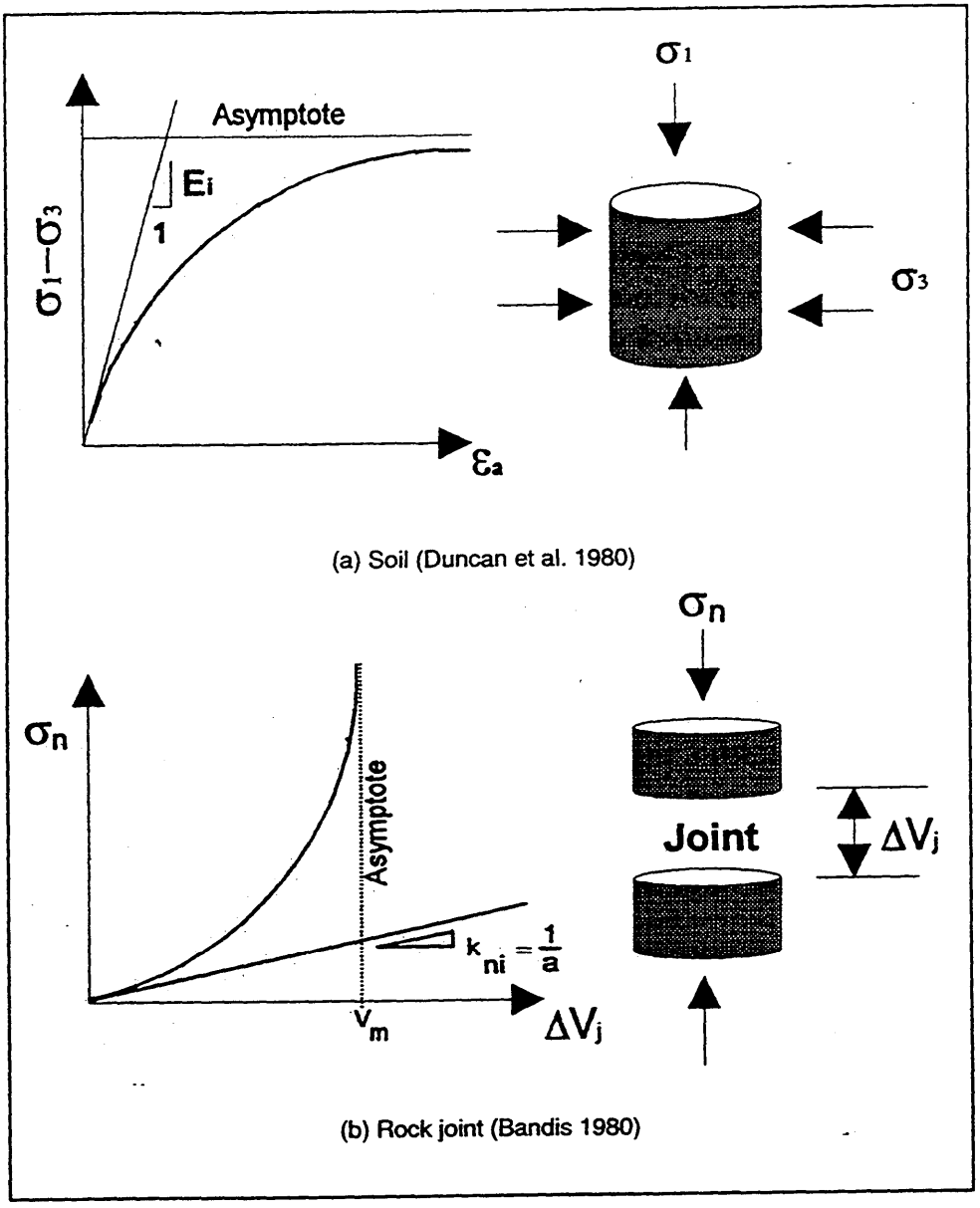

Figure 63. General hyperbolic models for soil and rock

where

σ_1-σ_3 = principal stress difference

σ_n = effective normal stress

ϵ = strain

ΔV_j = joint closure

a = constant

b = constant

The parameters a and b are fitting parameters for the hyperbolic curve and depend on the data which the hyperbolic curve is intended to represent. For the hyperbolic curve shown in Figure 63a, the parameter, a, is equal to the reciprocal of the initial tangent modulus, E_i, and the parameter, b, is equal to the reciprocal of the asymptote of the hyperbolic curve, $(\sigma_1-\sigma_3)_{ult}$. The asymptote of the hyperbolic curve has been found to consistently overestimate the value of the principal stress difference at failure, $(\sigma_1-\sigma_3)_f$. The principal stress difference at failure is defined using the Mohr-Coulomb strength equation (Duncan and Chang 1970). The asymptote and principal stress difference at failure are related by the following equation:

$$(\sigma_1 - \sigma_3)_f = R_f (\sigma_1 - \sigma_3)_{ult} \tag{28}$$

where R_f is always smaller than unity and usually varies between 0.5 to 0.9 for most soils (Duncan et al. 1978). For the curve shown in Figure 63b, the parameter, a, is equal to the reciprocal of the initial tangent normal stiffness, K_{ni}, and the parameter, a/b, is equal to the maximum joint closure, V_m.

Discussion of Bandis' Joint Closure Model

The relationship of joint closure to normal stress proposed by Bandis (1980), and discussed in Bandis, Lumsden, and Barton (1983), and Bandis, Barton, and Christianson (1985) was chosen for use in this study based on its simplicity. The parameters needed to characterize a joint are:

a. The joint roughness coefficient, *JRC*.

b. The joint wall compressive strength, *JCS*.

c. The unconfined compressive strength of the rock adjacent to the joint wall.

d. The residual friction angle, φ_r.

e. The conducting aperture, *e*.

f. The mechanical aperture, *E*.

The parameters needed for the model can be found from inexpensive field tests, which include a tilt test and the Schmidt hammer rebound test (Bandis 1980; Barton, Bandis, and Bakhtar 1985). These tests provide the parameters of joint roughness coefficient, *JRC*, and the joint compressive strength, *JCS*, respectively.

Bandis conducted a series of normal closure tests on 64 interlocked jointed block samples. The samples were composed of fresh and weathered slate, dolerite, limestone, siltstone, and sandstone subjected to multiple loading/ unloading cycles. Gale (1982b) noted the importance of testing natural fractures to develop stress-closure relationships. Artificial tension fractures produce extremely tight, rough fractures as compared to natural fractures which distort the behavior relative to natural fractures. Bandis (1980) conducted tests on both weathered and unweathered joints.

The effect of multiple loading cycles on rock joint aperture was also addressed by Bandis (1980). His research showed that the normal stress-normal deformation relationships of a wide variety of natural interlocked joints are highly nonlinear, irrespective of the rock joint type. This relationship exists through repeated loadings. Since the relationship is nonlinear, a single value of the normal stiffness cannot represent the total behavior. A hyperbolic relationship was found to suitably represent the normal stress versus joint closure behavior. Multiple loading cycles are shown in Figure 64. As seen from the figure, a load-unload cycle produces some permanent set or irrecoverable closure, V_r. This closure decreases for successive cycles as the joint "seats" itself. The amount of set for the second and third cycles of loading is small compared to the first cycle. Also, the magnitude of the joint stiffness, K_{ni}, increases with repeated joint loadings as the joint "seats" itself. The third or fourth cycle represents the in situ condition of the rock joint. The nonlinear behavior of the joint closure persists throughout repeated cycles of loading for both weathered and unweathered rock samples. Significant hysteresis persists between loading and unloading during all cycles of loading. Finally, fresh joints have some elastic recovery, whereas weathered joints have less. Weathered joints are also more deformable than fresh joints.

The hyperbolic model developed by Bandis (1980) and reported in Bandis, Lumsden, and Barton (1983) is shown in Figure 65. This model will predict the joint closure with normal stress given the loading cycle, the initial mechanical aperture, E_o, the joint compressive strength, *JCS*, and the joint roughness coefficient, *JRC*. Bandis found that both the load and unload curves for all the samples of rock could be represented by a hyperbolic curve. The unload portion of a cycle is offset from the origin by the amount of irrecoverable closure, as shown in Figure 64.

A representative test sample from Bandis' (1980) experimental work and the one that was used in this study is shown in Figure 66. The sample is a fresh dolerite. The composite curve representing several loading cycles is shown in Figure 67.

The rock sample was loaded and the total deformation, ΔV_p of the joint was recorded. The deformation of an intact rock sample, ΔV_r, was also recorded under the same conditions. The total deformation ΔV_t is related to the joint closure, ΔV_j by the following equation:

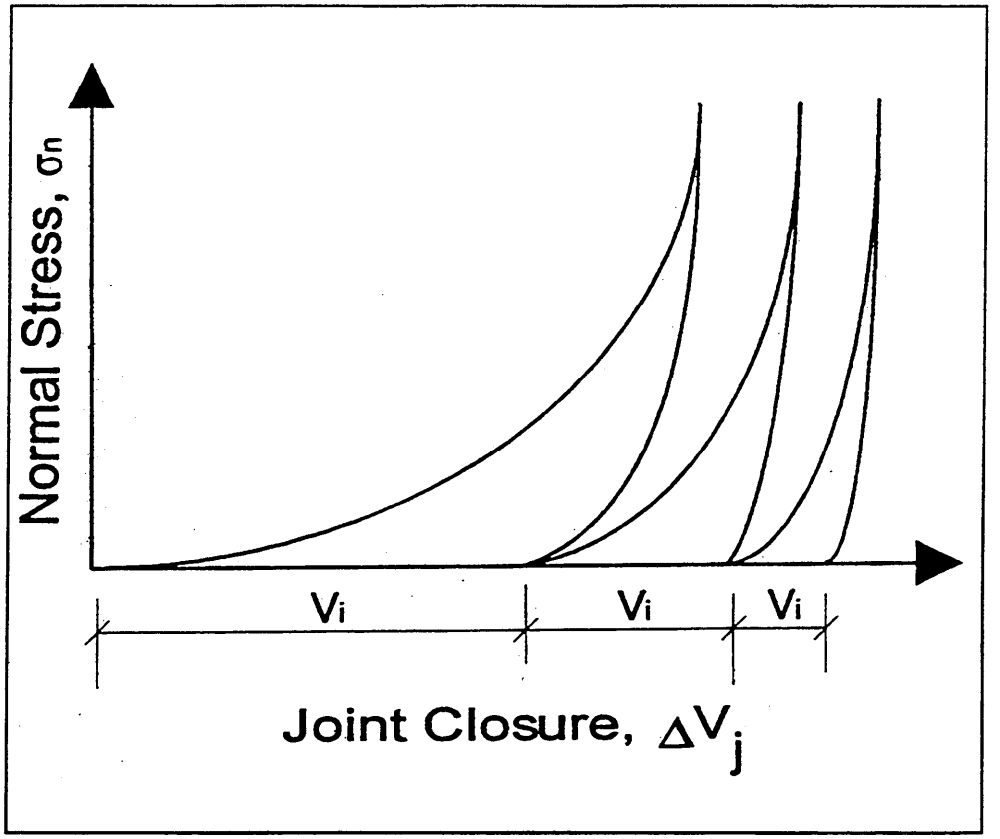

Figure 64. Multiple loading cycles and irrecoverable closure

$$\Delta V_t = \Delta V_j + \Delta V_r \tag{29}$$

where ΔV_r is defined as

$$\Delta V_r = \frac{\sigma_n}{c} \tag{30}$$

and c is the elastic modulus of the rock. At very large normal stresses (approximately 1.04×10^6 psf (50 MPa)), the slope of the σ_n-ΔV_t curve approaches the slope of the load deformation curve for intact rock. Therefore, the maximum joint closure will equal the value of the total deformation at this large normal stress minus the elastic compression of the rock.

Bandis fitted his experimental data using Equation 29 inserting Equations 27 and 30. The resulting equation used to fit the experimental data is equal to

$$\Delta V_t = \frac{\sigma_n a}{1.0 + \sigma_n b} + \frac{\sigma_n}{c} \tag{31}$$

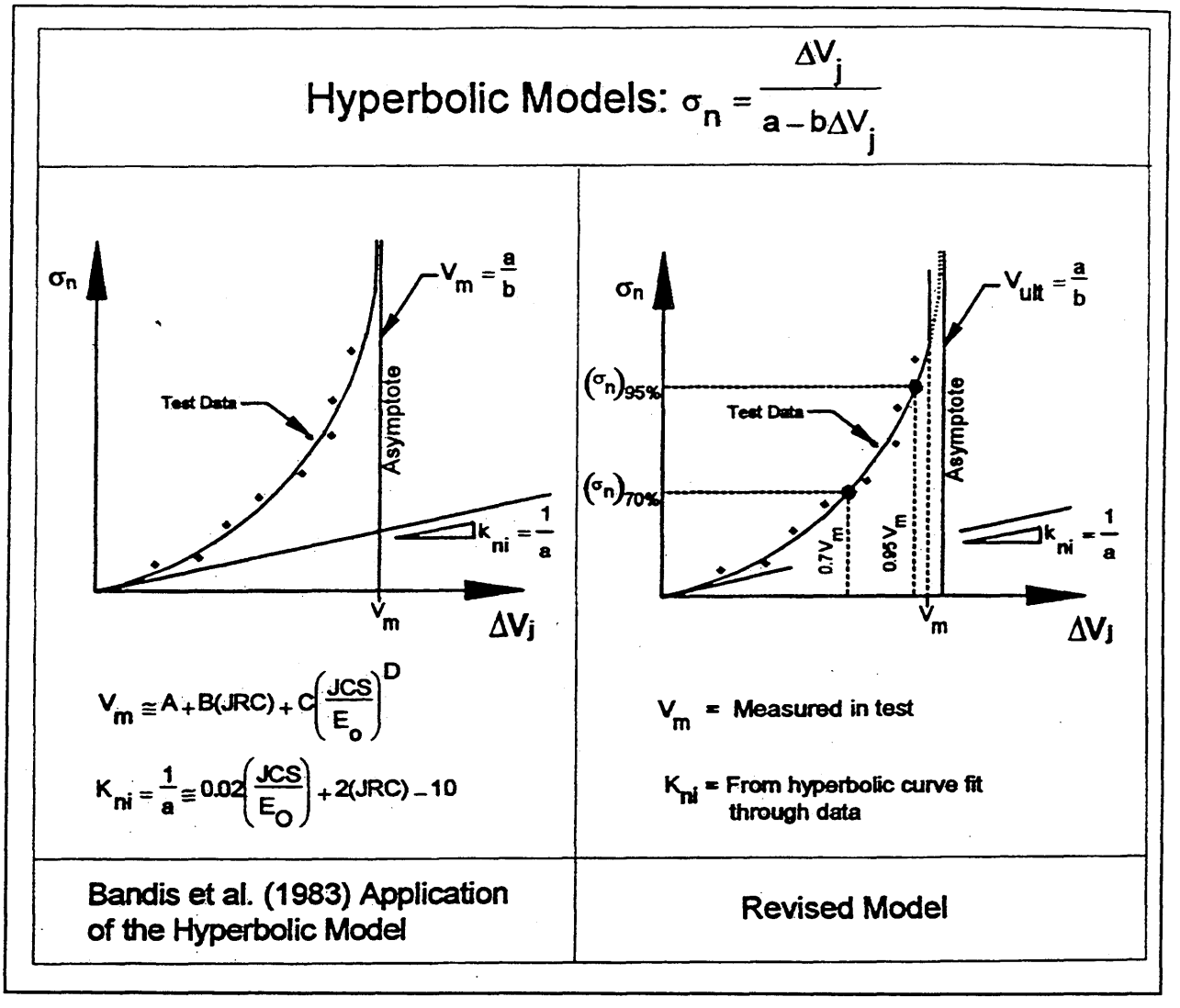

Figure 65. Two models for normal closure of joints

Inserting the values of the constants a and b yields

$$\Delta V_t = \frac{\sigma_n V_m}{K_{ni} V_m + \sigma_n} + \frac{\sigma_n}{c} \tag{32}$$

The fitting parameters c, V_m, and K_{ni} were found from a nonlinear regression analysis of the experimental data. The elastic curve measured for intact rock displayed a slight nonlinear behavior as shown in Figure 66 which was accounted for by subtracting the nonlinear contribution from the computed V_m. The magnitude of the nonlinear contribution was equal to the point where the slope of the elastic curve at approximately 1.04×10^6 psf (50 MPa) intercepted the x-axis. From a statistical analysis of the data, Bandis arrived at the model shown in

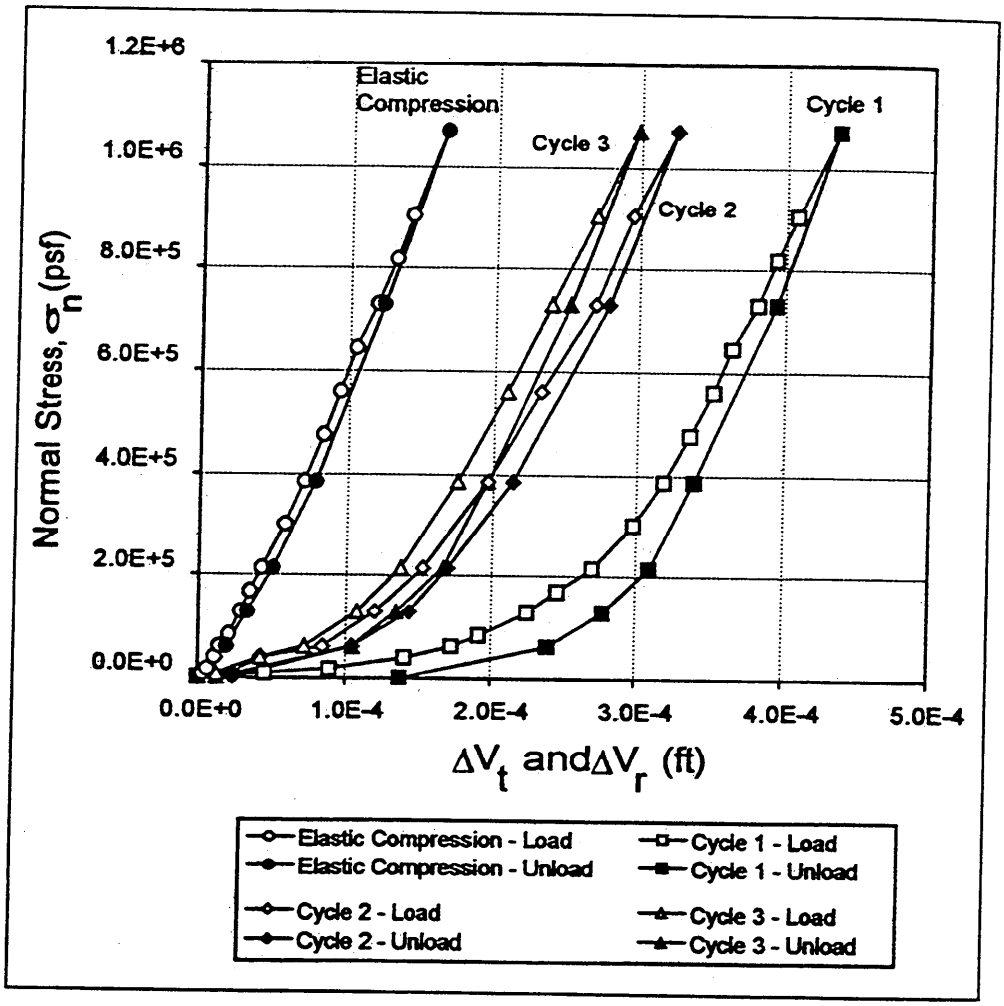

Figure 66. Laboratory results showing normal stress (σ_n) - total deformation (ΔVt) relationships for fresh dolerite under repeated loading cycles, and intact rock compression curves (after Bandis 1980) (1 ft = 0.305 m, 1 MPa = 20,885.5 psf)

Figure 65. From the experimental data, multiple regression of sets of data relating V_m to E_o, JCS, and JRC yielded the following equations for V_m and K_{ni}:

$$V_m = A + B(JRC) + C\left(\frac{JCS}{E_0}\right)^D \tag{33}$$

$$K_{ni} = 0.0178\left(\frac{JCS}{E_o}\right) + 1.748(JRC) - 7.154 \tag{34}$$

The empirical relationships defined in Equations 33 and 34 were formulated in SI units and are valid for unfilled interlocked joints within the following range of parameters provided that the initial stress condition does not exceed 1×10^{-3} MPa:

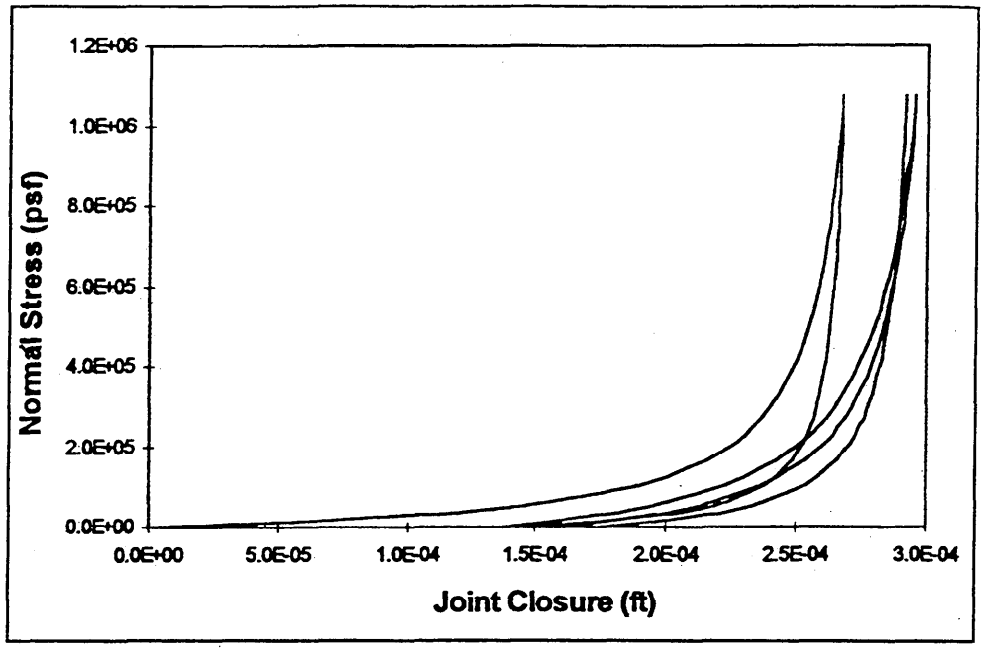

Figure 67. Composite curve for three cycles of load/unload for dolerite rock sample (1 ft = 0.305 m, 1 MPa = 20,885.5 psf)

a. $JRC = 5 - 15$.

b. $JCS = 22 - 182$ MPa.

c. $E_o = 0.10 - 0.60$ mm.

Equations 33 and 34 are based on values of E_o, JCS, and JRC that are for a specific rock sample. The coefficients A, B, C, and D are different for loading cycles one through three. Large permanent set and hysteresis occurs for the first loading cycle which represents a disturbed sample. Loading cycles three or four represent the in situ condition of the rock where sample disturbances have largely been removed. For loading cycles one through three, the coefficients are shown in Table 10.

Table 10
Coefficients for Empirical Equation for V_m (After Bandis 1980)

Coefficients	Cycle 1	Cycle 2	Cycle 3
A	-0.2960 ± 0.1258	-0.1005 ± 0.0530	-0.1031 ± 0.0680
B	-0.0056 ± 0.0022	-0.0073 ± 0.0031	-0.0074 ± 0.0039
C	2.2410 ± 0.3504	1.0082 ± 0.2351	1.1350 ± 0.3261
D	-0.2450 ± 0.1086	-0.2301 ± 0.1171	-0.2510 ± 0.1029
r^2	0.675	0.546	0.589

For cycles two and three, the value of E_o used in Equations 33 and 34 for the loading portion of a cycle is equal to

$$E_{on} = E_o - \sum_{1}^{n-1} \left(V_{in} \right) \tag{35}$$

where

n = number of the load-unload cycle

E_o = initial mechanical aperture for cycle 1

E_{on} = initial mechanical aperture for cycle n

V_{in} = irrecoverable closure for cycle n

This essentially reduces the initial mechanical aperture of cycle one for the irrecoverable closures obtained in cycles two and three.

From Bandis (1980) both the loading and unloading behavior of a rock joint was found to follow a hyperbolic relationship. The maximum closure of the unloading hyperbola for a particular cycle is computed as

$$V_{mn-u} = V_{mn} - V_{in} \tag{36}$$

where

V_{mn-u} = maximum closure of unloading hyperbola for cycle n

V_{mn} = maximum closure computed for loading portion of cycle n

The value of K_{ni} for the unloading hyperbola can be computed using Equation 34 with E_o replaced by

$$E_{on-u} = E_o - \sum_{1}^{n} \left(V_{in} \right) \tag{37}$$

where E_{on-u} = initial mechanical aperture for cycle n.

The irrecoverable closure, V_i, or permanent set is difficult to predict but can be approximated by the use of Figure 68. This figure shows a definite trend of decreasing permanent set with increased joint compressive strength, increased number of load cycles, or decreasing initial joint aperture.

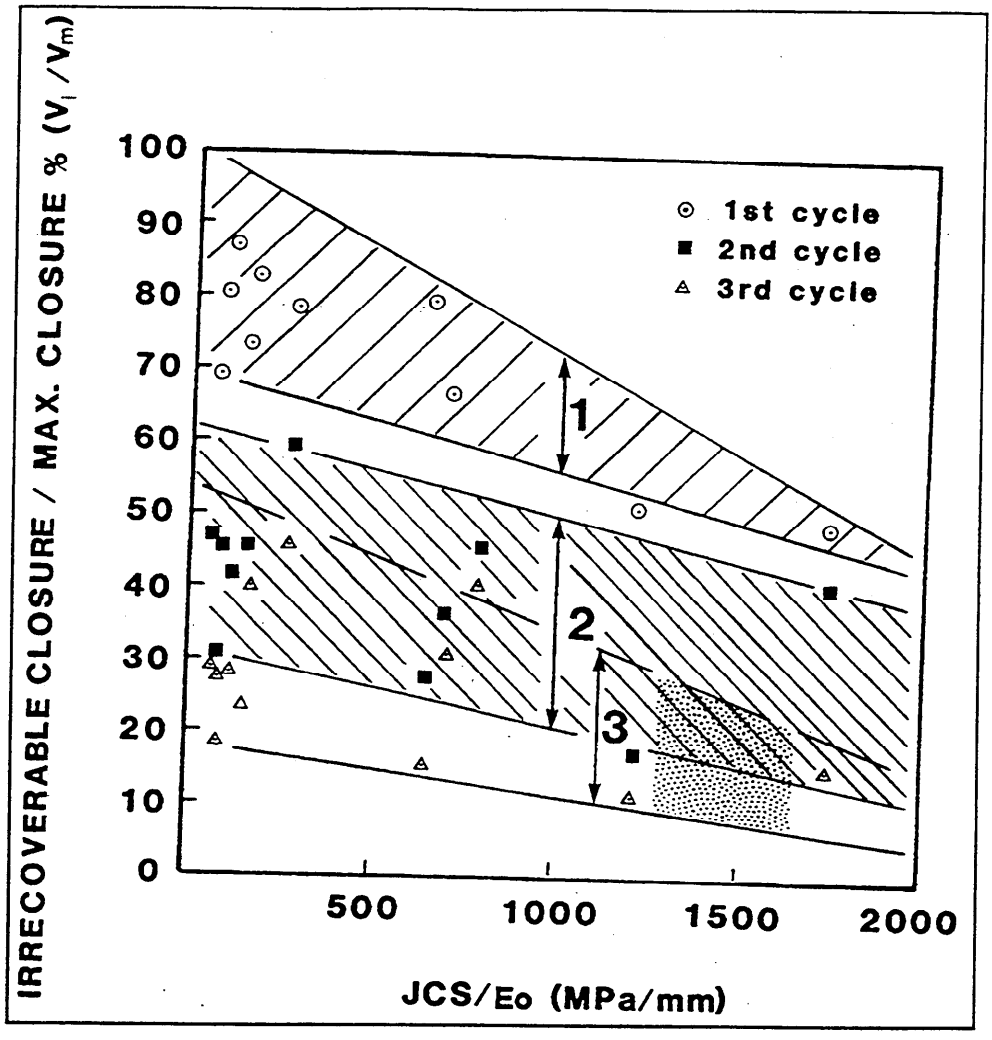

Figure 68. Plot showing that irrecoverable closure reduces with number of cycles, JCS value, and with the smallness of the initial joint aperture, E_o (after Bandis 1982) (1 MPa/mm = 0.00368 psi/in.)

Application of Bandis' Model

Applying the model proposed by Bandis as shown in Figure 65 presented several challenges. It was first thought that the Bandis' model could be used "as is" to predict the closure behavior of the dolerite rock joint. The experimental fit of the test data for the fresh dolerite sample using Equation 32 is shown in Figure 69a. As can be seen from the figure, Equation 32 fits the data quite well. The joint closure curve shown in Figure 69b is computed using Equation 38.

$$\Delta V_j = \frac{\sigma_n V_m}{K_{ni} V_m + \sigma_n} \tag{38}$$

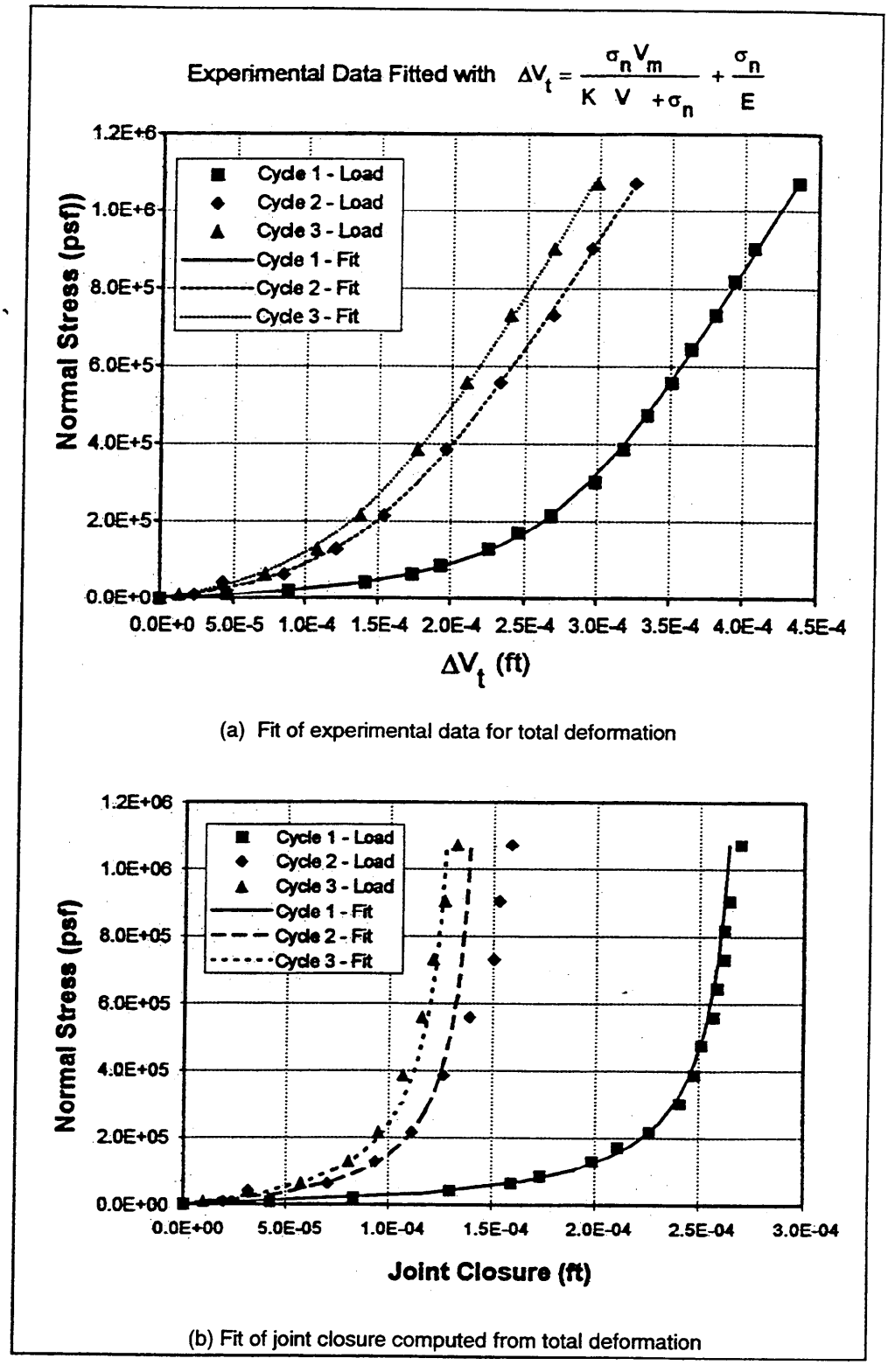

Figure 69. Fit of Bandis' experimental data for fresh dolerite (1 ft = 0.305 m, 1 MPa = 20,885.5 psf)

The value of V_m computed from the curve fitting procedure was corrected for the nonlinear behavior of the rock that is seen in Figure 66. The correction consisted of reducing the value of V_m by the amount equal to the nonlinear contribution of compression of the intact rock sample. From Figure 69, it can be seen that the hyperbolic equation provides an acceptable fit for the experimental data. The values of V_m and K_{ni} are computed from a linear regression analysis of the experimental data.

If the empirical equations proposed by Bandis are used to compute V_m and K_{ni}, the fit shown in Figure 70a results. Equations 33 and 34 with measured values of $\grave{E}_o$, *JRC*, and *JCS* were used to compute V_m and K_{ni}. The empirical equations for V_m and K_{ni} do not provide an acceptable fit of the experimental data. Figure 70, shows the effect of using Equation 34 to compute K_{ni} and using the values of V_m obtained from the experimental testing. A better fit results, but V_m still needs improvement.

Tables 11 and 12 compare measured values of V_m and K_{ni} to values computed using Equations 33 and 34 for loading cycles one and three for several samples analyzed by Bandis. As shown in Table 11, the empirical equations for V_m and K_{ni} provide a better approximation of the actual V_m and K_{ni} for cycle one than for cycle three.

This study shows the fit of the data is more dependent on the value of V_m than K_{ni}. This fact is apparent from Figure 70b. Therefore, a better approximation of V_m is needed. The hyperbolic model proposed by Bandis underestimates the value of V_m even when using the experimental results. V_m is the asymptote of the hyperbolic curve and therefore will only be reached at an infinite normal stress. The value of normal stress used in the testing is not large enough to approach V_m. This is not implying that the value of normal stress applied in the testing is not large enough to produce "closure" of the joint. It is important to realize the value of V_m as used in the Bandis' application of the hyperbolic model is a curve fitting parameter and therefore mathematically is only reached at an infinite stress. A better procedure is needed to account for the underestimation of joint closure at maximum normal stresses.

Revision of Bandis' Joint Closure Model

Since the use of the empirical equations to compute V_m and K_{ni} did not result in a fit of the data that was deemed acceptable, a revised model was developed from the experimental data. This revised model is shown in Figure 71. The model is an adaptation of the model proposed by Duncan and Chang (1970) for soils.

The model accounts for the underestimation of V_m by providing a factor, R_f, relating the ultimate value of closure, V_{ult} (the asymptote of the curve), to the actual value of V_m measured from testing. The factor R_f is defined as

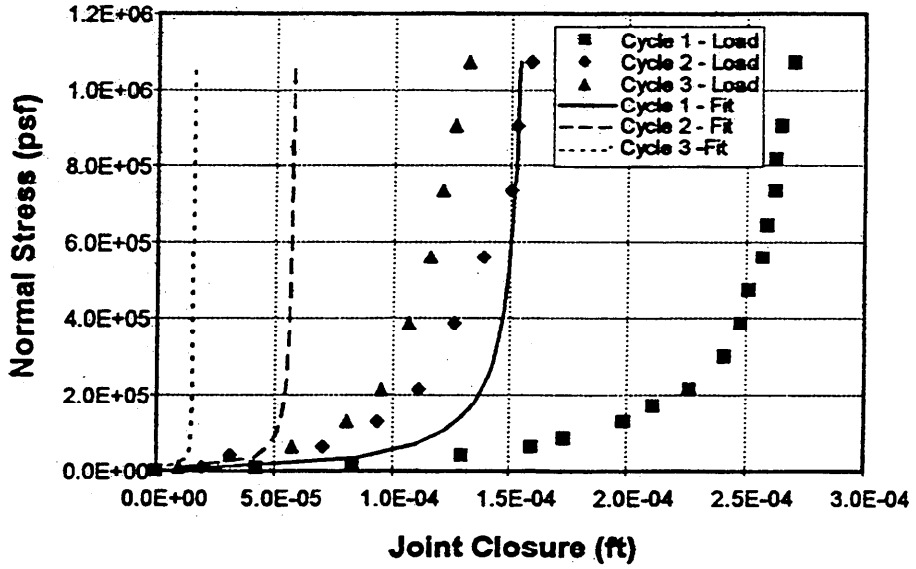

(a) Fit of experimental data using Bandis' equations for V_m and K_{ni}

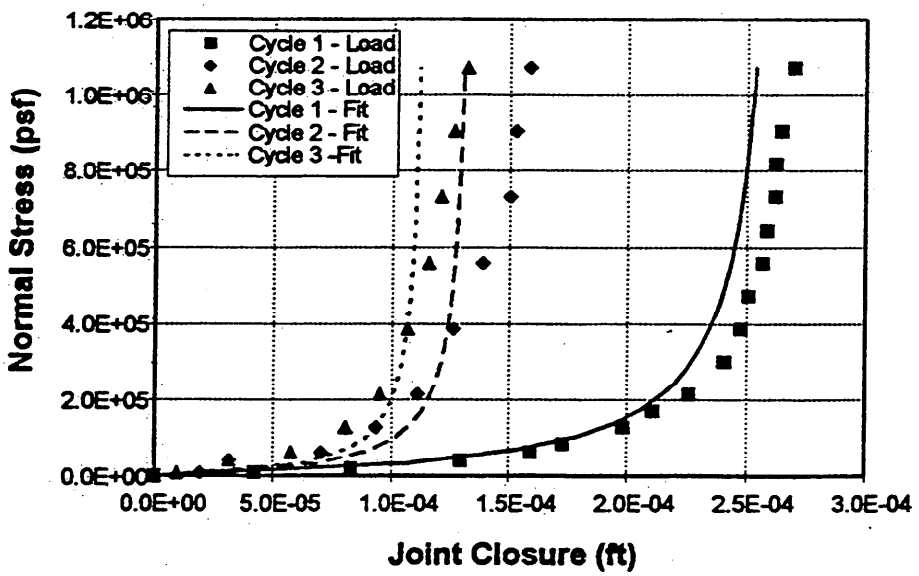

(b) Fit of experimental data using Bandis' equation for K_{ni} and values of V_m from experimentation

Figure 70. Two different fits of Bandis' experimental data showing the effects of the fitting parameters (1 ft = 0.305 m, 1 MPa = 20,885.5 psf)

Table 11
Comparison of Measured Maximum Closure (V_m) and Initial Normal Stiffness (K_{ni}) to Values Computed Using Bandis' Empirical Equations for Cycle 1 Loading[1]

Sample	JCS MPa	JRC	E_o mm	V_m (mm)		% Difference from Measured V_m	K_{ni} MPa/mm		% Difference from Measured K_{ni}
				Measured	Calculated		Measured	Calculated	
Slate, No. 3	175	4.0	0.10	0.063	0.041	-34.5	26.90	30.99	15.2
Dolerite, No. 1	182	8.8	0.15	0.081	0.048	-40.6	22.70	29.83	31.4
Limestone, No. 10	157	7.6	0.20	0.105	0.099	-5.6	25.90	20.10	-22.4
Sandstone, No. 16	44	7.4	0.25	0.255	0.294	15.3	4.10	8.91	117.4
Siltstone, No. 3	105	8.8	0.15	0.135	0.105	-22.3	18.00	20.69	14.9
Limestone, No. 1	162	9.8	0.25	0.072	0.108	49.9			
Sandstone, No. 2	68	11.9	0.25	0.190	0.205	7.8			

[1] 304.8 mm = 1 ft, 1 MPa = 20,885.5 psi.

Table 12
Comparison of Measured Maximum Closure (V_m) and Initial Normal Stiffness (K_{ni}) to Values Computed Using Bandis' Empirical Equations for Cycle 3 Loading[1]

Sample	JCS MPa	JRC	E_o mm	V_i Measured mm		V_m (mm)		% Difference from Measured V_m	K_{ni} (MPa/mm)		% Difference from Measured K_{ni}
				Cycle 1	Cycle 2	Measured	Calculated		Measured	Calculated	
Slate, No. 3	175	4.0	0.10	0.031	0.013	0.026	0.041	59.5	210.20	55.46	-73.6
Dolerite, No. 1	182	8.8	0.15	0.042	0.007	0.035	0.023	-35.1	99.01	40.30	-59.3
Limestone, No. 10	157	7.6	0.20	0.082	0.011	0.015	0.054	257.7	171.50	32.25	-81.2
Sandstone, No. 16	44	7.4	0.25	0.211	0.023	0.051	0.152	198.3	26.46	54.73	106.8
Siltstone, No. 3	105	8.8	0.15	0.090	0.017	0.036	0.051	41.7	84.42	51.69	-38.8
Limestone, No. 1	162	9.8	0.25	0.057	0.005	0.013	0.048	268.4			
Sandstone, No. 2	68	11.9	0.25	0.149	0.025	0.022	0.087	294.4			

[1] 304.8 mm = 1 ft, 1 MPa = 20,885.5 psf.

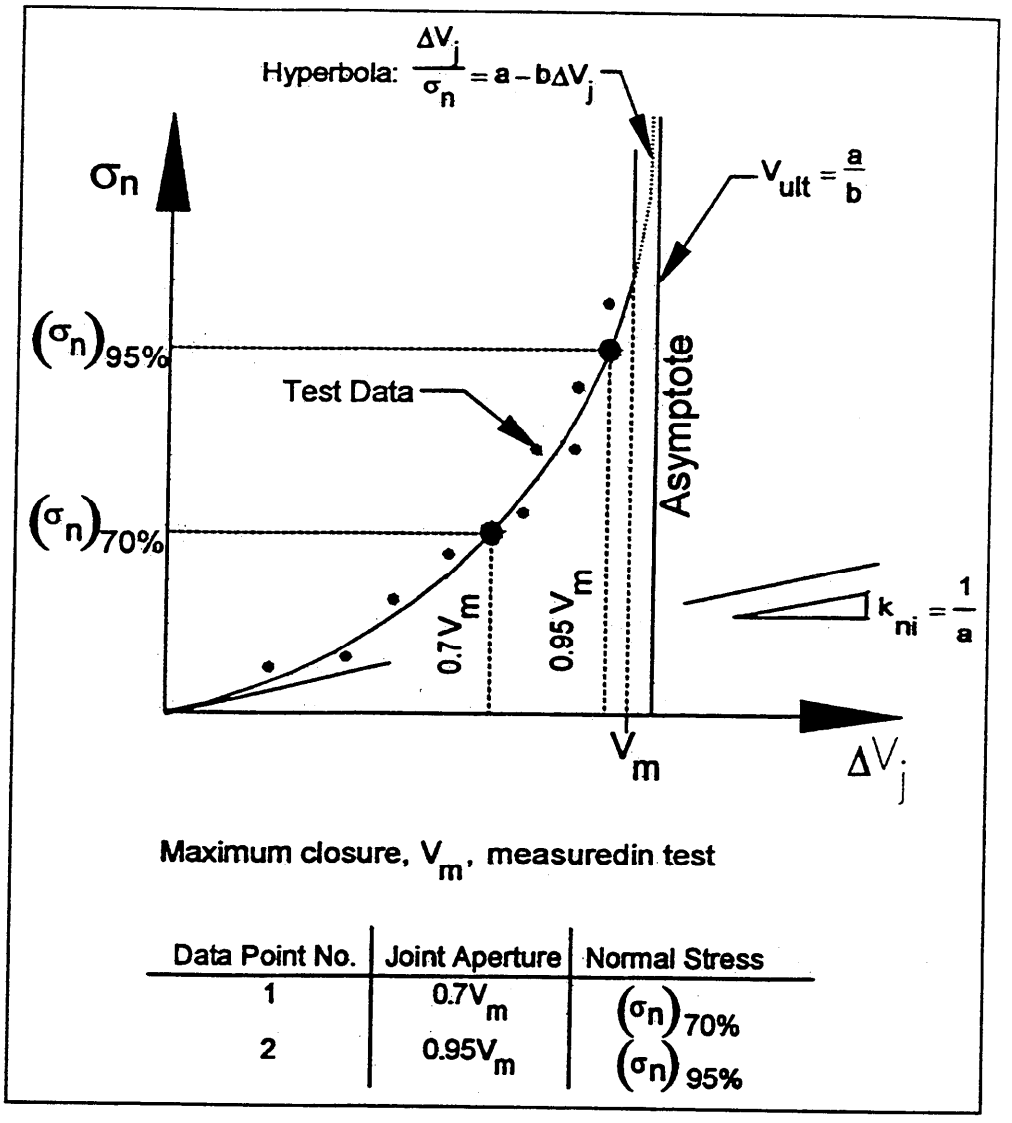

Data Point No.	Joint Aperture	Normal Stress
1	$0.7V_m$	$(\sigma_n)_{70\%}$
2	$0.95V_m$	$(\sigma_n)_{95\%}$

Figure 71. Hyperbolic model of joint closure

$$V_m = R_f \times V_{ult} \tag{39}$$

Two points from the experimental σ_n-ΔV_j curve are used to develop the fit. The normal stresses at 70 and 95 percent of V_m are taken from the experimental curve. This will give initial values of V_{ult}, K_{ni}, and R_f to be used in the hyperbolic joint model. The resulting hyperbolic curve is compared with the test data for the rock joint using standard spreadsheet software with graphical capabilities. The values of V_{ult}, K_{ni}, and R_f can then be adjusted to better fit the data. The steps involved in determining the parameters V_{ult}, K_{ni}, and R_f are summarized below (refer to Equation 27 for a definition of parameters a and b):

a. Calculate $1/V_{ult}$

$$\frac{1}{V_{ult}} = \frac{b}{a} = \frac{\left[\frac{(\sigma_n)_{95\%}}{0.95V_m}\right] - \left[\frac{(\sigma_n)_{70\%}}{0.70V_m}\right]}{(\sigma_n)_{95\%} - (\sigma_n)_{70\%}} \tag{40}$$

b. Compute K_{ni} as

$$K_{ni} = \frac{1}{a} = \frac{1}{2}\left[\frac{(\sigma_n)_{70\%}}{0.7V_m} - \frac{(\sigma_n)_{70\%}}{V_{ult}}\right] + \frac{1}{2}\left[\frac{(\sigma_n)_{95\%}}{0.95V_m} - \frac{(\sigma_n)_{95\%}}{V_{ult}}\right] \tag{41}$$

c. R_f is equal to

$$R_f = \frac{V_m}{V_{ult}} \tag{42}$$

d. The hyperbolic equation given in Equation 27 may now be rearranged to yield

$$\Delta V_j = \frac{\sigma_n}{K_{ni} + \frac{\sigma_n}{V_{ult}}} \tag{43}$$

This procedure is used to fit both the load and unload portions of the test data. The resulting fit of the loading curve for cycle one using this procedure resulted in $1/V_{ult} = 3{,}545$ 1/ft (11.63 1/mm), $K_{ni} = 2.027 \times 10^8$ psf/ft (31.84 MPa/mm), and $R_f = 0.957$. The unloading curve for cycle one had $1/V_{ult} = 7{,}455$ 1/ft (24.46 1/mm), $K_{ni} = 2.332 \times 10^8$ psf/ft (36.64 MPa/mm), and $R_f = 0.986$.

The experimental data are over a stress range that is much larger than the stress range used in this study. Therefore, a method must be used to construct a load/unload curve for a particular cycle that is in the normal stress range of interest. Figure 72 depicts the method developed for use in this study to construct such a curve. The load and unload curves intersect at the maximum normal stress. The unload curve is shifted over by the amount of irrecoverable closure. The unload curve, $\Delta V_{j\text{-}ue}$, is clipped at the desired normal stress, $[\Delta V_{j\text{-}ue}]_{max}$, and shifted back by the amount Δ to intersect the load curve, ΔV_j. The curve $\Delta V_{j\text{-}uf}$ is the final unload curve which intersects the load curve at the maximum normal stress of interest, $[\Delta V_j]_{max}$. Figure 72 presents the equations to compute this composite load/unload curve for the stress range of interest. This is one procedure to compute a load/unload curve for a required stress range. Barton (1982) suggests another procedure which consists of replacing V_m with the

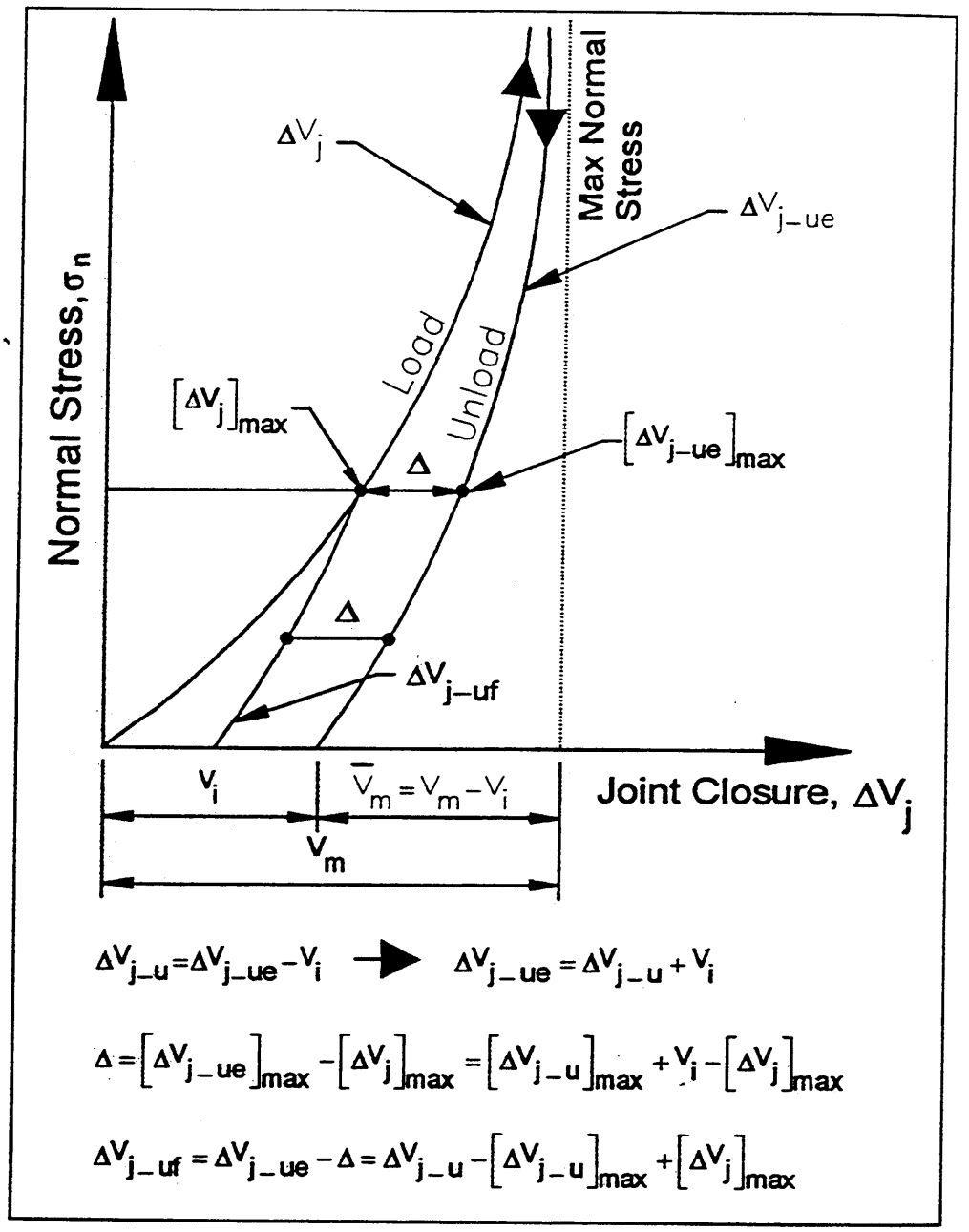

Figure 72. Construction of load-unload curve for cycle 1

closure associated with the maximum normal stress desired. Both procedures account for the dependency of the joint closure on the maximum normal stress applied to the joint.

The experimental data were fitted using the modified hyperbolic model, and the result is shown in Figure 73. The fit of the cycle one load/unload curve is shown in the top part of Figure 73. The middle figure shows the cycle two load/ unload curve added. Finally, the bottom figure shows all cycles of loading/ unloading. Note that the maximum closure is progressively less for each cycle.

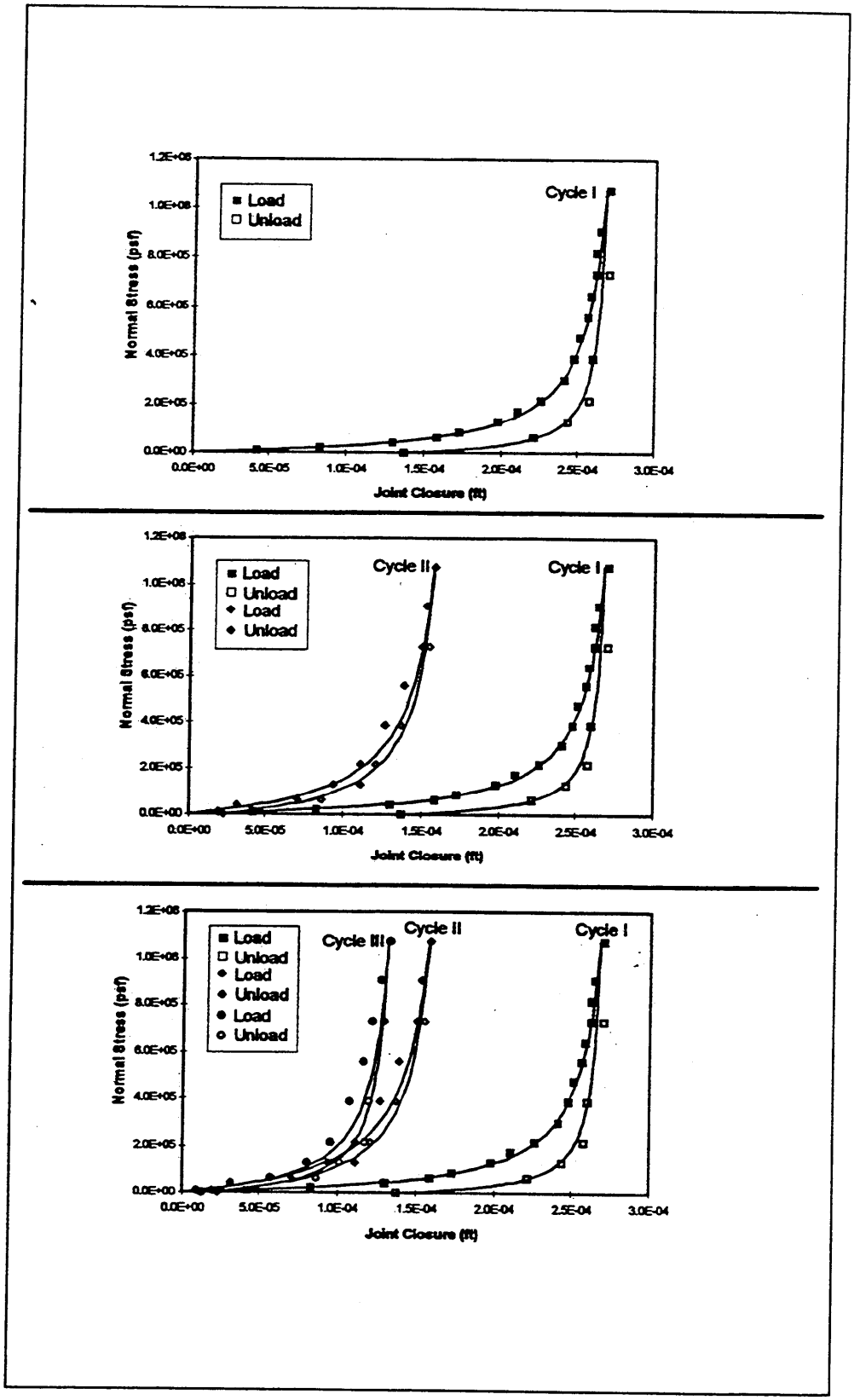

Figure 73. Hyperbolic fit of experimental data obtained for fresh dolerite (1 ft = 0.305 m, 1 MPa = 20,885.5 psf)

The model developed thus far for predicting joint closure has been for one cycle of full loading and unloading. Figure 74 shows three cycles of both full and partial loading and unloading . In an actual analysis, a joint may not experience full loading and unloading. The starting point for a partial unload curve may be computed by keeping track of the maximum normal stress of the previous cycle. A partial loading cycle would use the minimum normal stress of the previous unload cycle as a starting point.

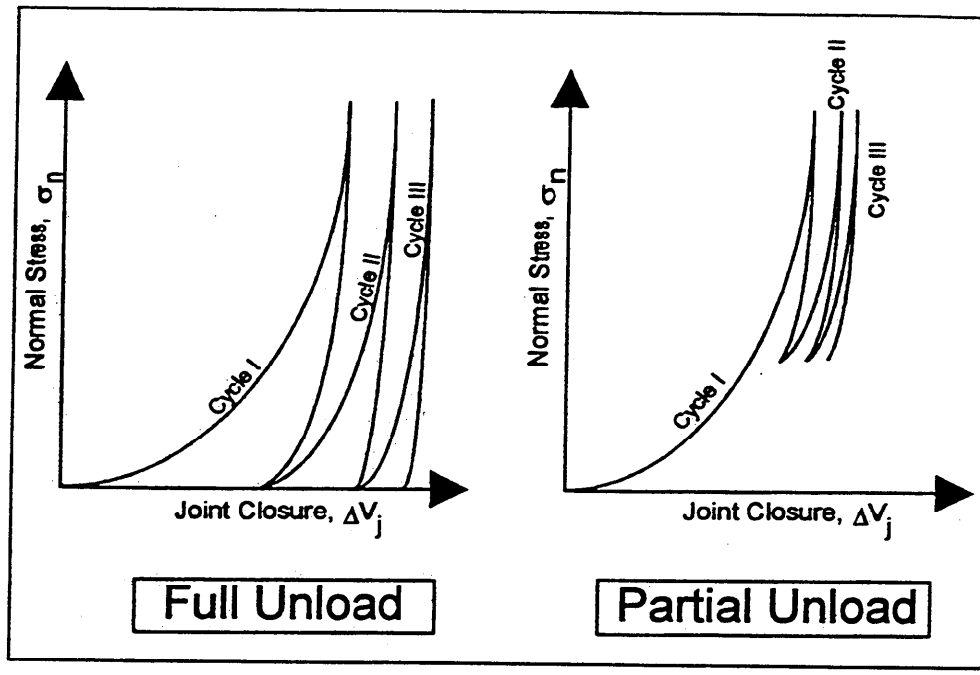

Figure 74. Subsequent cycles showing full and partial unloading

Generalizations About Rock Joint Closure Behavior

From the work performed by Bandis (1980), many observations can be made about the behavior of a rock joint as related to the properties of the rock and rock joint. The following list touches on some of these relationships to provide a better understanding of the behavior of rock joint closure:

a. The amount of maximum closure is generally less than the average initial joint aperture and is in the range of 0.3 to 0.9 times the average joint aperture.

b. Actual contact areas at maximum closure generally range from 40 to 70 percent of the total sample area.

c. The maximum closure, V_m, for samples with similar initial mechanical aperture, E_o, depend primarily on the joint compressive strength of the rock, *JCS*.

d. V_m decreases linearly as the joint roughness coefficient, *JRC*, increases irrespective of the *JCS*.

e. Weathered joints produced larger V_m than unweathered because the joints usually have larger E_o and lower *JCS* than similar unweathered joints.

f. V_m decreases exponentially with decreasing E_o and increasing *JCS*.

g. The normal stiffness, K_n, depends on aperture size, *JCS*, and *JRC* in that order of relative importance.

h. As the *JRC* of a joint increases, the initial normal stiffness, K_{ni}, increases.

i. K_n increases with increasing *JCS* and decreasing E_o.

j. The irrecoverable closure, V_r, decreases with increasing *JCS* and decreasing E_o.

Modeling of Joint Closure and Opening Using SOILSTRUCT-ALPHA

Finite element analyses were performed to examine the behavior of the rock joint beneath the structure shown in Figure 62 under varying normal loads due to raising and lowering of the pool elevation. The finite element program SOILSTRUCT-ALPHA (Ebeling, Duncan, and Clough 1990) was used to perform these analyses. This program is a general purpose finite element program for 2-D plane-strain analysis of soil-structure interaction problems. The program can accommodate incremental construction analyses. This version was developed to model the base separation of the dam from the foundation as discussed in Chapter 2.

The rock joint beneath the structure was represented by using the Goodman-Taylor-Brekke interface elements. This interface element is a four-noded element with adjacent pairs of nodes having the same coordinates; therefore, the element has zero thickness. The properties of this interface element are defined by an interface normal stiffness, k_n, and an interface shear stiffness, k_s. These stiffness values relate the average relative displacement of the interface element, either normal or tangential, to the corresponding incremental normal stress or shear stress for each increment in load as shown in Equations 44 and 45.

$$\Delta\sigma_n = k_n \Delta_n \tag{44}$$

$$\Delta\tau = k_s \Delta_s \tag{45}$$

The shear stiffness is represented by a hyperbolic shear stress-displacement relationship. The normal stiffness is represented as a linear response. To model the nonlinear normal stress versus joint closure relationship of the rock joint, the normal stiffness of the interface elements had to be adjusted based on the value of the normal stress and the loading cycle (which is applied incrementally). A bilinear fit of the hyperbolic model was used in the analyses. This bilinear fit is shown in Figure 75 for each cycle of load/unload. As seen in the figure, the second and third cycles of load/unload have essentially the same normal stiffnesses. Also, both the loading curve and the unloading curve have essentially the same normal stiffnesses. Therefore, the normal stiffnesses used for cycles two and three for both the loading and unloading curves were identical. This also implies that the joint seats after the second cycle and the response of the joint becomes elastic in nature under the range of normal stresses analyzed. Table 13 gives the criteria used to assign normal stiffnesses to the interface elements.

Example of Hydraulic Structure Interaction with Rock Foundation

Noorishad, Witherspoon, and Brekke (1971) and Brekke et al. (1972) conducted a study of a dam on a jointed foundation. This study concentrated on the differences in assuming a rigid network of joints versus a network of joints whose apertures were dependent on fluid flow forces. One of the example problems considered was a dam on a rock foundation. The rock foundation consisted of an orthogonal set of joints with a certain statistical distribution of joint aperture. The study concluded that the dependency of aperture size on flow forces should be considered and that the impact on uplift pressure distributions beneath a structure could be significant. The study undertaken and detailed in this discussion considers the effect of a single rock joint located beneath a dam and the impact of this joint on the structural stability of the dam. The dependency of the joint aperture on flow pressures and the effect of multiple loading cycles is taken into account.

Overview of finite element study

The loading sequence to model the gravity dam section shown in Figure 62 is shown in Figure 76. As shown in the figure, the initial condition (Case I) assumes a single rock joint in the foundation of constant aperture equal to 4.92×10^{-4} ft (150 μm). The rock joint is classified as a tight joint according to criteria sited in Lee and Farmer (1993), after Barton 1973) that states that an aperture of 3.28×10^{-4} ft (100 μm) to 8.20×10^{-4} ft (250 μm) is a tight joint. Case C depicts the construction of the dam in 13 lifts, which essentially compresses the rock joint across the entire width of the dam. The remaining load cases depict the subsequent raising and lowering of the pool elevations to produce three cycles of

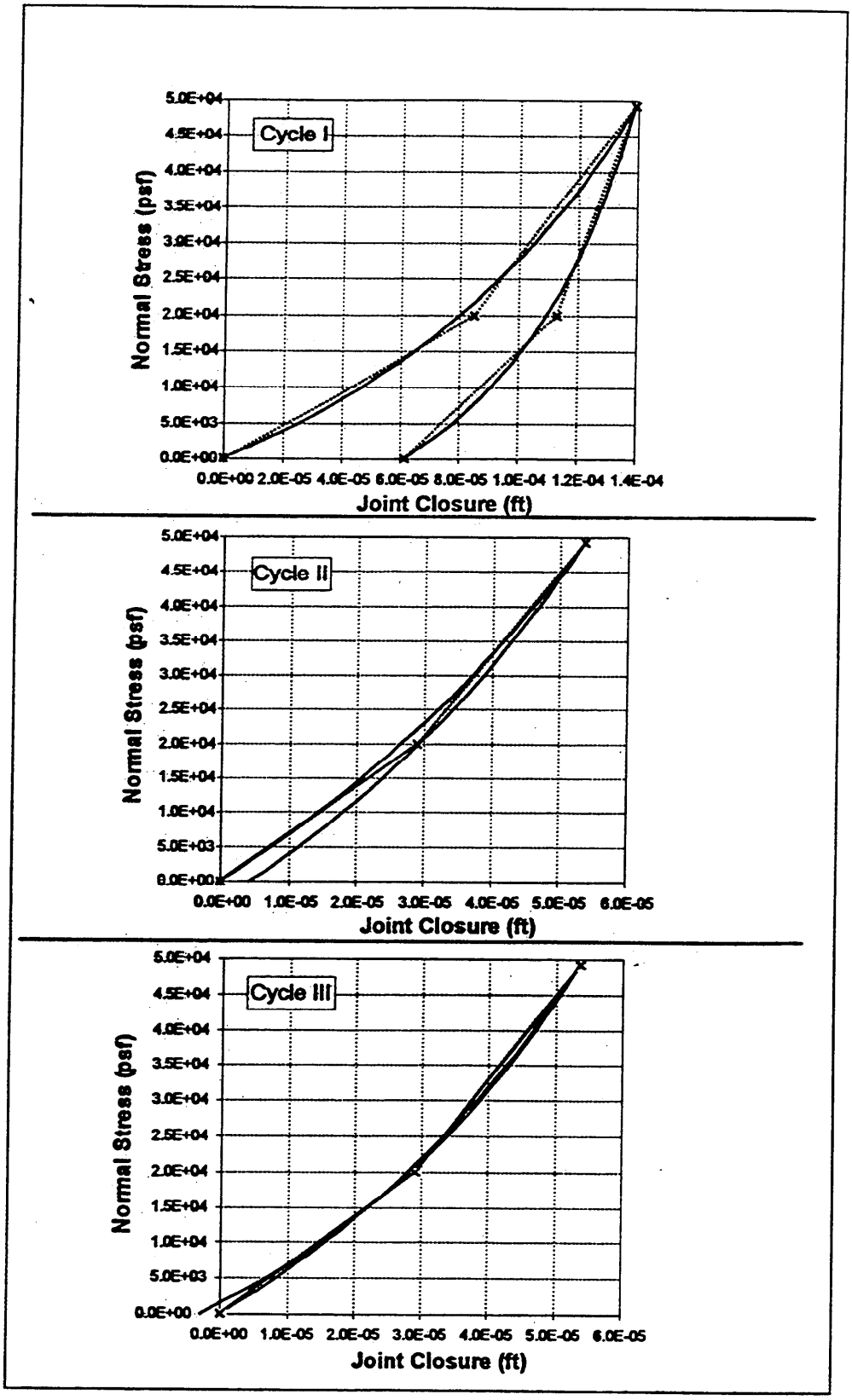

Figure 75. Bilinear fit of the hyperbolic joint model for use in finite element analyses (1 ft = 0.305 m, 1 MPa = 20,885.5 psf)

Table 13
Interface Normal Stiffnesses Used in Finite Element Analyses

Cycle	k_n (psf/ft)[1]			
	σ_n < 20,000 psf		σ_n > 20,000 psf	
	Load	Unload	Load	Unload
1	2.353×10^8	3.881×10^8	5.407×10^8	1.120×10^9
2	6.897×10^8	6.897×10^8	1.192×10^9	1.192×10^9
3	6.897×10^8	6.897×10^8	1.192×10^9	1.192×10^9

[1] 1 MPa/m = 6,365.9 psf/ft; 1 MPa = 20,885.5 psf.

load and unload. Cases P1R, P2R, and P3R depict the raising of the pool while cases P1L, P2L, and P3L depict the lowering of the pool. As pool P1R was raised, the rock joint opened at the heel and compressed at the toe from the condition in load case C. As the pool was lowered in load case P1L, the rock joint compressed at the heel and opened at the toe. This behavior continued through two more cycles of loading/unloading.

Representative rock sample used for analysis

A representative rock sample from Bandis' experimental work was chosen for use in the numerical model of uplift behavior. A sample was chosen that maximized the change in permeability of the joint with normal stress. The sample chosen was a "tight joint," which meant that the initial joint aperture was less that 8.2×10^{-4} ft (250 μm). The sample also possessed a large change in aperture (compared to the initial aperture) over the stress range of interest, thus resulting in a large change in permeability. A large change in permeability will produce the greatest change in uplift pressures developed in the rock joint. The effects of aperture size on rock joint permeability and uplift pressures is discussed more fully with examples in Ebeling and Pace (1996a, 1996b).

The rock sample chosen was a fresh dolerite with the following properties:

a. $E_o = 0.15$ mm.

b. $JCS = 182$ MPa.

c. $JRC = 8.8$.

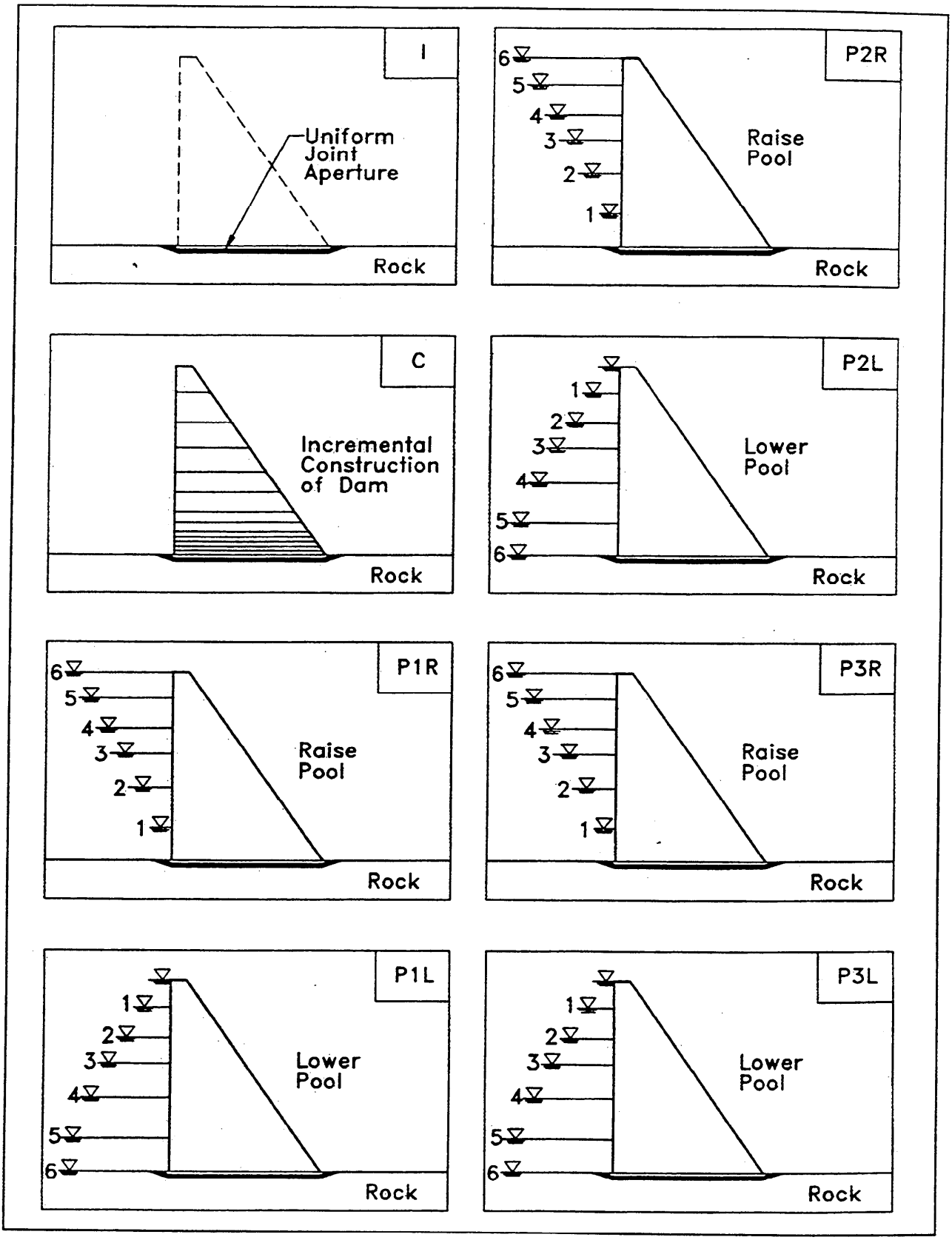

Figure 76. Load cases modeled in the finite element analyses

The *JRC* ranges from 0 (smooth) to 20 (rough), so a value of 8.8 could be classified as medium rough. The test results of this sample for three loading cycles is summarized in Table 14.

Table 14
Experimental Test Results for Dolerite Rock Sample[1]

Cycle	Maximum Closure (mm)	Permanent Set (mm)
1	0.081	0.042
2	0.041	0.007
3	0.035	0.004

[1] 304.8 mm = 1 ft.

Analytical concerns

The first concern that must be explored is the validity of the cubic law to predict flow within a rock joint. As discussed in Chapter 4, the cubic law is derived by assuming that the flow of water in a rock joint occurs between two smooth parallel plates. Many researchers have investigated this question over the years with varying conclusions. Iwai (1976) found that the cubic law is valid at low stress levels for natural, rough, uneven discontinuities when the discontinuity is open. From Iwai's research, flow in rock fractures was found to obey the cubic law if the aperture was larger than 6.562×10^{-5} ft (20 μm) and the Reynolds number was no greater than about 100. Witherspoon et al. (1980) concluded that the cubic law was valid for apertures down to 1.312×10^{-5} ft (4 μm), normal stresses up to 4.177×10^{5} psf (20 MPa), and fractures that were open or closed. Also, the results were not dependent on the rock type. Tsang and Witherspoon (1981) studied the hydromechanical behavior of a single horizontal rough-walled fracture. They concluded that the cubic law held if the effects of roughness were accounted for by replacing the fracture aperture with a statistical average. Gale (1982a) found that the cubic law broke down for rough deformable fractures subjected to stresses between 2.089×10^{5} psf and 3.133×10^{5} psf (10 and 15 MPa). Gale found that this maximum value of stress could be lower for natural fractures. Gale (1982b) found that the cubic law did not apply to rough, deformable, induced, or natural fractures when the residual apertures were computed on the basis of flowrates measured at stresses exceeding 6.266×10^{5} psf (30 MPa).

One fact that is very evident from the above-mentioned research is that is it very difficult to produce a completely closed fracture (the stress levels must be very high, approximately 4.177×10^{6} psf to 6.266×10^{6} psf (200 to 300 MPa) (Kranz et al. 1979). Several key factors that were considered by the various researchers were the levels of stress involved, the roughness of the rock apertures, and whether the fractures were open (no contact between adjacent walls) or closed (some contact between adjacent walls). For this study, the maximum normal stress applied to the foundation is approximately 6.266×10^{4} psf (3 MPa). Therefore, the cubic law is assumed to apply to our rock joint.

The next concern that must be addressed is the condition of flow within the rock joint. That is, is the flow turbulent or laminar? The cubic law assumes a linear relationship between the flow velocity and the pressure gradient and thus is valid only for laminar flow conditions. The condition of flow may be predicted by examining the Reynolds number and the roughness of the joint. As stated earlier, Iwai (1976) found from his research that laminar flow existed when the Reynold's number was no greater than 100. The Reynolds number at which turbulent flow initiates decreases with increasing aperture roughness. Wilson (1970) reported in his research that turbulent flow conditions occurred only when abnormally large fractures were subjected to abnormally large gradients. Louis (1969) performed extensive research of both laminar and turbulent flow conditions on smooth and rough joints. From his work, he established five regions of flow governed by varying flow laws. The regions of flow are delineated by a surface roughness index and the Reynolds number. The surface roughness index, S, is computed as

$$S = \frac{R_r}{D_h} \tag{46}$$

where

R_r = height of the surface asperities

D_h = equivalent hydraulic diameter, equal to $2a$.

a = average conducting aperture

The Reynolds number, R_e, for flow between parallel plates is equal to

$$R_e = \frac{2va}{\nu} \tag{47}$$

where

v = mean flow velocity

ν = kinematic viscosity

The Reynolds number defines the relationship of the inertial forces to the viscous forces in the flow region. The lower the Reynolds number, the more important the contribution of the viscous forces are to the flow. The higher the Reynolds number, the more important the inertial forces are to the flow and the more likely turbulence is to occur. For the problem under consideration, the Reynolds number is computed to be approximately 10; therefore, laminar flow is assumed to prevail.

The last concern involves the effect of surface roughness on the mechanical aperture. The mechanical aperture, E, is the actual aperture of the rock joint. This value is difficult to obtain due to the effects of surface roughness and

contact areas. Therefore, the effect of stress on aperture can be seen only through hydraulic testing to obtain a conducting aperture, e, that represents the true mechanical aperture, E. The theoretical conducting aperture derived according to the smooth parallel plate flow model is often considerably smaller than the true mechanical aperture. Flow channel tortuosity and roughness are probably responsible for the differences (Barton 1982). Barton (1982) proposed a relationship given by Equation 48 that relates the conducting to the mechanical aperture.

$$e = \frac{JRC^{2.5}}{\left(\frac{E}{e}\right)^2} \text{ in } \mu\text{m} \tag{48}$$

where

E = mechanical aperture (μm)

e = conducting aperture (μm)

JRC = joint roughness coefficient

Equation 48 was formulated in SI units and is valid only if E is greater than or equal to e within a range of 1μm (3.281×10^{-6} ft) to 1,000μm (3.251×10^{-3} ft). This relationship was used in this study and accounts for the effects of surface roughness and tortuousity.

Discussion of analysis procedure

With the assumptions that the example problem possesses laminar flow and that the cubic law is valid, the fluid pressures within the rock joint can be computed. The following discussion will highlight the major steps involved in the analysis procedure. The properties used in the analyses are given in Table 15. The properties of the interface elements were previously discussed and are given in Table 13 and shown in Figure 75.

Table 15
Properties of Concrete and Rock Used in Finite Element Analyses

Structure	Unit Weight (pcf)[1]	Modulus of Elasticity (psf)	Poisson's Ratio
Concrete Dam	150	5.04×10^8	0.2
Rock Foundation	0	5.04×10^8	0.2

[1] 0.157 kN/m³ = 1 pcf, 1 MPa = 20,885.5 psf.

A value of 0 pcf (0 kN/m³) for the unit weight of the rock foundation was used because deformations from the gravity turn-on analysis were not desired. The rock foundation was assumed to be in place with a rock joint of a specific size.

The composite modulus assigned to the rock foundation was determined using relationships developed by Benson (1986) as discussed in Chapter 2.

Figure 76 shows the load cases, and Figure 77 shows the six pool elevations that were considered in the analyses. As shown in Figure 77, the changes in pool elevations were approximately 50 ft (15.24 m). Figure 78 shows the finite element grid used in the analysis which consists of 1,868 nodes, 1,775 elements, and 29 interface elements located at the base of the dam. Figure 79 shows the lift numbers and lift elevations on the structure for load case C. Figure 80 shows both the pool elevations and construction lifts of the dam.

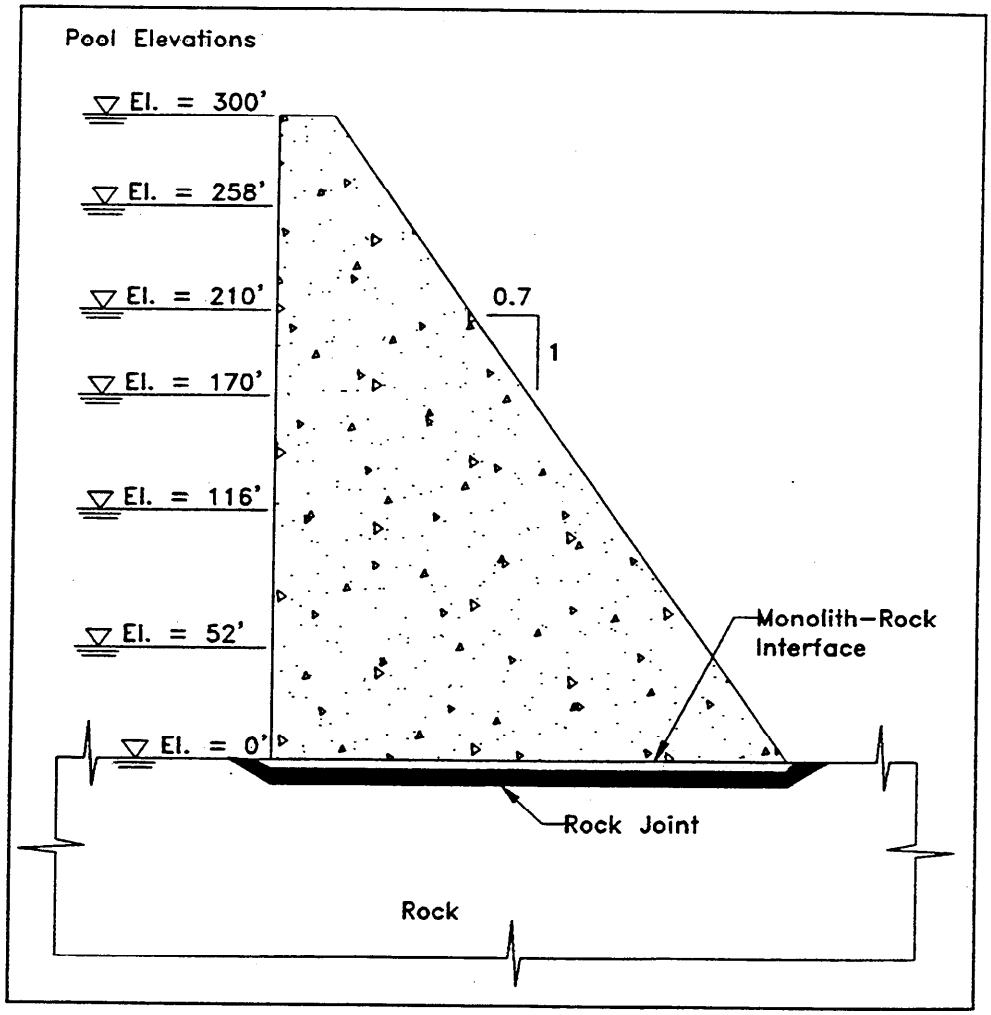

Figure 77. Pool elevations used in the analysis to model the raising and lowering of the reservoir (1 ft = 0.305 m)

The dam was incrementally constructed in 13 lifts with smaller lift heights being used at lower elevations progressing to larger lift heights at higher elevations. Smaller lift heights were used initially to prevent artificially large stress gradients at the corners of the structure (refer to Chapter 2). Small lifts must be used while the structure is still "flexible," and larger lifts may be used after the

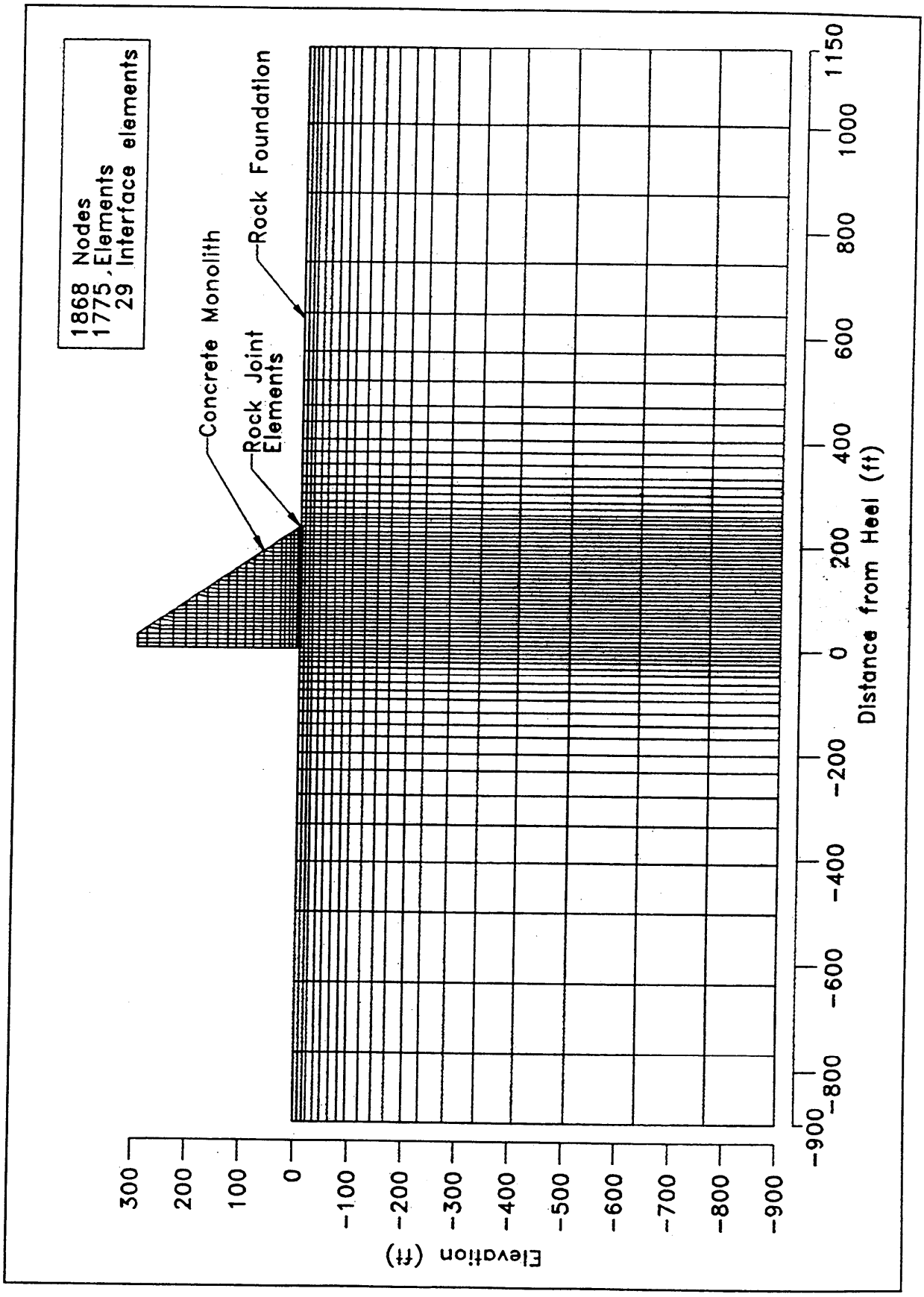

Figure 78. Finite element mesh used in analyses (1 ft = 0.305 m)

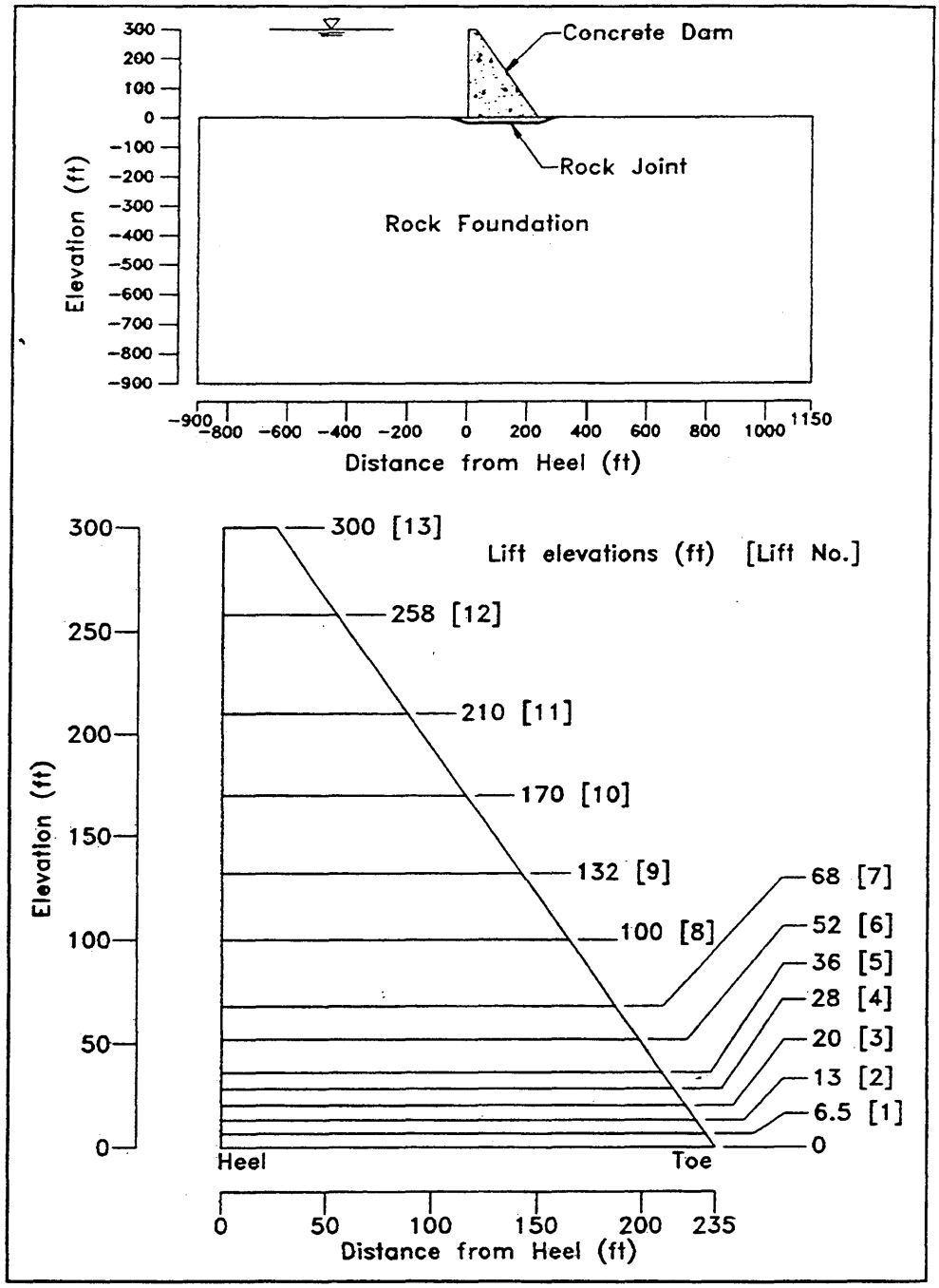

Figure 79. Elevations used in the analysis to model the incremental construction of the dam (1 ft = 0.305 m)

structure has obtained sufficient height to produce a stiffer structure. Both the rock foundation and dam were modeled as linear elastic materials. The interface representing the rock joint was modeled using a bilinear stress-displacement relationship as discussed previously.

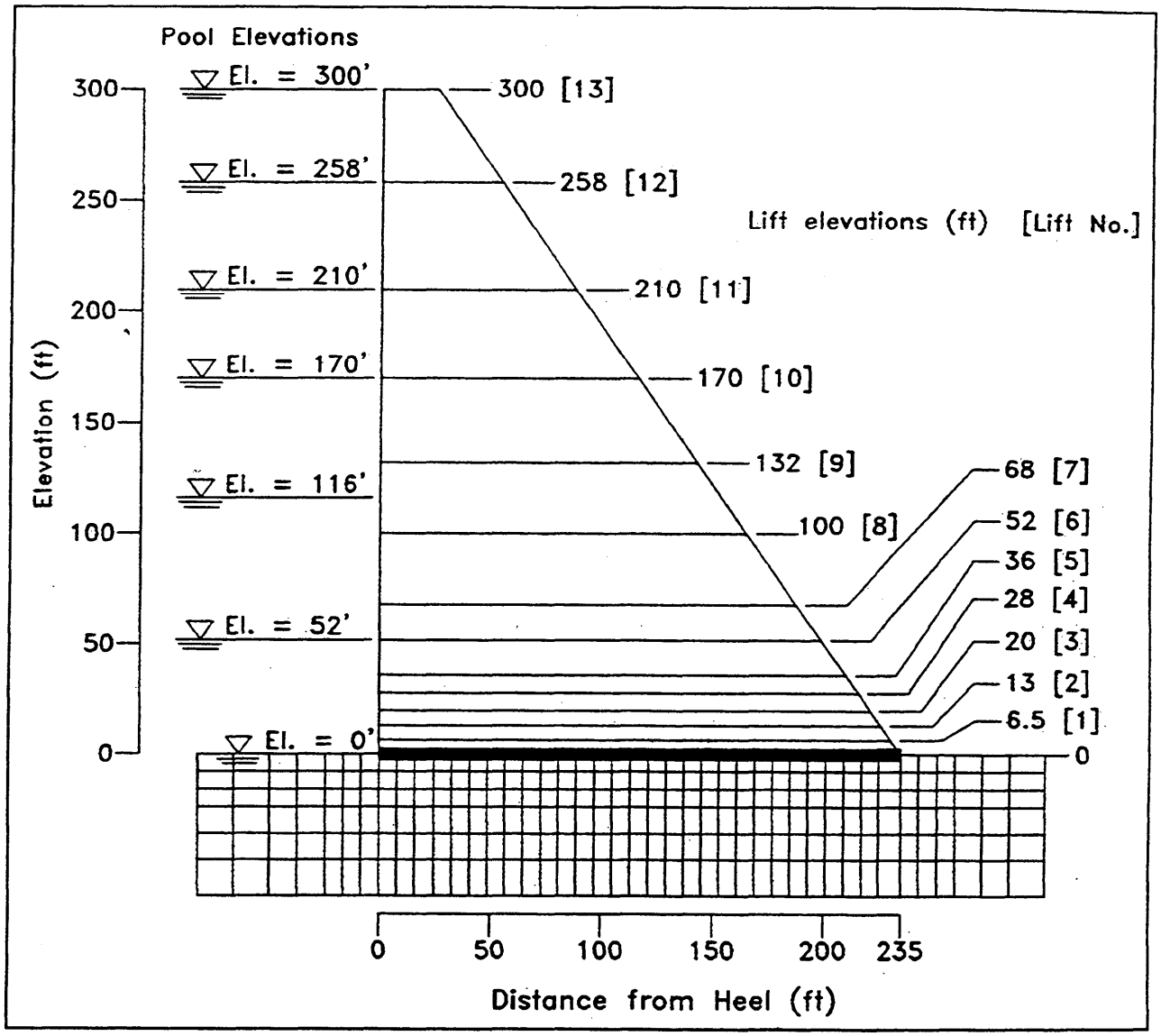

Figure 80. Construction lifts and pools increments used in analyses (1 ft = 0.305 m)

After the dam was constructed, the pool elevations were raised and lowered incrementally. The uplift pressure distribution for each pool elevation was determined by accounting for the changes in rock joint aperture caused by changes in normal stresses on the dam foundation. The uplift pressures were applied upward on the dam and downward on the rock foundation. The permeability of each of the interface elements used to model the rock joint was re-evaluated when there was a change in the aperture of the rock joint. The 1-D steady-state flow analysis of the rock joint was performed using these new values of permeability. This resulted in a change in uplift distribution along the rock joint, even for the case of constant elevations of reservoir and tailwater. The steps involved in determining the correct uplift distribution for a pool elevation is summarized in Figure 81. The cubic law relationship given Chapter 4 is used to compute the permeability, k, of the rock joint as

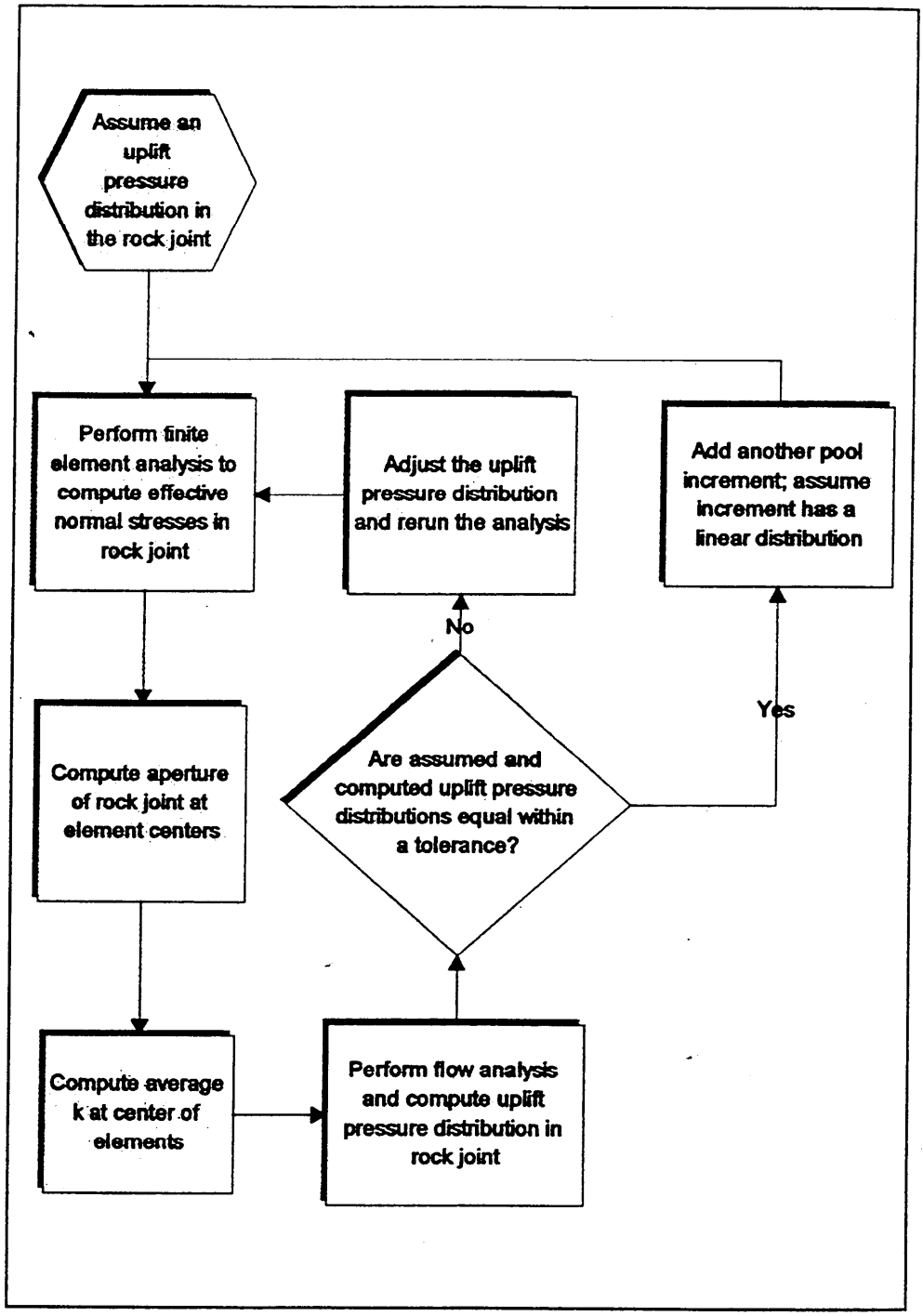

Figure 81. Analysis procedure for computing uplift pressure distribution in rock joint

$$k = \frac{\gamma_w e^2}{12\mu} \tag{49}$$

where

e = conducting aperture of the rock joint

γ_w = unit weight of water

μ = dynamic viscosity

Only the permeability of the rock joint was considered in this analysis. The matrix permeability of the rock was not included. Matrix permeability is only important if there are no continuous rock joints or the rock joint apertures are less than 3.28×10^{-5} ft (μm) (Louis 1969).

As the pool elevations were raised and lowered, the rock joint was loaded and unloaded as shown in Figure 82 for a total of three cycles. The heel experienced full unload and reload while the toe only experienced a partial load and unload. For a specific cycle, the mechanical aperture, E, is calculated as

$$E = E_{on} - \Delta E \tag{50}$$

where

E_{on} = initial mechanical aperture at the start of cycle n

ΔE = change in aperture computed from the joint closure curve

Equation 50 computes the mechanical aperture of the rock joint. Using this aperture in Equation 48 produces the conducting aperture of the joint. The conducting aperture was computed for interface elements across the width of the dam. Using the conducting aperture, Equation 49 was used to compute the permeability of the joint. A 1-D steady-state finite element flow analysis computer program was used to compute the uplift pressure in each interface element. The uplift distribution computed was compared to the assumed distribution as shown in Figure 81,and the distribution was adjusted and the analysis rerun if necessary. This procedure was used for each pool increment and decrement of loading.

Discussion of analysis results

Figure 83 shows the distribution of base pressures computed within the interface elements after construction of the dam. The base pressure distribution is nonlinear. Recall that a linear base pressure distribution is assumed in the conventional equilibrium analysis (EM 1110-2-2200). The largest base pressure is

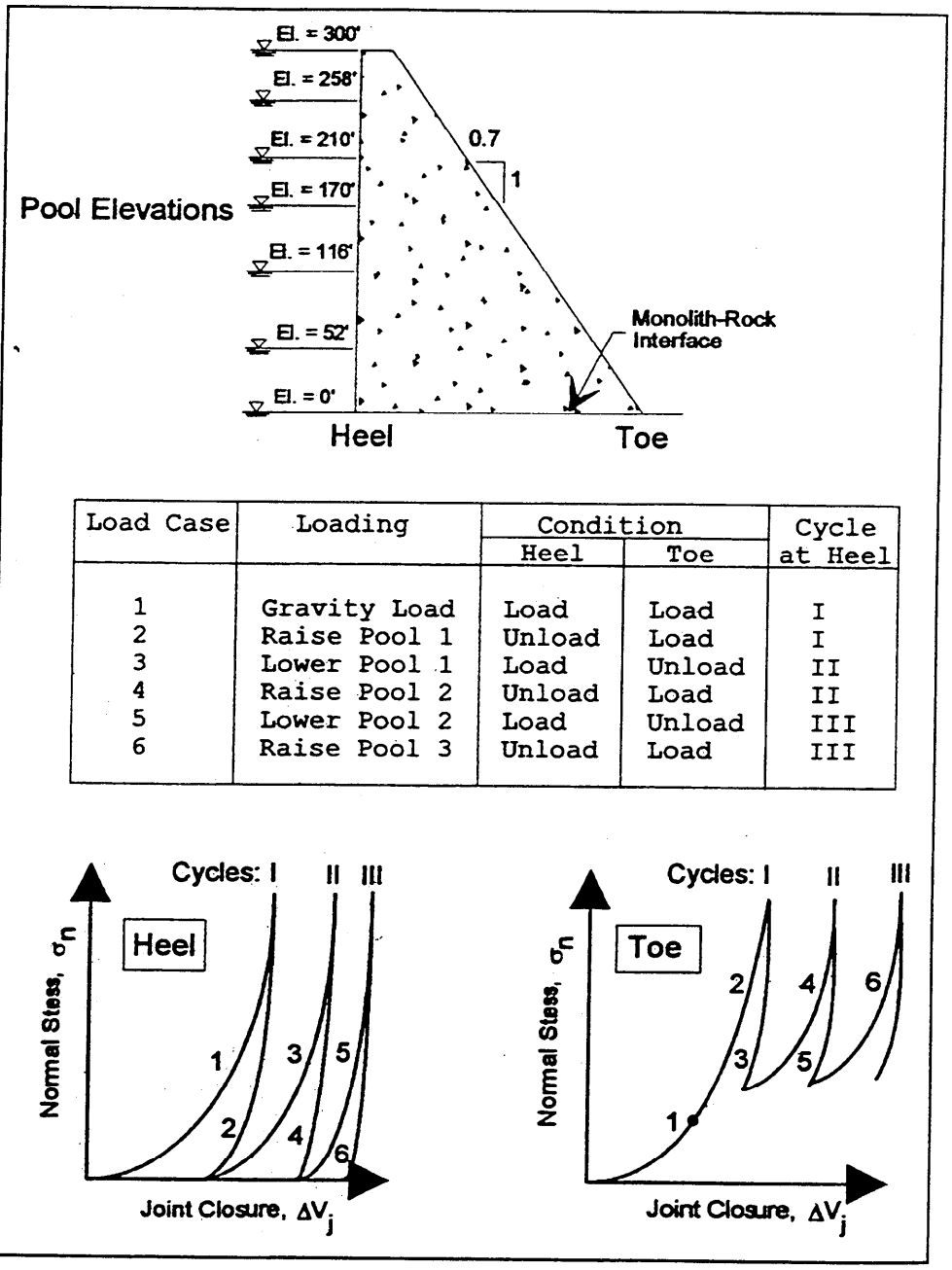

Load Case	Loading	Condition		Cycle at Heel
		Heel	Toe	
1	Gravity Load	Load	Load	I
2	Raise Pool 1	Unload	Load	I
3	Lower Pool 1	Load	Unload	II
4	Raise Pool 2	Unload	Load	II
5	Lower Pool 2	Load	Unload	III
6	Raise Pool 3	Unload	Load	III

Figure 82. Sequence of loading cycles performed in finite element analyses (1 ft = 0.305 m)

computed below the heel of the dam, consistent with the concentration of mass within this region of the dam. The distributions of vertical stresses computed within the 2-D elements located directly above and directly below the dam-to-foundation interface region are also shown in this figure. Close agreement is seen in Figure 83 among the three vertical stress distributions.

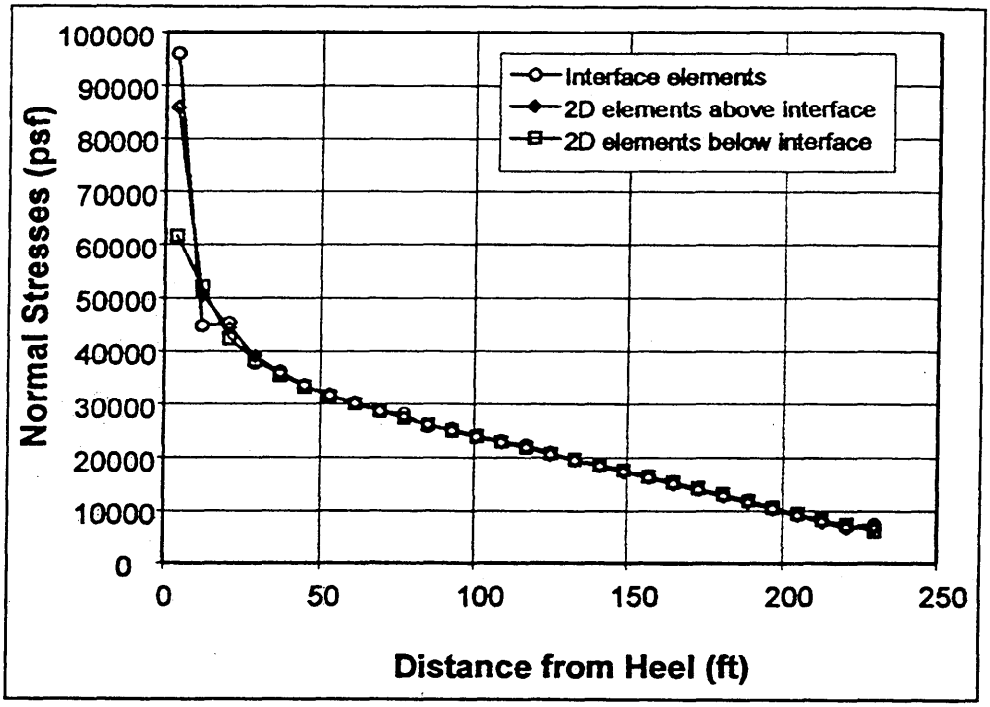

Figure 83. Normal stresses at end of construction for elements above, at, and below the interface (1 ft = 0.305 m, 1 MPa = 20,885.5 psf)

The distribution of normal stresses across the base of the dam is shown in Figure 84 for the various stages of loading. This base pressure distribution is nonlinear and differs from the assumed linear distribution shown in Figure 62. The construction of the dam and lowering of the pool elevations produce higher compressive stresses at the heel of the dam than the toe. Conversely, raising of the pool elevations produces lower stresses at the heel of the dam than the toe. Note that the raising of the pool to the top of the dam causes the base of the dam to separate from the foundation (zero normal stresses). The dam separates for a distance of approximately 49 ft (14.93 m) or 21 percent of the base width. Full uplift pressures are applied to this region consistent with Corps design guidance (EM 1110-2-2200). Upon lowering of the pool, the heel of the structure contacts the foundation again producing compressive stresses at the heel.

Figure 85 shows the variation of the mechanical aperture across the width of the dam. As seen from the figure, the construction of the dam causes a decrease in the rock joint aperture across the dam with a larger decrease at the heel. The raising of pool 1 (load case P1R) causes the heel to separate from the foundation and the aperture of the rock joint at the toe to decrease. When the pool is lowered, the rock joint aperture does not return to the after-construction condition because the joint is stiffer. The stiffness of the joint increases with each loading cycle, as shown in Figure 75 and Table 13.

The distribution of uplift pressure across the base of the dam is shown in Figure 86 for several intermediate pool elevations and reservoir filling/emptying

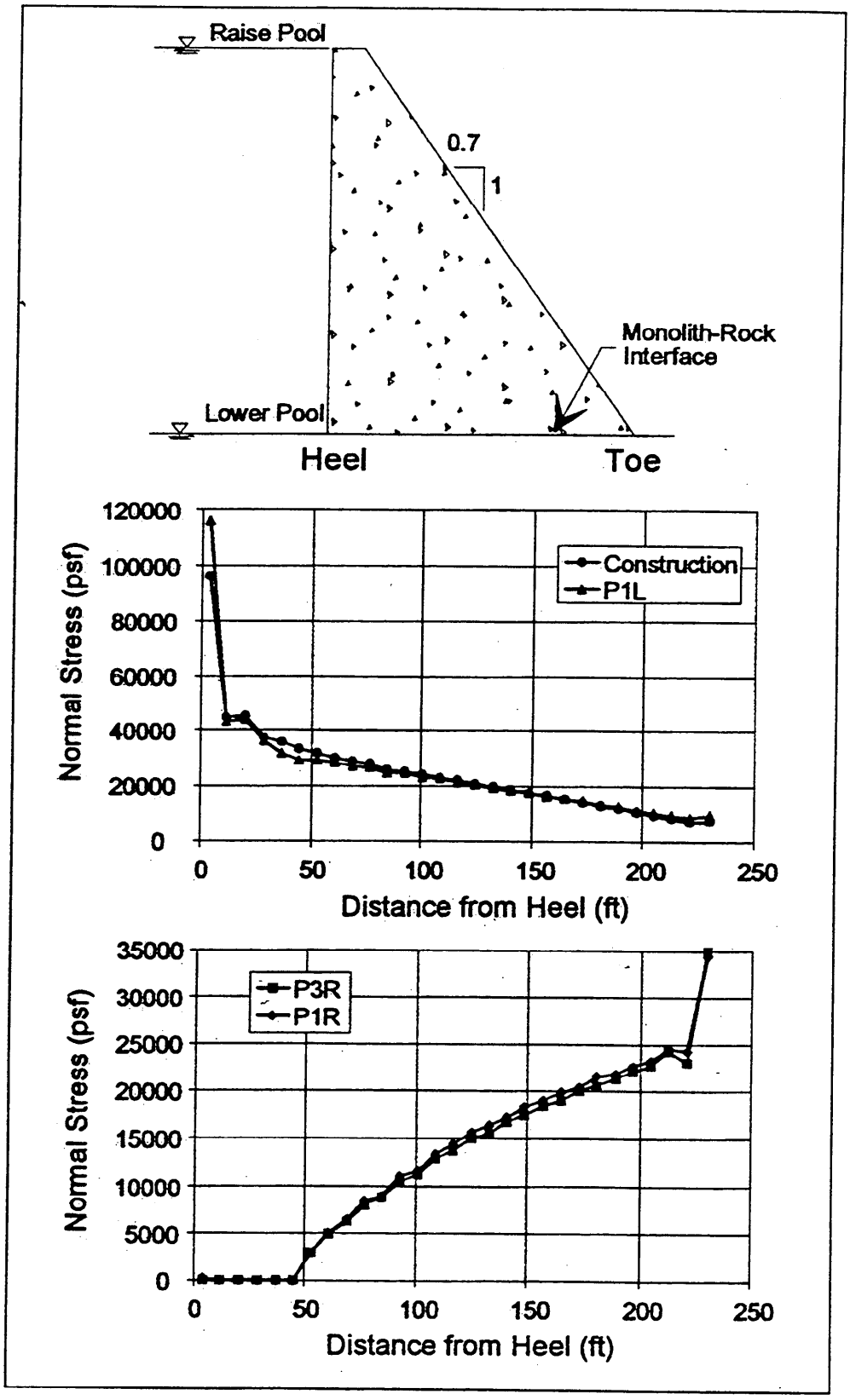

Figure 84. Plots of the normal stresses in the interface elements for various stages of loading (1 ft = 0.305 m, 1 MPa = 20,885.5 psf)

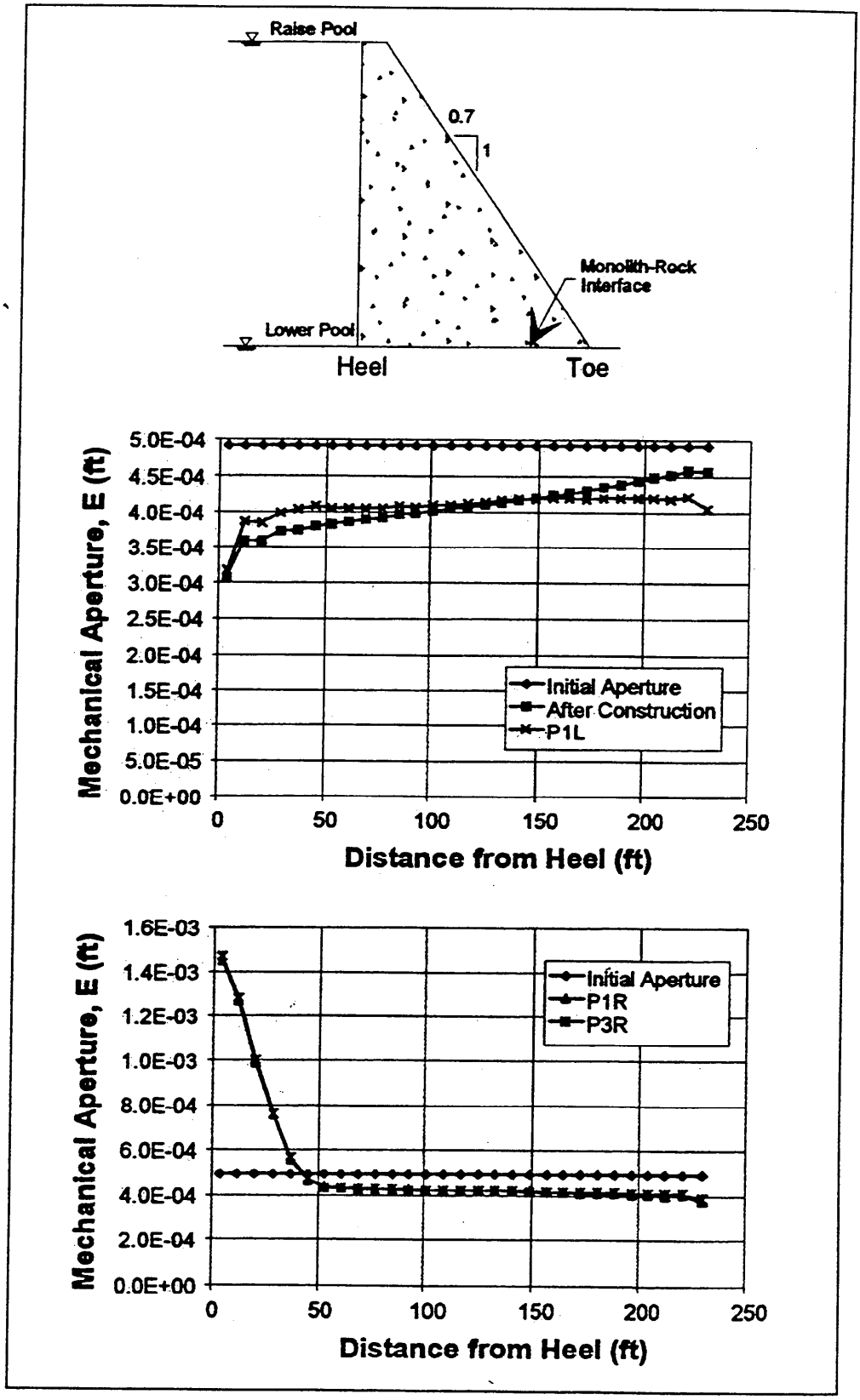

Figure 85. Variation of mechanical aperture across the monolith-rock interface (1 ft = 0.305 m)

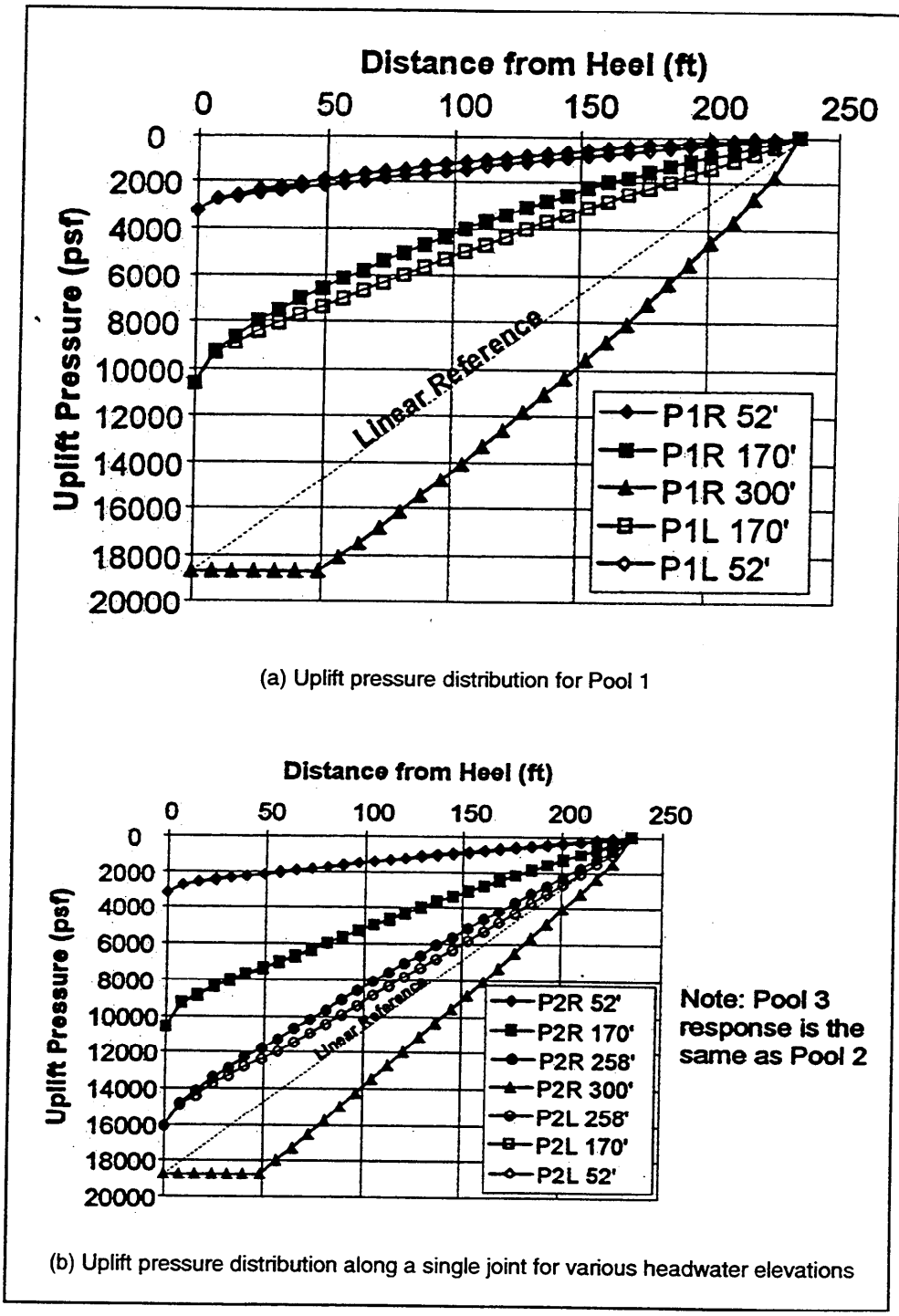

Figure 86. Uplift pressure distribution along a single joint for various headwater elevations (1 ft = 0.305 m, 1 MPa = 20,885.5 psf)

cycles. All distributions of uplift pressures shown in this figure are nonlinear. The distributions of uplift pressure for the intermediate pool elevations (corresponding to pool elevations of 170 ft (51.81m) or less) are concave upward, reflecting a joint taper increasing in the direction of flow. This uplift pressure distribution is more favorable to the stability of the dam than the nonsite-specific linear uplift pressure distribution given in EM 1110-2-2200. Conversely, the top pool elevation of 300 ft (91.43m) produces a concave downward distribution of uplift pressure, reflecting a joint taper decreasing in the direction of flow. For this case, full uplift pressures are applied across the interface region which has separated from the rock foundation (i.e., the region of zero normal effective base pressure), consistent with Corps design criteria. This uplift pressure distribution is less favorable than the conventional linear assumption. The uplift pressure distribution is dependent on the initial joint aperture which provides the starting point for aperture changes. In this study, the initial joint aperture was assumed to be a constant value. The final uplift pressure distributions could vary significantly dependent upon the initial apertures assumed. As noted previously, a study of the uplift pressure distribution in a tapered joint is described in Ebeling and Pace (1996a).

Figure 86 also shows that the magnitude of the uplift pressure distribution increased slightly due to performance of the joint during the multiple loading/unloading cycles. The results shown in Figures 86 are distinctly nonlinear. Note that had the changes in aperture of this tight joint been negligible during the raising and lowering of the reservoir, there would have been no change in uplift pressure distribution with load/unload cycles. Additionally, if the aperture was a constant value, the distribution of uplift pressures would be linear and consistent with the linear nonsite-specific uplift pressure distribution given in EM 1110-2-2200.

The uplift head at specific locations on the base of the dam is seen to vary nonlinearly with uplift head as shown in Figure 87. The heel and the toe vary linearly because boundary conditions (i.e., reservoir and tailwater pressure heads) are specified at these locations. Intermediate points on the base of the dam vary nonlinearly with head reflecting the effect of changes in the aperture of the tight joint due to the raising and lowering of the reservoir. The pressure head also increases at a particular point with increased loading cycles. Load cases P2 and P3 produce identical pressure distributions because the normal stiffnesses were identical for these cycles. Note that had the changes in aperture of the tight joint been negligible during the raising and lowering of the reservoir, the results shown in Figure 87 would have been linear.

Effect of rock joint on dam stability

The effect of considering the separation of the gravity dam from the rock foundation and the variation of uplift pressures with rock joint apertures produced the following differences from the conventional analysis shown in Figure 62:

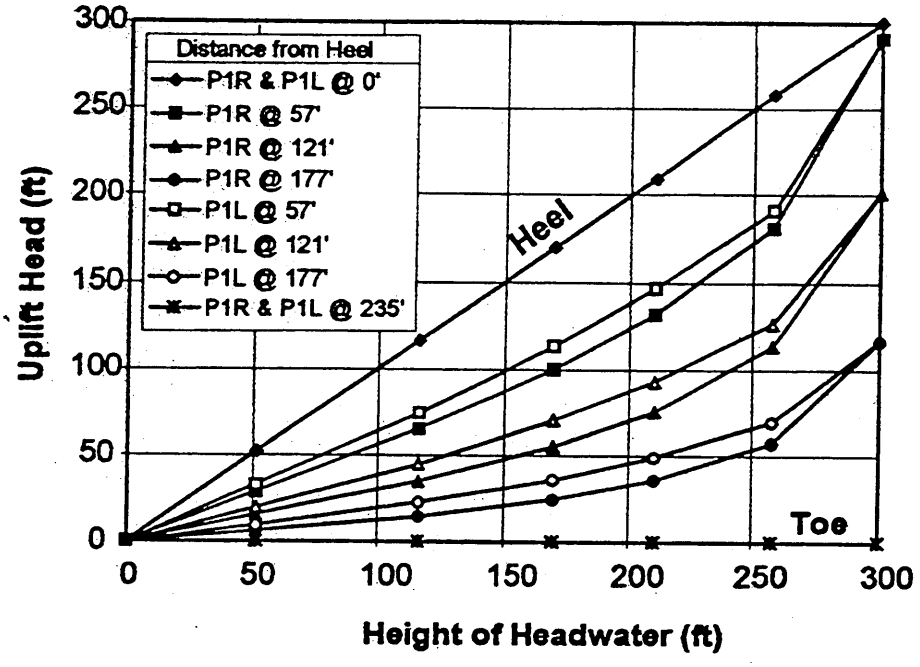

(a) Variation of uplift head for Pool 1

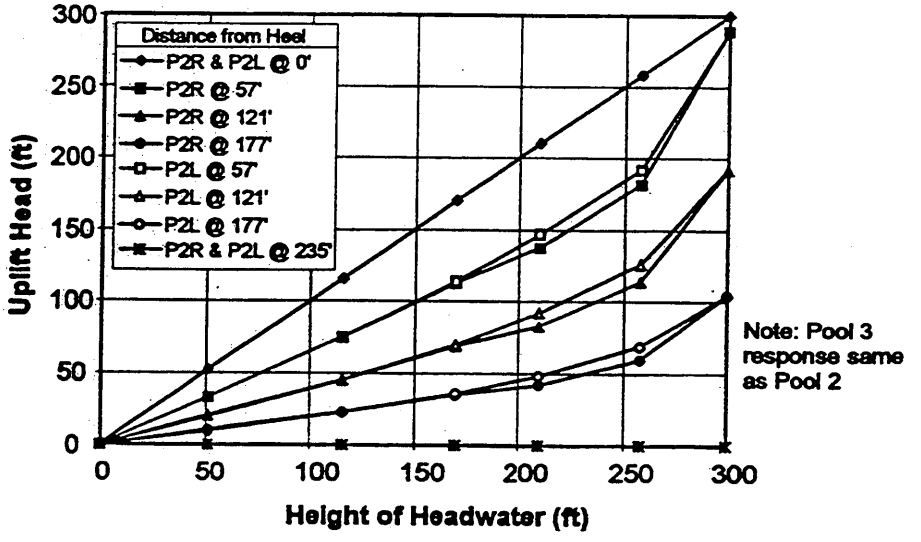

(b) Variation of uplift head at five locations along the joint headwater elevation

Figure 87. Variation of uplift head at five locations along the joint with headwater elevation (1 ft = 0.305 m)

a. The conventional analysis assumed a linear non-site-specific pressure distribution with a pressure head value of 300 ft (91.43 m) (full pool) at the heel varying linearly to 0 ft (0 m) at the toe. The final pressure distribution from the finite element analyses is shown in Figure 86. The magnitude of the uplift force computed from this distribution is 2,837 kips (12,619.6 kN). The magnitude of the uplift force computed from the conventional analysis is 2,200 kips (9,786 kN). This corresponds to a 29-percent difference in the uplift force. This large difference is due to the increase in uplift force resulting from the separation of the dam from the foundation.

b. The dam was designed using criteria that resulted in 100 percent of the base of the dam being in compression; therefore, the resultant of the base pressures lies within the middle third of the base of the dam. The finite element analysis resulted in approximately 79 percent of the base of the dam being in compression.

c. In this study, the example dam was subjected to a more severe loading in terms of pool elevation than the normal operating condition. EM 1110-2-2200 provides for a decreased percentage of the base of the dam in compression for more severe (i.e., higher pool) but infrequent loadings. For an unusual loading condition (e.g. standard project flood) or an extreme condition (probable maximum flood) EM 1110-2-2200 requires that the resultant of the base pressures lie within the middle half or within the base, respectively. Therefore, for this study conventional stability criteria are satisfied because the resultant is within the middle half of the base of the dam. The comparisons presented here demonstrate variations that can be obtained from using conventional stability criteria and using a more comprehensive analysis procedure. For this study, a more severe loading (higher pool) was used in the analyses to study the effects of the separation of the base of the dam from the foundation. The separation of the base of the dam from the foundation produced uplift pressures that were greater than pressures computed using a linear uplift pressure distribution. Had the dam not separated from the foundation, the uplift pressures would have been less than the pressures computed using a linear uplift pressure distribution.

Conclusions

The analysis presented in this chapter resulted in several lessons being learned about the application of the empirical equations developed by Bandis for representing the behavior of rock joints subjected to normal loads. First and foremost, a better approximation of V_m is needed. This parameter greatly affects the hyperbolic fit of the experimental data. The empirical equations sometimes overpredict or underpredict the values of V_m and K_{ni}. The equations have been found to be very good for predicting trends based on parameters that are readily computed from simple field and laboratory tests. If experimental or field data are available, the use of this data is preferred in developing a hyperbolic model representing the normal stress versus joint closure behavior of a rock joint. Use of the improved

rock joint closure/opening model that was developed during this study is recommended.

An analysis as described in this chapter that models the dam, rock joint, and foundation interaction can account for the coupled behavior between rock joint aperture, normal loading, and uplift pressures. The study did not include the effects of shear-induced dilatancy, but a more complete analysis would need to account for the coupled behavior between normal loading and dilatancy caused by shear. Further study is planned to incorporate both the effects of normal and shear stresses on the rock joint aperture and the associated effects on uplift pressures.

The study demonstrates that the rock joint aperture can at times produce favorable or unfavorable uplift pressure distributions compared to the conventional non-site-specific linear assumption given in EM 1110-2-2200 depending upon the reservoir levels. The uplift pressure distribution depends upon the direction of the taper of the joint. The behavior of the rock joint produced nonlinear uplift pressure distributions across the base of the dam and also produced nonlinear changes in pressure head at specific locations on the base due to changes in pool elevations. This behavior is consistent with observations made on existing gravity dams (Stone and Webster 1992).

Nonlinear uplift pressure distributions result from a varying rock joint aperture. If the rock joint aperture was a constant value along the entire joint, the uplift pressure distributions would have been linear. Nonlinear changes in the pressure head at a point on the base of the dam result from aperture variations due to changes in normal stresses caused by varying pool elevations. If the distribution of rock joint aperture remained constant (i.e., a single value or tapered variation) throughout the raising and lowering of the pool elevations, the pressure head at a point would have varied linearly with changes in pool elevations. It is the varying of rock joint aperture with normal stresses that produce the nonlinear changes.

Using an analysis procedure that accounts for the stiffness of the dam, rock foundation, and rock joint and the variation of the rock joint aperture with normal stresses provides insight into the variation of uplift pressure distribution with normal loading. This coupling of rock joint aperture with developed uplift pressures is absent from the conventional analysis procedures. The size and distribution of the rock joint apertures can play a significant role in the development of uplift pressures exerted on the base of a dam and therefore influence the stability of the structure.

6 Summary and Conclusions

The U.S. Army Corps of Engineers is responsible for designing and maintaining a large number of navigation and flood-control structures. Many of the older massive concrete gravity hydraulic structures are routinely being examined (e.g., during periodic inspections) to determine if loadings have changed from those used in stability calculations showing that the structure meets stability criteria (required of new hydraulic structures). The engineering procedures discussed in this report are intended to be applied to those hydraulic structures which do not meet the current Corps' criteria prior to embarking on remediation and/or rehabilitation.

Calculating Safety of Rock-Founded Massive Concrete Gravity Structures

The procedures currently used for evaluating the safety of existing massive hydraulic structures are the conventional equilibrium methods. These methods are the same general methods used in the design of these structures. These engineering procedures have been used for decades by civil engineers to design new hydraulic structures and analyze existing structures. The conditions of equilibrium are insufficient for a complete analysis of all aspects of structure-foundation interaction involved in the stability and performance of these structures (soil-structure-foundation interaction in the case of earth retaining structures). Therefore, conventional equilibrium methods necessarily involve assumptions regarding aspects of the loading forces and the resisting forces that act on the hydraulic structures.

Although the conditions and assumptions employed in the conventional equilibrium-based design methods are generally accepted as providing reasonable engineering procedures and although there have been few reported failures of hydraulic structures designed using these procedures, there is some uncertainty concerning their accuracy. Differences between actual field performance and calculations from conventional analysis have been noted for some existing hydraulic structures. Conventional design methods were developed based largely on classical limit equilibrium analysis without regard to deformation-related concepts. Today, analytical tools such as the finite element method are available which consider the manner in which the loads and resistance are developed as a function of the stiffnesses of the foundation rock, the structure-

foundation interface, and rock joints within the foundation. These analytical tools are discussed in Chapter 2 and were used to evaluate the conventional equilibrium-based design methods used to evaluate the safety of an existing hydraulic structure, Locks 27 Monolith 7E.

The results of the following load base-case analyses of Locks 27 Monolith 7E using SOILSTRUCT-ALPHA with interface elements, the discrete crack analysis using MERLIN, and the smeared crack analysis using CG-DAMS showed the conventional equilibrium analysis to be conservative. For example, the values of B_c/B computed using the three finite element analyses were within 2 percent of each other and averaged 72 percent, while the conventional equilibrium analysis resulted in 48.6 percent base area in compression. Secondly, all three finite element analyses resulted in nonlinear normal effective stress distributions, contrasting with the assumed linear stress distributions assumed in the conventional equilibrium analysis.

The results of the parametric study of effects of initial stress distributions within the lock wall on the results of the following load analyses of Locks 27 Monolith 7E gravity retaining wall showed the magnitude and distribution of initial stresses computed along the lock-wall-to-rock-foundation interface to be dependent on the method used for computing the effects of self-weight of the monolith. The incremental build-up analysis of the concrete monolith is the preferred method of analysis since it has been shown in case studies of instrumented retaining structures to provide more accurate results than those obtained through use of a gravity turn-on analysis (Clough and Duncan 1969).

Two methods are used to model the rock foundation. One approach is to account for the flexibility of the rock foundation by assigning the stiffness to a jointed rock foundation using empirical relationships that account for both the type of rock and the jointing within the rock mass comprising the foundation. The first approach uses a composite stiffness based on the stiffness of the intact rock along with the effects of jointing within the rock foundation and the effects of the deformations at rock joints. This approach was used in the analyses described in Chapter 2. The results of the parametric studies of composite rock foundation stiffness on the following load analyses of Locks 27 Monolith 7E gravity retaining wall showed that different initial stress distributions along the lock-wall-to-rock-foundation interface result in differences among the interface stress distributions after application of the following loads. However, the values of B_c/B computed after application of the following loads in the three analyses were nearly the same, with less than a 3-percent difference.

Downdrag on Backs of Rock-Founded Concrete Gravity Retaining Walls

Prior to 1994, the traditional assumption employed in the conventional equilibrium-based method for the design of rock-founded massive lock walls that retain earth was that the backfill exerts lateral earth loads corresponding to at-rest

conditions in the backfill and no shear along the backfill-to-wall interface. Calculations reported in Chapter 3 show that the assumption of zero shear force along the soil-wall interface is conservative. The calculation of the downdrag or shear forces on the backs of rock-founded concrete gravity retaining walls is discussed in this chapter. The calculation of this stabilizing shear force by use of a simplified procedure or by a complete soil-structure interaction analysis is discussed. These procedures are restricted to walls with engineered backfills that do not creep.

Calculation of Uplift Pressures Along Base of Monolith

A key stage in a stability evaluation of lock monoliths is the calculation (or assignment) of uplift pressures along the base of the hydraulic structure and/or along a critical rock joint or joints within the foundation. Using accurate piezometric instrumentation data at a site along with knowledge of the site geology is the preferred method for establishing uplift pressures. However, when instrumentation data are not available or when the reservoir levels to be analyzed exceed those for which the piezometric measurements were made, other procedures must be used to establish the distribution of flow and the corresponding uplift pressures. Four procedures are widely used by engineers to establish the uplift pressures along an imaginary section or sections through the structure-foundation interface and/or along a section or sections within the rock foundation. These four procedures are (a) a prescribed uplift distribution as given, for example, in an engineering manual specific to the particular hydraulic structure; (b) uplift pressures computed from confined, 1-D steady-state flow within a rock joint of constant aperture; (c) uplift pressures resulting from confined, 1-D steady-state flow within a tapered rock joint; or (d) flow-net-computed uplift pressures. Key aspects of each of these four procedures are discussed in Chapter 4.

Interaction of Hydraulic Structure, Rock Foundation, and Rock Joint

Two methods are used to model the rock foundation. One approach is to account for the flexibility of the rock foundation by assigning the stiffness to a jointed rock foundation using empirical relationships that account for both the type of rock and the jointing within the rock mass comprising the foundation. Chapter 2 describes this first approach, which uses a composite stiffness based on the stiffness of the intact rock along with the effects of jointing within the rock foundation and the effects of the deformations at rock joints. The second approach includes all aspects of the first approach, along with discrete modeling of key joints within the rock foundation and/or the hydraulic structure-rock foundation interface. This second approach is discussed in Chapter 5 for the problem of a single tight rock joint in the foundation of a gravity dam.

Additionally, uplift pressures within rock joint(s) are coupled with changes in rock joint aperture through the cubic law for flow. Chapter 5 contains a complete example showing the interaction between the gravity dam, rock foundation, and rock joint and the uplift pressures resulting from changes in applied loadings (i.e., changes in reservoir elevation). As the rock joint aperture opens and closes with the applied loading, the uplift pressures within the rock joint varies. The results show that the distribution of uplift pressures along the tight joint are nonlinear and that the shape of the uplift distribution varies with pool elevation. This example shows that changes in rock joint aperture impacts the distribution of uplift pressures in the case of tight joints, consistent with observations made on existing hydraulic structures (Stone and Webster 1992).

Field Investigation(s) Combined with Stability Evaluation

When an existing hydraulic structure fails to meet the stability criteria required of new structures, it is recommended that the engineering procedure used to analyze its stability be evaluated for conservativeness. Additional and more sophisticated engineering analyses using the procedures described in this report may be required to ascertain the true margin of safety. Once the key factor(s) affecting the stability calculations are identified, additional field investigations in the form of the installation of instrumentation (i.e., piezometers in the foundation and/or backfill), in situ testing (i.e., pressure meter and hydrofracture tests in the backfill to ascertain horizontal earth pressures, or field pumping tests to ascertain strata permeabilities), site investigations (i.e., field borings), and/or field sampling and laboratory testing (i.e., compression and/or shear tests on jointed rock specimens, direct shear and/or splitting tensile tests of the concrete), may be warranted.

Remediation and Rehabilitation

At some point during the course of the structural stability evaluation, it may be concluded that remediation or rehabilitation of the structure is required. This section lists some of the procedures being used to enhance the stability of hydraulic structures.

Rock-founded concrete gravity dams

One approach that has been used to improve the safety of a hydraulic structure such as a rock-founded concrete gravity dam is to restrict the maximum elevation of the normal operation pool. Another common rehabilitation procedure for concrete dams may include "cleaning" existing drains in the foundation or adding additional drains. Grouting the rock foundation may both stiffen the foundation as well as reduce the uplift pressures. Lastly, installing posttensioned anchors has also been used to enhance "overturning" stability.

Rock-founded gravity lock walls retaining backfill

A significant portion of the loading on rock-founded gravity lock walls retaining backfills is the earth loads. With this in mind, one remediation procedure is to excavate a portion of the backfill. Other rehabilitation procedures include installing drains in the foundation or backfill or installing posttensioned anchors.

References

American Society for Testing and Materials. (1990). "Standard Test Method for Classification of Soils for Engineering Purposes," Practice No. D2487-90, *1990 Book of ASTM Standards*, 04.08, Philadelphia, PA .

ANATECH. (1993). "CG-DAMS: Concrete Gravity Dam Analysis Modular Software - Users Manual," Report RP2917-12, prepared for Electric Power Research Institute, Palo Alto, CA.

Bandis, S. C. (1980). *Experimental Studies of Scale Effects on Shear Strength, and Deformation of Rock Joints*, Ph.D Thesis, University of Leeds, Department of Earth Sciences, 384 pp. January, 1980.

Bandis, S. C., Lumsden, A. C., and Barton, N. R. (1983). "Fundamentals of Rock Joint Deformation," *International Journal of Rock Mechanics and Mining Sciences & Geomechanics Abstracts* 20(6), 249-268, December 1983.

Bandis, S. C., Barton, N. R., and Christianson, M. (1985). "Application of a New Numerical Model of Joint Behaviour to Rock Mechanics Problems," *Proceedings of the International Symposium on Fundamentals of Rock Joints*, pp. 345-355, 15-20 September 1985.

Barker, R. M., Duncan, J. M., Rojiani, K. B., Ooi, P. S. K, Tan, C. K., and Kim, S. G. (1991). *Manuals for the Design of bridge foundations, shallow foundations, driven piles, retaining walls and abutments, drilled shafts, estimating tolerable movements, load factor design specifications, and commentary*, Section 5.4 in "Part 1-Engineering for Shallow Foundations," Transportation Research Board, National Cooperative Highway Research Program Report 343, Washington, DC.

Barton, N. R. (1973). "Review of new shear strength criterion for rock joints," *Engineering Geology* 7(4), 287-332.

_____. (1982). *Modeling Rock Joint Behavior from In Situ Block Tests: Implications for Nuclear Waste Repository Design*, Technical Report ONWI-308, Office of Nuclear Waste Isolation, Battelle Memorial Institute, Columbus, OH.

Barton, N., Bandis, S., and Bakhtar, K. (1985). "Strength, deformation and conductivity coupling of rock joints," *International Journal of Rock Mechanics and Mining Sciences & Geomechanics Abstracts* 22(3), 121-140.

Benson, C. P. (1986). "Literature review of rock properties for analysis of navigation structures founded on rock," Masters Thesis, Department of Civil Engineering, Virginia Tech.

Bieniawski, Z.T. (1978). "Determining rock mass deformability: experience from case histories," *Int. Journal Rock Mech. Min. Sci. & Geomech. Abstr.* 15, 237-247.

Brekke, T. L., Witherspoon, P. A., Maini, Y. N. T., and Noorishad, J. (1972). "Coupled stress and flow analysis of fractured dam foundations and rock slopes", *Proceedings of the Symposium on Percolation Through Fissured Rock*, International Society for Rock Mechanics and International Association of Engineering Geology, Stuttgart, T4-J, 1-8.

Clough, G. W., and Duncan. J. M. (1969). "Finite element analyses of port allen and old river locks, Contract Report S-69-6, U.S. Army Engineer Waterways Experiment Station, Vicksburg, MS.

_____. (1991). "Earth Pressures," Chapter 6 in *Foundation Engineering Handbook*, Second Edition, edited bu H.Y. Fang, Van Nostrand Reinhold, New York.

Duncan, J. M., Byrne, P., Wong, K. S., and Mabry, P. (1978). "Strength, stress-strain and bulk modulus parameters for finite element analyses of stresses and movements in soil masses," Report, No. UCB/GT/78-02, College of Engineering, Office of Research Services, University of California, Berkeley, CA.

Duncan, J. M., and Chang, C. Y. (1970). "Nonlinear analysis of stress and strain in soils," *journal of soil mechanics and foundations division, ASCE* 96(SM5), 1629-1653.

Duncan, J. M., and Goodman, R. E. (1968). "Method of analysis for rock slopes," U.S. Army Engineer Waterways Experiment Station, Vicksburg, MS.

Ebeling, R. M., Clough, G. W., Duncan, J. M., and Brandon, T. L. (1992). "Methods of evaluating the stability and safety of gravity earth retaining structures founded on rock," Technical Report REMR CS-29, U.S. Army Engineer Waterways Experiment Station, Vicksburg, MS.

Ebeling, R. M., Duncan, J. M., and Clough, G. W. (1990). "Methods of evaluating the stability and safety of gravity earth retaining structures founded on rock - phase 2 study," Technical Report ITL-90-7, U.S. Army Engineer Waterways Experiment Station, Vicksburg, MS.

Ebeling, R. M., and Filz ,G. M. (1997). "Soil-structure interaction analyses of rock-founded gravity and cantilevered retaining walls," Technical Report in publication, U.S. Army Engineer Waterways Experiment Station, Vicksburg, MS.

Ebeling, R. M., and Mosher, R. L. (1996). "Red River u-frame Lock No. 1 backfill-structure-foundation interaction," American Society of Civil Engineers Journal of Geotechnical Engineering 122(3), 216-225.

Ebeling, R. M., Mosher, R. L., Abraham, K., and Peters, J. F. (1993). "Soil-structure interaction study of Red River Lock and Dam No. 1 subjected to sediment loading," Technical Report ITL-93-3, U.S. Army Engineer Waterways Experiment Station, Vicksburg, MS.

Ebeling, R. M., and Pace, M. E. (1996a). "Uplift pressures resulting from flow along tapered rock joints," *The REMR Bulletin* 13(1), 1-4, U.S. Army Engineer Waterways Experiment Station, Vicksburg, MS.

_____. (1996b). "Variation in uplift pressures with changes in loadings along a single rock joint below a gravity dam," *The REMR Bulletin* 13(1), 1-4, U.S. Army Engineer Waterways Experiment Station, Vicksburg, MS.

Ebeling, R. M., Peters, J. F., and Clough, G. W. (1992). "User's guide for the incremental construction soil-structure interaction program SOILSTRUCT," Technical Report ITL-90-6, U.S. Army Engineer Waterways Experiment Station, Vicksburg, MS.

Ebeling, R. M., and Wahl, R. E. (1997). "Soil-structure-foundation interaction analysis of the new roller-compacted concrete north lock wall at McAlpine Lock," Technical Report ITL-97-5, U.S. Army Engineer Waterways Experiment Station, Vicksburg, MS.

Engineering Computer Graphics Laboratory. (1993). "FASTSEEP," Brigham Young University, Provo, UT.

Filz, G. M., and Duncan, J. M. (1997 Sep). "Vertical shear forces on non-moving walls: theory," *American Society of Civil Engineers Geotechnical Journal* 123(9).

_____. (1992). "An Experimental and analytic study of earth loads on rigid retaining walls," Geotechnical Engineering Research Report prepared by Virginia Polytechnical Institute and State University, Blacksburg, VA, for U.S. Army Engineer Waterways Experiment Station, Vicksburg, MS.

Filz, G. M., Duncan, J. M., and Ebeling, R. M. (1997 Sep). "Vertical Shear forces on non-moving walls: applications," *American Society of Civil Engineers Geotechnical Journal* 123(9).

Fukuoka, M. (1980). "Static and dynamic earth pressures on retaining walls," *Proceedings Third Australia-New Zealand Conference on Geomechanics, Wellington* 3, 37-46.

Gale, J. E. (1982a). "Fundamental hydraulic characteristic of fractures from field and laboratory investigations," *AWRC Conference on Groundwater in Fractured Rock, August 31-September 3, 1982,* 79-93.

_____. (1982b). "The Effects of fracture type (induced versus natural) on the stress-fracture closure-fracture permeability relationships," *Proceedings of the 23rd U.S. Symposium on Rock Mechanics*, University of California, Berkeley.

Goodman, R. E. (1974). "The Mechanical properties of joints, *Proc. 3rd Congress on International Society for Rock Mechanics* 1(Part A), 127-140 Denver, CO.

Goodman, R. E., Taylor, R. L., and Brekke, Tor, L. (1968). "A model for the mechanics of jointed rock," *Journal of the Soil Mechanics and Foundations Division* 94(SM3), 637-659.

Gould, J. P. (1970). "Lateral pressures on rigid permanent structures," Proceedings *Americn Socity of Civil Engineers Specialty Conference on Lateral Stresses in the Ground and Design of Earth Retaining Structures*, Cornell University, Ithaca, NY, 219-269.

Grenoble, B. A. (1989). " Influence of geology on seepage and uplift in concrete gravity dam foundation," Ph.D. diss., University of Colorado, Denver, CO.

Grenoble, B. A., Amadei, B. P., Illangasekare, T. (1992). *Influence of rock discontinuities on seepage and uplift in concrete gravity dam foundaitons: a numerical approach*, 7, EPRI Contract R.P. 2917-97, Electric Power Research Institute, Palo Alto, CA.

Headquarters, Department of the Army. (1989). "Retaining and flood walls," Engineering Manual 1110-2-2502, Washington, DC.

_____. (1995). "Navigation locks," Engineering Manual 1110-2-2602, Washington, DC.

_____. (1995). "Gravity dam design," Engineering Manual 1110-2-2200, Washington, DC.

_____. (1994). "Engineering and design, stability of gravity retaining walls - vertical shear," Engineering Technical Letter 1110-2-352, Washington, DC.

Headquarters, Deaprtment of the Army. (1993). "Fracture Mechanics analysis of a gravity lock monolith," Engineering Technical Letter 1110-2-344, Washington, DC.

_____. (1987). "Stability criteria for existing concrete navigation structures on rock foundations," Engineering Technical Letter 1110-2-310, Washington, DC.

Hilmer, __. (1986). "Evaluation of a ten-year measuring program at Eibach Lock."

Holtz, R. D. 1991. "Stress distribution and settlement of shallow foundations," Chapter 5 in 2nd edition of *Foundation Engineering Handbook*, edited by H-Y Fang, Van Nostrand Reinhold, New York.

Iwai, K. (1976). *Fundamental Studies of Fluid Flow Through a Single Fracture*, Ph.D Thesis, University of California, Berkeley, CA.

Janbu, N. (1963). "Soil compressibility as determined by oedometer and triaxial tests," *European Conference on Soil Mechanics and Foundation Engineering, Wiesbaden* 1, 19-2; 2, 83-87.

_____. (1965). "Consolidation *of Clay Layers Based On Non-Linear Stress-Strain," Proceedings, 6th International Conference on Soil Mechanics and Foundation Engineering, Montreal* 2, 83-87.

_____. (1967). "Settlement calculations based on the tangent modulus concept," Bulletin No. 2, University of Trondheim, Norwegian Institute of Technology, Norway.

_____. (1985). "Soil models in offshore engineering," *Geotechnique* 35(3), 241-281.

Kany, M. (1972). "Measurement of earth pressures on a cylinder 30m in diameter (pump storage plant)," *Proceedings Fifth European Conference on Soil Mechanics*, Madrid, 535-542.

Kranz, R. L., Frankel, A. D., Engelder, T., and Scholz, C. H. (1979). "The Permeability of whole and jointed barre granite," *International Journal of Rock Mechanics and Mining Sciences* 16, 225-234.

Kulhawy, F. H. (1978). "Geotechnical model for rock foundation settlement," Jour. Geotech. Eng. Div., Americn Society of Civil Engineers 104(GT2), 211-227.

Lee, C.-H., and Farmer, I. (1993). *Fluid Flow in Discontinuous Rocks*, Chapman & Hill, London.

Long, J. C. S. (1985). "Verification and characteristics of continuum behavior of fractured rock at AECL underground research laboratory," Technical Report BMI/OCRD-17.LBL-14975.

Long, J. C. S., Remer, J. S., Wilson, C. R., and Witherspoon, P. A. (1982). "Porous media equivalents for networks of discontinuous fractures," *Water Resources Research* 18, 645-658.

Louis, C. A. (1969). *A study of groundwater flow in jointed rock and its influence on the stability of rock masses*, Rock Mechanics Research Report No. 10, Imperial College, London.

Matsuo, M., Kenmochi, S., and Yagi, H. (1978). "Experimental study on earth pressure of retaining wall by field tests," Soils and Foundations 18(3), 27-41.

Meyerhof, G. G., and Fellenius, B. H., Ed. (1985). *Canadian Foundation Engineering Manual*, 2nd edition, Canadian Geotechnical Society, Canada.

Noorishad, J., Witherspoon, P. A., and Brekke, T. L. (1971). *A method for coupled stress and flow analysis of fractured rock masses*, Geotechnical Engineering Pub. No. 71-6, Department of Civil Engineering, University of California, Berkeley, CA.

Peterson, M., Kulhawy, F., Nucci, L., and Wasil, B. (1976). "Stress-deformation behavior of soil-concrete interfaces," Contract Report B-49 to Niagara Mohawk Power Corp., Dept. of Civil Engineering, Syracuse Univ., Syracuse, NY.

Reich, R., Cervenka, J., and Souma, V. (1993). "MERLIN, a three-dimensional finite element program based on a mixed-iterative solution strategy for problems in elasticity, plasticity, and linear and nonlinear fracture mechanics," Technical Report to Electric Power Research Institute, Palo Alto, CA.

Robinson, P. C. (1982). "Namnet-network flow program," AERE Report R-10510, Harwell, UKAERE.

Rouleau, A., and Gale, J. E. (1987). "Stochastic discrete fracture simulation of ground-water flow into an underground excavation in granite," International Journal of Rock Mechanics and Mining Sciences & Geomechanics Abstracts 24(1), 99-112.

Shapiro, A., and Andersson, J. (1983). "Steady State fluid response in fractured rock: a boundary element solution for a coupled, discrete fracture continuum model," *Water Resources Research* 19(4), 959-969.

Sherif, M. A., Ishibashi, I., and Lee, C. D. (1982). "Earth Pressures against rigid retaining walls," ASCE Journal of Geotechnical Engineering Division 108(5), 679-695.

Stone and Webster Engineering Corporation. (1992). "Uplift pressures, shear strengths, and tensile strengths for stability analysis of concrete gravity dams," EPRI TR-100345s, Vol 1, report to Electric Power Research Institute, Palo Alto, CA.

Terzaghi, K. (1934a). "Large Retaining wall tests, I - pressure of dry sand," *Engineering News Record*, Feb 1, 136-140.

_____. (1934b). "Large Retaining wall tests, ii - pressure of saturated sand," *Engineering News Record*, Feb 22, 259-262.

_____. (1929). "Effect of minor geologic details on the safety of dams," AIME Technical Publication 215, 31-44.

Tracy, F.T. (1983). "User's guide for a plane and axisymmetric finite element program for steady-state seepage problems," Instruction Report K-83-4, U.S. Army Engineer Waterways Experiment Station, Vicksburg, MS.

Tsang, Y. W., and Witherspoon, P. A. (1981). "Hydromechanical behavior of a deformable rock fracture subject to normal stress," *Journal of Geophysical Research* 86(10), 9287-9298.

Vogt, N., Chara, G., Hilmer, K. Nowack, F., and Grimm, G. (1986). "Auswertung einer zehnjahridgen mebreihe an der schleuse eibach," Bautechnik, Ernst and Sohn, Berlin.

Wilson, R. W. (1970). *An Investigation of laminar flow in fractured porous rocks*, Ph.D Thesis, University of California, Berkeley, CA.

Witherspoon, P. A., Wang, J. S. Y., Iwai, K., and Gale, J. E. (1980). "Validity of cubic law for fluid flow in a deformable rock fracture," *Water Resources Research* 16(6), 1016-1024.

Zhang, X., Sanderson, D. J., Harkness, R. M., and Last, N. C. (1996). "Evaluation of the 2-d permeability tensor for fractured rock masses," International Journal of Rock Mechanics and Mining Sciences & Geomechanics Abstracts 33(1), 17-37.

_____. (1989). "A two-dimensional model of en-echelon jointed rock masses with multi-discontinuity geometry parameters," *Rock Mechanics Rock Engineering* 22, 231-242.

Appendix A Resultant Forces and Equilibrium Calculations for Base Case SOILSTRUCT-ALPHA Following Load Analysis of Locks 27 Monolith 7E

This appendix summarizes the results of the SOILSTRUCT-ALPHA finite element following load analyses of Locks 27 Monolith 7E gravity retaining wall (Chapter 2 base-case analysis) in terms of resultant forces acting on the monolith at each stage of loading. Calculations summarized herein ensure that these forces and moments are in equilibrium. Additionally, selected results of the conventional equilibrium analyses of the monolith are compared with the results of SOILSTRUCT-ALPHA base case analyses.

Following Loads Applied to Locks 27 Gravity Retaining Wall

In all following load analyses described in Chapter 2 and this appendix, it was assumed that the monolith was loaded by a predefined lateral pressure of given magnitude and distribution. The soil backfill was not represented in the analysis. Lateral pressures were established using conventional concepts for earth and water loadings on retaining wall systems and were applied to the wall in a series of steps to determine the response of the structure to gradually increasing loads. Therefore, the magnitudes and distributions of the loadings were uncoupled from the action of the wall-foundation system. Regardless of how much the wall moved or of the form of the structure movement, the loading was not changed. This form of loading is termed "following load analysis."

The loads acting on the monolith in the following load analyses shown in Figure A1(a) have four basic components. First is the force W, equal to the vertical loads induced by the weight of the monolith and the weight of the wedge of soil

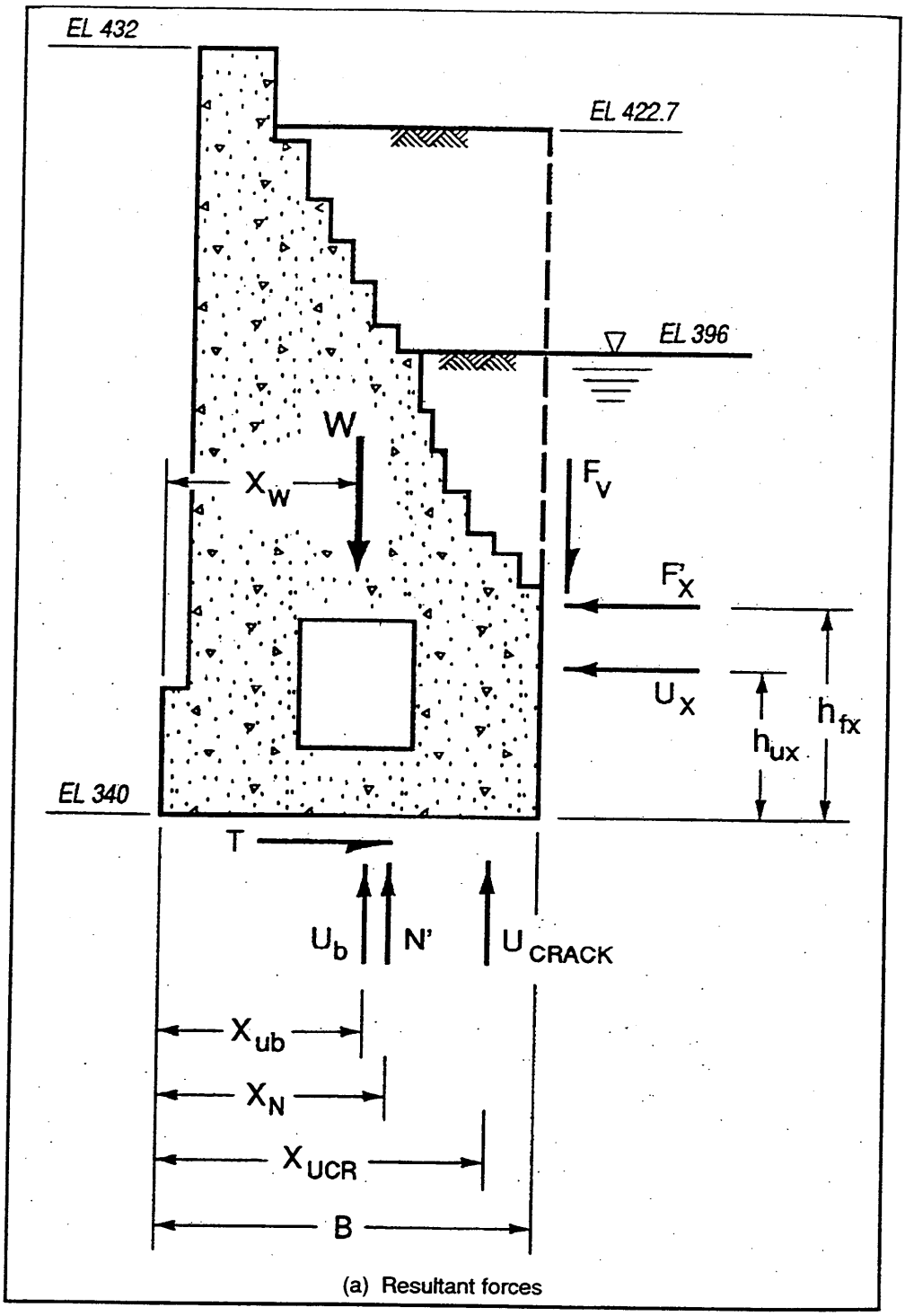

Figure A1. Forces acting on monolith (Continued)

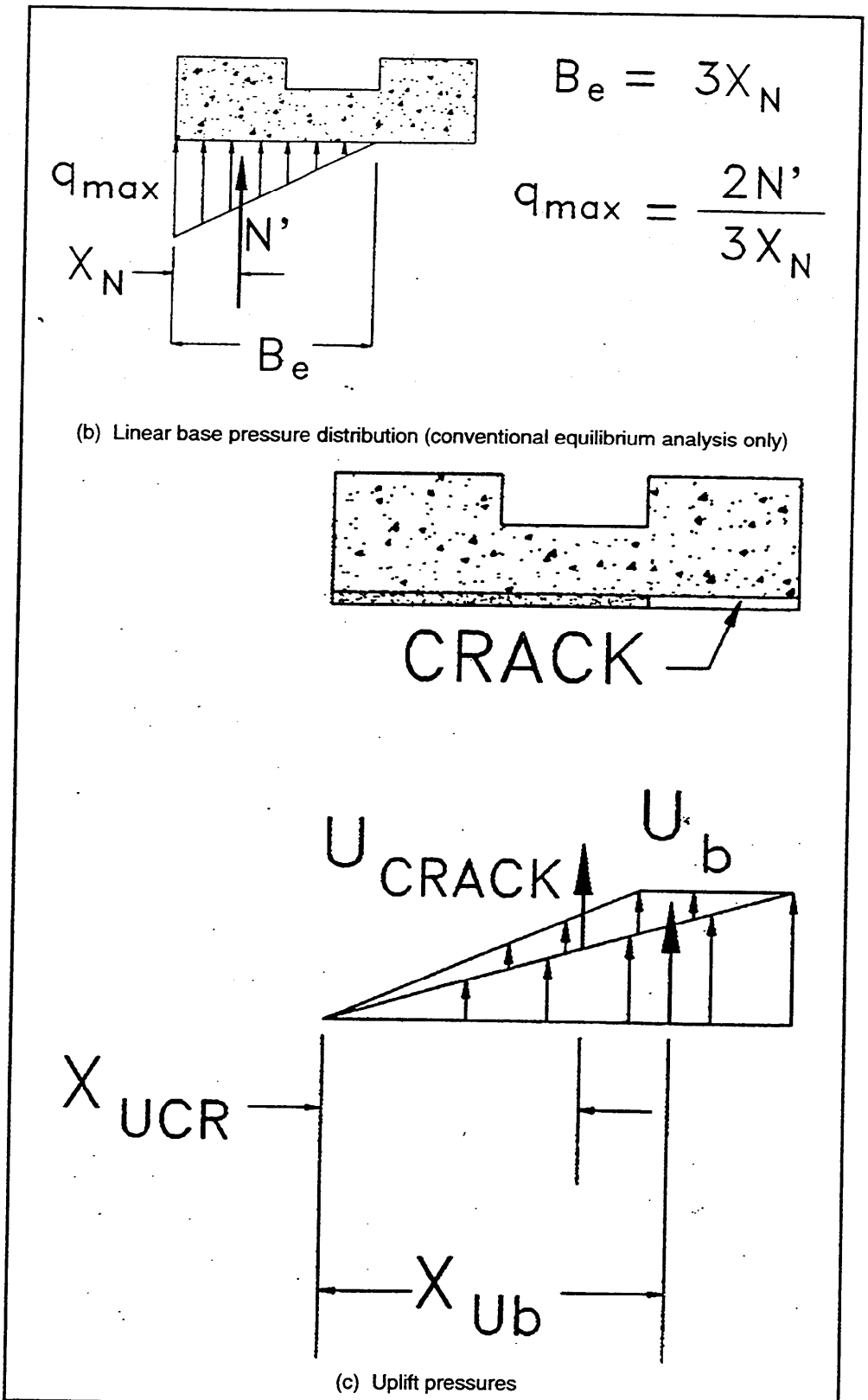

Figure A1. (Concluded)

backfill contained in the region bounded by the monolith-backfill interface and the vertical plane originating at the heel of the monolith. Second is the lateral effective stress assumed to be generated by the soil backfill and water in the backfill, designated as F'_x and U_x, respectively. Third is the vertical shear force directed downward along the plane extending vertically from the heel of the wall through the backfill, designated as F'_v. Fourth is the water pressure acting along the base of the monolith and the pressure resulting from water flow along the interface between the monolith and the rock foundation, designated as U_b and U_{CRACK}, respectively.

The loading scheme used in the following load analyses was described in Chapter 2 (see Figure 3 in the main text). In the base case analysis, the self-weight of the monolith and soil wedge were computed by means of the gravity turn-on analysis procedure using SOILSTRUCT-ALPHA. Next, the placement of the backfill and raising of the water table were done in 14 increments (Figure A2(c)) to the elevations[1] shown in Figures A2(a) and (b). Note that the water table was raised concurrent with the "placement" of the backfill lifts.

At-rest earth pressures were assigned normal to the plane extending vertically from the heel of the wall through the backfill for each of 14 loading increments (Figure 11 in Chapter 2). Lateral earth pressures corresponded to an at-rest earth pressure coefficient K_o of 0.45. A vertical shear force was assigned to this plane (Figure 3 in Chapter 2). A shear force corresponding to a vertical earth pressure coefficient K_v of 0.09 was assigned in all analyses.

The monolith and foundation were assumed to be impervious. Water flow from the backfill to the pool in front of the monolith was confined to the interface between the base of the monolith and the foundation. A linear head loss was assigned to this interface region where the monolith maintained contact with the foundation. For the interface region where the monolith had separated from its foundation, hydrostatic water pressures corresponding to the hydrostatic head within the backfill were assigned. Water pressures were assigned along the interface as shown in Figure A1(c) in all analyses.

For each lift elevation, the value for F'_x is given in Figure A3 and equals the resultant of the horizontal effective earth pressure distribution shown in Figure 11 (Chapter 2). The value for F'_x was computed using Equation 1 (see main text) with K_o equal to 0.45 with hydrostatic water pressures within the backfill. F_v in Figure A3 equals the resultant of the vertical shear stress distribution shown in Figure 3 (Chapter 2) and was computed using Equation 3 (see main text) with K_v equal to 0.09 for each lift elevation. U_x in Figure A3 equals the resultant of the horizontal water pressure distribution, assuming a hydrostatic water table in the backfill and computed using Equation 4 (see main text) for each lift elevation.

[1] All elevations (el) cited herein are in feet referenced to the National Geodetic Vertical Datum.

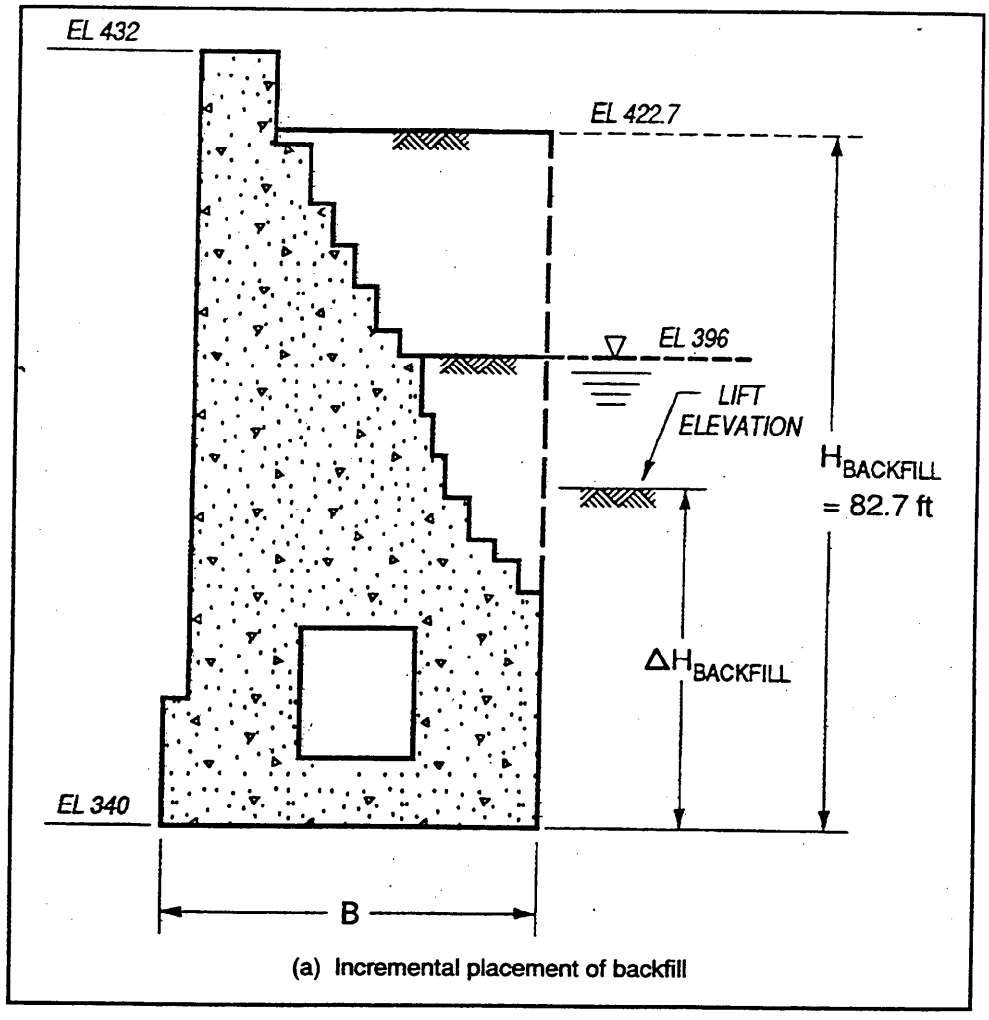

Figure A2. Stages of backfill and water loadings following load analyses (1 ft = 0.305 m) (Sheet 1 of 3)

Resultant Forces Computed From the Results of the Finite Element Analyses

The distributions of effective stresses normal to the monolith-to-rock interface were integrated in all finite element analyses to compute the resultant effective normal force N' in all analyses. The shear stress distributions were also converted to the resultant shear force T in similar fashion. Zero tensile strength is assumed for the material comprising the monolith-to-rock foundation interface in this problem. Figure A4 gives the horizontal equation of equilibrium for the monolith. Figure A5 summarizes the values for the forces F'_x and U_x and the value for T computed from the results of the finite element analyses with each lift elevation. This check showed that the shear stress distributions computed using the finite element method were consistent with the horizontal loads applied to the monolith for every load case.

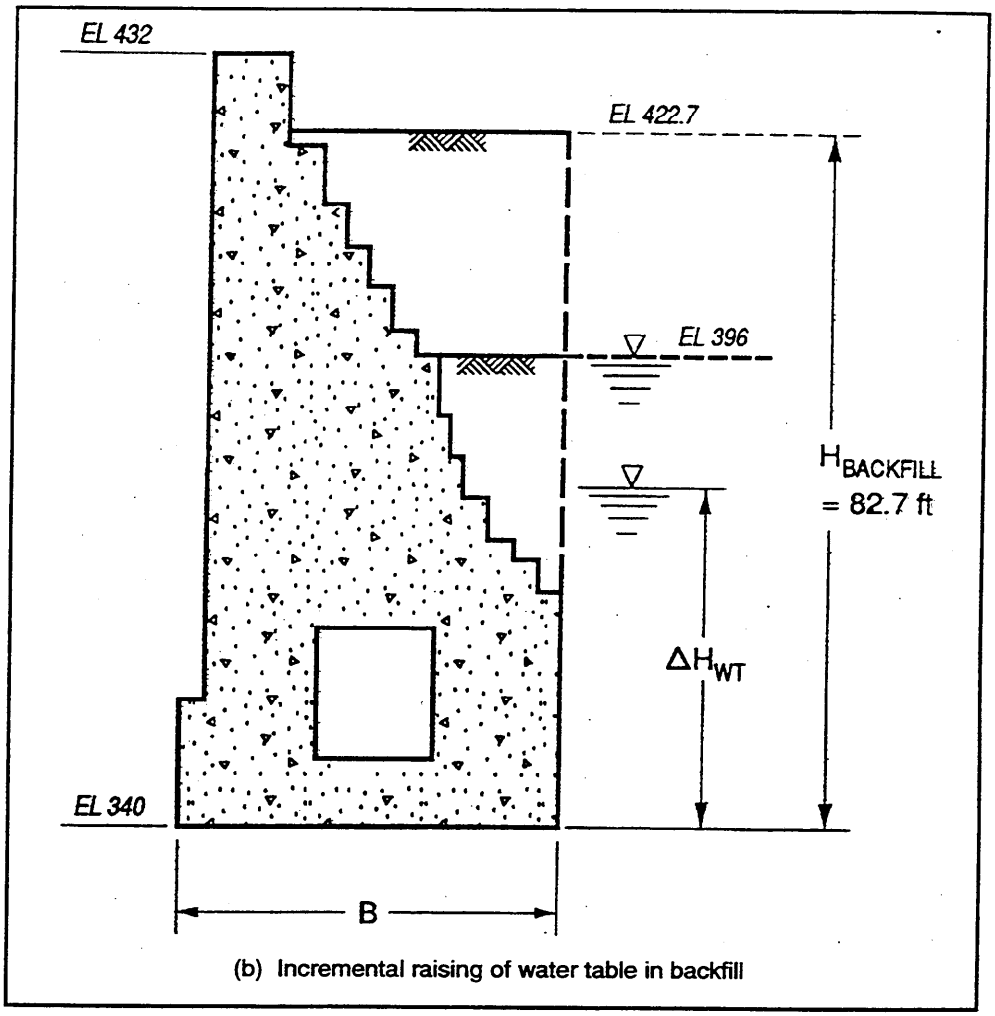

(b) Incremental raising of water table in backfill

Figure A2. (1 ft = 0.305 m) (Sheet 2 of 3)

In all finite element analyses, a crack is assumed to develop when the effective stresses computed along the interface are other than compressive. If a crack develops, hydrostatic water pressures are assumed along the cracked portion of the base, as idealized in Figure A6(a). The total uplift force normal to the imaginary section through the base of the monolith in Figure A6(a) is equal to the sum of the uplift forces U_b and U_{CRACK}. U_b is the resultant force for a *linear* uplift pressure distribution along the interface (Figure A6(b)). U_{CRACK} is the resultant force of uplift pressures in excess of the linear uplift pressure diagram extending from the heel to the toe of the wall. When no crack is present, U_{CRACK} equals zero, and the total uplift equals U_b. Figure A7 summarizes the values for the forces U_b and U_{CRACK} with each lift elevation. In all following load finite element analyses, uplift pressures exceeding the linear uplift pressure diagram (Figure A6(a)) and corresponding to U_{CRACK} were applied after application of the final following loads (corresponding to lift elevation 422.7).

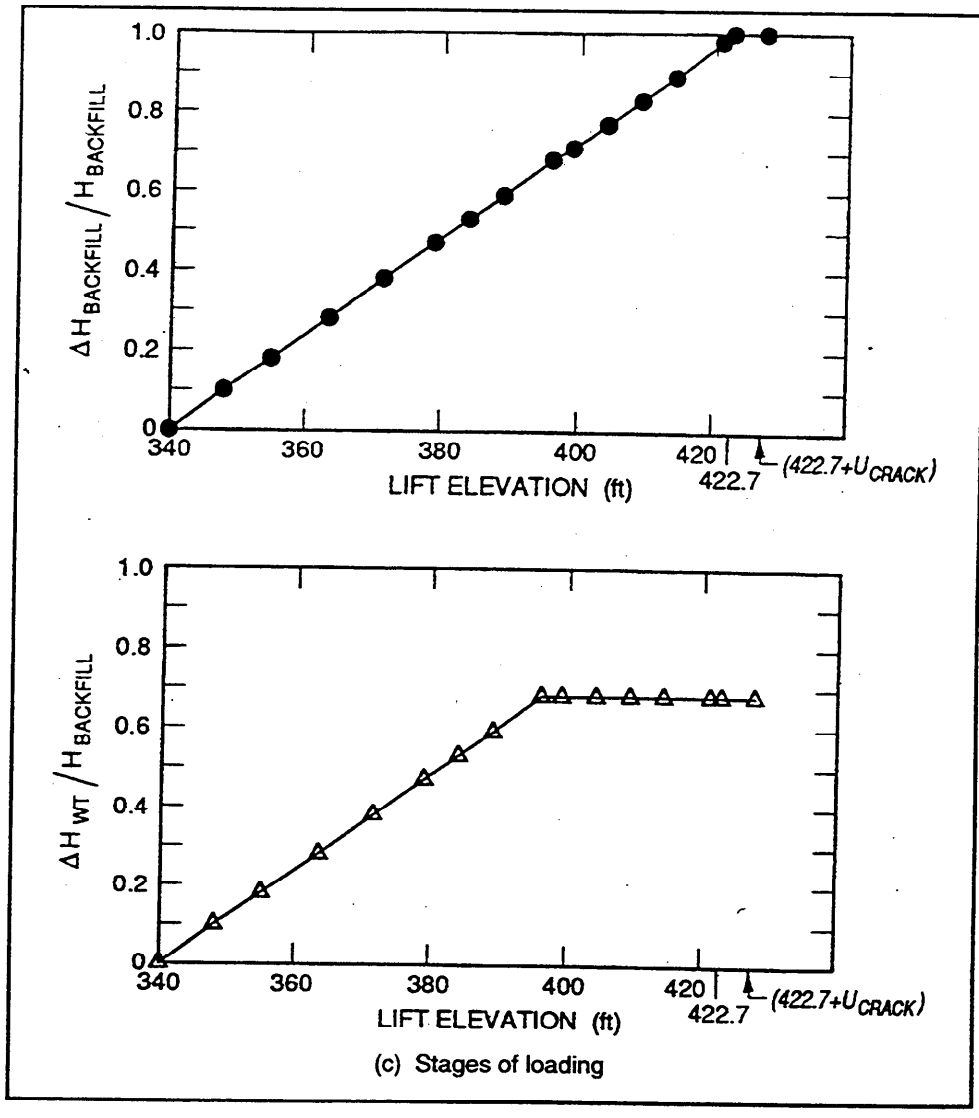

Figure A2. (1 ft = 0.305 m) (Sheet 3 of 3)

Figure A8 gives the vertical equation of equilibrium for the monolith. Figure A9 summarizes the values for the force N' computed from the effective interface pressures that were computed from the finite element analyses for each lift elevation. A check using the vertical equation for equilibrium showed N' and, thus, the effective normal interface stress distributions computed using the finite element method, to be consistent with the vertical loads applied to the monolith for every load case.

Figure A10 gives the equation used to compute the mobilized angle of interface friction along the base of the monolith. Figure A11 summarizes the values for the forces T and N' computed from the results of the finite element analyses and the value for $\delta_{mobilized}$ with each lift elevation. This figure shows that the values for $\delta_{mobilized}$ vary nonlinearly with lift elevations.

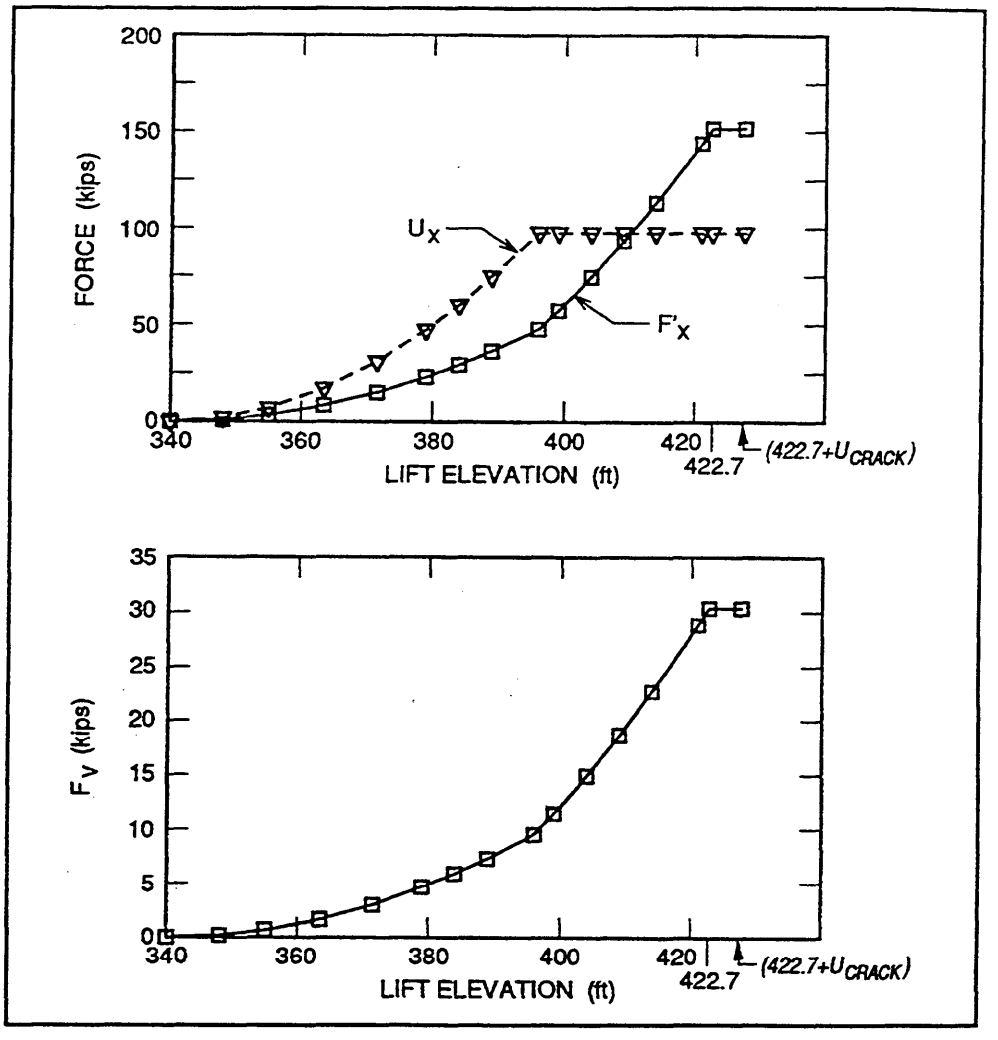

Figure A3. Variation in resultant forces along a vertical plane extending through the backfill from the heel of the monolith (1 ft = 0.305 m, 1 kip = 4.448 kN)

Figure A12 gives the equation of moment equilibrium about the toe of the monolith. Figure A13 summarizes the values for the moment $N'x_N$, the overturning moment M_{OVER}, and the resisting moment M_{STABLE}, computed using the results from the finite element analyses for each lift elevation. A check using the moment equilibrium about the toe showed the values for $N'x_N$ to be consistent with the other stabilizing moments and the overturning moments for every load case. Figure A14 summarizes the values for the moments M_{OVER} and M_{STABLE}, x_N and B_e/B for each lift elevation. The term B_e is the width of the effective base contact and is determined as the base region with compressive effective stresses for each backfill lift elevation. Recall that B equals 45 ft (13.7 m) and corresponds to the base width of the monolith.

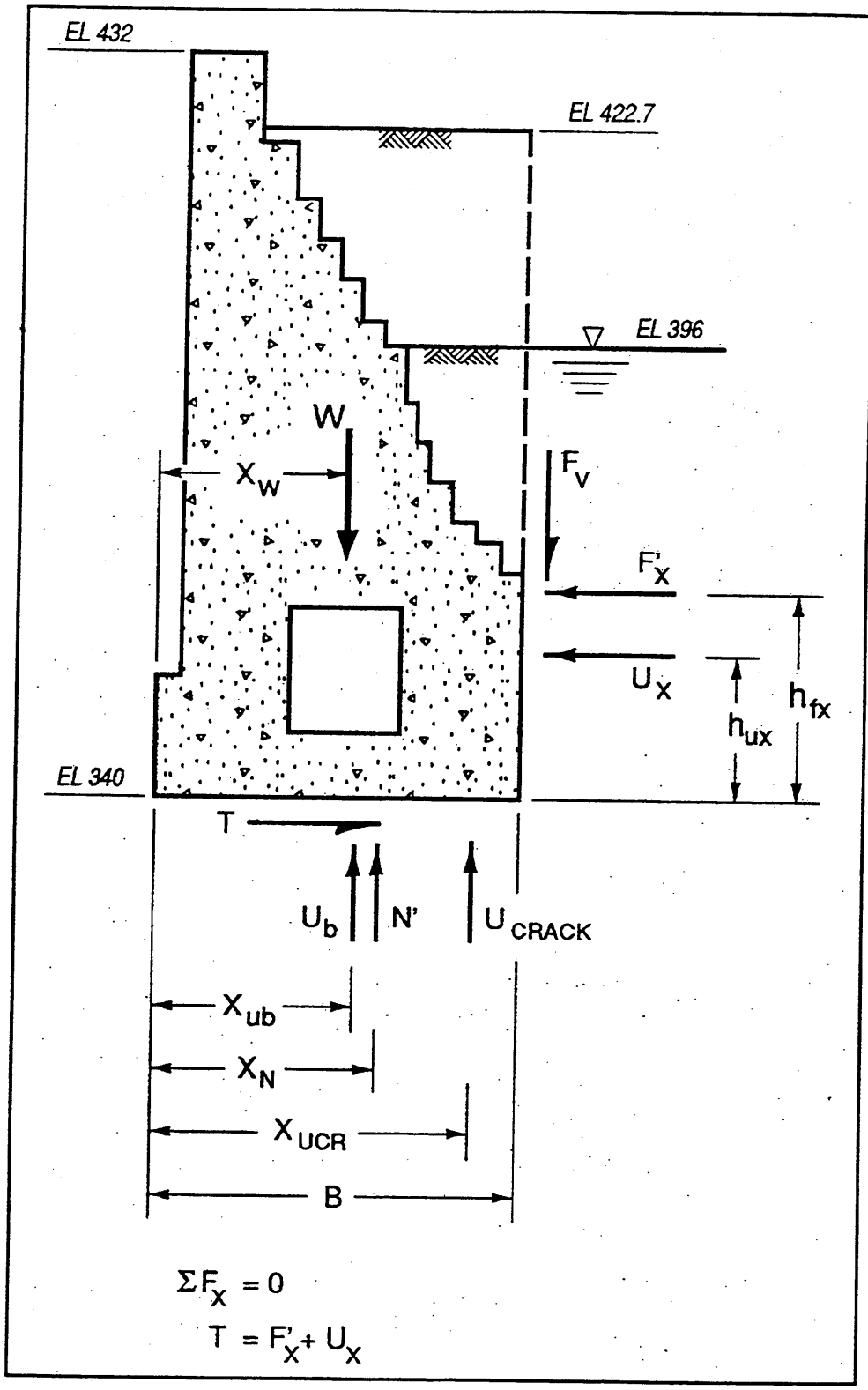

Figure A4. Equilibrium of horizontal forces

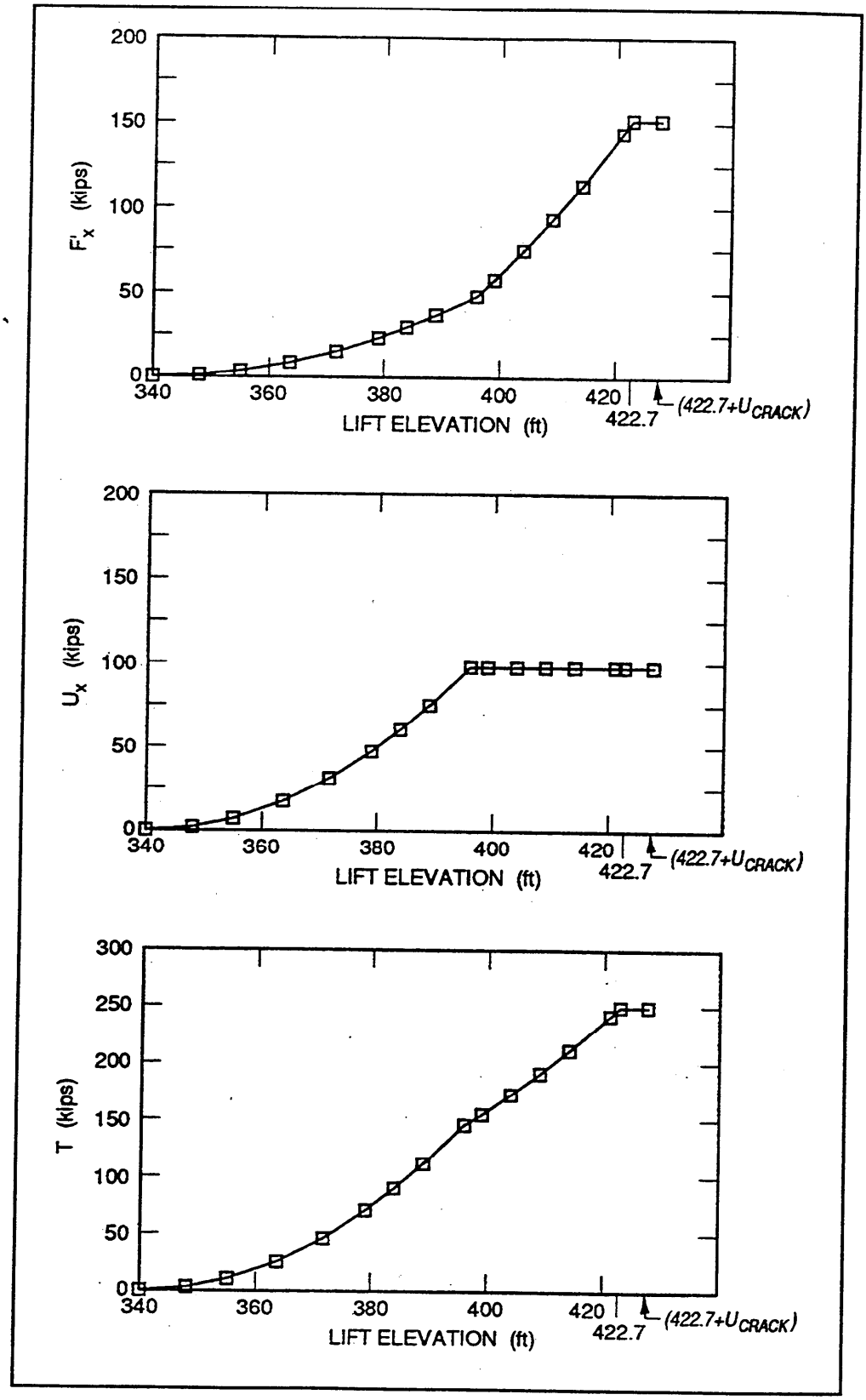

Figure A5. Variations in values of F'_x, U_x, and T with lift elevations (1 ft = 0.305 m, 1 kip = 4.448 kN)

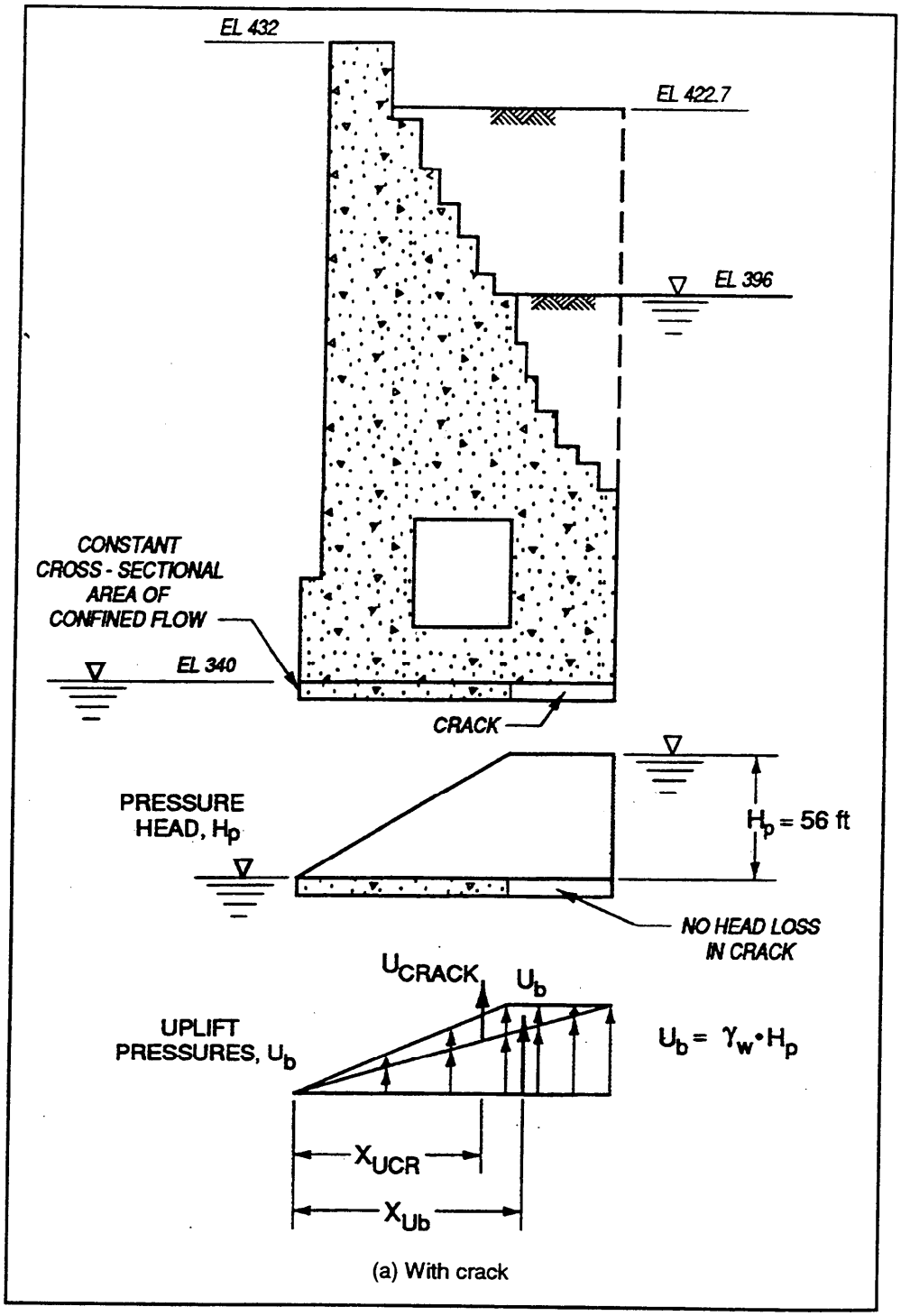

Figure A6. Confined flow along interface (1 ft = 0.305 m) (Continued)

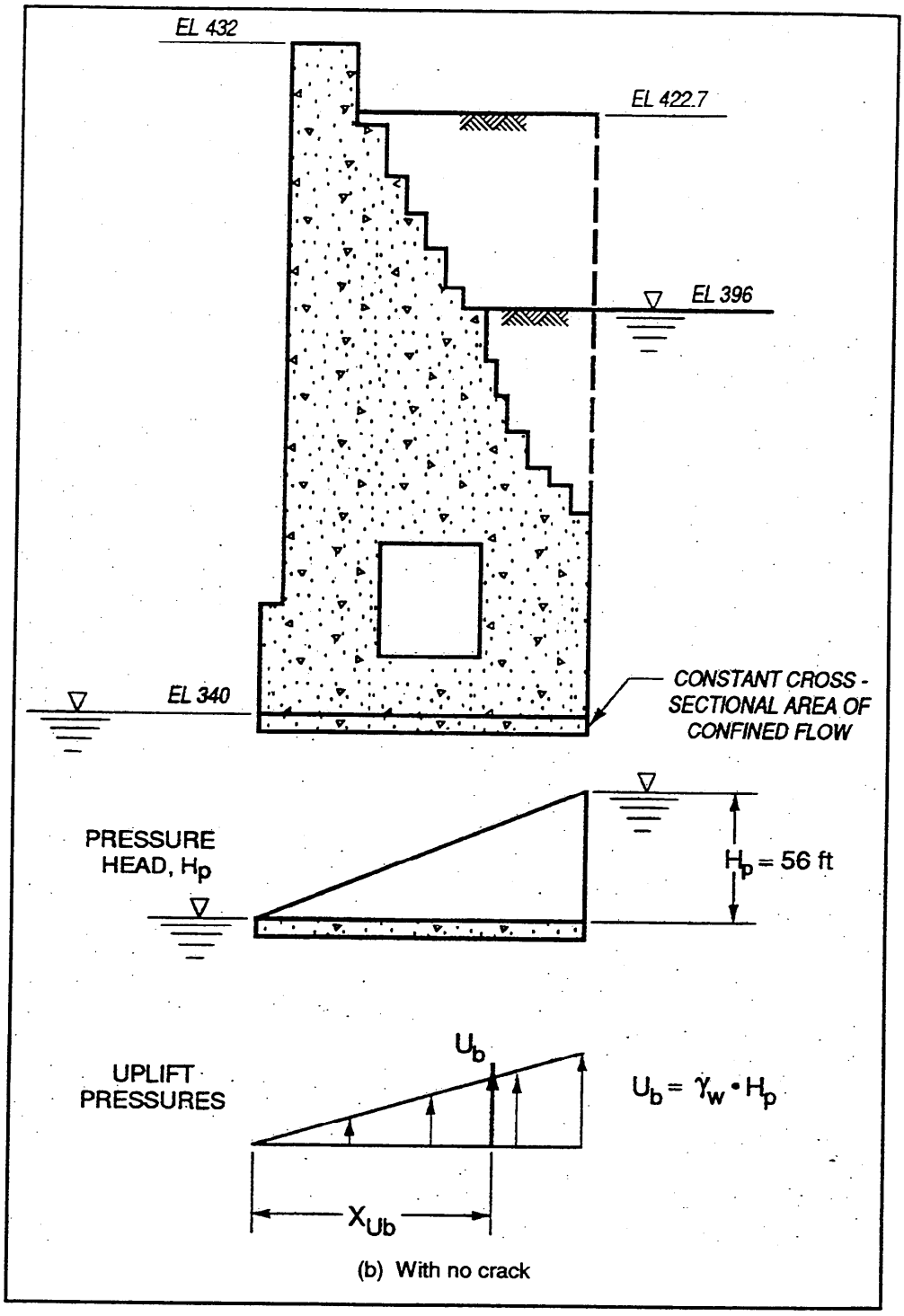

Figure A6. (1 ft = 0.305 m) (Concluded)

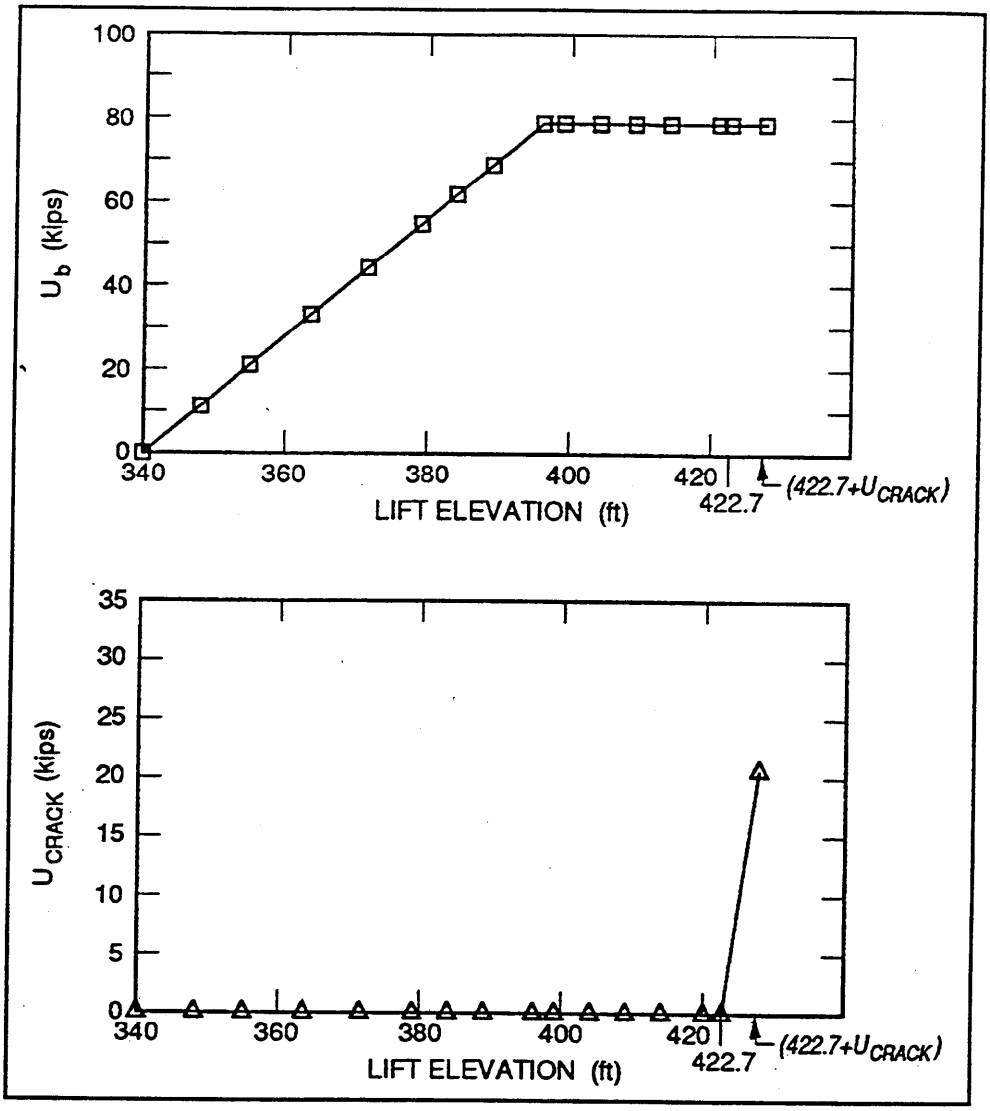

Figure A7. Variations in values of U_b and U_{CRACK} with lift elevations (1 ft = 0.305 m, 1 kip = 4.448 kN)

Comparisons of Equilibrium Calculations Resulting From the Finite Element Analyses and the Conventional Equilibrium Analyses

Figure A15 shows the variations in resultant values for forces T and N' and x_N from the conventional force equilibrium and finite element analyses for each lift elevation. The results in this figure show that the resultant forces and points of applications are consistent for the two methods of analysis.

Figure A16 shows the variations in values for force N', base area in compression B_e, and B_e/B from the results of conventional force equilibrium and finite

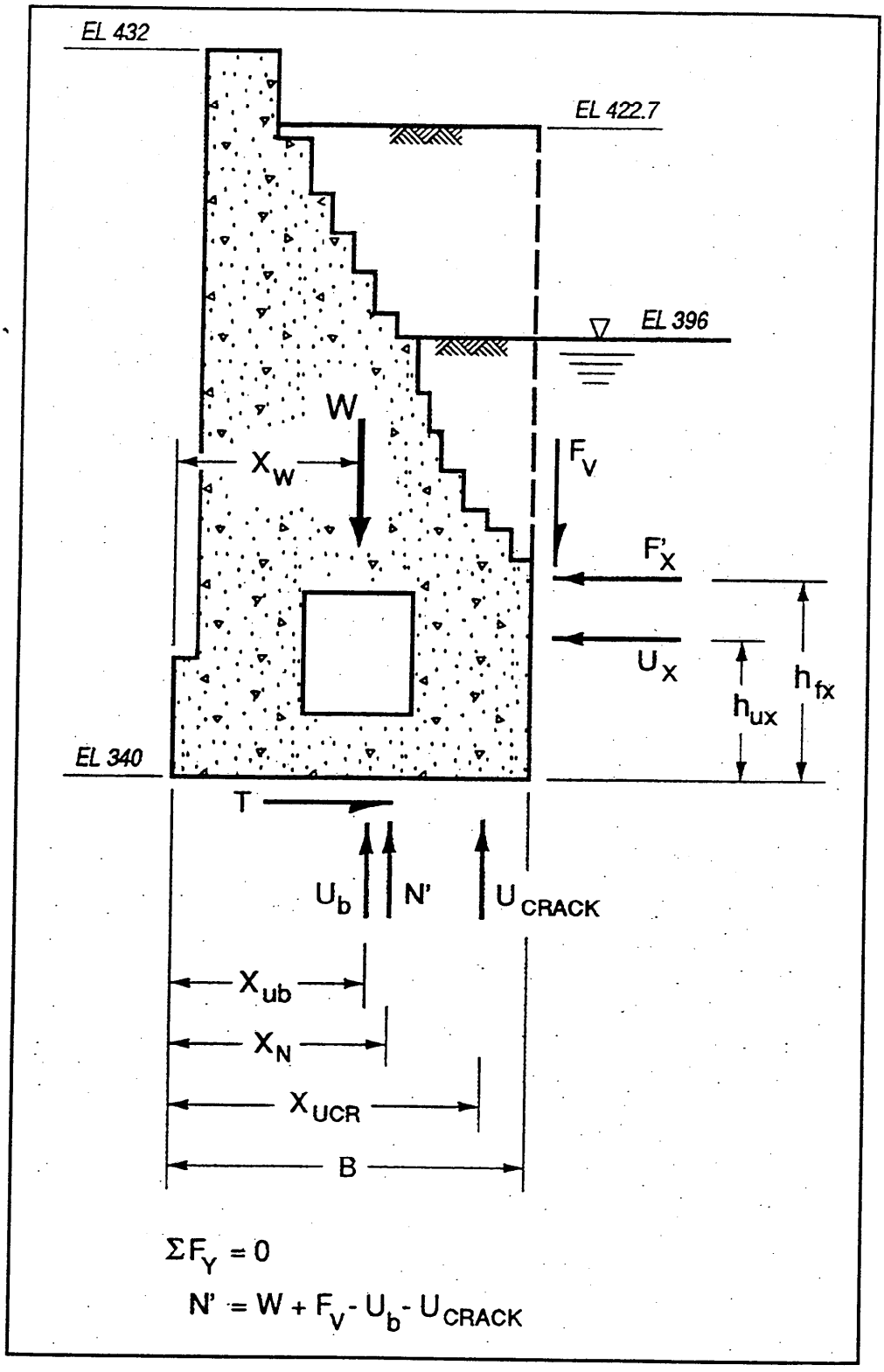

Figure A8. Equilibrium of vertical forces

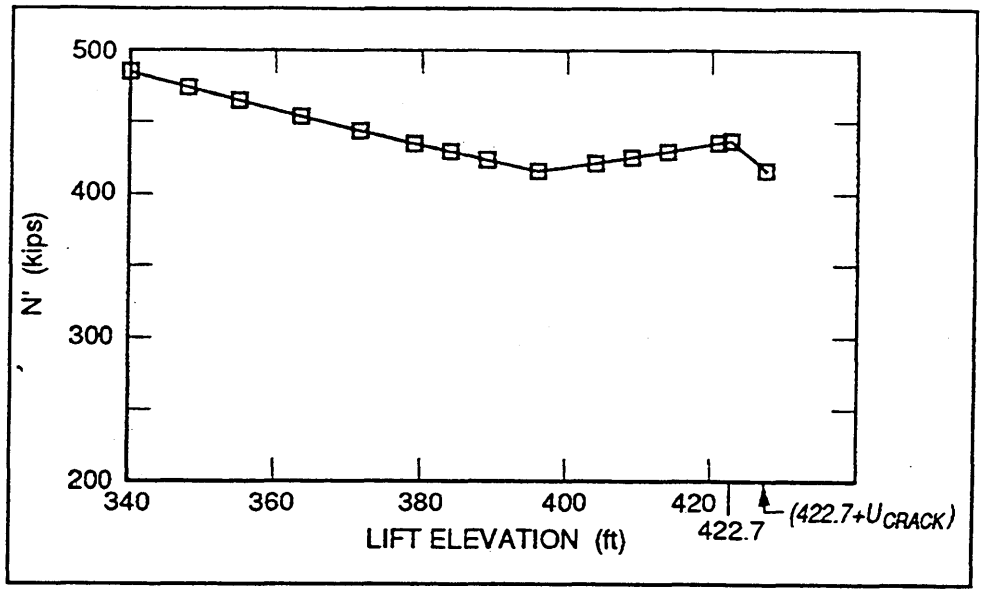

Figure A9. Variations in values of N' with lift elevations (1 ft = 0.3048 N, 1 kip = 4.448 kN)

element analyses for each lift elevation. This figure shows that the finite element analysis results in significantly more base area in compression than does the conventional force equilibrium analysis. Differences in the results shown in this figure relate to the assumed linear distribution of effective stress along the interface for the conventional force equilibrium method of analysis (Figure A1(b)). Recall that the finite element method computations are under no such restrictions.

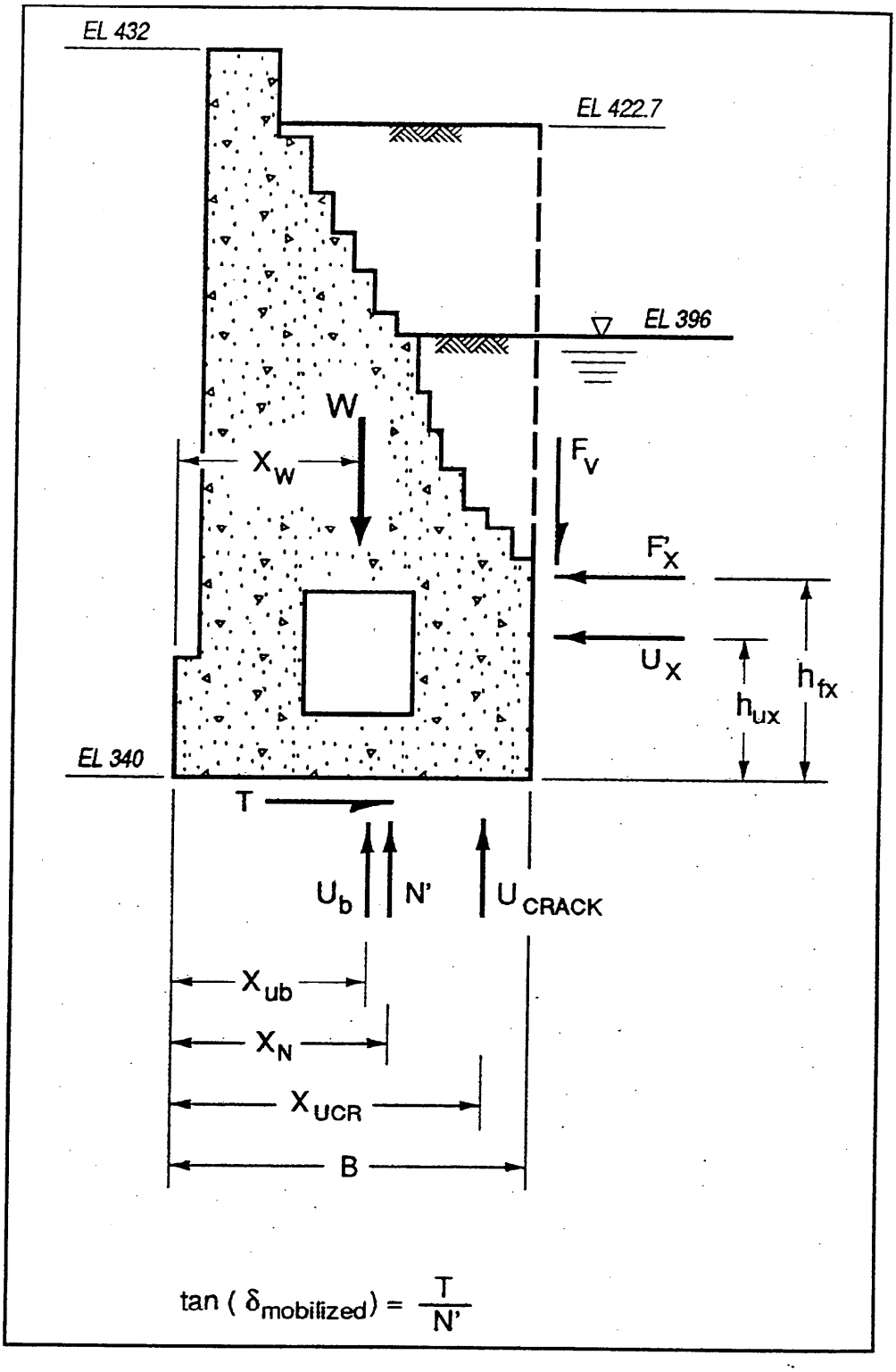

Figure A10. Mobilized friction along base

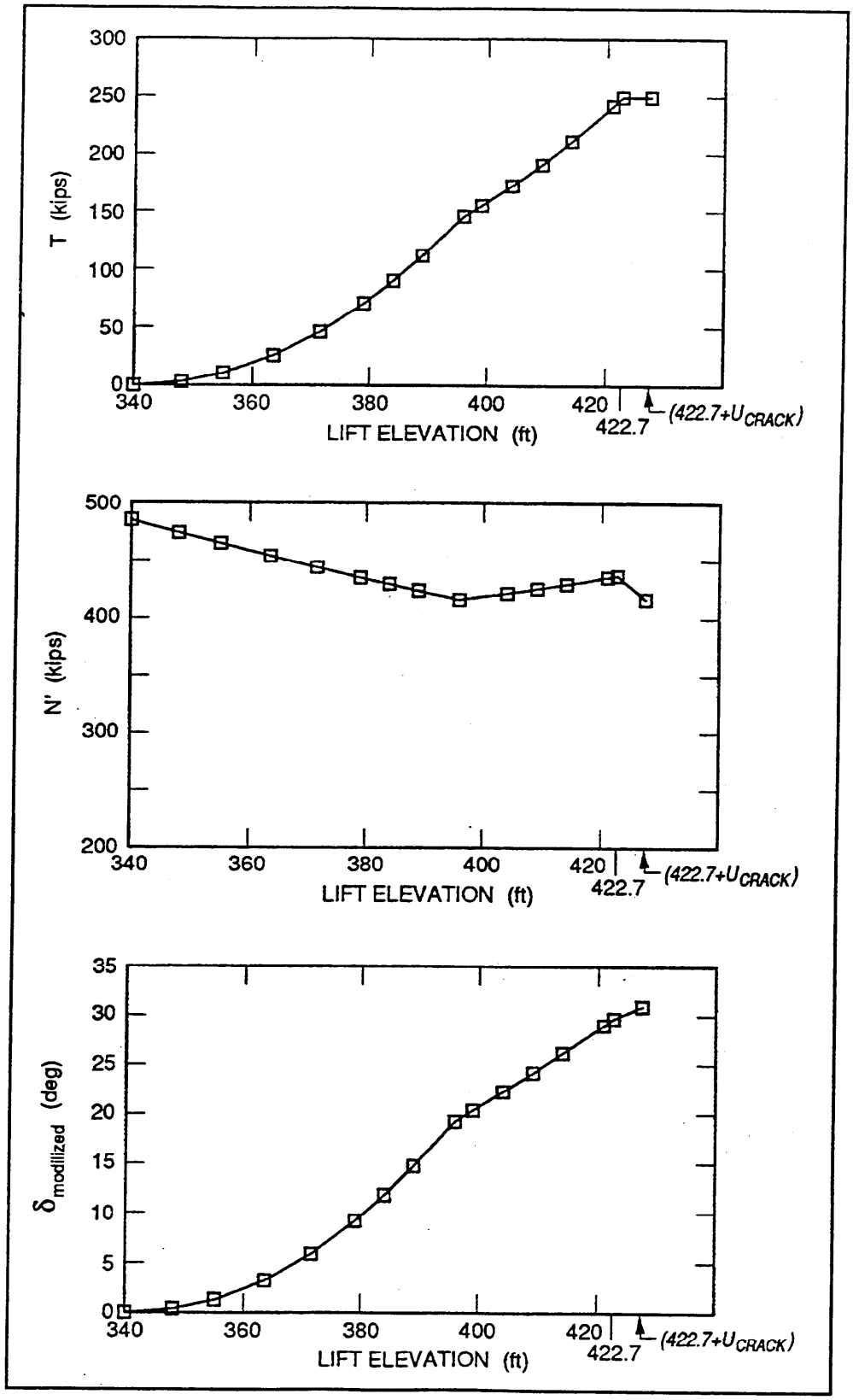

Figure A11. Variations in values of T, N', and $\delta_{mobilized}$ with lift elevations (1 ft = 0.305 m, 1 kip = 4.448 kN)

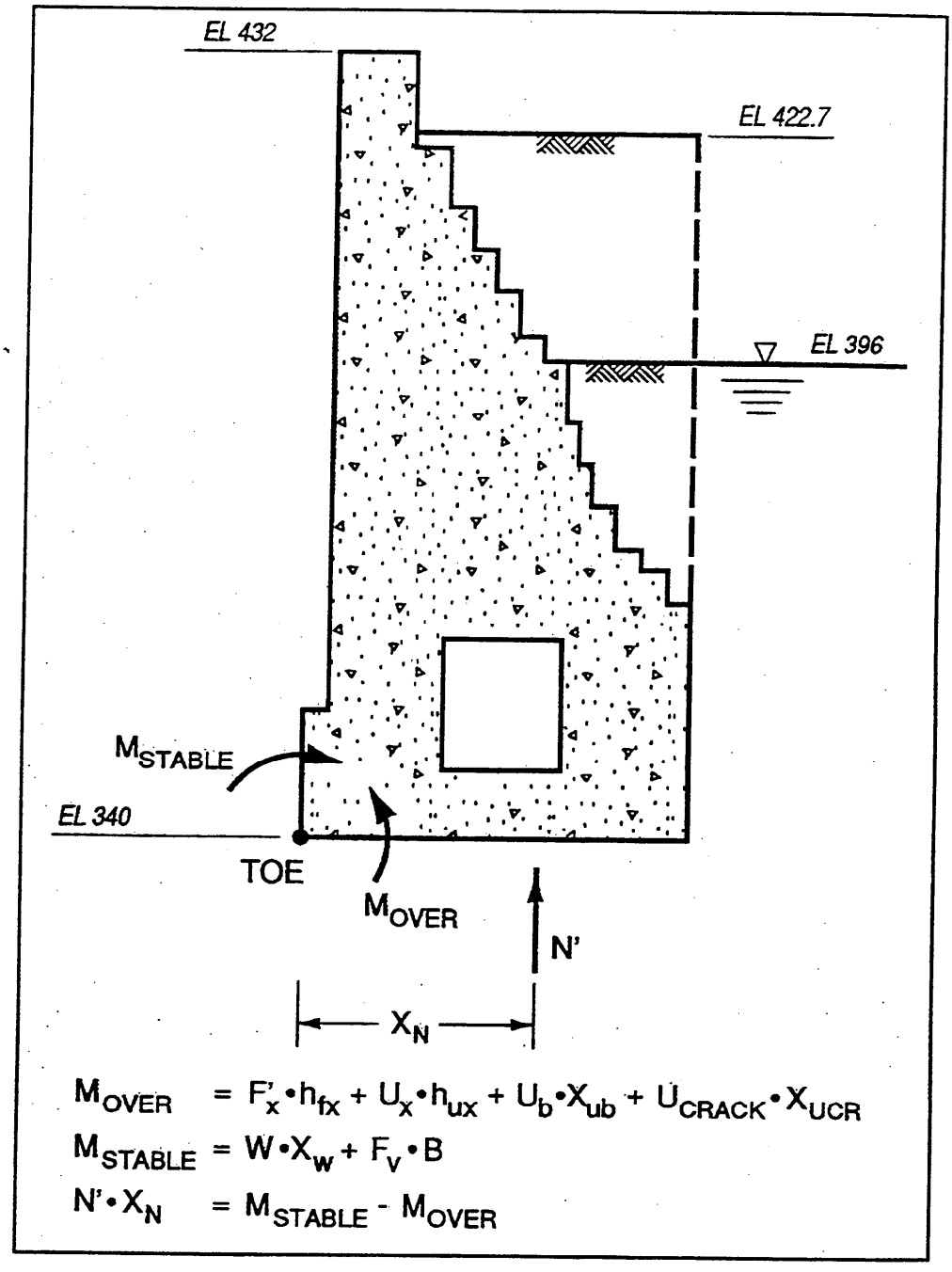

Figure A12. Moment equilibrium

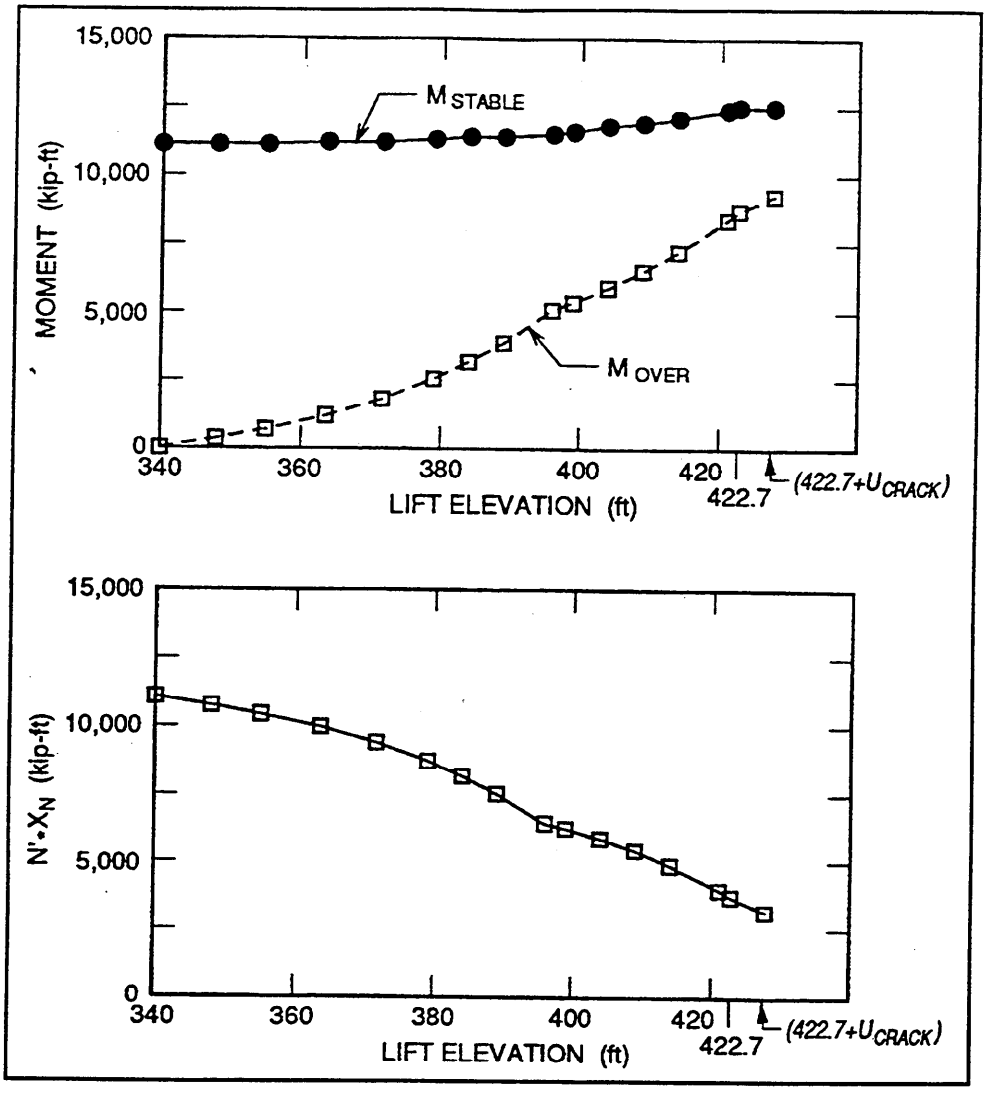

Figure A13. Variations in values of M_{OVER}, M_{STABLE}, and $N' \cdot x_N$ with lift elevations (1 ft = 0.305 m, 1 kip-ft = 1,356.1 kN-m)

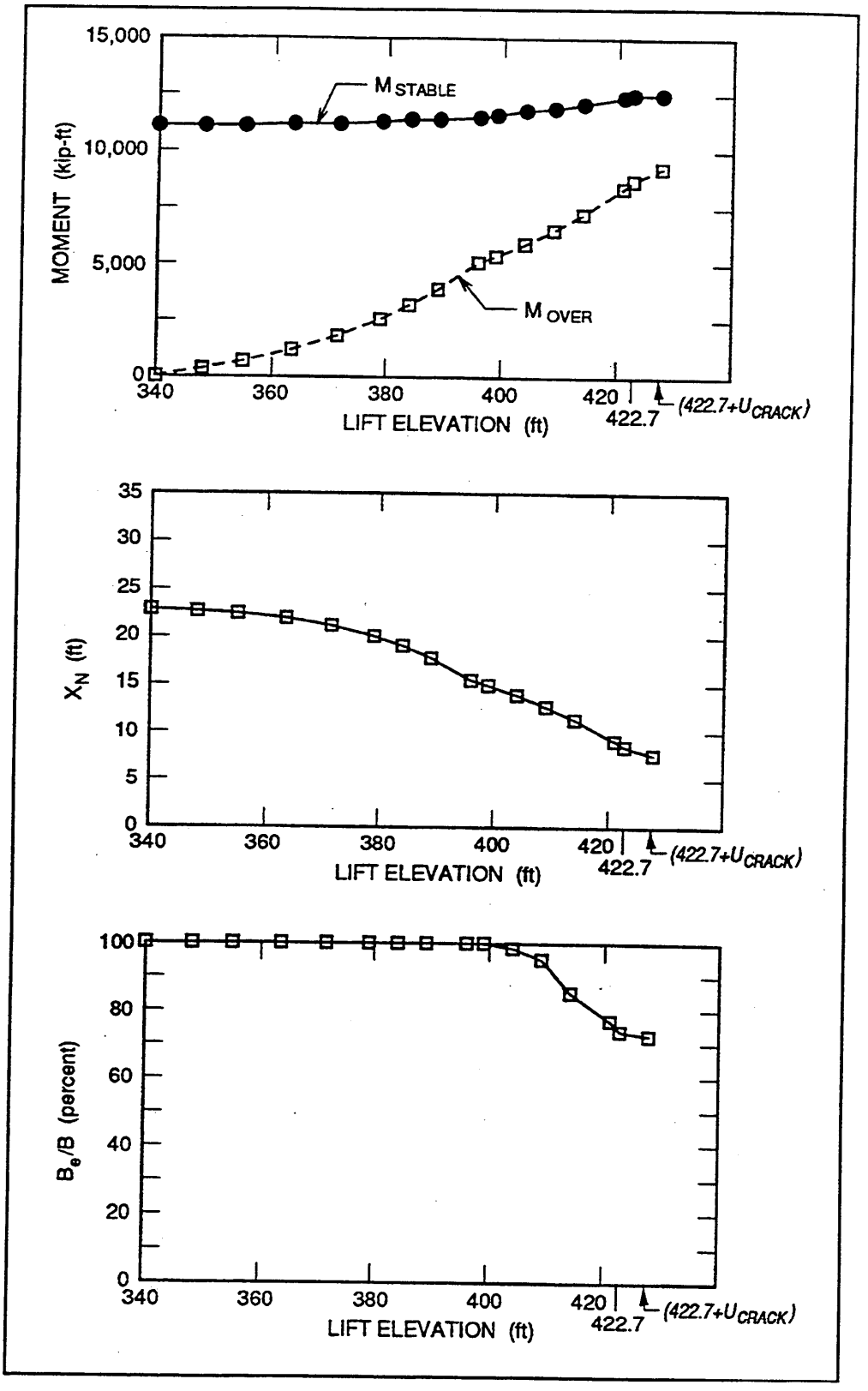

Figure A14. Variations in values of M_{OVER}, M_{STABLE}, X_m and B_e/B with lift elevations (1 ft = 0.305 m, 1 kip-ft = 1,356.1 kN-m)

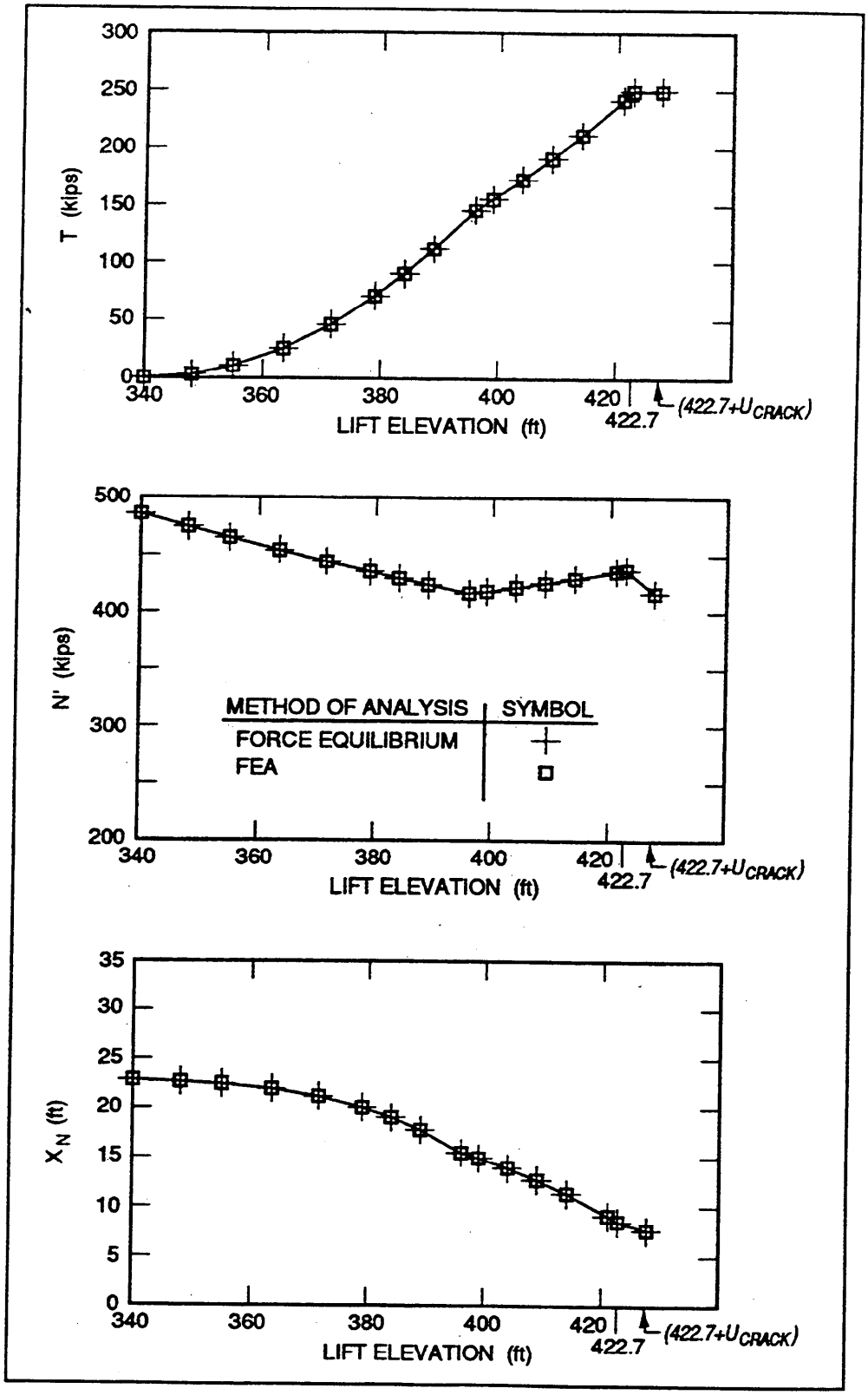

Figure A15. Variations in values of T, N', and X_N from results of conventional force equilibrium and finite element analyses (1 ft = 0.305 m, 1 kip = 4.448 kN)

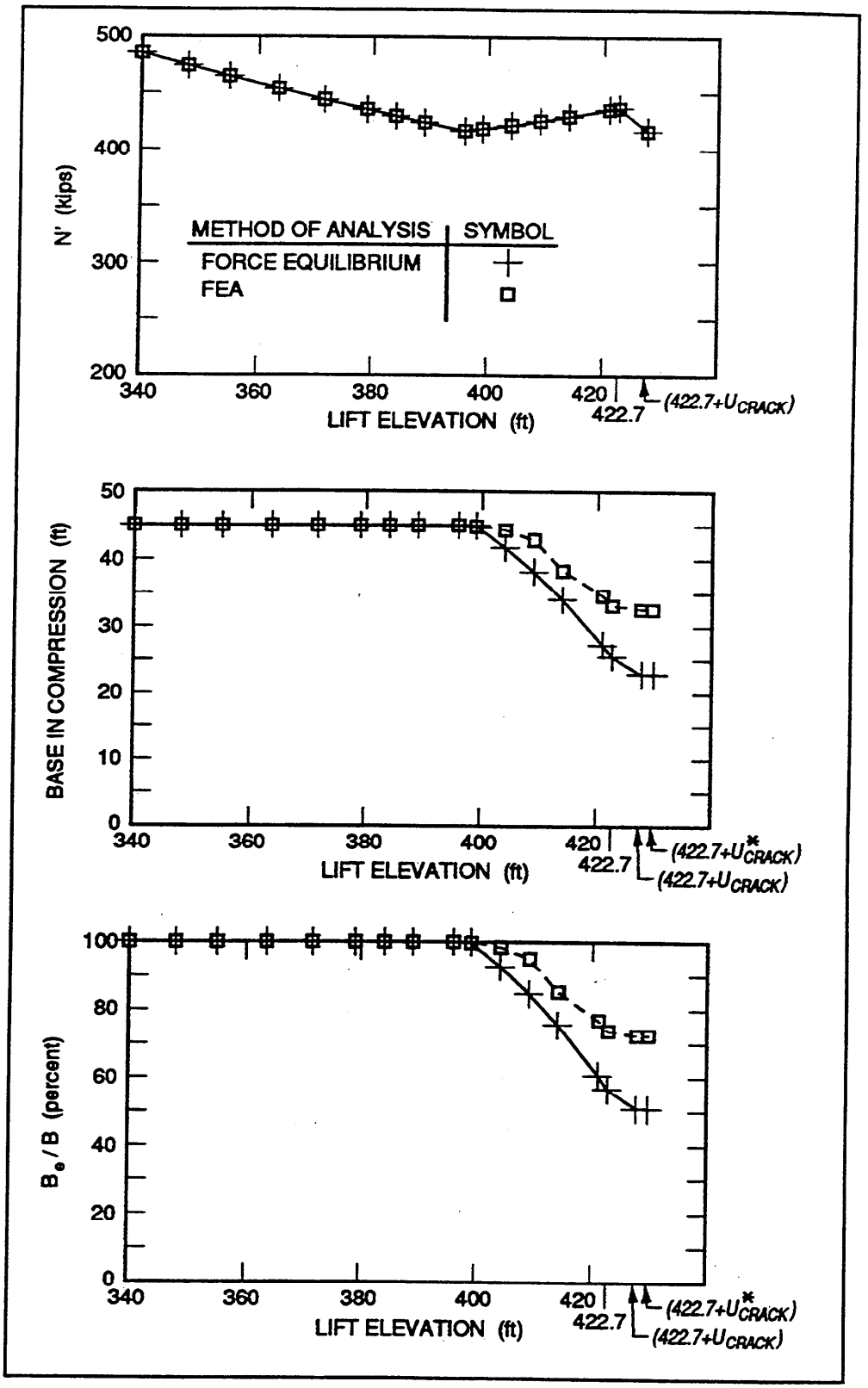

Figure A16. Variations in values of N', B_e, and B_e/B from results of conventional force equilibrium and finite element analyses (1 ft = 0.305 m, 1 kip = 4.448 kN)

Appendix B
Settlement Analyses of a Partially Submerged One-Dimensional Soil Column

There are two major requirements for the assignment of material parameters in the complete soil-structure interaction analysis of Locks 27 Monolith 7E using the backfill placement method that is incorporated in SOILSTRUCT-ALPHA. One requirement is that the material properties assigned to the soil used to model the backfill possess an at-rest earth pressure coefficient equal to 0.45. The second requirement is that the stress-strain model for the soil representing the backfill be representative of the soil comprising the backfill. Calculations described in this appendix were used in the assignment of values for the hyperbolic stress-strain soil model of the backfill.

This appendix summarizes the results of two settlement analyses of a partially submerged one-dimensional (1-D) soil column. Settlement of the soil column resulted from self-weight. Calculations were made using SOILSTRUCT-ALPHA and Janbu's tangent modulus method. This pair of finite element and 1-D closed-form analyses were used to finalize the material parameters assigned to soil that comprises the backfill in the SOILSTRUCT-ALPHA backfill placement analysis of Locks 27 Monolith 7E. Site-specific triaxial test data were unavailable for the Locks 27 backfill. Material parameters were assigned in the finite element analyses based on empirical correlations to the results for similar types of soils for which hyperbolic stress-strain curve material parameters are available.

The free field within the backfill of the Figure 38 (Chapter 3 in the main text) two-dimensional (2-D) finite element mesh of Locks 27 Monolith 7E gravity retaining wall analysis is located along a vertical section at a distance of three times the height of the backfill, measured from the heel. This free field section serves as the model for the 1-D soil column discussed in this appendix. The compression (settlement) of the soil model that comprises the free field will be the same as that for a 1-D (constrained) settlement analysis because:

a. The surface elevation of the backfill is constant (elevation 422.7[1]).

b. At any given elevation in the free field, the soil layers possess uniform compressibility.

c. A hydrostatic water table exists throughout the backfill (el 396).

d. The horizontal strain ϵ_x equals zero.

e. The vertical settlement at any given elevation in the free field backfill is uniform.

One-Dimensional Settlement Analysis of a Partially Submerged 1-D Soil Column Using SOILSTRUCT-ALPHA

Figure B1 shows the SOILSTRUCT-ALPHA finite element model of the 1-D soil column used in this appendix. The soil column is 82.7 ft (25.2 m) high and is submerged over nearly two-thirds of its height (56 ft (17.1 m)). Water pressures are assumed hydrostatic within the backfill, and the rise in the water table is assumed concurrent with the placement of the soil lifts. These two assumptions are consistent with the backfill placement analysis of Locks 27 Monolith 7E, described in Chapter 3(see main text). The finite element mesh for the soil column comprises 29 soil layers, with 20 of these layers below the water table. The elevations of the nodes defining the soil elements in this figure were the same elevations as the nodes defining the free field section in Figure 38 (Chapter 3). Interface elements of approximately zero shear stiffness and very large normal stiffness were included along the vertical faces of the mesh shown in Figure B1 to take advantage of the postprocessing capability within SOILSTRUCT-ALPHA. SOILSTRUCT-ALPHA computes the horizontal and vertical resultant forces and their points of application (elevation) along specified regions of interface elements using the normal and shear stress data. Each column of 29 interface elements defined a single region in this backfill placement analysis. These results expedited the calculation of the horizontal earth pressure coefficient K_h (equivalent to an at-rest coefficient K_o in the 1-D soil column) for the finite element analysis of the soil column. One requirement of the material properties assigned to the soil used to model the backfill was that the soil possess an at-rest earth pressure coefficient equal to 0.45.

Total unit weights equal to 125 and 130 pcf (2,002 and 2,082 kg/m^3) were assigned to the soils above and below the water table, respectively. Material properties assigned to the hyperbolic stress-strain relationship for the soil elements are given in Table B1. The values for the parameters listed in this table are typical of clean sands (e.g., SW or SP (Unified Soil Classification System)) of

---

[1] All elevations (el) cited herein are in feet referenced to the National Geodetic Vertical Datum.

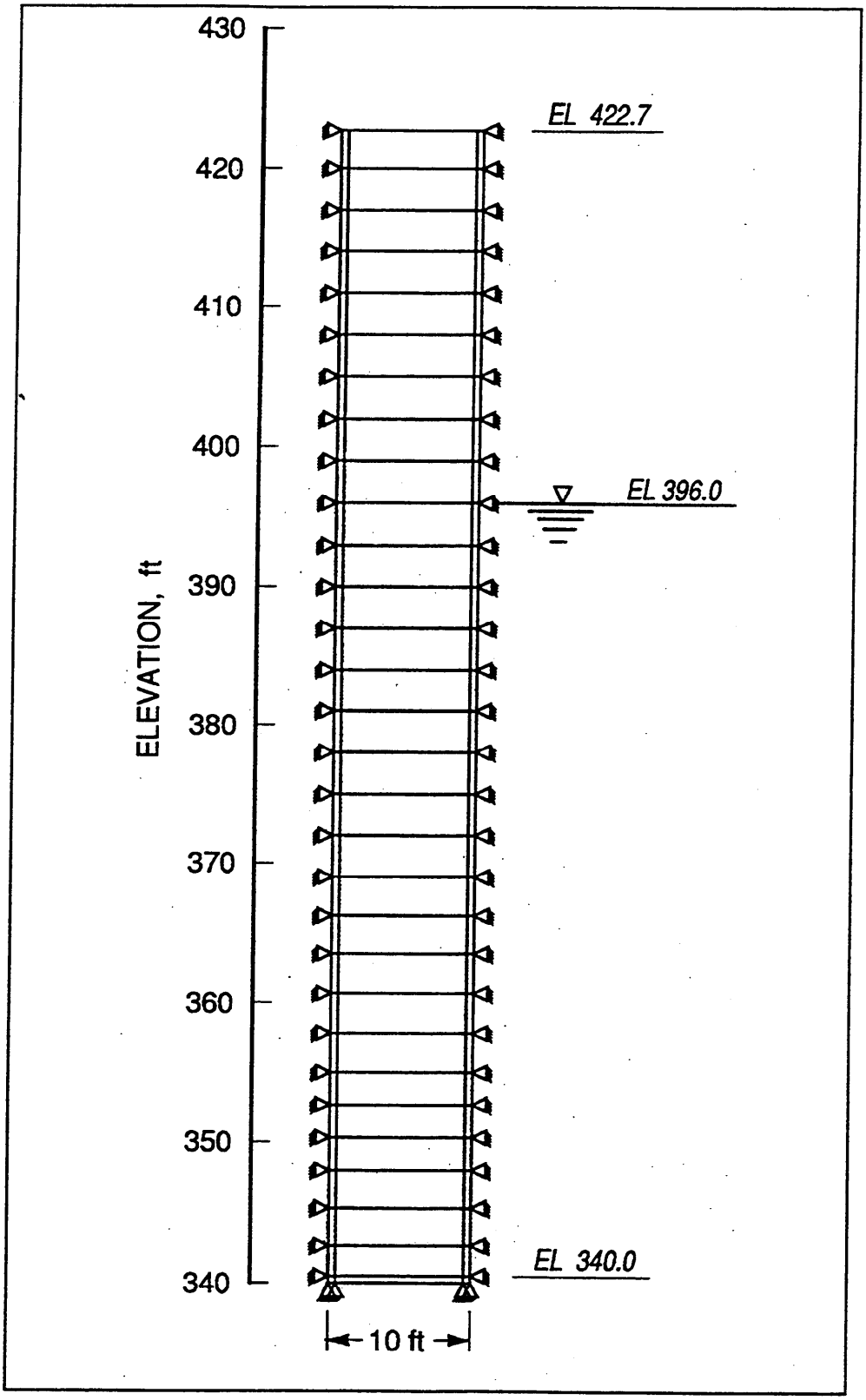

Figure B1. Finite element mesh for 1-D column analysis (1 ft = 0.305 m)

Table B1
Hyperbolic Stress-Strain and Strength Parameters[1]

Backfill	Unit Weight pcf (kg/m³)	Strength Parameters		Hyperbolic Parameters						
		c' psf (MPa)	ϕ' deg	K5	n	K_{UR}	K_B	m	υ_{nom}	R_F
Moist Sand	125.0 (2002)	0 (0)	35	500	0.5	600	200	0.5	0.088	0.7
Submerged Sand	130.0 (2082)	0 (0)	35	500	0.5	600	200	0.5	0.088	0.7

[1]Note:

$$\textit{Tangent Modulus, } E_t = E_i \left(1 - R_F\, SL\right)^2$$

$$\textit{Initial Modulus, } E_i = K\, P_a \left(\frac{\sigma_3'}{P_a} \right)^n$$

$$\textit{Stress Level, } SL = \left(\sigma_1 - \sigma_3 \right) / \left(\sigma_1 - \sigma_3 \right)_{Failure}$$

$$\left(\sigma_1 - \sigma_3 \right)_{Failure} = \frac{2\, c' \cos \phi + 2\, \sigma_3' \sin \phi}{1 - \sin \phi}$$

$$\textit{Unload-Reload Modulus, } E_{UR} = K_{UR}\, P_a \left(\frac{\sigma_3'}{P_a} \right)^n$$

$$\textit{Bulk Modulus, } B = \frac{E_i}{\left(3 - 6\, \upsilon_{nom} \right)}$$

$$\textit{Bulk Modulus, } B = K_B\, P_a \left(\frac{\sigma_3'}{P_a} \right)^m$$

υ_{nom} = *Nominal value of Poisson's ratio*

$$\textit{Poisson's ratio, } \upsilon = \frac{1}{2} \left[1 - \left[\left(1 - 2\, \upsilon_{nom} \right) \left(1 - R_F\, SL \right)^2 \right] \right]$$

P_A = atmospheric pressure

Table B2
Material Properties for Interface Elements Comprising SOILSTRUCT-ALPHA Finite Element Model of 1-D Soil Column Analysis[1]

Material Region	k_n psf/ft (MPa/m)	k_s psf/ft (MPa/m)
Interface	1.0×10^8 (15,708.7)	1 (1.57×10^{-4})

[1] Note:

Equations for Interface Model

The normal stress at the center of the interface element is given by

$$\sigma_n = k_n \Delta_n$$

where Δ_n is the average relative displacement normal to the interface element. The shear stress at the center of the interface element is given by

$$\tau_s = k_s \Delta_s$$

where Δ_s is the average relative shear displacement along the interface element.

medium density. The material properties assigned to the interface elements are given in Table B2.

One of the material parameters assigned to the soil is the value for the nominal Poisson's ratio. The nominal Poisson's ratio υ_{nom} used in SOILSTRUCT-ALPHA differs from the traditional strength of material's definition of Poisson's ratio υ. The compete derivation of υ_{nom} and its corresponding value of υ is given in Appendix C. Using the relationship

$$K_o = \frac{1 - (1 - 2\,\nu_{nom})\left[1 - R_F \dfrac{(1 - \sin\phi)(1 - K_o)}{2\,K_o \sin\phi}\right]^2}{1 + (1 - 2\,\nu_{nom})\left[1 - R_F \dfrac{(1 - \sin\phi)(1 - K_o)}{2\,K_o \sin\phi}\right]^2} \qquad \text{(C7)}$$

υ_{nom} is computed equal to 0.088 for the Table 1 material properties with K_o equal to 0.45. Using the following relationship from Appendix C,

$$\nu = \frac{1 - (1 - 2\,\nu_{nom}) * (1 - R_F\,SL)^2}{2} \qquad \text{(C8)}$$

with $R_F = 0.7$, $SL = 0.457$, and $\upsilon_{nom} = 0.088$ results in υ equal to 0.309. SL was computed using SOILSTRUCT-ALPHA to be 0.457, on average, for the 29 soil elements of Figure B1.

In 1978, a bulk modulus formulation was developed by Duncan and his colleagues for use in SOILSTRUCT (Ebeling, Peters, and Clough 1992 (see References at end of main text)). This formulation is given in Table B1. The bulk modulus is intended to replace Poisson's ratio as the second elastic parameter. Calculation of corresponding (and equivalent) value of the bulk modulus number K_b for the bulk modulus formulation is made using Equation C10 and described in the last section of Appendix C. With $K = 500$, $\upsilon_{nom} = 0.088$, and the bulk modulus exponent $m = n = 0.5$, K_b equals 202.26 (listed as a value of 200 in Table B1).

The backfill placement analysis of the Figure B1 soil column was conducted in 29 lifts or, equivalently, 29 load increments using SOILSTRUCT-ALPHA. The groundwater level was assumed to rise as the backfill was placed. With water pressures assumed hydrostatic at any given elevation, a buoyant unit weight equal to 67.6 pcf (1,082.8 kg/m ^{3}) was assigned to the 20 layers of soil below the water table (below el 396) in the backfill placement analysis. The distributions of horizontal effective stress and vertical effective stress with elevation computed within the soil elements after placement of the final (29th) lift are shown in Figure B2. The integral over the height of the soil column of the horizontal effective stresses, labeled σ'_x in Figure B2, is equal to the horizontal effective force F'_x. The horizontal effective force F'_x was computed by SOILSTRUCT-ALPHA using the normal effective stresses within the interface elements to be equal to 151,859 lb (675,502.5 N). The value of the horizontal earth pressure coefficient K_h is computed to be 0.45 by

$$K_h = \frac{F'_h}{\int_{el\ 340}^{el\ 422.7} \sigma'_y\, dy} \tag{B1}$$

The denominator is the integral of the vertical effective stress (i.e., the effective overburden pressure) distribution in Figure B2 with depth and is designated as F'_y. The force F'_y equals 337,452 lb (1,501,061 N). With the lateral strain ϵ_x equal to zero along the soil column, K_h (Equation B2) is equivalent to K_σ.

Settlements calculated using SOILSTRUCT-ALPHA are listed in Table B3 for the nodes corresponding to the four lift elevations identified in Figure B3 (els 360.67, 378, 396, and 411). El 340 (base) and el 422.7 (top of backfill) are included for reference in this table. Table B4 summarizes the initial and final effective overburden pressures as well as the fraction of the final effective overburden base pressure (el 340) for each lift elevation.

Two settlement values corresponding to the initial and final values are listed for each node in Table B3. The initial value is equal to zero in all cases and occurs when the stage of backfill placement (identified by lift number in

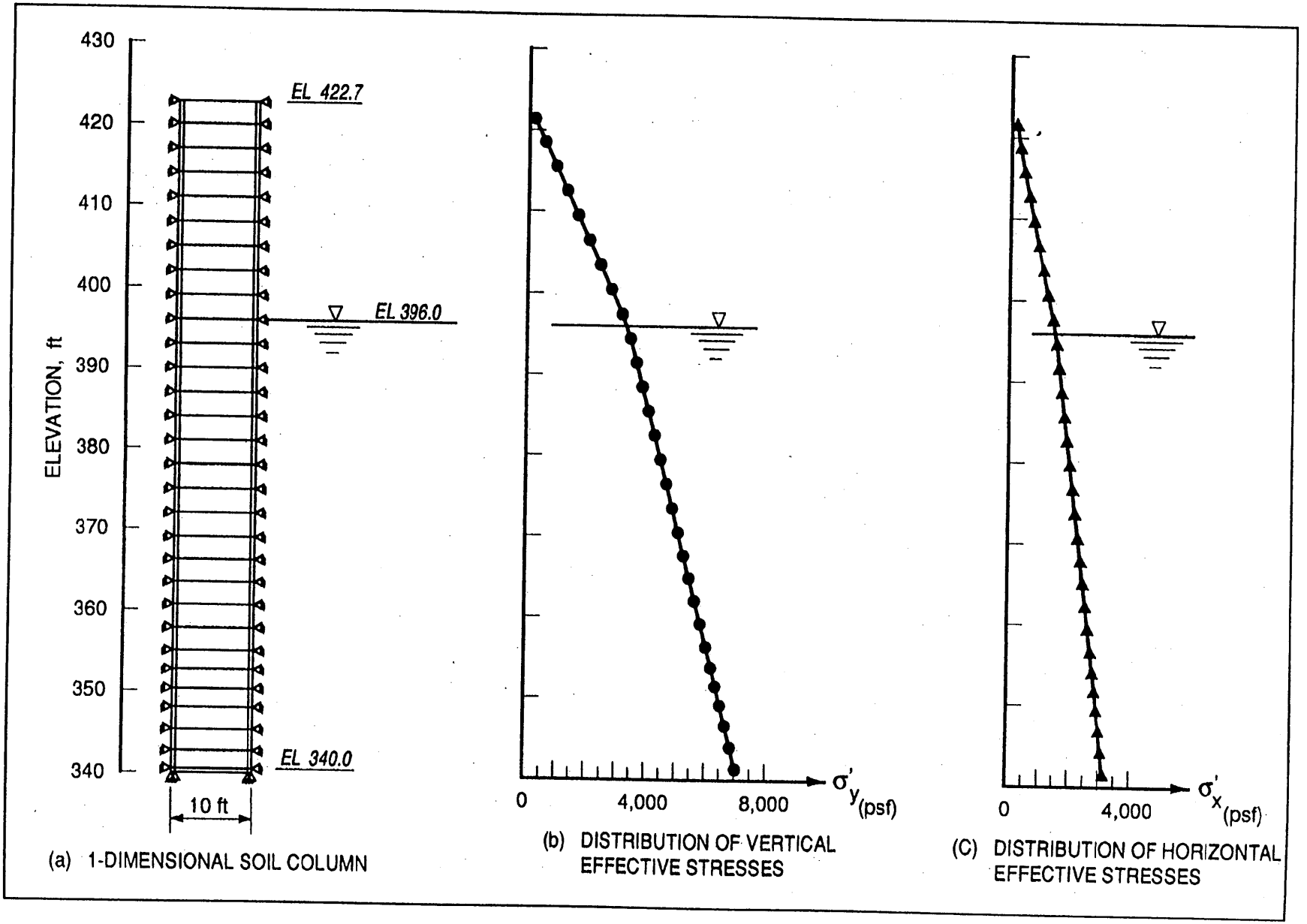

Figure B2. Results of 1-D soil column analysis using SOILSTRUCT (1 ft = 0.305 m, 1 MPa = 20,885.5 psf)

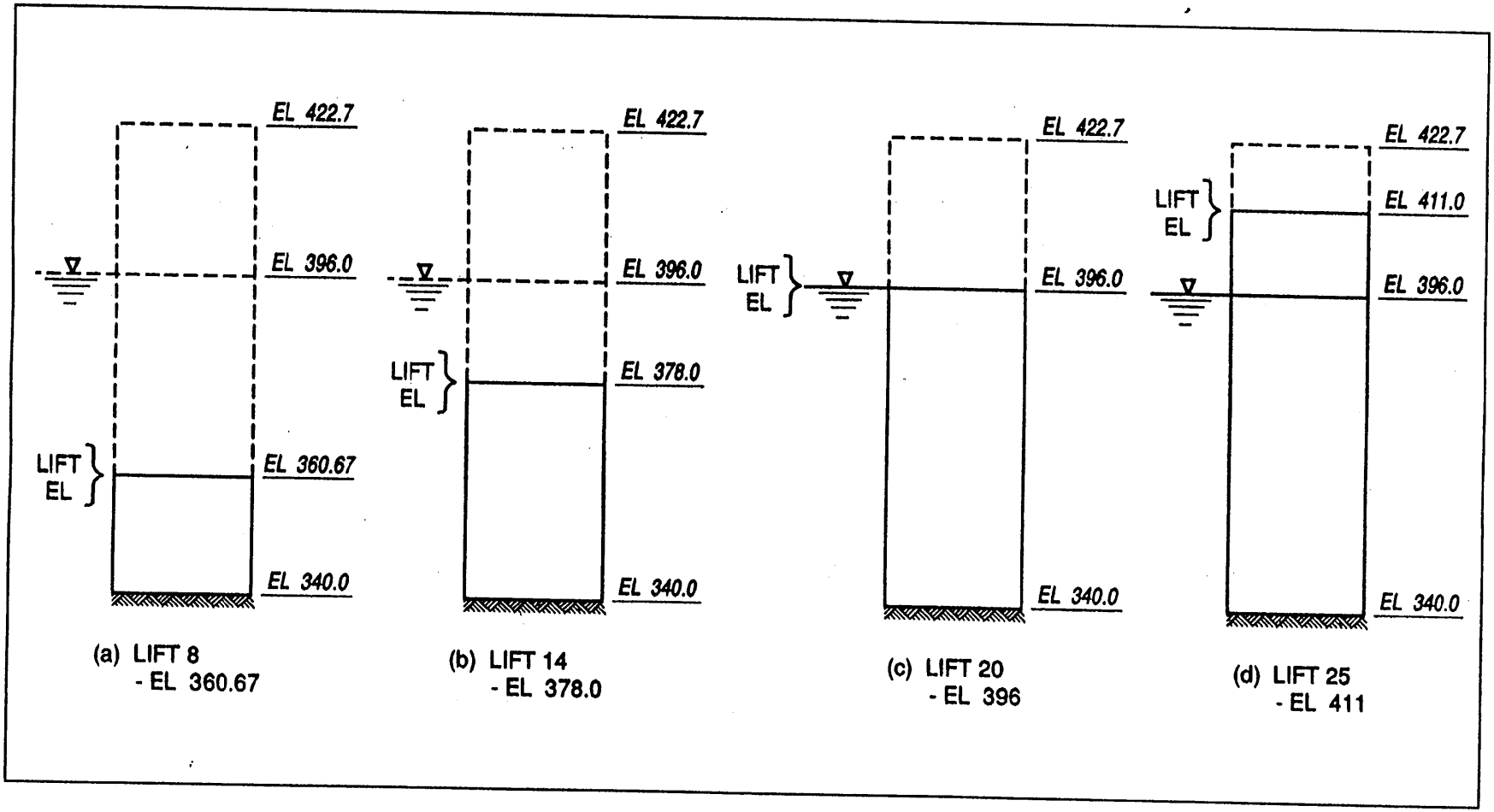

Figure B3. Four lift stages of the backfill placement analysis used in the evaluation

Table B3
Settlements at Select Backfill Elevations Due to Self-Weight of Backfill and Calculated Using SOILSTRUCT-ALPHA

El of Node ft (m)	Initial			Final		
	Lift	Backfill El ft (m)	s ft (m)	Lift	Backfill El ft (m)	s ft (m)
340 (103.6)	Base	340 (103.6)	0 (0)	29	422.7 (128.83)	0 (0)
360.67 (109.93)	8	360.67 (109.93)	0 (0)	29	422.7 (128.83)	0.190071 (0.057933)
378 (115.21)	14	378 (115.21)	0 (0)	29	422.7 (128.83)	0.269503 (0.0821755)
396 (120.7)	20	396 (120.7)	0 (0)	29	422.7 (128.83)	0.289522 (0.088246)
411 (125.27)	25	411 (125.27)	0 (0)	29	422.7 (128.83)	0.152937 (0.046615)
422.7 (128.85)	29	422.7 (128.85)	0 (0)	29	422.7 (128.83)	0 (0)

Table B4
Range in Effective Overburden Pressures for Select Elevations in Backfill

Lift	El ft (m)	Effective Overburden Pressure, σ'_v		Final σ'_v @ El / Final σ'_v @ El 340
		Initial psf (kPa)	Final psf (kPa)	
Base	340 (103.6)	0 (0)	7,123 (341)	1.0
8	360.67 (109.93)	0 (0)	5,726 (274)	0.8
14	378 (115.21)	0 (0)	4,554 (218)	0.64
20	396 (120.7)	0 (0)	3,337 (159.77)	0.47
25	411 (125.27)	0 (0)	1,462 (70)	0.21
29	422.7 (128.85)	0 (0)	0 (0)	0

Figure B3) attains an elevation equal to the nodal point elevation in the backfill placement analysis. Recall that in a backfill placement analysis, nodal point settlements result from the self-weight of the backfill *above* the elevation of the nodal point. The second value of settlement for each node is computed after placement of the final (29th) lift in the backfill placement analysis. A rigid base is assumed so the settlement is 0 at el 340 (base). The settlement at el 422.7, the top of the backfill (lift 29), will also be equal to 0 since loading is due to self-weight of the soil *above* each given lift elevation. The Table B3 results show that the largest settlements are calculated within the middle half, as compared to the lower and upper quarters, of the backfill.

Settlement Analysis of a Partially Submerged 1-D Soil Column Using Janbu's Tangent Modulus Method

Janbu (1963, 1965, 1967, 1985) developed an approach for calculating the settlement of a soil column in one-dimensional compression (i.e., lateral strains equal to zero) that accounts for nonlinear stress-strain response of soils (also described in Holtz (1991), Meyerhof and Fellenius, 1985, and Section 5.4 of Barker et al. (1991). This analytical approach was shown by Janbu to be applicable to nearly all types of soils. Appendix D describes the theoretical development of a relationship for vertical strain to be used to calculate the settlement of a 1-D soil column using Janbu's tangent modulus method. The relationship derived in Appendix D is used to calculate the settlements of the submerged portion of the Figure B1 soil column in Appendix E and the settlements of the "dry" portion of the soil column in Appendix F. The settlements result from the self-weight of the backfill during backfill placement. The derivations given in Appendixes E and F assume concurrent rise of a hydrostatic water table with placement of backfill lifts.

The total settlement s within the *submerged portion* of the backfill of height h_3 (Figure E1 or E2) due to the self-weight of backfill above this elevation (of height $h_2 + h_1$) is calculated using

$$s = s_A - s_B \tag{E1}$$

with

$$s_A = \frac{4}{3} * \frac{1}{m} * \frac{1}{\gamma_b} * \frac{1}{\sigma_a^{1/2}} \left[\left(\gamma_t * h_1 + \gamma_b * h_2 + \gamma_b * h_3 \right)^{3/2} - \left(\gamma_t * h_1 + \gamma_b * h_2 \right)^{3/2} \right] \tag{E2}$$

and

$$s_B = \frac{4}{3} * \frac{1}{m} * \gamma_b^{1/2} * \frac{1}{\sigma_a^{1/2}} * (h_3)^{3/2} \tag{E3}$$

The total settlement s within the *dry portion* of the backfill at height $[h_2 + h_3]$ in Figures F1 or F2 is due to the self-weight of backfill above this elevation (of height h_1) and is calculated using

$$s = s_1 + s_2 \tag{F1}$$

where

$$s_1 = \frac{4}{3} * \frac{1}{m} * \gamma_t^{1/2} * \frac{1}{\sigma_a^{1/2}} \left[(h_1 + h_2)^{3/2} - (h_1)^{3/2} - (h_2)^{3/2}\right] \tag{F2}$$

and

$$s_2 = \frac{4}{3} * \frac{1}{m} * \frac{1}{\gamma_b} * \frac{1}{\sigma_a^{1/2}} \left[(\gamma_t h_1 + \gamma_t h_2 + \gamma_b h_3)^{3/2} - (\gamma_t h_1 + \gamma_t h_2)^{3/2}\right] - \frac{4}{3} * \frac{1}{m} * \frac{1}{\gamma_b} * \frac{1}{\sigma_a^{1/2}} \left[(\gamma_t h_2 + \gamma_b h_3)^{3/2} - (\gamma_t h_2)^{3/2}\right] \tag{F3}$$

Table B5 lists settlements calculated using Janbu's tangent modulus method for the select lift elevations 360.67, 378, 396, and 411 (Figure B3). El 340 (base) and el 422.7 (top of backfill) are included for reference. Equations E1, E2, and E3 are used to calculate the settlement due to self-weight of the backfill for el 360.67 (lift 8), el 378 (lift 14), and el 396 (lift 20). Equations F1, F2, and F3 are used to calculate the settlement due to self-weight of the backfill for el 411 (lift 25). A modulus number m equal to 250 and stress exponent a equal to 0.5 were assigned to the soil (using the values given in Figure D2 as a guide). A rigid base is assumed so the settlement is 0 at el 340. The settlement at el 422.7, the top of the backfill (lift 29), will also be equal to 0 since loading is due to self-weight of the soil *above* each given lift elevation. The largest settlements are calculated within the middle half as compared to the lower and upper quarters of the backfill, as was observed for the results of the SOILSTRUCT-ALPHA backfill placement analysis.

Table B5
Settlements at Select Backfill Elevations Due to Self-Weight of Backfill and Calculated Using Janbu's Tangent Stiffness Method[1]

Lift	El ft (m)	h_1 ft (m)	h_2 ft (m)	h_3 ft (m)	s_A ft (m)	s_B ft (m)	s_1 ft (m)	s_2 ft (m)	s ft (m)
Base	340 (103.63)	-	-	-	-	-	-	-	0 (0)
8	360.67 (109.93)	26.7 (8.14)	35.33 (10.77)	20.67 (6.3)	0.2618 (0.0797)	0.0896 (0.0273)	-	-	0.1722 (0.0525)
14	378 (115.21)	26.7 (8.14)	18 (5.49)	38 (11.58)	0.5039 (0.1535)	0.2233 (0.0680)	-	-	0.2806 (0.0855)
20	396 (120.70)	26.7 (8.14)	0 (0)	56 (17.07)	0.7003 (0.2135)	0.3994 (0.1217)	-	-	0.3009 (0.0917)
25	411 (125.27)	11.7 (3.57)	15 (4.57)	56 (17.07)	-	-	0.0516 (0.0157)	0.1091 (0.0332)	0.1607 (0.0489)
29	422.7 (128.83)	-	-	-	-	-	-	-	0 (0)

[1] Note:
For elevations at and below el 396,

$$s = s_A - s_B \quad \text{(E1)}$$

For elevations above el 396,

$$s = s_1 + s_2 \quad \text{(F1)}$$

with

$\gamma_{t\text{-}A}$ = 125 pcf (2,002 kg/m^3)
$\gamma_{t\text{-}B}$ = 130 pcf (2,082 kg/m^3)
$\gamma_{b\text{-}B}$ = 67.6 pcf (1,082.6 kg/m^3)
m = 250
σ_a = 2116.8 psf (101 kPa)

Comparison of Results From the Settlement Analyses Using SOILSTRUCT-ALPHA and Janbu's Tangent Modulus Method

SOILSTRUCT-ALPHA uses a hyperbolic representation for the nonlinear stress-strain relationship for soil, as described by Duncan and Chang (1970). Consolidated-drained triaxial test results were not available for the backfill of Locks 27 Monolith 7E. To determine the hyperbolic constitutive model parameters, correlations between the soil type (sand) and its density (medium dense to dense) with data in the literature (Duncan et al. 1978) were made in order to assign the model parameters for the complete soil-structure interaction analysis.

Table B6
Comparisons of Settlements at Select Elevations After Backfilling to El 422.7, Computed Using SOILSTRUCT-ALPHA and Janbu's Tangent Stiffness Method

El of Node ft (m)	SOILSTRUCT-ALPHA			Janbu's Tangent Stiffness Method			$\frac{s_{Janbu}}{s_{SOILSTRUCT}}$
	Lift	Backfill El ft (m)	s ft (m)	Lift	Backfill El ft (m)	s ft (m)	
340 (103.63)	29	422.7 (128.83)	0 (0)	29	422.7 (128.83)	0 (0)	-
360.67 (109.93)	29	422.7 (128.83)	0.190071 (0.057963)	29	422.7 (128.83)	0.1722 (0.0524)	0.906
378 (115.21)	29	422.7 (128.83)	0.269503 (0.0821445)	29	422.7 (128.83)	0.2806 (0.0855)	1.041
396 (120.70)	29	422.7 (128.83)	0.289522 (0.0882463)	29	422.7 (128.83)	0.3009 (0.0917)	1.039
411 (125.27)	29	422.7 (128.83)	0.152937 (0.0466151)	29	422.7 (128.83)	0.1607 (0.0489)	1.051
422.7 (128.83)	29	422.7 (128.83)	0 (0)	29	422.7 (128.83)	0 (0)	-

This provided a basis for assigning values to the stiffness parameters K (modulus number) and n (exponent), and R_F (failure ratio). A settlement analysis was also undertaken using Janbu's tangent modulus method to gain insight into the compression characteristics for the parameters assigned to the hyperbolic stress-strain curve used in SOILSTRUCT-ALPHA analyses.

Table B6 summarizes the settlements calculated using SOILSTRUCT-ALPHA and Janbu's tangent stiffness method at four select nodes within the backfill. The average ratio of the settlements computed using the two calculation methods, designated as $s_{Janbu}/s_{SOILSTRUCT}$ in this table, equals 1.009. This average ratio shows that the values of the parameters assigned to the hyperbolic stress-strain soil model used in SOILSTRUCT-ALPHA are consistent with the stiffness characteristics for this type of soil according to Janbu's tangent stiffness method.

Appendix C
Derivation of Nominal Poisson's Ratio Used in SOILSTRUCT-ALPHA

SOILSTRUCT-ALPHA is a general-purpose finite element program for two-dimensional (2-D) plain strain analysis of soil-structure interaction problems. It calculates displacements and stresses due to incremental construction and/or load application and is capable of modeling nonlinear stress-strain material behavior by means of the incremental application of loads. The ALPHA version of SOILSTRUCT accounts for the possibility of base separation near the heel of the wall (Ebeling, Duncan, and Clough 1990; Ebeling et al. 1992 (see References in main text)). This appendix summarizes the derivation of a nominal Poisson's ratio used in the constitutive relationship of soils that is incorporated in SOILSTRUCT-ALPHA. The relationships given in the appendix assume drained stress-strain behavior for the soil.

The constitutive relationship used for all 2-D elements is Hooke's law. SOILSTRUCT-ALPHA uses an incremental, equivalent linear method of analysis to model nonlinear material behavior. In this type of analysis, the incremental changes in stresses are related to the incremental strains through the linear relationship

$$\begin{Bmatrix} \Delta\sigma_x \\ \Delta\sigma_y \\ \Delta\tau_{xy} \end{Bmatrix} = \frac{3B}{9B - E_t} \begin{bmatrix} (3B + E_t) & (3B - E_t) & 0 \\ (3B - E_t) & (3B + E_t) & 0 \\ 0 & 0 & E_t \end{bmatrix} \begin{Bmatrix} \Delta\epsilon_x \\ \Delta\epsilon_y \\ \Delta\gamma_{xy} \end{Bmatrix}$$

in which

$\Delta\sigma_x$ = normal stress increment

$\Delta\sigma_y$ = normal stress increment

$\Delta\tau_{xy}$ = shear stress increment

$\Delta\epsilon_x$ = normal strain increment

$\Delta\epsilon_y$ = normal strain increment

$\Delta\gamma_{xy}$ = shear strain increment

E_t = tangent Young's modulus

B = bulk modulus

If an element is undergoing primary loading, the tangent modulus is evaluated in accordance with stresses in that element using the following expressions developed by Duncan and Chang (1970):

$$E_t = E_i \ (1 - R_F \ SL \ )^2$$

with the initial Young's modulus (Janbu 1963) given by

$$E_i = K \ P_a \left(\frac{\sigma_3'}{P_a} \right)^n$$

where K is the modulus number and n is the modulus exponent, which control the effects of effective confining pressure on the hyperbolic stress strain model. P_a is atmospheric pressure.

The stress level SL within each element is calculated using

$$SL = (\sigma_1 - \sigma_3) / (\sigma_1 - \sigma_3)_{Failure}$$

with

$$(\sigma_1 - \sigma_3)_{Failure} = \frac{2 \ c' \cos \phi + 2 \ \sigma_3' \sin \phi}{1 - \sin \phi}$$

The Mohr-Coulomb shear strength parameters c' and ϕ' and failure ratio R_F control the the level of mobilized shear strength on the stress-strain curve. The formulation for the bulk modulus B used in the ALPHA version of SOILSTRUCT is given by

$$B = \frac{E_i}{3 \ (1 - 2 \ \nu_{nom})} \qquad \text{(C1)}$$

Because the relationship for B uses E_i rather than E_t, the term for the "plain strain" bulk modulus M_b becomes approximate.

$$\begin{Bmatrix} \Delta\sigma_x \\ \Delta\sigma_y \\ \Delta\tau_{xy} \end{Bmatrix} = \begin{bmatrix} (M_b + M_d) & (M_b - M_d) & 0 \\ (M_b - M_d) & (M_b + M_d) & 0 \\ 0 & 0 & M_d \end{bmatrix} \begin{Bmatrix} \Delta\epsilon_x \\ \Delta\epsilon_y \\ \Delta\gamma_{xy} \end{Bmatrix}$$

where

$$M_b = \frac{3\,B}{2\,(1 + \nu_{nom})}$$

$$M_d = G = \frac{E_t}{2\,(1 + \nu_{nom})}$$

Because the plain strain bulk modulus relationship is an approximate formulation, a nominal value for Poisson's ratio, designated as υ_{nom} is used. The value for υ_{nom} differs from the traditional value for Poisson's ratio (according to the strength of materials definition), which is designated as υ in this report.

Thus, the relationships between incremental strains and incremental stresses are defined by two engineering constants, the Young's modulus and υ_{nom}. The remainder of this appendix is devoted to the derivation of relationships that can be used to define the value of υ_{nom} in terms of other engineering parameters and in terms of the traditional value for υ.

Relationship Between K_o and the Traditional Poisson's Ratio for Confined Compression

This section derives the relationship between K_o and the traditional Poisson's ratio υ. The relationship between horizontal strain ϵ_x and the vertical and lateral stresses, σ_y, σ_x, and σ_z, respectively, is given by

$$\epsilon_x = \frac{1}{E}\left[\,\sigma_x - \nu\,(\,\sigma_y + \sigma_z\,)\,\right]$$

In confined compression, the lateral strains equal zero. Thus,

$$0 = \frac{1}{E}\left[\,\sigma_x - \nu\,(\,\sigma_y + \sigma_z\,)\,\right]$$

Rearranging,

$$\sigma_x - \nu * \sigma_z = \nu * \sigma_y$$

The at-rest earth pressure coefficient K_o is the effective horizontal earth pressure (i.e., σ_x and σ_z) divided by the effective overburden pressure σ_y. Introducing the at-rest earth pressure coefficient for the case of σ_z equal to σ_x and rearranging, the relationship becomes

$$K_o = \frac{\nu}{1 - \nu} \tag{C2}$$

Relationship Between K_o, Bulk Modulus, and Young's Modulus

This section derives the relationship between K_o, B, and E. The change in mean stress σ_{mean} is related to the change in volumetric strain ϵ_v ($= \epsilon_x + \epsilon_y + \epsilon_z$) by the bulk modulus B,

$$\sigma_{mean} = B\ \epsilon_v$$

or

$$B = \frac{\sigma_{mean}}{\epsilon_v}$$

The relationships between stresses and strains are

$$\epsilon_x = \frac{1}{E}\left[\ \sigma_x - \nu\ (\ \sigma_y + \sigma_z\ )\ \right]$$

$$\epsilon_y = \frac{1}{E}\left[\ \sigma_y - \nu\ (\ \sigma_z + \sigma_x\ )\ \right]$$

and

$$\epsilon_z = \frac{1}{E}\left[\ \sigma_z - \nu\ (\ \sigma_x + \sigma_y\ )\ \right]$$

For isotropic compression under a normal stress equal to σ_o (i.e., $\sigma_x = \sigma_y = \sigma_z = \sigma_o$) with no shear,

$$\epsilon_v = \epsilon_x + \epsilon_y + \epsilon_z = \frac{3\,\sigma_o}{E}(1 - 2\,\nu)$$

Thus, with σ_{mean} [$= (\sigma_x + \sigma_y + \sigma_z)/3$] equal to σ_o, the relationship for bulk modulus in terms of Young's modulus and Poisson's ratio is given by

$$B = \frac{E}{3\,(1 - 2\,\nu)}$$

Rearranging,

$$\nu = \frac{3\,B - E}{6\,B} \tag{C3}$$

Introducing Equation C3 into Equation C2 gives

$$K_o = \frac{6\,B * (3\,B - E)}{6\,B * [6\,B - (3\,B - E)]} = \frac{3\,B - E}{3\,B + E} \tag{C4}$$

Relationship Between K_o and the Nominal Poisson's Ratio

This section derives the relationship between K_o and the nominal Poisson's ratio υ_{nom}. Introducing Equation C1 into Equation C4,

$$K_o = \frac{\dfrac{3\,E_i}{3\,(1 - 2\,\nu_{nom})} - E_t}{\dfrac{3\,E_i}{3\,(1 - 2\,\nu_{nom})} - E_t}$$

Simplifying,

$$K_o = \frac{E_i - (1 - 2\,\nu_{nom}) * E_t}{E_i + (1 - 2\,\nu_{nom}) * E_t}$$

Introducing the Duncan and Chang relationship

$$E_t = E_i \left(1 - R_F \, SL \right)^2$$

results in

$$K_o = \frac{1 - \left(1 - 2 \, \nu_{nom} \right) * \left(1 - R_F \, SL \right)^2}{1 + \left(1 - 2 \, \nu_{nom} \right) * \left(1 - R_F \, SL \right)^2} \qquad \text{(C5)}$$

Assuming the Jaky approximation for K_o (valid for normally consolidated soils),

$$K_o = 1 - \sin \phi$$

and with

$$\sigma_3' = K_o \, \sigma_1'$$

for the one-dimensional (constrained) settlement problem where σ'_1 equals σ'_v, σ'_3 equals σ'_h, and σ'_1 equals $K_o * \sigma'_3$, the stress level for c' equals 0 is given by

$$SL = \frac{\left(\sigma_1 - \sigma_3 \right)}{\left(\sigma_1 - \sigma_3 \right)_{Failure}} = \frac{\left(\frac{1}{K_o} - 1 \right) \sigma_3'}{\frac{2 \sin \phi}{1 - \sin \phi} \sigma_3'}$$

Simplifying,

$$SL = \frac{\left(1 - \sin \phi \right) * \left(1 - K_o \right)}{2 \, K_o \sin \phi} \qquad \text{(C6)}$$

Introducing Equation C6 into Equation C5 results in

$$K_o = \frac{1 - \left(1 - 2 \, \nu_{nom} \right) * \left(1 - R_F \, \frac{\left(1 - \sin \phi \right) \left(1 - K_o \right)}{2 \, K_o \sin \phi} \right)^2}{1 + \left(1 - 2 \, \nu_{nom} \right) * \left(1 - R_F \, \frac{\left(1 - \sin \phi \right) \left(1 - K_o \right)}{2 \, K_o \sin \phi} \right)^2} \qquad \text{(C7)}$$

For example, assigning $K_o = 0.45$, $\phi = 35$ degrees, $R_F = 0.7$, and solving for υ_{nom} by trial and error using Equation C7 results in υ_{nom} equal to 0.088.

Relationship Between the Nominal and the Traditional Poisson's Ratio

This section derives the relationship between the nominal Poisson's ratio υ_{nom} and the traditional Poisson's ratio υ. Given Equation C3,

$$\nu = \frac{3\,B - E}{6\,B} \tag{C3}$$

and introducing Equation C1, the bulk modulus formulation used in SOILSTRUCT-ALPHA, results in

$$\nu = \frac{\dfrac{3\,E_i}{3\,(1 - 2\,\nu_{nom})} - E_t}{6\,\dfrac{E_i}{3\,(1 - 2\,\nu_{nom})}}$$

Simplifying,

$$\nu = \frac{E_i - (1 - 2\,\nu_{nom}) * E_t}{2 * E_i}$$

Introducing the Duncan and Chang relationship for E_t results in

$$\nu = \frac{E_i - (1 - 2\,\nu_{nom}) * E_i\,(1 - R_F\,SL)^2}{2 * E_i}$$

Simplifying,

$$\nu = \frac{1 - (1 - 2\,\nu_{nom}) * (1 - R_F\,SL)^2}{2} \tag{C8}$$

For example, assigning $R_F = 0.7$, $SL = 0.457$, and $\upsilon_{nom} = 0.088$ results in υ equal to 0.309.

Relationship Between the Nominal Poisson's Ratio and the Bulk Modulus Formulation

In 1978, a bulk modulus formulation was developed by Duncan and his colleagues for use in SOILSTRUCT.

$$B = K_B P_a \left(\frac{\sigma_3'}{P_a} \right)^m$$

The bulk modulus B is intended to replace Poisson's ratio as the second elastic parameter. Ebeling, Peters, and Clough (1992) implemented this bulk modulus formulation in another verison of SOILSTRUCT. This version of SOILSTRUCT was modified to analyze a densely reinforced soil berm proposed for construction at Red River Lock No. 1 (Ebeling et al. 1993). This section of the appendix develops a relationship between the coefficient K_b, used in the bulk modulus formulation, and the nominal Poisson's ratio υ_{nom}

Starting with the relationship

$$B = \frac{E_i}{3 (1 - 2 \nu_{nom})} \tag{C1}$$

and introducing the bulk modulus formulation for B and the Janbu initial Young's modulus formulation

$$E_i = K P_a \left(\frac{\sigma_3'}{P_a} \right)^n$$

results in

$$\nu_{nom} = \frac{1}{2} \left(1 - \frac{1}{3} \frac{K_{ur}}{K_B} \right) \tag{C9}$$

when m equals n. Rearranging,

$$K_B = \frac{K}{3 (1 - 2 \nu_{nom})} \tag{C10}$$

For example, assigning $K = 500$, $\upsilon_{nom} = 0.088$, and $m = n = 0.5$ results in K_b equal to 202.26 (approximately 200).

Appendix D
Theoretical Development of Relationship for Vertical Strain in One-Dimensional Soil Column Using Janbu's Tangent Modulus Method

Janbu (1963, 1965, 1967, 1985, see References in main text) developed an approach for calculating the settlement of a soil column in one-dimensional (1-D) compression (i.e., lateral strains equal to zero) that accounts for nonlinear stress-strain response of soils (also described in Holtz 1991, Meyerhof and Fellenius 1985, and Section 5.4 of Barker et al. 1991). This analytical approach was shown by Janbu to be applicable to nearly all types of soils. This appendix describes the theoretical development of a relationship for vertical strain to be used to calculate the settlement of a 1-D soil column using Janbu's tangent modulus method. The relationship derived in this appendix is used to calculate the settlements of the soil columns given in Appendixes E, F, and G, and rebound of the soil column in Appendix H.

The settlement s of a 1-D soil column is calculated by integrating with *depth* z the vertical strains $\epsilon_z(z)$ induced in the soil column under some type of loading (i.e., the self-weight of the soil in the case of the backfill placement analysis of a soil column).

$$s = \int_0^H \epsilon_z(z)\, dz$$

Because the vertical strains are likely to vary with depth z in the soil column, they are denoted as a function of z in this equation. Janbu recognized that the load-deformation relationship in 1-D compression of an element of soil (at depth z in a soil column) is nearly always nonlinear, as idealized in the example shown in Figure D1. Thus, the slope of this curve, referred to as the tangent constrained modulus M_v, decreases in value as the vertical effective stress increases. The

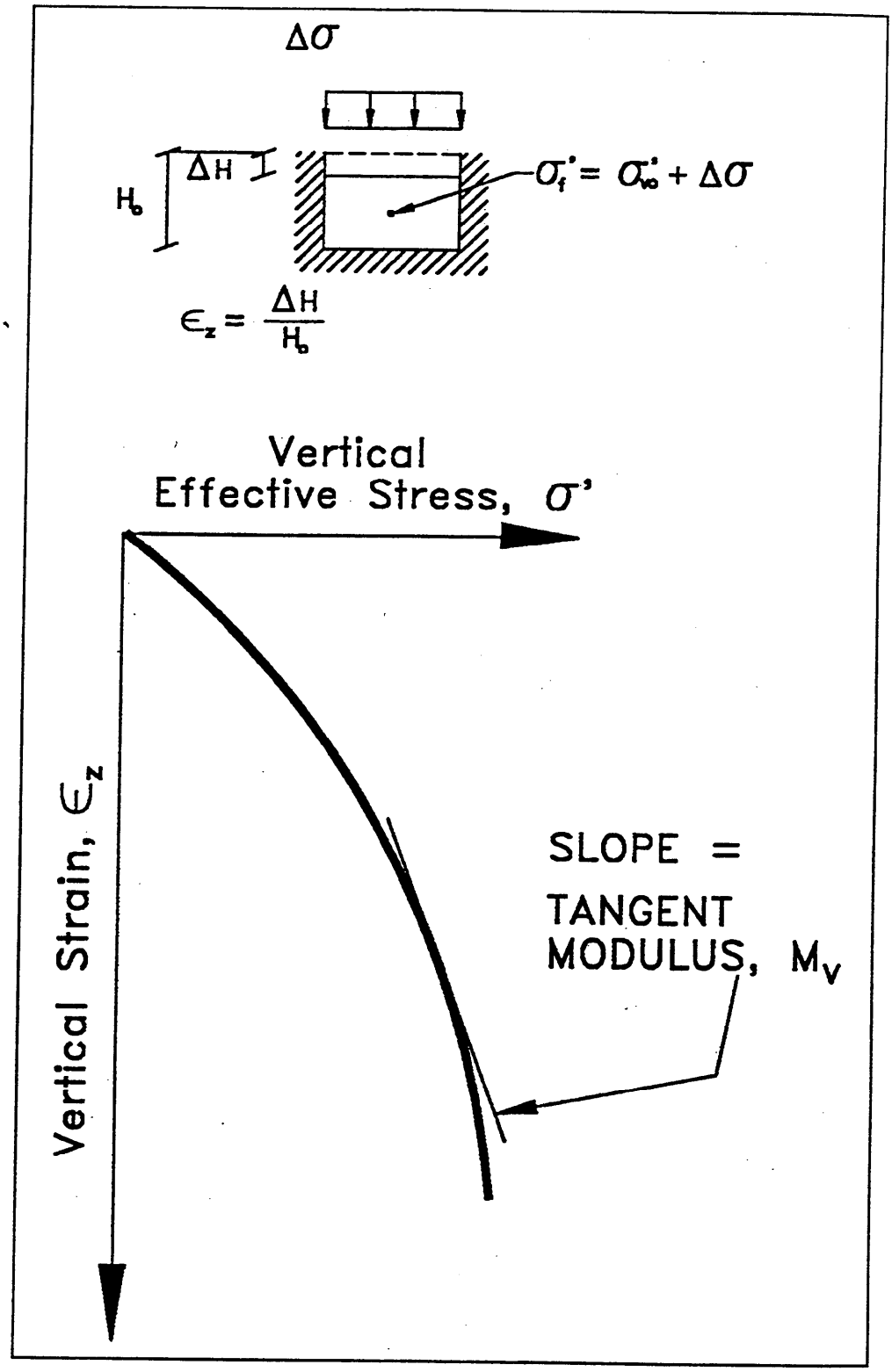

Figure D1. Nonlinear stress-strain relation typical for soils

tangent constrained modulus M_v relates the increment in vertical strain to the increment in effective vertical stress

$$\Delta\sigma_z' = M_v \, \Delta\epsilon_z$$

or

$$\Delta\epsilon_z = \frac{1}{M_v} \Delta\sigma_z'$$

Using the results of 1-D consolidation tests, Janbu showed that the tangent constrained modulus can by described at any given effective stress σ' within a soil element (which is in the same direction as the strain) by the following relationship

$$M_v = m\sigma_a \left(\frac{\sigma'}{\sigma_a} \right)^{1-a}$$

and is applicable for a wide variety of soils. The stress σ_a is a reference stress and is usually taken as atmospheric pressure. The values for the coefficient m and exponent a are determined by fitting the Janbu relationship for M_v to the consolidation test data. Figure D2 lists values typical of modulus numbers m and stress exponent a for sands and gravels. Additionally, the coefficient of volume change m_v is the inverse of the tangent constrained modulus.

$$m_v = \frac{1}{M_v} = \frac{1}{m\sigma_a} * \frac{1}{\left(\frac{\sigma'}{\sigma_a} \right)^{1-a}}$$

$$m_v = \frac{1}{m\sigma_a} * \left(\frac{\sigma'}{\sigma_a} \right)^{-(1-a)} = \frac{1}{m\sigma_a} * \left(\frac{\sigma'}{\sigma_a} \right)^{a-1}$$

Thus, the vertical strain within a soil element or, equivalently, at a specified depth z within a soil column, which is subjected to an increase in vertical effective stress from σ'_{vo} to σ'_f, is given by

$$\epsilon_z = \int_{\sigma'_{vo}}^{\sigma'_f} \frac{1}{M_v} \, d\sigma'$$

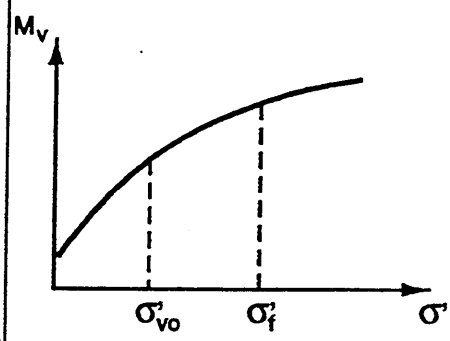

$a \approx 0.5$

$$M_v = m\,\sigma_a \left(\frac{\sigma'}{\sigma_a}\right)^{0.5} = m\sqrt{\sigma_a \sigma'}$$

$$\varepsilon_z = \frac{2}{m} \cdot \left[\left(\frac{\sigma'_f}{\sigma_a}\right)^{0.5} - \left(\frac{\sigma'_{vo}}{\sigma_a}\right)^{0.5}\right]$$

M_v = JANBU'S TANGENT CONSTRAINED MODULUS

σ_a = ATMOSPHERIC PRESSURE

TYPICAL VALUES OF THE STRESS EXPONENT a AND THE MODULUS NUMBER m

SOIL TYPE	STRESS EXPONENT, a	MODULUS NUMBER, m
GRAVEL	0.5	400-40
SAND		
DENSE	0.5	400-250
COMPACT	0.5	250-150
LOOSE	0.5	150-100

Figure D2. Values typical of modulus numbers *m* and stress exponent *a* for sands and gravels (after Meyerhof and Fellenius 1985)

Introducing Janbu's relationship, the relationship for vertical strain becomes

$$\epsilon_z = \int_{\sigma'_{wo}}^{\sigma'_f} \frac{1}{m} * \frac{1}{\sigma_a} * \left(\frac{\sigma'}{\sigma_a}\right)^{a-1} d\sigma$$

Using an exchange of variables, let

$$w = \frac{\sigma'}{\sigma_a}, \quad then \quad w' = \frac{dw}{d\sigma} = \frac{1}{\sigma_a} \quad or \quad d\sigma = \sigma_a\, dw$$

Substituting these new variables into the relationship for vertical strain,

$$\epsilon_z = \int_{\sigma'_{vo}}^{\sigma'_f} \frac{1}{m} * \frac{1}{\sigma_a} * w^{a-1} * \sigma_a \, dw$$

Integrating,

$$\epsilon_z = \int_{\sigma_{vo}}^{\sigma'_f} \frac{1}{m} * w^{a-1} \quad dw = \frac{1}{m} \left[\frac{1}{a} \quad w^a \right]_{\sigma'_{vo}}^{\sigma'_f}$$

and simplifying

$$\epsilon_z = \frac{1}{m} * \frac{1}{a} * \left[\left(\frac{\sigma'}{\sigma_a} \right)^a \right]_{\sigma'_{vo}}^{\sigma'_f}$$

The vertical strain induced at a specified depth z in a soil column and subjected to an increase in effective stress to σ'_f is given by

$$\epsilon_z = \frac{1}{m} * \frac{1}{a} * \left[\left(\frac{\sigma'_f}{\sigma_a} \right)^a - \left(\frac{\sigma'_{vo}}{\sigma_a} \right)^a \right] \tag{D1}$$

For $a = 0.5$, this relationship becomes

$$\epsilon_z = \frac{2}{m} \left[\left(\frac{\sigma'_f}{\sigma_a} \right)^{1/2} - \left(\frac{\sigma'_{vo}}{\sigma_a} \right)^{1/2} \right] \tag{D2}$$

and, thus, the tangent constrained modulus M_v at vertical effective stress σ' is given by

$$M_v = m\sigma_a \sqrt{\frac{\sigma'}{\sigma_a}} = m \sqrt{\sigma' \, \sigma_a}$$

The value of M_v increases with increasing σ', as shown in Figure D2.

Appendix E
Theoretical Development of Settlement Analysis of Submerged Portion of One-Dimensional Soil Column Using Janbu's Tangent Modulus Method - Concurrent Rise of Hydrostatic Water Table With Placement of Backfill

Janbu (1963, 1965, 1967, 1985, see References in main text) developed an approach for calculating the settlement of a soil column in one-dimensional (1-D) compression (i.e., lateral strains equal to zero) that accounts for nonlinear stress-strain response of soils (also described in Holtz 1991, Meyerhof and Fellenius 1985, and Section 5.4 of Barker et al. 1991). This analytical approach was shown by Janbu to be applicable to nearly all types of soils. This appendix describes the theoretical development of the relationship used to calculate settlements within the *submerged portion* of a 1-D soil column using Janbu's tangent modulus method for the case of *a rise in a ground-water level as the backfill is placed.*

Figure E1 shows the 1-D soil column being used in the assignment of values for the hyperbolic stress-strain soil model for the backfill in the backfill placement analysis described in Chapter 3 (see main text). The total unit weights of the soil above and below the water table (elevation 396[1]) equal 125 pcf and 130 pcf (2,002 and 2,082 kg/m^3), respectively. The relationships derived in this appendix calculate settlement at the lift elevation (height h_3) identified in the

[1] All elevations (el) cited herein are in feet referenced to the National Geodetic Vertical Datum.

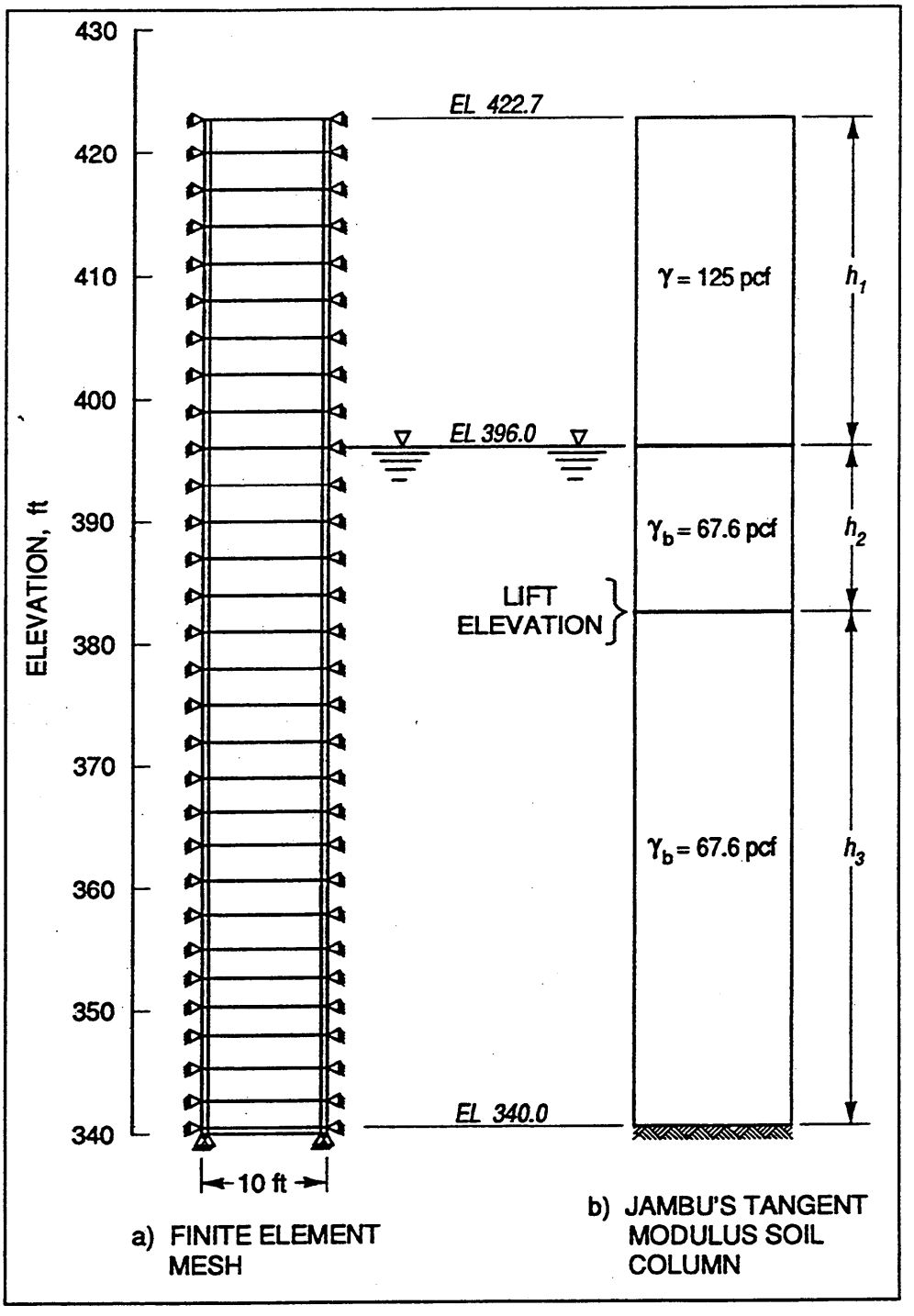

Figure E1. One-dimensional column analysis - lift elevation below the water table (1 ft = 0.305 m, 1 pcf = 16.018 kg/m^3)

submerged portion of the Figure E1 soil column due to the self-weight of the soil above this lift elevation $[h_1 + h_2]$. Hydrostatic water pressures are assumed at all stages of the analyses.

The settlement s of the submerged portion of the Figure E1 1-D soil column is calculated by integrating with *depth* z the vertical strains $\epsilon_z(z)$ induced in the soil column under some type of loading, which is the self-weight of the soil in the case of the backfill placement analysis of the soil column described in this section.

$$s = \int_0^H \epsilon_z(\, z\,)\, dz$$

Because the vertical strains are likely to vary with depth z in the soil column, they are denoted as a function of z in this equation. Janbu recognized that the load-deformation relationship in 1-D compression of an element of soil (at depth z in a soil column) is nearly always nonlinear. Using the results of 1-D consolidation tests, Janbu showed that the tangent constrained modulus M_v can by described at any given effective stress σ' within a soil element (which is in the same direction as the strain) by the following relationship

$$M_v = m\sigma_a \left(\frac{\sigma'}{\sigma_a}\right)^{1-a}$$

and is applicable for a wide variety of soils. The stress σ_a is a reference stress and is usually taken as atmospheric pressure. The values for the coefficient m and exponent a are determined by fitting the Janbu relationship for M_v to consolidation test data. Appendix D showed the relationship for the vertical strain ϵ_z induced at a specified depth z in a soil column and subjected to an increase in effective stress from σ'_{vo} to σ'_f to be

$$\epsilon_z = \frac{2}{m}\left[\left(\frac{\sigma'_f}{\sigma_a}\right)^{1/2} - \left(\frac{\sigma'_{vo}}{\sigma_a}\right)^{1/2}\right] \qquad \text{(D2)}$$

for $a = 0.5$ (Figure D2, typical value for sands and gravel).

The settlement at height h_3 (Figure E1) in the submerged portion of the Figure E1 soil column is calculated using

$$s = \int_o^{h_3} \epsilon_z\, dz$$

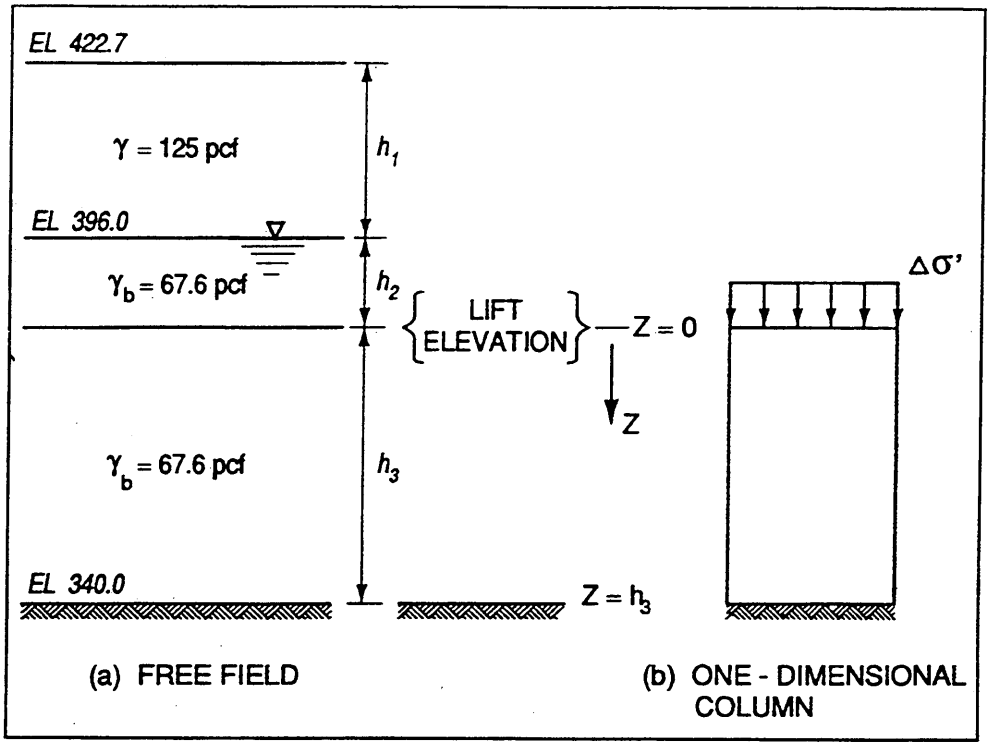

Figure E2. One-dimensional column - lift elevation below the water table (1 pcf = 16.018 kg/m^3)

The distribution of ϵ_z over depth h_3 is due to the self-weight of the soil column above this elevation and designated as $\Delta\sigma'$ in Figure E2. The overburden pressure $\Delta\sigma'$ is calculated on an effective stress basis because of the assumption of the concurrent rise in water table with the placement of each soil lift. Introducing Janbu's relationship for vertical strain ϵ_z (Equation D2), the relationship for settlement s becomes

$$s = \int_o^{h_3} \frac{2}{m} \left[\left(\frac{\sigma_f'}{\sigma_a} \right)^{1/2} - \left(\frac{\sigma_{vo}'}{\sigma_a} \right)^{1/2} \right] dz$$

Introducing

$$\sigma_{vo}' = \gamma_b * z$$

and

$$\sigma_f' = \sigma_{vo}' + \Delta\sigma'$$

where

$$\Delta\sigma' = \gamma_t * h_1 + \gamma_b * h_2$$

Thus σ_f' becomes

$$\sigma_f' = \gamma_t * h_1 + \gamma_b * h_2 + \gamma_b * z$$

the relationship for the settlement s at a given elevation becomes

$$s = \int_o^{h_3} \frac{2}{m} \left[\left(\frac{\gamma_t * h_1 + \gamma_b * h_2 + \gamma_b * z}{\sigma_a} \right)^{1/2} - \left(\frac{\gamma_b * z}{\sigma_a} \right)^{1/2} \right] dz$$

Designating the first and second terms inside the integral as terms A and B, respectively

$$s = s_A - s_B \tag{E1}$$

The contribution of term A to the total settlement s, designated s_A, is given by

$$s_A = \int_o^{h_3} \frac{2}{m} \, q^{1/2} \, dz$$

where the variable q is defined as

$$q = \frac{\gamma_t * h_1 + \gamma_b * h_2 + \gamma_b * z}{\sigma_a}$$

Differentiating q

$$\frac{dq}{dz} = \frac{\gamma_b}{\sigma_a} \quad or \quad dz = \frac{\sigma_a}{\gamma_b} \, dq$$

The settlement term A in terms of the variable q is

$$s_A = \int_o^{h_3} \frac{2}{m} \, q^{1/2} * \frac{\sigma_a}{\gamma_b} \, dq$$

Evaluating the integral,

$$s_A = \frac{2}{m} * \frac{2}{3} q^{3/2} * \frac{\sigma_a}{\gamma_b} \Big|_o^{h_3}$$

Replacing the variable q and evaluating the limits,

$$s_A = \frac{4}{3} * \frac{1}{m} * \left[\left(\frac{\gamma_t * h_1 + \gamma_b * h_2 + \gamma_b h_3}{\sigma_a} \right)^{3/2} * \frac{\sigma_a}{\gamma_b} - \left(\frac{\gamma_t * h_1 + \gamma_b * h_2 + o}{\sigma_a} \right)^{3/2} * \frac{\sigma_a}{\gamma_b} \right]$$

$$s_A = \frac{4}{3} * \frac{1}{m} * \frac{1}{\gamma_b} * \frac{1}{\sigma_a^{1/2}} \left[\left(\gamma_t * h_1 + \gamma_b * h_2 + \gamma_b * h_3 \right)^{3/2} - \left(\gamma_t * h_1 + \gamma_b * h_2 \right)^{3/2} \right] \quad \text{(E2)}$$

The contribution to total settlement by term B, designated s_B, is given by

$$s_B = \int_o^{h_3} \frac{2}{m} \left[\left(\frac{\gamma_b * z}{\sigma_a} \right)^{1/2} \right] dz$$

Introducing the variable r, s_B becomes

$$s_B = \int_o^{h_3} \frac{2}{m} r^{1/2} \, dz$$

where

$$r = \frac{\gamma_b * z}{\sigma_a}$$

and

$$\frac{dr}{dz} = \frac{\gamma_b}{\sigma_a} \quad or \quad dz = \frac{\sigma_a}{\gamma_b}\, dr$$

The complete relationship for s_B is

$$s_B = \int_o^{h_3} \frac{2}{m}\, r^{1/2} * \frac{\sigma_a}{\gamma_b}\, dr$$

Evaluating the integral

$$s_B = \frac{2}{m} * \frac{\sigma_a}{\gamma_b} * \frac{2}{3}\, r^{3/2} \Big|_o^{h_3}$$

Replacing the variable r

$$s_B = \frac{2}{m} * \frac{\sigma_a}{\gamma_b} * \frac{2}{3} \left[\left(\frac{\gamma_b\, z}{\sigma_a} \right)^{3/2} \right]_o^{h_3}$$

Evaluating the limits

$$s_B = \frac{4}{3} * \frac{1}{m} * \frac{\sigma_a}{\gamma_b} \left[\left(\frac{\gamma_b\, h_3}{\sigma_a} \right)^{3/2} - O \right]$$

results in

$$s_B = \frac{4}{3} * \frac{1}{m} \frac{\gamma_b^{3/2}}{\gamma_b} \frac{\sigma_a}{\sigma_a^{3/2}}\, h_3^{3/2}$$

Simplifying

$$s_B = \frac{4}{3} * \frac{1}{m} * \gamma_b^{1/2} * \frac{1}{\sigma_a^{1/2}} * (h_3)^{3/2} \qquad \text{(E3)}$$

The total settlement s within the submerged portion of the backfill of height h_3 due to the self-weight of backfill above this elevation (of height $h_2 + h_1$) is given by

$$s = s_A - s_B \tag{E1}$$

with

$$s_A = \frac{4}{3} * \frac{1}{m} * \frac{1}{\gamma_b} * \frac{1}{\sigma_a^{1/2}} \left[\left(\gamma_t * h_1 + \gamma_b * h_2 + \gamma_b * h_3 \right)^{3/2} - \left(\gamma_t * h_1 + \gamma_b * h_2 \right)^{3/2} \right]$$

and

$$s_B = \frac{4}{3} * \frac{1}{m} * \gamma_b^{1/2} * \frac{1}{\sigma_a^{1/2}} * (h_3)^{3/2} \tag{E3}$$

Appendix F
Theoretical Development of Settlement Analysis of Moist Portion of One-Dimensional Soil Column Using Janbu's Tangent Modulus Method - Concurrent Rise of Hydrostatic Water Table With Placement of Backfill

Janbu (1963, 1965, 1967, 1985, see References in main text) developed an approach for calculating the settlement of a soil column in one-dimensional (1-D) compression (i.e., lateral strains equal to zero) that accounts for nonlinear stress-strain response of soils (also described in Holtz 1991, Meyerhof and Fellenius 1985, and Section 5.4 of Barker et al. 1991). This analytical approach was shown by Janbu to be applicable to nearly all types of soils. This appendix describes the theoretical development of the relationship used to calculate settlements within the "moist" portion (i.e., above the water table) of a 1-D soil column using Janbu's tangent modulus method for the case of *a rise in a ground-water level as the backfill is placed.*

Figure F1 shows the 1-D soil column being used in the assignment of values for the hyperbolic stress-strain soil model for the backfill in the backfill placement analysis described in Chapter 3 (see main text). The total unit weights of the soil above and below the water table (elevation 396[1]) equal 125 pcf and 130 pcf (2,002 and 2,082 kg/m^3), respectively. The relationships derived in this appendix calculate settlement at the lift elevation (height $[h_2 + h_3]$) in the moist portion of the Figure F1 soil column due to the self-weight of the soil above this

[1] All elevations (el) cited herein are in feet referenced in the National Geodetic Vertical Datum.

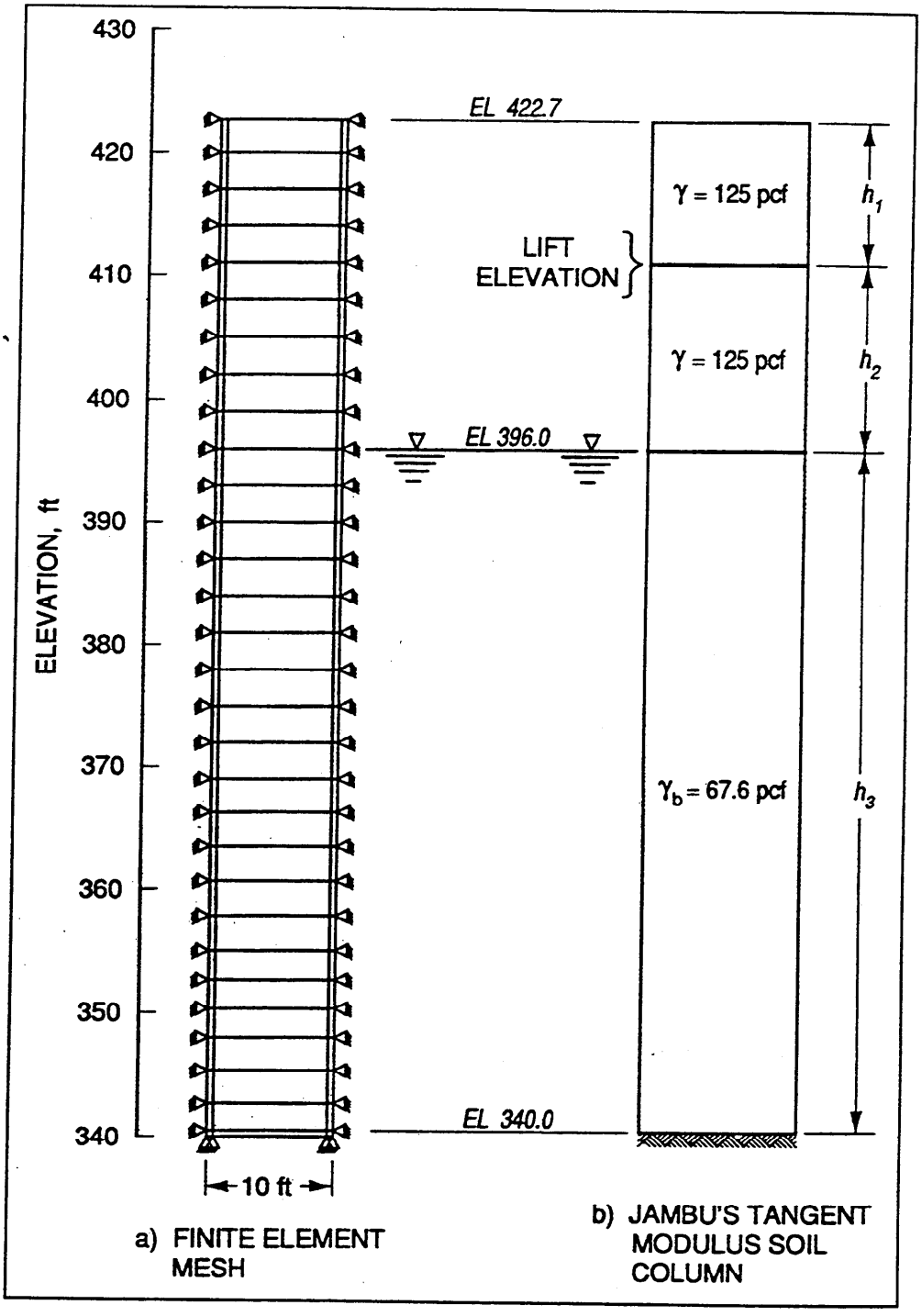

Figure F1. One-dimensional column analysis - lift elevation above the water table (1 ft = 0.305 m, 1 pcf = 16.018 kg/m^3)

lift elevation (h_1). Hydrostatic water pressures are assumed at all stages of the analyses.

The settlement s of the moist portion of the Figure F1 1-D soil column is calculated by integrating with *depth* z the vertical strains $\epsilon_z(z)$ induced in the soil column under some type of loading, which is the self-weight of the soil in the case of the backfill placement analysis of the soil column described in this section.

$$s = \int_0^H \epsilon_z(z)\, dz$$

Because the vertical strains are likely to vary with depth z in the soil column, they are denoted as a function of z in this equation. Janbu recognized that the load-deformation relationship in 1-D compression of an element of soil (at depth z in a soil column) is nearly always nonlinear. Using the results of 1-D consolidation tests, Janbu showed that the tangent constrained modulus M_v can by described at any given effective stress σ' within a soil element (which is in the same direction as the strain) by the following relationship

$$M_v = m\sigma_a \left(\frac{\sigma'}{\sigma_a} \right)^{1-a}$$

and is applicable for a wide variety of soils. The stress σ_a is a reference stress and is usually taken as atmospheric pressure. The values for the coefficient m and exponent a are determined by fitting the Janbu relationship for M_v to consolidation test data. Appendix D showed the relationship for the vertical strain ϵ_z induced at a specified depth z in a soil column and subjected to an increase in effective stress from σ'_{vo} to σ'_f to be

$$\epsilon_z = \frac{2}{m} \left[\left(\frac{\sigma'_f}{\sigma_a} \right)^{1/2} - \left(\frac{\sigma'_{vo}}{\sigma_a} \right)^{1/2} \right] \qquad \text{(D2)}$$

for $a = 0.5$ (Figure D2, typical value for sands and gravel).

The settlement at height $[h_2 + h_3]$ (Figure F1) in the moist portion of the Figure E1 soil column is calculated using

$$s = \int_o^{h_2+h_3} \epsilon_z\, dz = \int_o^{h_2} \epsilon_z\, dz + \int_{h2}^{h3} \epsilon_z\, dz$$

The distribution of ϵ_z over depth $[h_2 + h_3]$ is due to the self-weight of the soil column above this elevation and is designated as $\Delta\sigma'$ in Figure F2. The

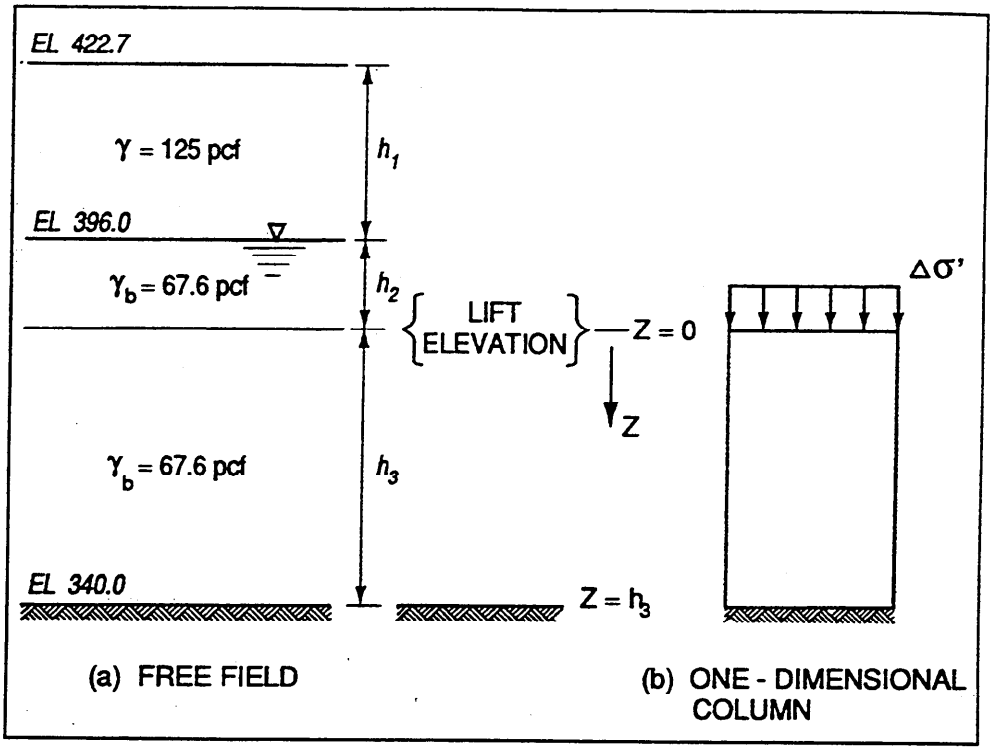

Figure F2. One-dimensional column - lift elevation above the water table (1 pcf = 16.018 kg/m^3)

overburden pressure $\Delta\sigma'$ is calculated on an effective stress basis because of the assumption of the concurrent rise in water table with the placement of each soil lift. Figure F3 shows the distributions of initial and final vertical effective stresses σ'_{vo} and σ'_f, where

$$\sigma'_{vo} = \gamma_t * z$$

and

$$\sigma'_f = \sigma'_{vo} + \Delta\sigma'$$

with

$$\Delta\sigma' = \gamma_t * h_1$$

Thus σ'_f becomes

$$\sigma'_f = \gamma_t * h_1 + \gamma_t * z$$

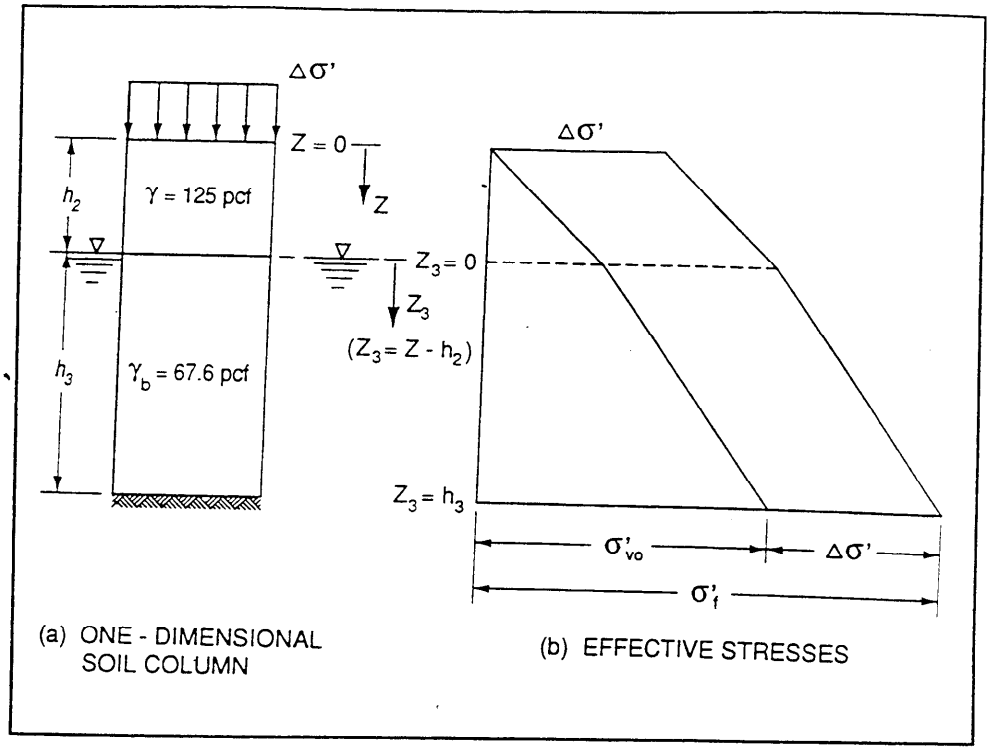

Figure F3. Distributions of initial and final vertical effective stresses (1 ft = 0.305 m, 1 pcf = 16.018 kg/m^3)

The total settlement s within the *moist portion* of the backfill of height $[h_2 + h_3]$ (Figures F1 or F2) due to the self-weight of backfill above this elevation (of height h_1) is given as

$$s = s_1 + s_2 \tag{F1}$$

where

$$s_1 = \int_o^{h2} \epsilon_z dz$$

and

$$s_2 = \int_{z=h_2}^{z=h_2+h_3} \epsilon_z dz$$

Introducing Janbu's relationship for vertical strain ϵ_z (Equation D2), the settlement term s_1 becomes

$$s_1 = \int_o^{h_2} \frac{2}{m} \left[\left(\frac{\gamma_t h_1 + \gamma_t z}{\sigma_a} \right)^{1/2} - \left(\frac{\gamma_t z}{\sigma_a} \right)^{1/2} \right] dz$$

Designating the first and second terms inside the integral as terms A and B, respectively

$$s_1 = s_A - s_B$$

Evaluating the contribution of term A to settlement s_1, designated s_A, is given by

$$s_A = \int_o^{h_2} \frac{2}{m} \left(\frac{\gamma_t h_1 + \gamma_t z}{\sigma_a} \right)^{1/2} dz$$

where the variable q is defined as

$$q = \frac{\gamma_t h_1 + \gamma_t z}{\sigma_a}$$

Differentiating q

$$\frac{dq}{dz} = \frac{\gamma_t}{\sigma_a} \quad or \quad dz = \frac{\sigma_a}{\gamma_t} dq$$

The settlement term A in terms of the variable q is

$$s_A = \int_o^{h2} \frac{2}{m} q \, dz = \int_o^{h2} \frac{2}{m} q \frac{\sigma_a}{\gamma_t} dq$$

Evaluating the integral,

$$s_A = \frac{2}{m} * \frac{2}{3} * q^{3/2} * \frac{\sigma_a}{\gamma_t} \Big|_o^{h_2}$$

Replacing the variable q and evaluating the limits,

$$s_A = \frac{4}{3} * \frac{1}{m} * \left[\left(\frac{\gamma_t * h_1 + \gamma_t h_2}{\sigma_a} \right)^{3/2} * \frac{\sigma_a}{\gamma_t} - \left(\frac{\gamma_t * h_1}{\sigma_a} \right)^{3/2} * \frac{\sigma_a}{\gamma_t} \right]$$

and simplifying,

$$s_A = \frac{4}{3} * \frac{1}{m} * \gamma_t^{1/2} * \frac{1}{\sigma_a^{1/2}} \left[(h_1 + h_2)^{3/2} - (h_1)^{3/2} \right]$$

The contribution to settlement term 1 by term *B*, designated s_B, is given by

$$s_B = \int_o^{h_2} \frac{2}{m} \left(\frac{\gamma_t z}{\sigma_a} \right)^{1/2} dz$$

where

$$r = \frac{\gamma_t}{\sigma_a} z$$

and

$$\frac{dr}{dz} = \frac{\gamma_t}{\sigma_a} \quad or \quad dz = \frac{\sigma_a}{\gamma_t} * dr$$

The complete relationship for s_B is

$$s_B = \int_o^{h_2} \frac{2}{m} r^{1/2} dz = \int_o^{h_2} \frac{2}{m} r^{1/2} * \frac{\sigma_a}{\gamma_t} * dr$$

Evaluating the integral

$$s_B = \frac{2}{m} * \frac{\sigma_a}{\gamma_t} * \frac{2}{3} \left[r^{3/2} \right]_o^{h2}$$

Replacing the variable *r*,

$$s_B = \frac{4}{3} * \frac{1}{m} * \frac{\sigma_a}{\gamma_t} * \left[\left(\frac{\gamma_t h_2}{\sigma_a} \right)^{3/2} - o \right]$$

or

$$s_B = \frac{4}{3} * \frac{1}{m} \gamma_t^{1/2} * \frac{1}{\sigma_a^{1/2}} (h_2)^{3/2}$$

Recall that the settlement term s_1 is given by

$$s_1 = s_A - s_B$$

Introducing terms s_A and s_B,

$$s_1 = \frac{4}{3} * \frac{1}{m} * \gamma_t^{1/2} * \frac{1}{\sigma_a^{1/2}} [(h_1 + h_2)^{3/2} - (h_1)^{3/2} - (h_2)^{3/2}] \qquad \text{(F2)}$$

Recall the total settlement is defined as

$$s = s_1 + s_2$$

where the second term s_2 is defined as

$$s_2 = \int_{z=h_2}^{z=h_2+h_3} \epsilon_z \, dz$$

Introducing Janbu's relationship for vertical strain ϵ_z (Equation D2),

$$s_2 = \int_{z=h_2}^{z=h_2+h_3} \frac{2}{m} \left[\left(\frac{\sigma_f'}{\sigma_a} \right)^{1/2} - \left(\frac{\sigma_{vo}'}{\sigma_a} \right)^{1/2} \right] dz$$

where

$$\sigma_f' = \sigma_{vo}' + \Delta\sigma'$$

Additionally,

$$\sigma_f' = \gamma_t h_1 + \gamma_t h_2 + \gamma_b z_3$$

$$\sigma_{vo}' = \gamma_t h_2 + \gamma_b z_3$$

where

$$z_3 = z - h_2$$

Rearranging,

$$z = z_3 + h_2$$

Differentiating z

$$\frac{dz}{dz_3} = 1 \quad or \quad dz = dz_3$$

The settlement term s_2 is

$$s_2 = \int_{z_3 + h_2 = h_2}^{z_3 + h_2 = h_2 + h_3} \frac{2}{m} \left[\left(\frac{\sigma_f'}{\sigma_a} \right)^{1/2} - \left(\frac{\sigma_{vo}'}{\sigma_a} \right)^{1/2} \right] dz_3$$

or, equivalently,

$$s_2 = \int_{z_3 = o}^{z_3 = h_3} \frac{2}{m} \left[\left(\frac{\sigma_f'}{\sigma_a} \right)^{1/2} - \left(\frac{\sigma_{vo}'}{\sigma_a} \right)^{1/2} \right] dz_3$$

Replacing σ'_f and σ'_{vo}

$$s_2 = \int_o^{h_3} \frac{2}{m} \left[\left(\frac{\gamma_t h_1 + \gamma_t h_2 + \gamma_b z_3}{\sigma_a} \right)^{1/2} - \left(\frac{\gamma_t h_2 + \gamma_b z_3}{\sigma_a} \right)^{1/2} \right] dz_3$$

Designating the first and second terms inside the integral as terms s_C and s_D respectively,

$$s_2 = s_c - s_D$$

The contribution of term C to the settlement term s_2, designated s_C, is given by

$$s_C = \int_o^{h_3} \frac{2}{m} \left(\frac{\gamma_t h_1 + \gamma_t h_2 + \gamma_b z_3}{\sigma_a} \right)^{1/2} dz_3$$

Let

$$u = \frac{\gamma_t h_1 + \gamma_t h_2 + \gamma_b z_3}{\sigma_a}$$

Differentiating u

$$\frac{du}{dz_3} = \frac{\gamma_b}{\sigma_a} \quad or \quad dz_3 = \frac{\sigma_a}{\gamma_b} du$$

The settlement term s_C in terms of the variable u is

$$s_c = \int_o^{h_3} \frac{2}{m} u^{1/2} dz_3 = \int_o^{h_3} \frac{2}{m} u^{1/2} * \frac{\sigma_a}{\gamma_b} * du$$

Evaluating the integral,

$$s_C = \frac{2}{m} * \frac{2}{3} * u^{3/2} * \frac{\sigma_a}{\gamma_b} \Big|_0^{h_3}$$

Replacing the transformation variable u and evaluating the limits,

$$s_C = \frac{4}{3} * \frac{1}{m} * \frac{\sigma_a}{\gamma_b} \left[\left(\frac{\gamma_t h_1 + \gamma_t h_2 + \gamma_b h_3}{\sigma_a} \right)^{3/2} - \left(\frac{\gamma_t h_1 + \gamma_t h_2}{\sigma_a} \right)^{3/2} \right]$$

$$s_C = \frac{4}{3} * \frac{1}{m} * \frac{1}{\gamma_b} * \frac{1}{\sigma_a^{1/2}} * \left[(\gamma_t h_1 + \gamma_t h_2 + \gamma_b h_3)^{3/2} - (\gamma_t h_1 + \gamma_t h_2)^{3/2} \right]$$

The contribution to settlement term s_2 by term D, designated s_D, is given by

$$s_D = \int_o^{h_3} \frac{2}{m} \left[\left(\frac{\gamma_t h_2 + \gamma_b z_3}{\sigma_a} \right)^{1/2} \right] dz_3$$

Let

$$\nu = \frac{\gamma_t h_2 + \gamma_b z_3}{\sigma_a}$$

Differentiating υ

$$\frac{d\nu}{dz_3} = \frac{\gamma_b}{\sigma_a} \quad or \quad dz_3 = \frac{\sigma_a}{\gamma_b} d\nu$$

The complete relationship for s_D is

$$s_D = \int_o^{h_3} \frac{2}{m} \nu^{1/2} \frac{\sigma_a}{\gamma_b} d\nu$$

Evaluating the integral

$$s_D = \frac{2}{m} * \frac{2}{3} * \frac{\sigma_a}{\gamma_b} * [\nu^{3/2}]_o^{h_3}$$

Replacing the variable υ and evaluating the limits,

$$s_D = \frac{4}{3} * \frac{1}{m} * \frac{\sigma_a}{\gamma_b} * \left[\left(\frac{\gamma_t h_2 + \gamma_b h_3}{\sigma_a} \right)^{3/2} - \left(\frac{\gamma_t h_2}{\sigma_a} \right)^{3/2} \right]$$

Simplifying

$$s_D = \frac{4}{3} * \frac{1}{m} * \frac{1}{\gamma_b} * \frac{1}{\sigma_a^{1/2}} * [(\gamma_t h_2 + \gamma_b h_3)^{3/2} - (\gamma_t h_2)^{3/2}]$$

Recall the settlement term s_2 is given by

$$s_2 = s_C - s_D$$

Introducing terms s_C and s_D,

$$s_2 = \frac{4}{3} * \frac{1}{m} * \frac{1}{\gamma_b} * \frac{1}{\sigma_a^{1/2}} \left[(\gamma_t h_1 + \gamma_t h_2 + \gamma_b h_3)^{3/2} - (\gamma_t h_1 + \gamma_t h_2)^{3/2} \right]$$

$$- \frac{4}{3} * \frac{1}{m} * \frac{1}{\gamma_b} * \frac{1}{\sigma_a^{1/2}} \left[(\gamma_t h_2 + \gamma_b h_3)^{3/2} - (\gamma_t h_2)^{3/2} \right] \qquad \text{(F3)}$$

Appendix G
Theoretical Development of Settlement Analysis of Moist One-Dimensional Soil Column Using Janbu's Tangent Modulus Method

Janbu (1963, 1965, 1967, 1985, see References in main text) developed an approach for calculating the settlement of a soil column in one-dimensional (1-D) compression (i.e., lateral strains equal to zero) that accounts for nonlinear stress-strain response of soils (also described in Holtz 1991, Meyerhof and Fellenius 1985, and Section 5.4 of Barker et al. 1991). This analytical approach was shown by Janbu to be applicable to nearly all types of soils. This appendix describes the theoretical development of the relationship used to calculate settlements within a "moist" (i.e., no water table) 1-D soil column using Janbu's tangent modulus method *as the backfill is placed.*

Figure G1 shows a moist 1-D soil column that would be used in the assignment of values for the hyperbolic stress-strain soil model for the backfill in the backfill placement analysis described in Chapter 3 (see main text). The relationships derived in this appendix are used to calculate settlements at any specified lift elevation within the Figure G1 soil column due to the self-weight of the moist soil above the lift elevation. This soil column comprises two soil regions, designated as regions A and B, that are distinguished by their total unit weights. The total unit weights in regions A and B (i.e., above and below elevation 396 [1]) equal 125 and 130 pcf (2,002.5 and 2,082.6 kg/m^3), respectively.

The settlement s of the Figure G1 1-D soil column at a specified lift elevation is calculated by integrating with *depth* z the vertical strains $\epsilon_z(z)$ induced in the soil column under some type of loading, which is the self-weight of the soil in the case of the backfill placement analysis of the soil column described in this section.

---

[1] All elevations (el) cited herein are in feet referenced to the National Geodetic Vertical Datum.

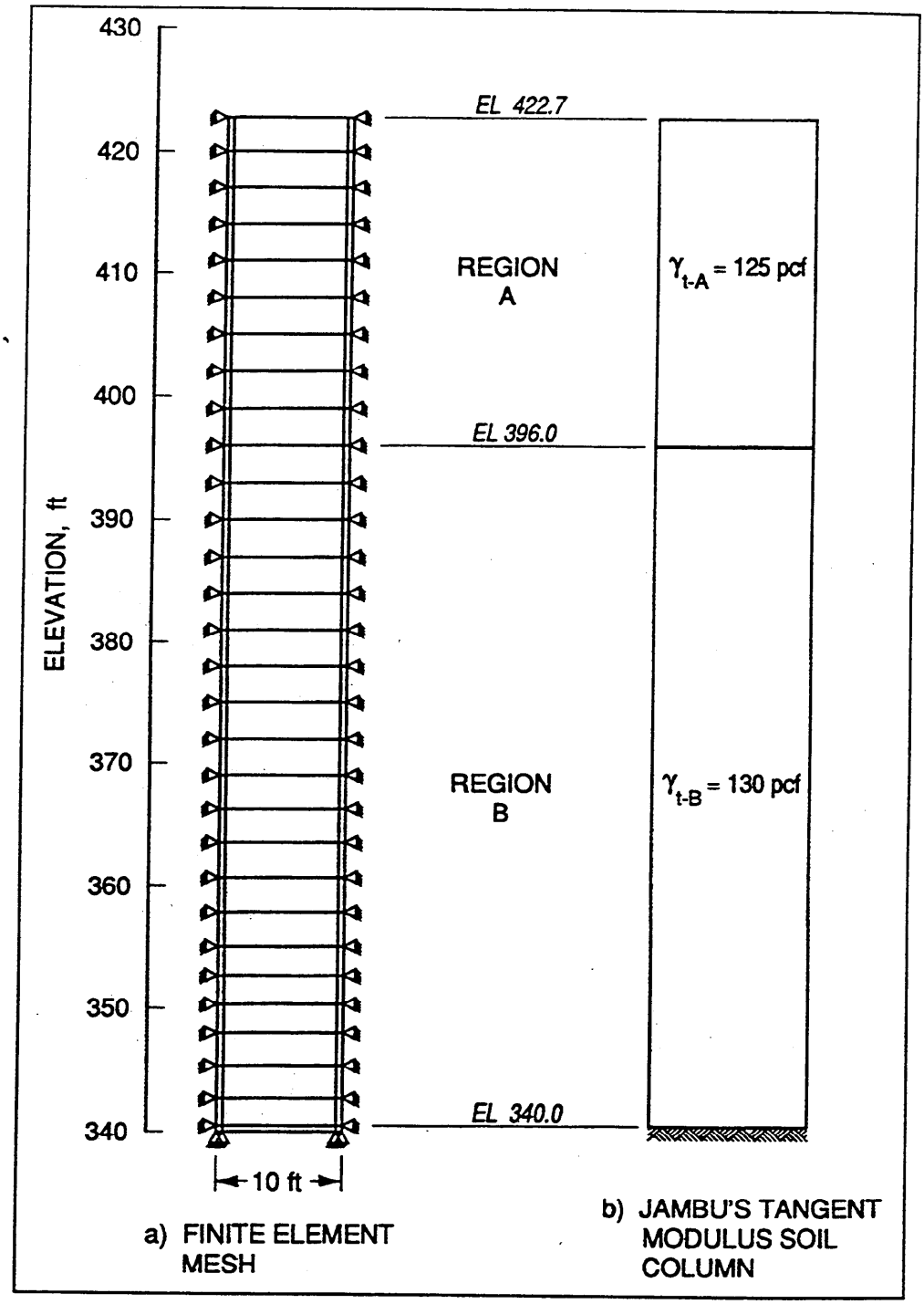

Figure G1. One-dimensional column analysis (1 ft = 0.305 m, 1 pcf = 16.018 kg/m^3)

$$s = \int_0^H \epsilon_z(z)\, dz$$

Because the vertical strains are likely to vary with depth z in the soil column, they are denoted as a function of z in this equation. Janbu recognized that the load-deformation relationship in 1-D compression of an element of soil (at depth z in a soil column) is nearly always nonlinear. Using the results of 1-D consolidation tests, Janbu showed that the tangent constrained modulus M_v can by described at any given effective stress σ' within a soil element (which is in the same direction as the strain) by the following relationship

$$M_v = m\sigma_a \left(\frac{\sigma'}{\sigma_a} \right)^{1-a}$$

and is applicable for a wide variety of soils. The stress σ_a is a reference stress and is usually taken as atmospheric pressure. The values for the coefficient m and exponent a are determined by fitting the Janbu relationship for M_v to consolidation test data. Appendix D showed the relationship for the vertical strain ϵ_z induced at a specified depth z in a soil column and subjected to an increase in effective stress from σ'_{vo} to σ'_f to be

$$\epsilon_z = \frac{2}{m} \left[\left(\frac{\sigma'_f}{\sigma_a} \right)^{1/2} - \left(\frac{\sigma'_{vo}}{\sigma_a} \right)^{1/2} \right] \qquad \text{(D2)}$$

for $a = 0.5$ (Figure D2, typical value for sands and gravel).

Settlement Within Region B

The settlement at the lift elevation at height h_3 (in region B) of the Figure G2 soil column is calculated using

$$s = \int_o^{h_3} \epsilon_z\, dz$$

The distribution of ϵ_z over depth h_3 is due to the self-weight of the soil column above this elevation and designated as $\Delta\sigma'$ in Figure G3. The overburden pressure $\Delta\sigma'$ is calculated on an effective stress basis. Introducing Janbu's relationship for vertical strain ϵ_z (Equation D2), the relationship for settlement s becomes

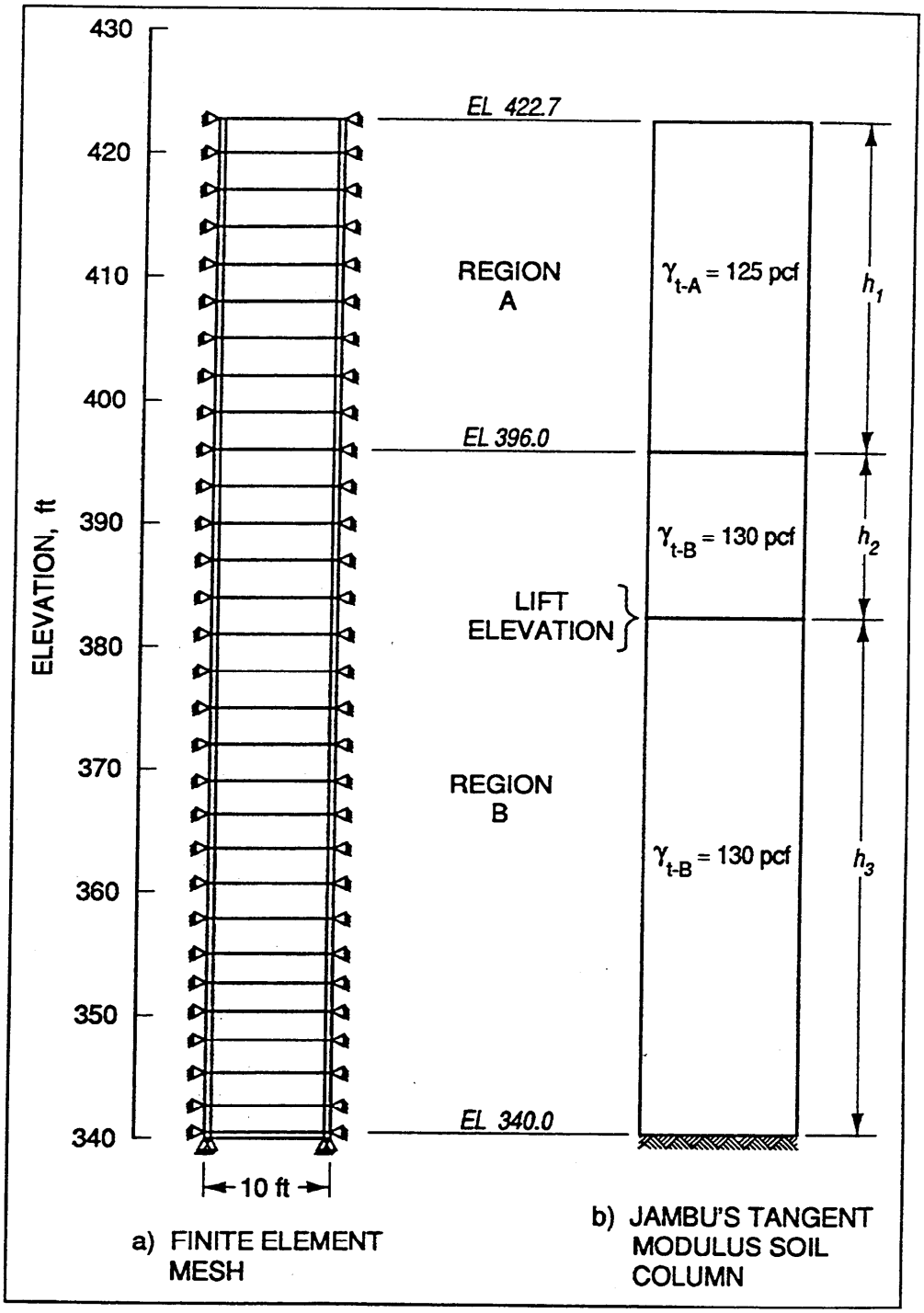

Figure G2. One-dimensional column analysis - lift elevation in region B (1 ft = 0.305 m, 1 pcf = 16.018 kg/m^3)

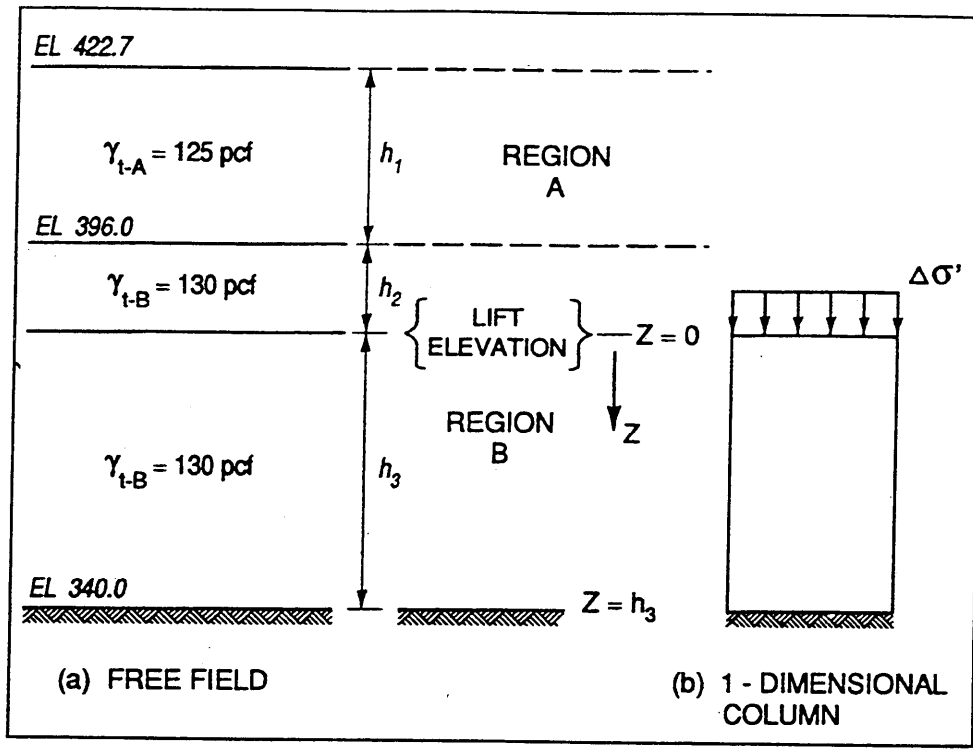

Figure G3. One-dimensional column - lift elevation in region B (1 pcf = 16.018 kg/m^3)

$$s = \int_o^{h_3} \frac{2}{m} \left[\left(\frac{\sigma_f'}{\sigma_a} \right)^{1/2} - \left(\frac{\sigma_{vo}'}{\sigma_a} \right)^{1/2} \right] dz$$

Introducing

$$\sigma_{vo}' = \gamma_{t-B} * z$$

and

$$\sigma_f' = \sigma_{vo}' + \Delta\sigma'$$

with

$$\Delta\sigma' = \gamma_{t-A} * h_1 + \gamma_{t-B} * h_2$$

for region B. Thus σ_f' in region B becomes

$$\sigma_f' = \gamma_{t-A} * h_1 + \gamma_{t-B} * h_2 + \gamma_{t-B} * z$$

The relationship for the settlement s at a given elevation becomes

$$s = \int_o^{h_3} \frac{2}{m} \left[\left(\frac{\gamma_{t-A} * h_1 + \gamma_{t-B} * h_2 + \gamma_{t-B} * z}{\sigma_a} \right)^{1/2} - \left(\frac{\gamma_{t-B} * z}{\sigma_a} \right)^{1/2} \right] dz$$

Designating the first and second terms inside the integral as terms A and B, respectively,

$$s = s_A - s_B \qquad \text{(G1)}$$

The contribution of term A to the total settlement s, designated s_A, is given by

$$s_A = \int_o^{h_3} \frac{2}{m} \, q^{1/2} \, dz$$

where the variable q is defined as

$$q = \frac{\gamma_{t-A} * h_1 + \gamma_{t-B} * h_2 + \gamma_{t-B} * z}{\sigma_a}$$

Differentiating q

$$\frac{dq}{dz} = \frac{\gamma_{t-B}}{\sigma_a} \quad or \quad dz = \frac{\sigma_a}{\gamma_{t-B}} \, dq$$

The settlement term A in terms of the variable q is

$$s_A = \int_o^{h_3} \frac{2}{m} \, q^{1/2} * \frac{\sigma_a}{\gamma_{t-B}} \, dq$$

Evaluating the integral,

$$s_A = \frac{2}{m} * \frac{2}{3} q^{3/2} * \frac{\sigma_a}{\gamma_{t-B}} \Big|_o^{h_3}$$

Replacing the variable q and evaluating the limits,

$$s_A = \frac{4}{3\,m}\left[\left(\frac{\gamma_{t-A} * h_1 + \gamma_{t-B} * h_2 + \gamma_{t-B} h_3}{\sigma_a}\right)^{3/2} * \frac{\sigma_a}{\gamma_{t-B}} - \left(\frac{\gamma_{t-A} * h_1 + \gamma_{t-B} * h_2 + o}{\sigma_a}\right)^{3/2} * \frac{\sigma_a}{\gamma_{t-B}}\right]$$

$$s_A = \frac{4}{3} * \frac{1}{m} * \frac{1}{\gamma_{t-B}} * \frac{1}{\sigma_a^{1/2}} \left[(\gamma_{t-A} * h_1 + \gamma_{t-B} * h_2 + \gamma_{t-B} * h_3)^{3/2} - (\gamma_{t-A} * h_1 + \gamma_{t-B} * h_2)^{3/2}\right] \quad \text{(G2)}$$

The contribution to total settlement by term B, designated s_B is given by

$$s_B = \int_o^{h_3} \frac{2}{m}\left[\left(\frac{\gamma_{t-B} * z}{\sigma_a}\right)^{1/2}\right] dz$$

Introducing the variable r, s_B becomes

$$s_B = \int_o^{h_3} \frac{2}{m} r^{1/2} \; dz$$

where

$$r = \frac{\gamma_{t-B} * z}{\sigma_a}$$

and

$$\frac{dr}{dz} = \frac{\gamma_{t-B}}{\sigma_a} \quad or \quad dz = \frac{\sigma_a}{\gamma_{t-B}} dr$$

The complete relationship for s_B is

$$s_B = \int_o^{h_3} \frac{2}{m} r^{1/2} * \frac{\sigma_a}{\gamma_{t-B}} dr$$

Evaluating the integral

$$s_B = \frac{2}{m} * \frac{\sigma_a}{\gamma_{t-B}} * \frac{2}{3} r^{3/2} \Big|_o^{h_3}$$

Replacing the variable r

$$s_B = \frac{2}{m} * \frac{\sigma_a}{\gamma_{t-B}} * \frac{2}{3} \left[\left(\frac{\gamma_{t-B} z}{\sigma_a} \right)^{3/2} \right]_o^{h_3}$$

Evaluating the limits

$$s_B = \frac{4}{3} * \frac{1}{m} * \frac{\sigma_a}{\gamma_{t-B}} \left[\left(\frac{\gamma_{t-B} h_3}{\sigma_a} \right)^{3/2} - O \right]$$

results in

$$s_B = \frac{4}{3} * \frac{1}{m} \frac{\gamma_{t-B}^{3/2}}{\gamma_{t-B}} \frac{\sigma_a}{\sigma_a^{3/2}} h_3^{3/2}$$

Simplifying

$$s_B = \frac{4}{3} * \frac{1}{m} * (\gamma_{t-B})^{1/2} * \frac{1}{\sigma_a^{1/2}} * (h_3)^{3/2} \qquad \text{(G3)}$$

The total settlement s at height h_3 (within region B) due to the self-weight of backfill above this elevation (of height $h_2 + h_1$) is given by

$$s = s_A - s_B \qquad \text{(G1)}$$

with

$$s_A = \frac{4}{3\,m} * \frac{1}{\gamma_{t-B}} * \frac{1}{\sigma_a^{1/2}} \left[\left(\gamma_{t-A} * h_1 + \gamma_{t-B} * h_2 + \gamma_{t-B} * h_3\right)^{3/2} - \left(\gamma_{t-A} * h_1 + \gamma_{t-B} * h_2\right)^{3/2} \right] \quad \text{(G2)}$$

and

$$s_B = \frac{4}{3} * \frac{1}{m} * (\gamma_{t-B})^{1/2} * \frac{1}{\sigma_a^{1/2}} * (h_3)^{3/2} \quad \text{(G3)}$$

If the total unit weights for the two regions are the same ($\gamma_t = \gamma_{t-A} = \gamma_{t-B}$), then equations G1 through G3 for total settlement s at height h_3 become

$$s = \frac{4}{3\,m} * \gamma_t^{1/2} * \frac{1}{\sigma_a^{1/2}} \left[\left(h_1 + h_2 + h_3\right)^{3/2} - \left(h_1 + h_2\right)^{3/2} - \left(h_3\right)^{3/2} \right] \quad \text{(G4)}$$

Settlement Within Region A

The settlement at the lift elevation at height $[h_2 + h_3]$ (in region A) of the Figure G4 soil column is calculated using

$$s = \int_o^{h_2 + h_3} \epsilon_z \, dz = \int_o^{h_2} \epsilon_z \, dz + \int_{h2}^{h3} \epsilon_z \, dz$$

The distribution of ϵ_z over depth $[h_2 + h_3]$ is due to the self-weight of the soil column above this elevation and is designated as $\Delta\sigma'$ in Figure G5. The overburden pressure $\Delta\sigma''$ is calculated on an effective stress basis. Figure G6 shows the distributions of the initial and final vertical effective stresses σ'_{vo} and σ'_f where

$$\sigma'_{vo} = \gamma_{t-A} * z$$

and

$$\sigma'_f = \sigma'_{vo} + \Delta\sigma'$$

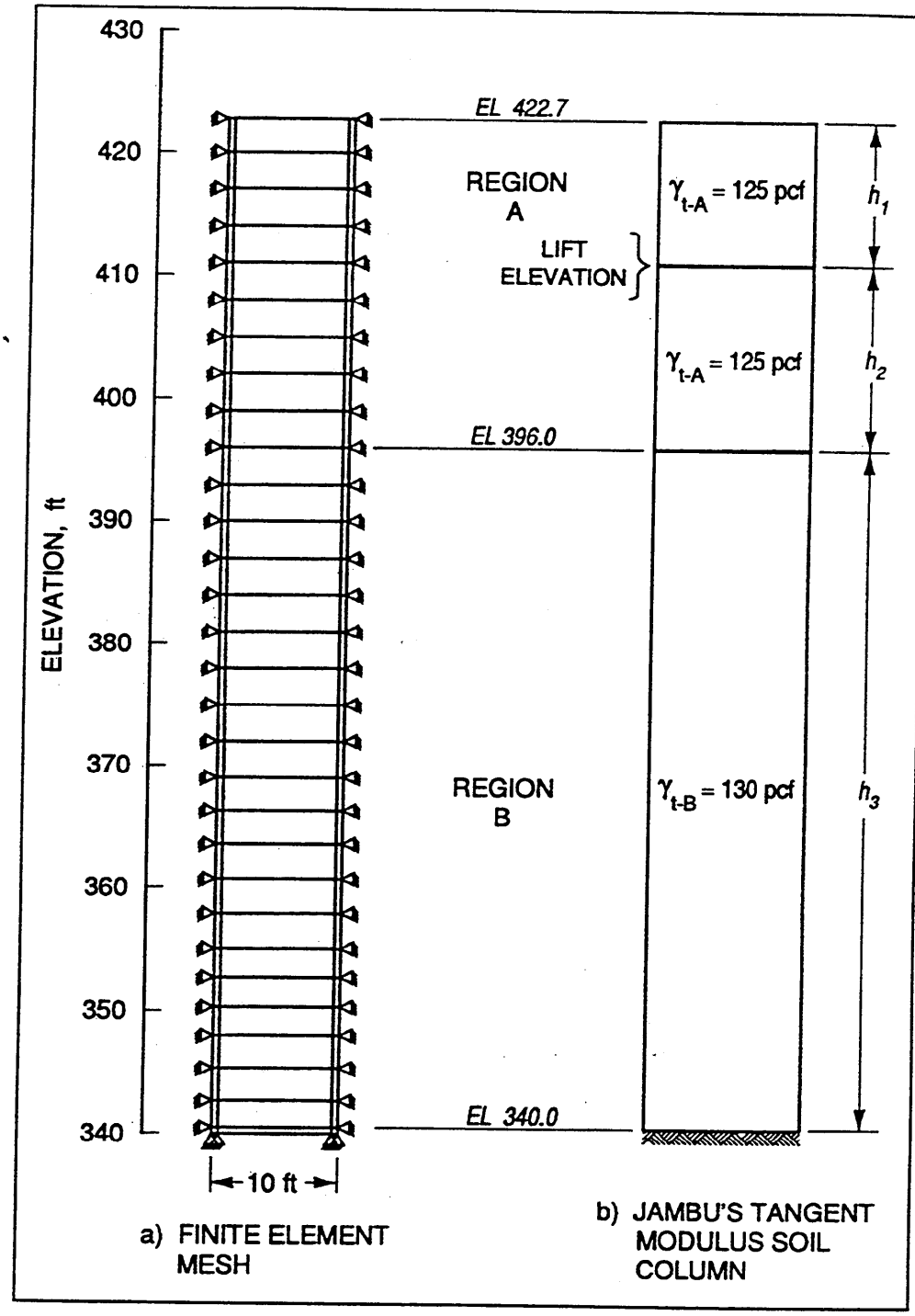

Figure G4. One-dimensional column analysis - lift elevation in region A (1 ft = 0.305 m, 1 pcf = 16.018 kg/m^3)

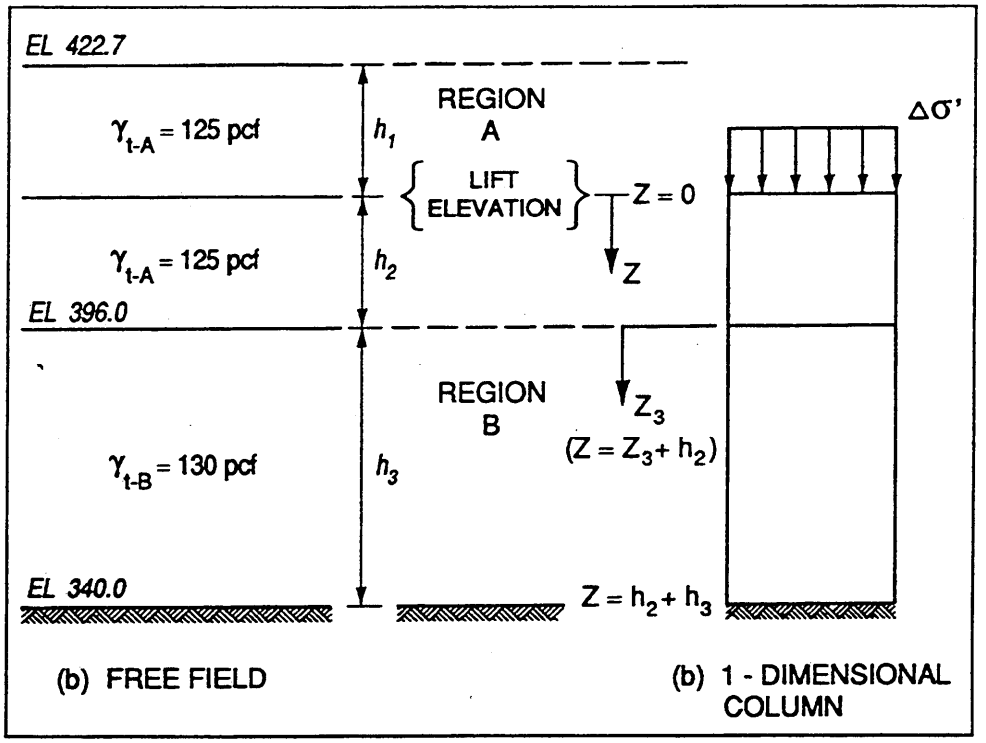

Figure G5. One-dimensional column - lift elevation in region A (1 pcf = 16.018 kg/m^3)

with

$$\Delta\sigma' = \gamma_{t\text{-}A} * h_1$$

for region A. Thus σ_f' in region A becomes

$$\sigma_f' = \gamma_{t\text{-}A} * h_1 + \gamma_{t\text{-}A} * z$$

The total settlement s within region A of the backfill of height $[h_2 + h_3]$ (Figures G4 or G5) due to the self-weight of backfill above this elevation (of height h_1) is given as

$$s = s_1 + s_2 \qquad \text{(G5)}$$

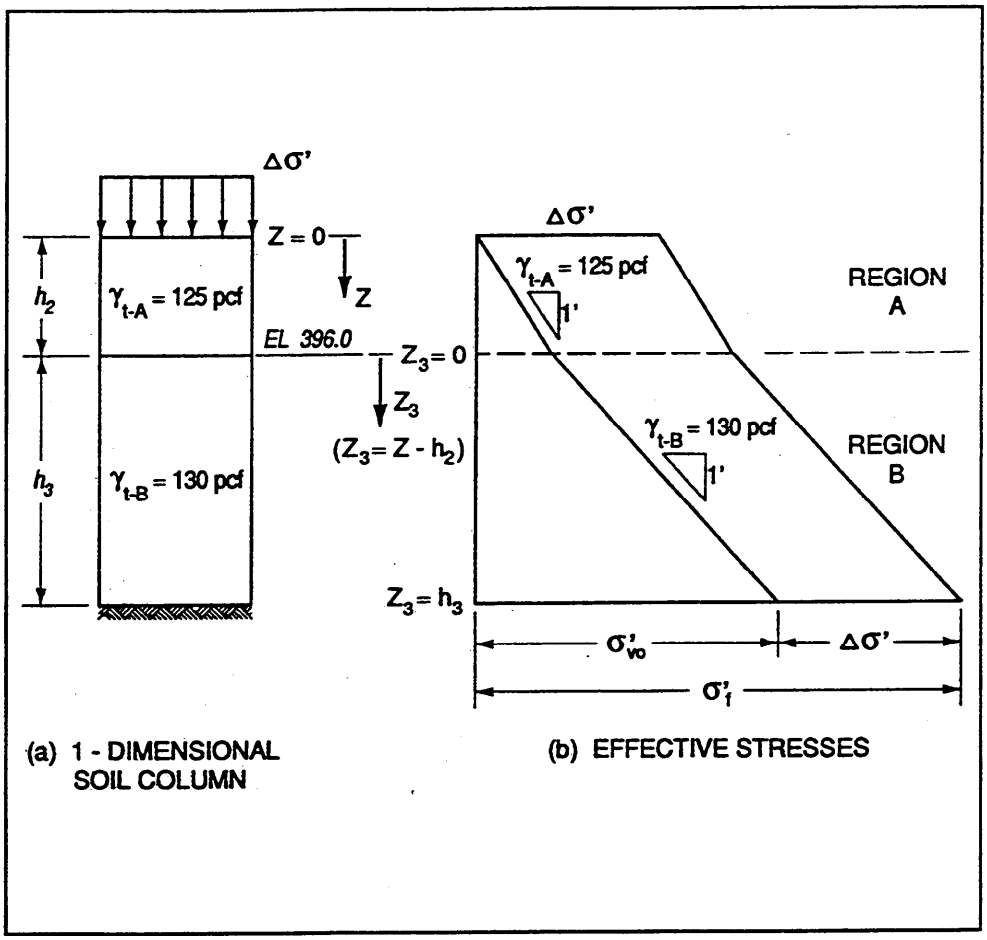

Figure G6. Distributions of initial and final vertical effective stresses (1 pcf = 16.018 kg/m^3)

where

$$s_1 = \int_o^{h2} \epsilon_z dz$$

and

$$s_2 = \int_{z=h_2}^{z=h_2+h_3} \epsilon_z dz$$

The first settlement term s_1 addresses the vertical strains ϵ_z in region A, while the second settlement term s_2 addresses the vertical strains ϵ_z in region B. Introducing Janbu's relationship for vertical strain ϵ_z (Equation D2), the settlement term s_1 becomes

$$s_1 = \int_o^{h_2} \frac{2}{m}\left[\left(\frac{\gamma_{t-A}h_1 + \gamma_{t-A}z}{\sigma_a}\right)^{1/2} - \left(\frac{\gamma_{t-A}z}{\sigma_a}\right)^{1/2}\right]dz$$

Designating the first and second terms inside the integral as terms A and B, respectively,

$$s_1 = s_A - s_B$$

Evaluating the contribution of term A to settlement s_1, designated s_A, is given by

$$s_A = \int_o^{h_2} \frac{2}{m}\left(\frac{\gamma_{t-A}h_1 + \gamma_{t-A}z}{\sigma_a}\right)^{1/2} dz$$

where the variable q is defined as

$$q = \frac{\gamma_{t-A}h_1 + \gamma_{t-A}z}{\sigma_a}$$

Differentiating q

$$\frac{dq}{dz} = \frac{\gamma_{t-A}}{\sigma_a} \quad or \quad dz = \frac{\sigma_a}{\gamma_{t-A}}\,dq$$

The settlement term A in terms of the variable q is

$$s_A = \int_o^{h2} \frac{2}{m} q\,dz = \int_o^{h2} \frac{2}{m} q \frac{\sigma_a}{\gamma_{t-A}}\,dq$$

Evaluating the integral,

$$s_A = \frac{2}{m} * \frac{2}{3} * q^{3/2} * \frac{\sigma_a}{\gamma_{t-A}} \Big|_o^{h_2}$$

Replacing the variable q and evaluating the limits,

$$s_A = \frac{4}{3} * \frac{1}{m} * \left[\left(\frac{\gamma_{t-A} * h_1 + \gamma_{t-A} h_2}{\sigma_a} \right)^{3/2} * \frac{\sigma_a}{\gamma_{t-A}} - \left(\frac{\gamma_{t-A} * h_1}{\sigma_a} \right)^{3/2} * \frac{\sigma_a}{\gamma_{t-A}} \right]$$

and simplifying,

$$s_A = \frac{4}{3} * \frac{1}{m} * (\gamma_{t-A})^{1/2} * \frac{1}{\sigma_a^{1/2}} \left[(h_1 + h_2)^{3/2} - (h_1)^{3/2} \right]$$

The contribution to settlement term 1 by term *B*, designated s_B, is given by

$$s_B = \int_o^{h_2} \frac{2}{m} \left(\frac{\gamma_{t-A} z}{\sigma_a} \right)^{1/2} dz$$

where

$$r = \frac{\gamma_{t-A}}{\sigma_a} z$$

and

$$\frac{dr}{dz} = \frac{\gamma_{t-A}}{\sigma_a} \quad or \quad dz = \frac{\sigma_a}{\gamma_{t-A}} * dr$$

The complete relationship for s_B is

$$s_B = \int_o^{h_2} \frac{2}{m} r^{1/2} dz = \int_o^{h_2} \frac{2}{m} r^{1/2} * \frac{\sigma_a}{\gamma_{t-A}} * dr$$

Evaluating the integral

$$s_B = \frac{2}{m} * \frac{\sigma_a}{\gamma_{t-A}} * \frac{2}{3} [r^{3/2}] \Big|_o^{h2}$$

Replacing the variable *r*,

$$s_B = \frac{4}{3} * \frac{1}{m} * \frac{\sigma_a}{\gamma_{t-A}} * \left[\left(\frac{\gamma_{t-A} h_2}{\sigma_a} \right)^{3/2} - o \right]$$

or

$$s_B = \frac{4}{3} * \frac{1}{m} \ (\gamma_{t-A})^{1/2} * \frac{1}{\sigma_a^{1/2}} \ (h_2)^{3/2}$$

Recall that the settlement term s_1 is given by

$$s_1 = s_A - s_B$$

Introducing terms s_A and s_B,

$$s_1 = \frac{4}{3} * \frac{1}{m} * (\gamma_{t-A})^{1/2} * \frac{1}{\sigma_a^{1/2}} \left[(h_1 + h_2)^{3/2} - (h_1)^{3/2} - (h_2)^{3/2} \right] \quad \text{(G6)}$$

Recall that the total settlement is defined as

$$s = s_1 + s_2$$

where the second term s_2 is defined as

$$s_2 = \int_{z=h_2}^{z=h_2+h_3} \epsilon_z \, dz$$

The second settlement term s_2 addresses the vertical strains ϵ_z in region B. Introducing Janbu's relationship for vertical strain ϵ_z (Equation D2),

$$s_2 = \int_{z=h_2}^{z=h_2+h_3} \frac{2}{m} \left[\left(\frac{\sigma_f'}{\sigma_a} \right)^{1/2} - \left(\frac{\sigma_{vo}'}{\sigma_a} \right)^{1/2} \right] dz$$

where

$$\sigma_f' = \sigma_{vo}' + \Delta\sigma'$$

Additionally,

$$\sigma_f' = \gamma_{t-A} h_1 + \gamma_{t-A} h_2 + \gamma_{t-B} z_3$$

$$\sigma_{vo}' = \gamma_{t-A} h_2 + \gamma_{t-B} z_3$$

where

$$z_3 = z - h_2$$

Rearranging,

$$z = z_3 + h_2$$

Differentiating z

$$\frac{dz}{dz_3} = 1 \quad or \quad dz = dz_3$$

The settlement term s_2 is

$$s_2 = \int_{z_3 + h_2 = h_2}^{z_3 + h_2 = h_2 + h_3} \frac{2}{m} \left[\left(\frac{\sigma_f'}{\sigma_a} \right)^{1/2} - \left(\frac{\sigma_{vo}'}{\sigma_a} \right)^{1/2} \right] dz_3$$

or, equivalently,

$$s_2 = \int_{z_3 = o}^{z_3 = h_3} \frac{2}{m} \left[\left(\frac{\sigma_f'}{\sigma_a} \right)^{1/2} - \left(\frac{\sigma_{vo}'}{\sigma_a} \right)^{1/2} \right] dz_3$$

Replacing σ'_f and σ'_{vo}

$$s_2 = \int_o^{h_3} \frac{2}{m} \left[\left(\frac{\gamma_{t-A} h_1 + \gamma_{t-A} h_2 + \gamma_{t-B} z_3}{\sigma_a} \right)^{1/2} - \left(\frac{\gamma_{t-A} h_2 + \gamma_{t-B} z_3}{\sigma_a} \right)^{1/2} \right] dz_3$$

Designating the first and second terms inside the integral as terms s_C and s_D respectively,

$$s_2 = s_C - s_D$$

The contribution of term C to the settlement term s_2 designated s_C is given by

$$s_C = \int_o^{h_3} \frac{2}{m} \left(\frac{\gamma_{t-A} h_1 + \gamma_{t-A} h_2 + \gamma_{t-B} z_3}{\sigma_a} \right)^{1/2} dz_3$$

Let

$$u = \frac{\gamma_{t-A} h_1 + \gamma_{t-A} h_2 + \gamma_{t-B} z_3}{\sigma_a}$$

Differentiating u

$$\frac{du}{dz_3} = \frac{\gamma_{t-B}}{\sigma_a} \quad or \quad dz_3 = \frac{\sigma_a}{\gamma_{t-B}} du$$

The settlement term s_C in terms of the variable u is

$$s_C = \int_o^{h_3} \frac{2}{m} u^{1/2} dz_3 = \int_o^{h_3} \frac{2}{m} u^{1/2} * \frac{\sigma_a}{\gamma_{t-B}} * du$$

Evaluating the integral,

$$s_C = \frac{2}{m} * \frac{2}{3} * u^{3/2} * \frac{\sigma_a}{\gamma_{t-B}} \Big|_0^{h_3}$$

Replacing the transformation variable u and evaluating the limits,

$$s_C = \frac{4}{3} * \frac{1}{m} * \frac{\sigma_a}{\gamma_{t-B}} \left[\left(\frac{\gamma_{t-A} h_1 + \gamma_{t-A} h_2 + \gamma_{t-B} h_3}{\sigma_a} \right)^{3/2} - \left(\frac{\gamma_{t-A} h_1 + \gamma_{t-A} h_2}{\sigma_a} \right)^{3/2} \right]$$

$$s_C = \frac{4}{3} * \frac{1}{m} * \frac{1}{\gamma_{t-B}} * \frac{1}{\sigma_a^{1/2}} * \left[\left(\gamma_{t-A} h_1 + \gamma_{t-A} h_2 + \gamma_{t-B} h_3 \right)^{3/2} - \left(\gamma_{t-A} h_1 + \gamma_{t-A} h_2 \right)^{3/2} \right]$$

The contribution to settlement term s_2 by term D, designated s_D, is given by

$$s_D = \int_o^{h_3} \frac{2}{m} \left[\left(\frac{\gamma_{t-A} h_2 + \gamma_{t-B} z_3}{\sigma_a} \right)^{1/2} \right] dz_3$$

Let

$$\upsilon = \frac{\gamma_{t-A} h_2 + \gamma_{t-B} z_3}{\sigma_a}$$

Differentiating υ

$$\frac{d\upsilon}{dz_3} = \frac{\gamma_{t-B}}{\sigma_a} \quad or \quad dz_3 = \frac{\sigma_a}{\gamma_{t-B}} d\upsilon$$

The complete relationship for s_D is

$$s_D = \int_o^{h_3} \frac{2}{m} \upsilon^{1/2} \frac{\sigma_a}{\gamma_{t-B}} d\upsilon$$

Evaluating the integral

$$s_D = \frac{2}{m} * \frac{2}{3} * \frac{\sigma_a}{\gamma_{t-B}} * \left[\upsilon^{3/2} \right] \Big|_o^{h_3}$$

Replacing the variable υ and evaluating the limits,

$$s_D = \frac{4}{3} * \frac{1}{m} * \frac{\sigma_a}{\gamma_{t-B}} * \left[\left(\frac{\gamma_{t-A} h_2 + \gamma_{t-B} h_3}{\sigma_a} \right)^{3/2} - \left(\frac{\gamma_{t-A} h_2}{\sigma_a} \right)^{3/2} \right]$$

Simplifying

$$s_D = \frac{4}{3} * \frac{1}{m} * \frac{1}{\gamma_{t-B}} * \frac{1}{\sigma_a^{1/2}} * \left[(\gamma_{t-A} h_2 + \gamma_{t-B} h_3)^{3/2} - (\gamma_{t-A} h_2)^{3/2}\right]$$

Recall the settlement term s_2 is given by

$$s_2 = s_C - s_D$$

Introducing terms s_C and s_D,

$$s_2 = \frac{4}{3} * \frac{1}{m} * \frac{1}{\gamma_{t-B}} * \frac{1}{\sigma_a^{1/2}} \left[(\gamma_{t-A} h_1 + \gamma_{t-A} h_2 + \gamma_{t-B} h_3)^{3/2} - (\gamma_{t-A} h_1 + \gamma_{t-A} h_2)^{3/2}\right]$$

$$- \frac{4}{3} * \frac{1}{m} * \frac{1}{\gamma_{t-B}} * \frac{1}{\sigma_a^{1/2}} \left[(\gamma_{t-A} h_2 + \gamma_{t-B} h_3)^{3/2} - (\gamma_{t-A} h_2)^{3/2}\right] \qquad \text{(G7)}$$

Thus, the total settlement s within region A of the backfill of height $[h_2 + h_3]$ (Figures G4 or G5) due to the self-weight of backfill above this elevation (of height h_1) is given as

$$s = s_1 + s_2 \qquad \text{(G5)}$$

where s_1 is computed using equation G6 and s_2 is computed using Equation G7.

If the total unit weights for the two regions are the same ($\gamma_t = \gamma_{t-A} = \gamma_{t-B}$), then Equations G5 through G7 for total settlement s at height $[h_2 + h_3]$ become

$$s = \frac{4}{3\,m} * \gamma_t^{1/2} * \frac{1}{\sigma_a^{1/2}} \left[(h_1 + h_2 + h_3)^{3/2} - (h_1)^{3/2} - (h_2 + h_3)^{3/2}\right] \qquad \text{(G8)}$$

It can be shown that Equation G8 for settlement in region A at height $[h_2 + h_3]$ is consistent with Equation G4 for settlement in region B at height h_3 by specifying a common elevation within the backfill for use in each of the equations (e.g., the elevation that is common to the bottom of region A and the top of region B). At the common elevation of 396 ft (120.7 m), h_2 is equal to zero (refer to the definitions for h_2 in regions B and A in Figures G3 and G5, respectively).

Appendix H
Theoretical Development of Rebound Analysis of One-Dimensional Soil Column Due to Postconstruction Rise in Water Table Using Janbu's Tangent Modulus Method

Janbu (1963, 1965, 1967, 1985, see References in main text) developed an approach for calculating the settlement of a soil column in one-dimensional (1-D) compression (i.e., lateral strains equal to zero) that accounts for nonlinear stress-strain response of soils (also described in Holtz 1991, Meyerhof and Fellenius 1985, and Section 5.4 of Barker et al. 1991). This analytical approach was shown by Janbu to be applicable to nearly all types of soils. This appendix describes the theoretical development of the relationships used to calculate rebound of a 1-D soil column using Janbu's tangent modulus method *due to a postconstruction rise in the water table.*

The ultimate settlement in a soil column due to the incremental construction of the backfill, followed by a postconstruction rise in the water table, is computed using two sets of calculations (Figure H1). First, the settlement at a specified lift elevation in the moist 1-D soil column, due to self-weight of the soil above this lift elevation, is calculated using the relationships given in Appendix G. Then, the rebound due to a postconstruction rise in a hydrostatic water table is calculated at the lift elevation using the relationships derived in this appendix. The ultimate settlement at the specified lift elevation within the backfill equals the sum from these two sets of calculations.

Figure H1 shows the 1-D soil column used in the assignment of values for the hyperbolic stress-strain soil model for the backfill in the backfill placement analysis (Chapter 3 in the main text) and the postconstruction, incremental rise in the water table. This soil column comprises two soil regions, designated as regions A and B, that are distinguished by their total unit weights. The total unit weights in

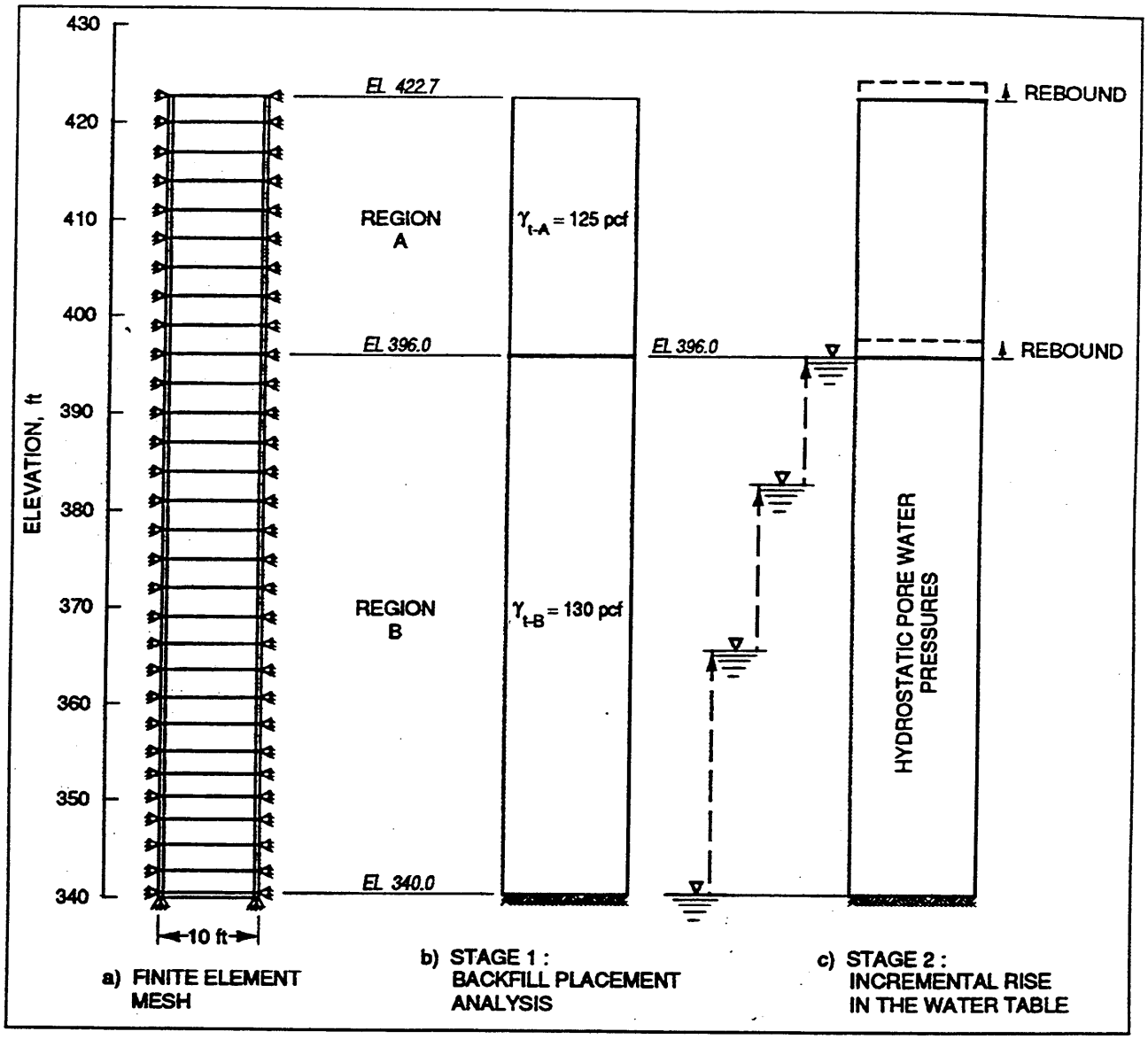

Figure H1. One-dimensional column analysis - postconstruction rise in the water table (1 ft = 0.305 m, 1 pcf = 16.018 kg/m^3)

regions A and B (i.e., above and below elevation 396[1]) equal 125 and 130 pcf (2,002 and 2,082 kg/m^3), respectively.

The first stage in the calculation of the settlement at a specified lift elevation is the backfill placement analysis of the Figure H1 soil column, which is used to model the incremental construction of the moist backfill. The relationships derived in Appendix G are used to calculate settlement s at a specified lift elevation in the Figure H1 soil column, due to the self-weight of the moist soil above the lift elevation using Janbu's tangent modulus method.

---

[1] All elevations (el) cited herein are in feet referenced to the National Geodetic Vertical Datum.

The second stage of the analysis is to calculate the rebound due to a post-construction rise in the water table of the Figure H1 soil column. The water table is raised incrementally in the finite element analysis of the soil column using SOILSTRUCT. Hydrostatic water pressures are assumed during this stage of unloading of the Figure H1 soil column. The rebound r of the 1-D soil column in Figure H1 is also calculated (using Janbu's tangent modulus method) by integrating with *depth* z the vertical strains $\epsilon_z(z)$ induced in the soil column under some type of loading, which is the reduction in overburden pressure with the incremental rise in a hydrostatic water table within the soil column, as described in this section.

$$r = \int_0^H \epsilon_z(z)\, dz$$

Because the vertical strains are likely to vary with depth z in the soil column, they are denoted as a function of z in this equation. Janbu recognized that the load-deformation relationship in 1-D compression of an element of soil (at depth z in a soil column) is nearly always nonlinear. Using the results of 1-D consolidation tests, Janbu showed that the tangent constrained modulus M_v can by described at any given effective stress σ' within a soil element (which is in the same direction as the strain) by the following relationship

$$M_v = m\sigma_a \left(\frac{\sigma'}{\sigma_a}\right)^{1-a}$$

and is applicable for a wide variety of soils. The stress σ_a is a reference stress and is usually taken as atmospheric pressure. The values for the coefficient m and exponent a are determined by fitting the Janbu relationship for M_v to consolidation test data. Appendix D showed the relationship for the vertical strain ϵ_z induced at a specified depth z in a soil column and subjected to an increase in effective stress from σ'_{vo} to σ'_f to be

$$\epsilon_z = \frac{2}{m}\left[\left(\frac{\sigma'_f}{\sigma_a}\right)^{1/2} - \left(\frac{\sigma'_{vo}}{\sigma_a}\right)^{1/2}\right] \qquad \text{(D2)}$$

for a = 0.5 (Figure D2, typical value for sands and gravel). Duncan et al. (1978) (see Table 5.5 in Section 5.4 of Barker et al. 1991) reevaluated Janbu's data and characterized values for the modulus number m typical of normally consolidated and overconsolidated sands, silts, and clays. The value for exponent a is equal to 0.5 for both normally consolidated and overconsolidated soils. The subscript "*ur*" is added to the modulus number m (e.g., m_{ur}) to represent overconsolidated soils. The subscript "*ur*" denotes that the value for m corresponds to unload-reload, since the rebound of the soil column due to a post-construction rise in water table is calculated using equation H1. Table 5.5 of Duncan et al. gives the modulus number m for normally consolidated, loose, medium dense, and dense

sands as equal to three times the modulus number m_{ur}. This multiplication factor of three increases to a factor of approximately 5 for silts and to 10 for clays.

The ultimate settlement s_{ult} at a specified lift elevation in the Figure H1 soil column due to the incremental construction of the backfill (resulting in settlement s and calculated using Appendix G equations), followed by the rebound r due to a postconstruction rise in the water table, is given by

$$s_{ult} = s + r$$

Derivation of the relationships used to calculate the rebound r (using Janbu's tangent modulus method) are given in the following two sections. The first section gives the equations used for any specified lift elevation within region B (i.e., below the water table), while the second section is for the case in which the specified lift elevation is within region A (i.e., above the water table).

Rebound Within Region B

The rebound at the lift elevation at height h_3 (in region B) of the Figure H2 soil column is calculated using

$$r = \int_o^{h_3} \epsilon_z \, dz$$

The distribution of ϵ_z over depth h_3 is due to the postconstruction rise in the hydrostatic water table below this elevation. Introducing Janbu's relationship for vertical strain ϵ_z (Equation D2), the relationship for rebound r becomes

$$r = \int_o^{h_3} \frac{2}{m_{ur}} \left[\left(\frac{\sigma_f'}{\sigma_a} \right)^{1/2} - \left(\frac{\sigma_{vo}'}{\sigma_a} \right)^{1/2} \right] dz$$

Introducing

$$\sigma_{vo}' = \gamma_{t-A} * h_1 + \gamma_{t-B} * h_2 + \gamma_{t-B} * z$$

and

$$\sigma_f' = \gamma_{t-A} * h_1 + \gamma_{b-B} * h_2 + \gamma_{b-B} * z$$

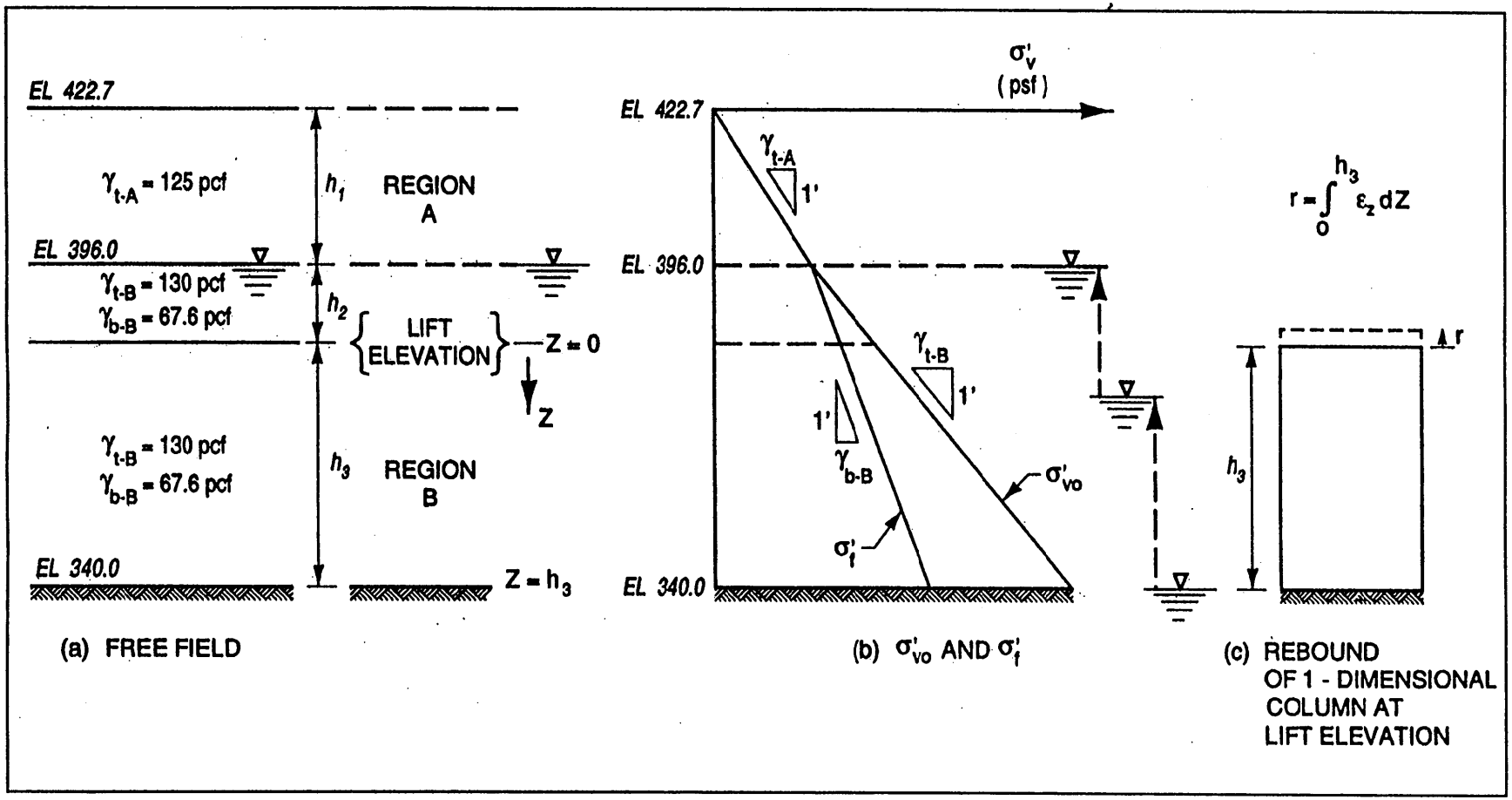

Figure H2. Lift elevation in region B with a postconstruction rise in the water table (1 ft = 0.305 m, 1 pcf = 16.018 kg/m^3)

for region B. Note that σ_f' is less than σ_{vo}' and the (final) elevation of the water table is at the interface between regions A and B (el 396 ft (120.7 m). The relationship for the rebound r at a given elevation becomes

$$r = \int_o^{h_3} \frac{2}{m_{ur}} \left[\left(\frac{\gamma_{t-A} * h_1 + \gamma_{b-B} * h_2 + \gamma_{b-B} * z}{\sigma_a} \right)^{1/2} - \left(\frac{\gamma_{t-A} * h_1 + \gamma_{t-B} * h_2 + \gamma_{t-B} * z}{\sigma_a} \right)^{1/2} \right] dz$$

Designating the first and second terms inside the integral as terms A and B, respectively,

$$r = r_A - r_B \tag{H1}$$

The contribution of term A to the total rebound r, designated r_A, is given by

$$r_A = \int_o^{h_3} \frac{2}{m_{ur}} q^{1/2} \, dz$$

where the variable q is defined as

$$q = \frac{\gamma_{t-A} * h_1 + \gamma_{b-B} * h_2 + \gamma_{b-B} * z}{\sigma_a}$$

Differentiating q

$$\frac{dq}{dz} = \frac{\gamma_{b-B}}{\sigma_a} \quad or \quad dz = \frac{\sigma_a}{\gamma_{b-B}} dq$$

The rebound term A in terms of the variable q is

$$r_A = \int_o^{h_3} \frac{2}{m_{ur}} q^{1/2} * \frac{\sigma_a}{\gamma_{b-B}} dq$$

Evaluating the integral,

$$r_A = \frac{2}{m_{ur}} * \frac{2}{3} q^{3/2} * \frac{\sigma_a}{\gamma_{b-B}} \Big|_o^{h_3}$$

Replacing the variable q and evaluating the limits,

$$r_A = \frac{4}{3m_{ur}} \left[\left(\frac{\gamma_{t-A} * h_1 + \gamma_{b-B} * h_2 + \gamma_{b-B} h_3}{\sigma_a} \right)^{3/2} * \frac{\sigma_a}{\gamma_{b-B}} - \left(\frac{\gamma_{t-A} * h_1 + \gamma_{b-B} * h_2 + o}{\sigma_a} \right)^{3/2} * \frac{\sigma_a}{\gamma_{b-B}} \right]$$

$$r_A = \frac{4}{3m_{ur}} * \frac{1}{\gamma_{b-B}} * \frac{1}{\sigma_a^{1/2}} \left[\left(\gamma_{t-A} * h_1 + \gamma_{b-B} * h_2 + \gamma_{b-B} * h_3 \right)^{3/2} - \left(\gamma_{t-A} * h_1 + \gamma_{b-B} * h_2 \right)^{3/2} \right] \quad \text{(H2)}$$

The contribution to total rebound by term B, designated r_B is given by

$$r_B = \int_o^{h_3} \frac{2}{m_{ur}} \left[\left(\frac{\gamma_{t-A} * h_1 + \gamma_{t-B} * h_2 + \gamma_{t-B} * z}{\sigma_a} \right)^{1/2} \right] dz$$

Introducing the variable t, r_B becomes

$$r_B = \int_o^{h_3} \frac{2}{m_{ur}} t^{1/2} \, dz$$

where

$$t = \frac{\gamma_{t-A} * h_1 + \gamma_{t-B} * h_2 + \gamma_{t-B} * z}{\sigma_a}$$

and

$$\frac{dt}{dz} = \frac{\gamma_{t-B}}{\sigma_a} \quad or \quad dz = \frac{\sigma_a}{\gamma_{t-B}} \, dt$$

The complete relationship for r_B is

$$r_B = \int_o^{h_3} \frac{2}{m_{ur}} t^{1/2} * \frac{\sigma_a}{\gamma_{t-B}} dt$$

Evaluating the integral

$$r_B = \frac{2}{m_{ur}} * \frac{\sigma_a}{\gamma_{t-B}} * \frac{2}{3} t^{3/2} \Big|_o^{h_3}$$

Replacing the variable t and evaluating the limits,

$$r_b = \frac{4}{3m_{ur}} \left[\left(\frac{\gamma_{t-A} * h_1 + \gamma_{t-B} * h_2 + \gamma_{t-B} h_3}{\sigma_a} \right)^{3/2} * \frac{\sigma_a}{\gamma_{t-B}} - \left(\frac{\gamma_{t-A} * h_1 + \gamma_{t-B} * h_2 + o}{\sigma_a} \right)^{3/2} * \frac{\sigma_a}{\gamma_{t-B}} \right]$$

$$r_B = \frac{4}{3m_{ur}} * \frac{1}{\gamma_{t-B}} * \frac{1}{\sigma_a^{1/2}} \left[\left(\gamma_{t-A} * h_1 + \gamma_{t-B} * h_2 + \gamma_{t-B} * h_3 \right)^{3/2} - \left(\gamma_{t-A} * h_1 + \gamma_{t-B} * h_2 \right)^{3/2} \right] \quad \text{(H3)}$$

The total rebound r at the lift elevation at height h_3 (within region B) due to the postconstruction rise in the hydrostatic water table below this elevation is given by

$$r = r_A - r_B \quad \text{(H1)}$$

with

$$r_A = \frac{4}{3m_{ur}} * \frac{1}{\gamma_{b-B}} * \frac{1}{\sigma_a^{1/2}} \left[\left(\gamma_{t-A} * h_1 + \gamma_{b-B} * h_2 + \gamma_{b-B} * h_3 \right)^{3/2} - \left(\gamma_{t-A} * h_1 + \gamma_{b-B} * h_2 \right)^{3/2} \right] \quad \text{(H2)}$$

and

$$r_B = \frac{4}{3m_{ur}} * \frac{1}{\gamma_{t-B}} * \frac{1}{\sigma_a^{1/2}} \left[\left(\gamma_{t-A} * h_1 + \gamma_{t-B} * h_2 + \gamma_{t-B} * h_3 \right)^{3/2} - \left(\gamma_{t-A} * h_1 + \gamma_{t-B} * h_2 \right)^{3/2} \right] \quad \text{(H3)}$$

If the total unit weights for the two regions are the same ($\gamma_t = \gamma_{t-A} = \gamma_{t-B}$ and with $\gamma_b = \gamma_t - \gamma_w$), then Equations H2 and H3 for terms r_A and r_B of r at height h_3 become

$$r_A = \frac{4}{3m_{ur}} * \frac{1}{\gamma_b} * \frac{1}{\sigma_a^{1/2}} \left[(\gamma_t * h_1 + \gamma_b * h_2 + \gamma_b * h_3)^{3/2} - (\gamma_t * h_1 + \gamma_b * h_2)^{3/2} \right] \quad \text{(H4)}$$

and

$$r_B = \frac{4}{3m_{ur}} * \frac{1}{\gamma_t} * \frac{1}{\sigma_a^{1/2}} \left[(\gamma_t * h_1 + \gamma_t * h_2 + \gamma_t * h_3)^{3/2} - (\gamma_t * h_1 + \gamma_t * h_2)^{3/2} \right] \quad \text{(H5)}$$

Rebound Within Region A

The rebound at the lift elevation at height $[h_2 + h_3]$ (in region A) of the Figure H3 soil column is calculated using

$$r = \int_o^{h_2 + h_3} \epsilon_z \, dz = \int_o^{h_2} \epsilon_z \, dz + \int_{h2}^{h3} \epsilon_z \, dz$$

The distribution of ϵ_z over depth $[h_2 + h_3]$ is due to the postconstruction rise in the hydrostatic water table below height h_3. The total rebound r is given as

$$r = r_1 + r_2$$

where

$$r_1 = \int_o^{h2} \epsilon_z dz$$

and

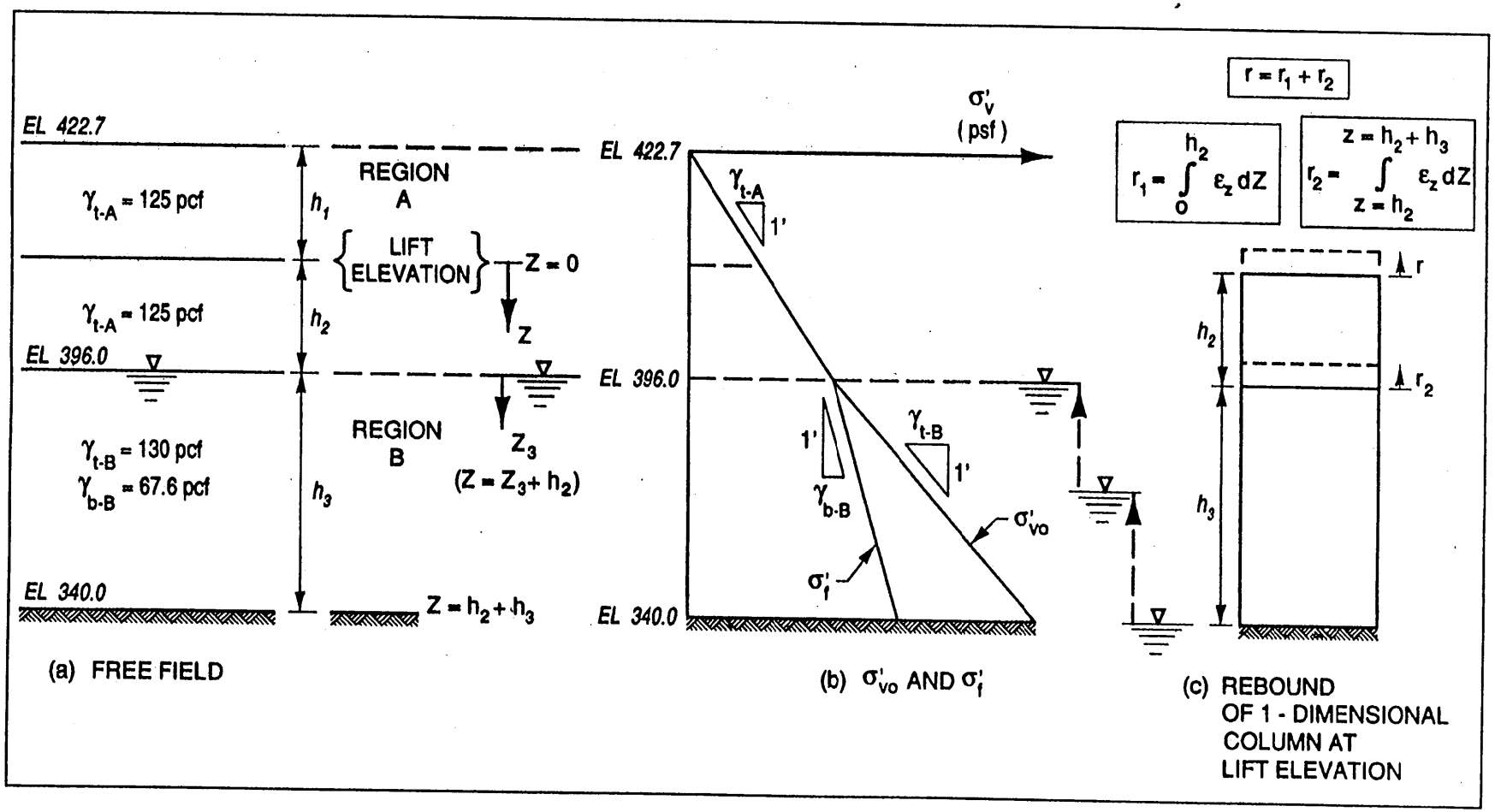

Figure H3. Lift elevation in region A with a postconstruction rise in the water table (1 ft = 0.305 m, 1 pcf = 16.018 kg/m^3)

$$r_2 = \int_{z=h_2}^{z=h_2+h_3} \epsilon_z \, dz$$

The first rebound term r_1 addresses the vertical strains ϵ_z in region A, while the second rebound term r_2 addresses the vertical strains ϵ_z in region B.

Figure H3 shows the distributions of the initial and final vertical effective stresses σ'_{vo} and σ'_f in region A to be equal to

$$\sigma'_{vo} = \gamma_{t-A} * h_1 + \gamma_{t-A} * z$$

and

$$\sigma'_f = \gamma_{t-A} * h_1 + \gamma_{t-A} * z$$

Introducing Janbu's relationship for vertical strain ϵ_z (Equation D2), the rebound term r_1 becomes

$$r_1 = \int_o^{h_2} \frac{2}{m_{ur}} \left[\left(\frac{\gamma_{t-A} h_1 + \gamma_{t-A} z}{\sigma_a} \right)^{1/2} - \left(\frac{\gamma_{t-A} h_1 + \gamma_{t-A} z}{\sigma_a} \right)^{1/2} \right] dz = 0$$

because σ'_{vo} equals σ'_f.

Thus, the total rebound is defined as

$$r = r_2 = \int_{z=h_2}^{z=h_2+h_3} \epsilon_z \, dz$$

The second rebound term s_2 addresses the vertical strains ϵ_z in region B, of height h_3 (Figure H3). Introducing Janbu's relationship for vertical strain ϵ_z (Equation D2),

$$r_2 = \int_{z=h_2}^{z=h_2+h_3} \frac{2}{m_{ur}} \left[\left(\frac{\sigma'_f}{\sigma_a} \right)^{1/2} - \left(\frac{\sigma'_{vo}}{\sigma_a} \right)^{1/2} \right] dz$$

with

$$\sigma'_{vo} = \gamma_{t-A} h_1 + \gamma_{t-A} h_2 + \gamma_{t-B} z_3$$

and

$$\sigma'_f = \gamma_{t-A} h_1 + \gamma_{t-A} h_2 + \gamma_{b-B} z_3$$

where

$$z_3 = z - h_2$$

Rearranging,

$$z = z_3 + h_2$$

Differentiating z

$$\frac{dz}{dz_3} = 1 \quad or \quad dz = dz_3$$

Note that σ'_f is less than σ_{vo}'. The rebound r (and term r_2) is

$$r = r_2 = \int_{z_3 + h_2 = h_2}^{z_3 + h_2 = h_2 + h_3} \frac{2}{m_{ur}} \left[\left(\frac{\sigma'_f}{\sigma_a} \right)^{1/2} - \left(\frac{\sigma'_{vo}}{\sigma_a} \right)^{1/2} \right] dz_3$$

or, equivalently,

$$r = r_2 = \int_{z_3 = o}^{z_3 = h_3} \frac{2}{m_{ur}} \left[\left(\frac{\sigma'_f}{\sigma_a} \right)^{1/2} - \left(\frac{\sigma'_{vo}}{\sigma_a} \right)^{1/2} \right] dz_3$$

Replacing σ'_f and σ'_{vo}

$$r = r_2 = \int_o^{h_3} \frac{2}{m_{ur}} \left[\left(\frac{\gamma_{t-A} h_1 + \gamma_{t-A} h_2 + \gamma_{b-B} z_3}{\sigma_a} \right)^{1/2} - \left(\frac{\gamma_{t-A} h_1 + \gamma_{t-A} h_2 + \gamma_{t-B} z_3}{\sigma_a} \right)^{1/2} \right] dz_3$$

Designating the first and second terms inside the integral as terms r_C and r_D respectively,

$$r = r_2 = r_c - r_D$$

The contribution of term C to the rebound r (or term r_2), designated r_C is given by

$$r_c = \int_o^{h_3} \frac{2}{m_{ur}} \left(\frac{\gamma_{t-A} h_1 + \gamma_{t-A} h_2 + \gamma_{b-B} z_3}{\sigma_a} \right)^{1/2} dz_3$$

Let

$$u = \frac{\gamma_{t-A} h_1 + \gamma_{t-A} h_2 + \gamma_{b-B} z_3}{\sigma_a}$$

Differentiating u

$$\frac{du}{dz_3} = \frac{\gamma_{b-B}}{\sigma_a} \quad or \quad dz_3 = \frac{\sigma_a}{\gamma_{b-B}} du$$

The rebound term r_C in terms of the variable u is

$$r_c = \int_o^{h_3} \frac{2}{m_{ur}} u^{1/2} dz_3 = \int_o^{h_3} \frac{2}{m_{ur}} u^{1/2} * \frac{\sigma_a}{\gamma_{b-B}} * du$$

Evaluating the integral,

$$r_c = \frac{2}{m} * \frac{2}{3} * u^{3/2} * \frac{\sigma_a}{\gamma_{b-B}} \Big|_0^{h_3}$$

Replacing the transformation variable u and evaluating the limits,

$$r_c = \frac{4}{3} * \frac{1}{m_{ur}} * \frac{\sigma_a}{\gamma_{b-B}} \left[\left(\frac{\gamma_{t-A} h_1 + \gamma_{t-A} h_2 + \gamma_{b-B} h_3}{\sigma_a} \right)^{3/2} - \left(\frac{\gamma_{t-A} h_1 + \gamma_{t-A} h_2}{\sigma_a} \right)^{3/2} \right]$$

$$r_c = \frac{4}{3} * \frac{1}{m_{ur}} * \frac{1}{\gamma_{b-B}} * \frac{1}{\sigma_a^{1/2}} * \left[\left(\gamma_{t-A} h_1 + \gamma_{t-A} h_2 + \gamma_{b-B} h_3 \right)^{3/2} - \left(\gamma_{t-A} h_1 + \gamma_{t-A} h_2 \right)^{3/2} \right]$$

The contribution to rebound r (and term r_2) by term D, designated r_D, is given by

$$r_D = \int_o^{h_3} \frac{2}{m_{ur}} \left[\left(\frac{\gamma_{t-A} h_1 + \gamma_{t-A} h_2 + \gamma_{t-B} z_3}{\sigma_a} \right)^{1/2} \right] dz_3$$

Let

$$\nu = \frac{\gamma_{t-A} h_1 + \gamma_{t-A} h_2 + \gamma_{t-B} z_3}{\sigma_a}$$

Differentiating υ

$$\frac{d\nu}{dz_3} = \frac{\gamma_{t-B}}{\sigma_a} \quad or \quad dz_3 = \frac{\sigma_a}{\gamma_{t-B}} d\nu$$

The complete relationship for r_D is

$$r_D = \int_o^{h_3} \frac{2}{m_{ur}} \nu^{1/2} \frac{\sigma_a}{\gamma_{t-B}} d\nu$$

Evaluating the integral

$$r_D = \frac{2}{m_{ur}} * \frac{2}{3} * \frac{\sigma_a}{\gamma_{t-B}} * [v^{3/2}]\Big|_o^{h_3}$$

Replacing the variable υ and evaluating the limits,

$$r_D = \frac{4}{3} * \frac{1}{m_{ur}} * \frac{\sigma_a}{\gamma_{t-B}} * \left[\left(\frac{\gamma_{t-A} h_1 + \gamma_{t-A} h_2 + \gamma_{t-B} h_3}{\sigma_a} \right)^{3/2} - \left(\frac{\gamma_{t-A} h_1 + \gamma_{t-A} h_2}{\sigma_a} \right)^{3/2} \right]$$

Simplifying

$$r_D = \frac{4}{3 m_{ur}} * \frac{1}{\gamma_{t-B}} * \frac{1}{\sigma_a^{1/2}} * \left[\left(\gamma_{t-A} h_1 + \gamma_{t-A} h_2 + \gamma_{t-B} h_3 \right)^{3/2} - \left(\gamma_{t-A} h_1 + \gamma_{t-A} h_2 \right)^{3/2} \right]$$

Recall that the rebound r (or term r_2) is given by

$$r = r_2 = r_c - r_D$$

Introducing terms r_C and r_D,

$$r_2 = \frac{4}{3\, m_{ur}} * \frac{1}{\gamma_{b-B}} * \frac{1}{\sigma_a^{1/2}} \left[\left(\gamma_{t-A} h_1 + \gamma_{t-A} h_2 + \gamma_{b-B} h_3 \right)^{3/2} - \left(\gamma_{t-A} h_1 + \gamma_{t-A} h_2 \right)^{3/2} \right]$$

$$- \frac{4}{3 m_{ur}} * \frac{1}{\gamma_{t-B}} * \frac{1}{\sigma_a^{1/2}} \left[\left(\gamma_{t-A} h_1 + \gamma_{t-A} h_2 + \gamma_{t-B} h_3 \right)^{3/2} - \left(\gamma_{t-A} h_1 + \gamma_{t-A} h_2 \right)^{3/2} \right] \qquad \text{(H6)}$$

If the total unit weights for the two regions are the same ($\gamma_t = \gamma_{t-A} = \gamma_{t-B}$ and $\gamma_b = \gamma_t - \gamma_w$), then Equation H6 for total rebound r at height $[h_2 + h_3]$ becomes

$$r = r_2 = \frac{4}{3\ m_{ur}} * \frac{1}{\gamma_b} * \frac{1}{\sigma_a^{1/2}} \left[\left(\gamma_t h_1 + \gamma_t h_2 + \gamma_b h_3 \right)^{3/2} \right.$$

$$\left. - \left(\gamma_t h_1 + \gamma_t h_2 \right)^{3/2} \right] \qquad \text{(H7)}$$

$$- \frac{4}{3 m_{ur}} * \frac{1}{\gamma_t} * \frac{1}{\sigma_a^{1/2}} \left[(\gamma_t h_1 + \gamma_t h_2 + \gamma_t h_3)^{3/2} - (\gamma_t h_1 + \gamma_t h_2)^{3/2} \right]$$

It can be shown that Equation H7 for rebound in region A at height $[h_2 + h_3]$ is consistent with Equations H1, H4, and H5 for rebound in region B at height h_3 by specifying a common elevation within the backfill for use in each of the equations (e.g., the elevation that is common to the bottom of region A and the top of region B). At the common elevation of 396 ft (120.7 m), h_2 is equal to zero (refer to the definitions for h_2 in regions B and A in Figures H2 and H3, respectively).

REPORT DOCUMENTATION PAGE

Form Approved
OMB No. 0704-0188

1. AGENCY USE ONLY *(Leave blank)*	2. REPORT DATE	3. REPORT TYPE AND DATES COVERED
	July 1997	Final report

4. TITLE AND SUBTITLE
Evaluating the Stability of Existing Massive Concrete Gravity Structures Founded on Rock

5. FUNDING NUMBERS

6. AUTHOR(S)
Robert M. Ebeling, Michael E. Pace, Ernest E. Morrison, Jr.

7. PERFORMING ORGANIZATION NAME(S) AND ADDRESS(ES)
U.S. Army Engineer Waterways Experiment Station
3909 Halls Ferry Road, Vicksburg, MS 39180-6199;
N.A.S. Fallon, 4755 Pasture Road, Fallon, NV89496

8. PERFORMING ORGANIZATION REPORT NUMBER
Technical Report
REMR-CS-54

9. SPONSORING/MONITORING AGENCY NAME(S) AND ADDRESS(ES)
U.S. Army Corps of Engineers
Washington, DC 20314-1000

10. SPONSORING/MONITORING AGENCY REPORT NUMBER

11. SUPPLEMENTARY NOTES

Available from National Technical Information Service, 5285 Port Royal Road, Springfield, VA 22161.

12a. DISTRIBUTION/AVAILABILITY STATEMENT

Approved for public release; distribution is unlimited

12b. DISTRIBUTION CODE

13. ABSTRACT (*Maximum 200 words*)

The U.S. Army Corps of Engineers is responsible for designing and maintaining a large number of navigation and flood-control structures. Many of the older massive concrete gravity hydraulic structures are being examined to determine if rehabilitation is required to meet stability criteria. The procedures currently used for evaluating the safety of existing massive hydraulic structures are the conventional equilibrium methods, which are the same general methods used in the design of these structures. Because the conditions of equilibrium are insufficient for a complete analysis of all aspects of structure-foundation interaction involved in the stability and performance of these structures (soil-structure-foundation interaction in the case of earth retaining structures), these conventional equilibrium methods necessarily involve assumptions regarding aspects of the loading forces and the resisting forces that act on the hydraulic structures.

Differences between actual field performance and calculations from conventional analysis have been noted for some existing hydraulic structures. Conventional design methods were developed based largely on classical limit equilibrium analysis without regard to deformation-related concepts. Today, analytical tools such as the finite element method (FEM) are available which consider the manner in which the loads and resistance are developed as a function of

14. SUBJECT TERMS

Concrete gravity dams	Rock joints
Earth pressures	Stability
Earth retaining structures	Uplift pressures

15. NUMBER OF PAGES
265

16. PRICE CODE

17. SECURITY CLASSIFICATION OF REPORT	18. SECURITY CLASSIFICATION OF THIS PAGE	19. SECURITY CLASSIFICATION OF ABSTRACT	20. LIMITATION OF ABSTRACT
UNCLASSIFIED	UNCLASSIFIED		

13. ABSTRACT (Concluded).

the stiffnesses of the foundation rock, the structure-foundation interface, and rock joints within the foundation. These analytical tools provide a means to evaluate the conventional equilibrium-based design methods used to evaluate the safety of existing hydraulic structures, and specifically, to identify and investigate key assumptions used in safety calculations from the conventional analysis.

The research investigation described in this report was undertaken to study the behavior of gravity hydraulic structures using the FEM of analysis and to compare the results of the finite element (FE) analysis with the results of conventional analysis. Specifically, the finite element method of analysis of rock-founded, massive concrete hydraulic structures and gravity retaining structures was used to study:

a. The magnitude and distribution of stresses developed along the base of the monolith.
b. The progressive development of excessive tensile stresses which result in a gap being formed at the interface between the base of the monolith and the rock foundation.
c. The magnitude of the stabilizing shear force developed on the back of a gravity earth retaining monolith with back geometry comprising a vertical lower section and a sloped upper section.
d. The magnitude and distribution of uplift pressures developed along the base of the monolith.
e. Progressive joint closure and opening within the rock foundation of a massive concrete dam and its impact on uplift pressures with the raising and lowering of the reservoir.

The evaluation of the stability of rock-founded, massive concrete hydraulic structures and gravity retaining structures using the FEM of analysis is well established in the case of concrete monoliths and rock foundations which are modeled as continuous media and are in full contact along the base to foundation interface. However, the FE procedure of analysis has only recently been applied to massive concrete hydraulic structures that are loaded so heavily that excessive tensile stresses develop and result in a gap being formed along the monolith-to-foundation interface and/or within the foundation. Three finite-element-based analytical procedures for analyzing hydraulic structures which may exhibit cracking during loading have been made available since the conclusion of the first Repair, Evaluation, Maintenance, and Rehabilitation (REMR) Research Program. During the first REMR Research Program, SOILSTRUCT-ALPHA was developed to model the separation of the base of a monolith from its rock foundation during loading using interface elements between the concrete monolith and the rock foundation. Another procedure is based on smeared crack theory and has been implemented in the computer program CG-DAMS. The third procedure uses discrete crack theory and has been implemented in the computer program MERLIN.

CG-DAMS, MERLIN, and SOILSTRUCT-ALPHA were used during this research to investigate the response of a massive concrete hydraulic structure to loadings which would induce cracking along the monolith-to-foundation interface according to calculations using the conventional equilibrium-based method of analysis of the structure. The hydraulic structure used in this comparative study is a gravity retaining wall at Locks 27 on the Mississippi River at St. Louis, MO.

A key stage in a stability evaluation of lock monoliths is the calculation (or assignment) of uplift pressures along the base of the hydraulic structure and/or along a critical rock joint or joints within the foundation. Four procedures widely used by engineers to calculate uplift pressures along the concrete monolith-to-rock foundation interface are reviewed using a series of example problems which illustrate key aspects of the procedures used to calculate uplift pressures.

Additionally, uplift pressures within rock joint(s) are coupled with changes in rock joint aperture through the cubic law for flow. A complete example showing the interaction between the gravity dam, rock foundation, and rock joint and the uplift pressures resulting from changes in applied loadings (i.e., changes in reservoir elevation) is included. As the rock joint aperture opens and closes with the applied loading, the uplift pressures within the rock joint varies. The results show the distribution of uplift pressures along the tight joint to be nonlinear and that the shape of the uplift distribution varies with pool elevation. This example shows that changes in rock joint aperture impacts the distribution of uplift pressures in the case of tight joints, consistent with observations made on existing hydraulic structures.